

**A Thesis for the Degree of Doctor of Philosophy**

**A second-order Boltzmann-based continuum  
model for simulation of dusty gas flows in non-  
equilibrium using a discontinuous Galerkin  
method**

**By**

**Omid Ejtehad**

**Department of Mechanical and Aerospace Engineering**

**Graduate School**

**Gyeongsang National University**

August, 2018

**A second-order Boltzmann-based continuum  
model for simulation of dusty gas flows in non-  
equilibrium using a discontinuous Galerkin  
method**

**A Dissertation Submitted to the Faculty of the Graduate School of  
the Gyeongsang National University**

**By  
Omid Ejtehad**

**In partial fulfillment of the requirements for the degree of  
Ph.D. in Engineering**

**August, 2018**

**Prof. Rho Shin Myong, Dissertation Supervisor**

**Approved by committees of the Graduate School of Gyeongsang National  
University in partial fulfilment of the requirements for the degree of  
Doctor of Philosophy**

**Dissertation Committee:**

Prof. Dr. Jae Hyun Park

Chairman

Prof. Dr. Soo-Yong Cho

Dr. Ji Hong Kim

Prof. Dr. Rakesh Kumar Mathpal

Prof. Dr. Rho Shin Myong

Supervisor

**Date: 2018.07**

**Department of Mechanical and Aerospace Engineering  
Graduate School  
Gyeongsang National University**

# Acknowledgement

I would like to extend my sincere gratitude to all the individuals who contributed to completion of this undertaking.

Firstly, I would like to thank Prof. Rho Shin Myong for providing me the opportunity to pursue my studies under his supervision. I am thankful for all the genuine ideas he provided, the research skills and techniques he taught me and above all, the paradigm changes he caused in my outlook on research. He is a great mentor in research and life.

I wish to thank the members of my dissertation committee: Professor Jae Hyun Park and Professor Soo-Yong Cho and from Gyeongsang National University, South Korea; Prof. Rakesh Kumar Mathpal from Indian Institute of Technology Kanpur, India, and Dr. Ji Hong Kim of Korea Aerospace Industries, LTD for their constructive feedback that helped me to finalize this thesis.

Thanks are also due to the funding of the Brain Korean 21 plus (BK 21+) program as well as National Research Foundation (NRF) of South Korea (NRF 2015-M1A3A3A02, 2017-R1A5A1015311) in terms of scholarships and grants.

I am also grateful to my fellow lab mates in Aerospace Computational Modeling Laboratory specially my Korean friends who made life in Korea for me as a foreigner much easier. I can't imagine going through all the administrative works either in university or daily life without their help. Moreover, I will not forget those many speechless nights we spent in lab together working on the projects to meet the deadlines. A special thanks goes to my Iranian friend, Amin Rahimi, with whom I shared the joy and bitterness of research in almost all stages of my Ph.D.

My sincere thanks also goes to the Iranian community in Jinju city, who were a source of energy in times when academic life was not smooth. I would like to specifically thank Vahid Hamdipour, who was beside me like a brother in hardships.

I place on record my sincere gratitude to my roommate in my first years of life out of the country (and my lifetime friend), Punyakishore Maibam, from whom I learned remarkable lessons.

I would take this opportunity to thank my grandfather who was an inspiration. He left us before I move to Korea, however, he was always in my heart during these years. I am also grateful to my grandmothers who kept in touch while I was miles and miles far from home. I was lucky to have the spiritual supports of my two loving grandmothers. I also owe a great debt of gratitude to my parents. It is not easy to put in words how grateful I am for all the supports I got from my parents during the course of Ph.D. and all the other stages of life.

Doing a Ph.D. and doing it in a foreign country, regardless of its scientific achievements and failures was a pleasant experience and I am thankful to all the people who were part of this experience or motivated me to take the first steps on this journey.

# **Dedication**

*To my parents*

*(Thanks for your never-ending care and support)*

# Table of Contents

<b>Acknowledgement .....</b>	<b>iii</b>
<b>Dedication .....</b>	<b>v</b>
<b>Table of Contents .....</b>	<b>vi</b>
<b>List of figures .....</b>	<b>xiii</b>
<b>List of tables.....</b>	<b>xxi</b>
<b>Nomenclatures .....</b>	<b>xxiii</b>
<b>Abstract.....</b>	<b>xxvii</b>
<b>Abstract in Korean.....</b>	<b>xxix</b>
<b>Chapter 1. Introduction.....</b>	<b>1</b>
1.1 Motivation .....	1
1.2 Background .....	3
1.2.1 Review of important works regarding ‘plume and plume impingement simulation’ .....	4
1.2.2 Review of important works regarding ‘ <i>erosion modeling</i> ’ .....	7
1.2.3 Review of important works regarding ‘rarefied multiphase flow’ .....	7
1.2.4 Other important works regarding the Lunar landing problem.....	8
1.3 Outline.....	9
<b>Chapter 2. Multiphase Flows .....</b>	<b>10</b>
2.1 A general categorization of multiphase flows.....	10

2.1.1 Gas-liquid or liquid-liquid flows .....	10
2.1.2 Gas-solid flows .....	11
2.1.3 Liquid-solid flows .....	12
2.1.4 Three-phase flows .....	12
2.2 Gas particulate flows .....	12
2.3 Fundamental definitions of gas-particle flows .....	15
2.3.1 The volume fraction .....	15
2.3.2 Particle spacing.....	16
2.3.3 Response times .....	16
2.3.4 Concentration and loading.....	17
2.3.5 Stokes number .....	17
<b>Chapter 3. Kinetic theory of gases .....</b>	<b>19</b>
3.1 Degree of non-equilibrium.....	19
3.1.1 Conventional classification of non-equilibrium regimes .....	21
3.1.2 Refining the conventional classification of non-equilibrium regimes .....	22
3.2 Singlet probability distribution function and macroscopic properties .....	25
3.3 Boltzmann transport equation (BTE) .....	27
3.3.1 <i>H</i> theorem .....	28
3.3.2 Collision invariants.....	29
3.4 Theory and simulation methods .....	29
3.4.1 Pure (or semi-simulation) methods .....	30

3.4.2 PDE-based approach .....	33
3.5 Extended moment equations .....	36
3.5.1 Conservation laws from Boltzmann equation .....	36
3.5.2 Boltzmann-based constitutive relationships .....	37
3.5.3 Extension to diatomic and polyatomic .....	44
<b>Chapter 4. Mathematical modeling of multiphase gas-particles flows.....</b>	<b>48</b>
4.1 A general categorization of models for multiphase flows .....	48
4.2 Model selection .....	49
4.3 Balanced laws (for the generic two-fluid model).....	54
4.3.1 Assumptions of two-fluid dusty gas model .....	54
4.3.2 Conservation laws .....	56
4.3.3 Three-dimensional conservation laws with axial symmetry .....	56
4.4 Constitutive relations .....	57
4.4.1 Volume fraction closure .....	58
4.4.2 Equation of state .....	58
4.4.3 Drag forces on spherical particles .....	58
4.4.4 Non-conserved variable of the gas phase .....	61
4.4.5 Non-conserved variables of the solid phase .....	63
4.5 Dimensionless form of the governing equations.....	70
4.5.1 The physical interpretation of non-dimensional parameters .....	72
4.6 Erosion Modeling.....	74

4.6.1 Stationary particle on the sediment bed.....	74
4.6.2 Forces on an entrained particle.....	75
4.6.3 Modes of particle motion.....	80
4.6.4 Phenomenology of soil erosion on the Lunar surface .....	82
<b>Chapter 5. Numerical approach .....</b>	<b>86</b>
5.1 Fundamentals of numerical simulation .....	86
5.1.1 Discretization methods .....	86
5.1.2 High order methods .....	88
5.2 A numerical framework based on a modal unstructured discontinuous Galerkin method.....	89
5.2.1 Review of literature .....	89
5.2.2 A modal DG formulation for inviscid (convection dominated) flows .....	91
5.2.3 A modal DG formulation for viscous (convection-diffusion problems) flows .....	95
5.3 Elemental transformation .....	96
5.3.1 One-dimensional elemental transformation .....	96
5.3.2 Two-dimensional elemental transformation.....	97
5.3.3 Three-dimensional elemental transformation.....	100
5.4 Basis functions .....	101
5.4.1 Basis functions for one-dimensional space .....	102
5.4.2 Basis functions for two-dimensional space .....	104
5.4.3 Basis functions for two-dimensional space .....	106

5.5 Numerical integration.....	106
5.6 Inviscid and viscous numerical flux functions.....	109
5.7 Positivity preserving scheme.....	112
5.8 Monotonicity preserving scheme .....	113
5.9 Boundary conditions .....	114
5.10 Novel source terms treatment.....	114
5.11 The numerical algorithm for solving constitutive equations.....	117
<b>Chapter 6. Numerical experiments on zeroth-order Euler-type systems of equation.....</b>	<b>122</b>
6.1 One-dimensional dusty gas flows .....	122
6.1.1 Verification study in the single-phase case (1-D) .....	122
6.1.2 Sod shock tube problem in dusty gas flows .....	124
6.1.3 Composite wave structures in the Sod problem of dusty gas flows .....	126
6.2 Two-dimensional dusty gas flows.....	133
6.2.1 Verification study in the single-phase case (2-D) .....	133
6.2.2 2-D explosion problem in dusty gas flows .....	135
6.2.3 Asymmetric explosion problem in dusty gas flows .....	138
6.2.4 2-D compression corner problem in dusty gas flow.....	143
6.2.5 Axisymmetric particle-laden under-expanded jet .....	153
<b>Chapter 7. Numerical experiments on first-order NSF-type systems of equation.....</b>	<b>157</b>

7.1 Flow past NACA0012 airfoil .....	157
7.2 Flow past triangular prism .....	164
7.2.1 Pure gas simulations .....	168
7.2.2 Dusty gas simulations.....	178
7.3 Axisymmetric particle-laden under-expanded jet .....	191
7.4 Tone producing under-expanded impinging jets.....	194
<b>Chapter 8. Numerical experiments on second-order NCCR-type systems of equation.....</b>	<b>199</b>
8.1 The problem of Lunar landing .....	199
8.2 Prevailing physics .....	200
8.3 The approach for simulation of the Lunar landing problem .....	201
8.4 Pure gas simulations.....	206
8.5 Verification of results with DSMC solutions for single-phase flow (pure gas).....	207
8.6 Verification of results with DSMC solutions for multiphase flow (dusty gas).....	212
8.6.1 Effect of particle diameter .....	216
8.6.2 Effect of pressure ratio .....	218
8.6.3 Effect of cohesive strength .....	218
8.6.4 Effect of erosion model parameters.....	219
8.7 Application of commercial CFD software package (FLUENT) .....	221
8.8 Applications of the model in pressure impactors .....	228
<b>Chapter 9. Conclusion and future works.....</b>	<b>232</b>

9.1 Concluding remarks .....	232
9.1.1 Conclusions regarding the zeroth-order constitutive relationships .....	232
9.1.2 Conclusions regarding the first-order constitutive relationships.....	234
9.1.3 Conclusions regarding the second-order constitutive relationships .....	235
9.2 Future works.....	236
<b>Appendix A. List of Moon and Mars missions with a soft landing .....</b>	<b>239</b>
<b>Appendix B. Derivation of conservation laws from the Boltzmann transport equation.....</b>	<b>242</b>
<b>Appendix C. Derivation of constitutive relations from the Boltzmann transport equation.....</b>	<b>247</b>
<b>Appendix D. Applied basis functions and integration process of the source term vector for triangular elements .....</b>	<b>250</b>
<b>Bibliography .....</b>	<b>253</b>

# List of figures

Fig. 1 Flow patterns (right) and flow pattern map (left) for vertical pipe flow of air and water. Reprinted from [57] with permission.....	11
Fig. 2 Various applications of dusty gas flows .....	13
Fig. 3 The realms of fluid flow regimes according to different parameters .....	23
Fig. 4 Definition of the ranges of the $N_\delta$ parameter overlaid with the classification of [94]. .....	25
Fig. 5 Classification of multiphase flows and the coupling effects based on particulate loading. Reprinted from [118] with permission.....	51
Fig. 6 The range of encountered regimes in the Lunar landing problem overlaid on the classification of the particulate flows based on number density and particles volume fraction .....	53
Fig. 7 A typical phase diagram determining the transition between granular flow regimes as a function of particle diameter. Reprinted from [144] with permission. ....	64
Fig. 8 Graphical categorization of different regions with various specifications. Regions 1-3 are quantified in the Table 9. ....	65
Fig. 9 Comparison of the expressions from equation (126) with data from MD simulations. Adapted from [138] with permission.....	70
Fig. 10 The various forces acting on particles on a sediment bed under the action of an external flow. Reprinted from [158] with permission. ....	75
Fig. 11 The physical mechanism of a) aerodynamic drag force, b) aerodynamic lift force and c) Magnus force on a spinning particle. Reprinted from [159] with permission. ....	76
Fig. 12 Aerodynamic drag coefficient for different flow regime in terms of Reynolds number. Reprinted from [159] with permission. ....	77

Fig. 13 Suspension, saltation, and creep of grains during wind erosion. Reprinted from [159] with permission.....	81
Fig. 14. Erosion mechanisms and their importance in lunar landing problem .....	84
Fig. 15 Structure of a numerical simulation. Reproduced based on [169].....	87
Fig. 16 Coordinate transformation .....	94
Fig. 17 Schematic diagram of the linear mapping of the 1D element.....	97
Fig. 18 Schematic diagram of the linear mapping of the 2D quadrilateral element. ....	98
Fig. 19 Schematic diagram of the linear mappings of the 2D triangular element. ....	100
Fig. 20 Schematic diagram of the linear mapping of the 3D tetrahedron element .....	101
Fig. 21 Comparison of typical mass matrices corresponding to Lagrange (right) and Legendre (left) bases.....	102
Fig. 22 Legendre polynomial space .....	104
Fig. 23 Polynomial space in terms of the Pascal's triangle of the full tensor product for rectangular elements (up to polynomial order of $P=6$ ). .....	105
Fig. 24 Polynomial space in terms of the Pascal's triangle of the full tensor product for triangular elements (up to polynomial order of $P=6$ ).....	106
Fig. 25 Schematic representation of number and location of required quadrature points used in numerical integration for (a) 1D elements, (b) 2D quadrilateral elements, (c) 2D triangular elements .....	108
Fig. 26 Schematic representation of number and location of required quadrature points used in numerical integration in a 3D tetrahedron element .....	109
Fig. 27. Comparison of various numerical fluxes for smooth solution of Euler equation; (left) profile, (right) Euclidean norm of density .....	123
Fig. 28. Schematic of the shock tube problem in dusty gas (pure gas versus dusty gas). 125	

Fig. 29. Solutions of the Sod's shock tube problem in dusty gas for two different time steps (P1 solution).....	128
Fig. 30. Schematic of various wave structures in the 1-D dusty gas flows: (a) The gas contact discontinuity and boundary particle path are initially located at the same position, (b) The particle boundary path is located at a distance from the gas phase contact discontinuity. ...	129
Fig. 31. Effects of initial dust concentration on the Sod's shock tube in the dusty gas (P <sup>1</sup> solution) .....	131
Fig. 32. Effects of location of the initial dust contact discontinuity (DCD) on the Sod's shock tube in the dusty gas at t=30 (P <sup>1</sup> solution).....	132
Fig. 33 Analysis of the order of the accuracy of the two-dimensional code for a smooth sine function problem.....	134
Fig. 34. Schematic of the pure gas (left) and dusty gas (right) 2-D explosion problems	136
Fig. 35. Grid independency test for the explosion test case (P <sup>1</sup> solution).....	137
Fig. 36. High order solutions of the explosion problem for pure gas (h=1/100, t=0.2)...	139
Fig. 37. Graphical presentation of time evolution of density in the multiphase explosion problem (P <sup>1</sup> solution).....	140
Fig. 38. Time evolution in the multiphase explosion problem (P <sup>1</sup> solution) .....	141
Fig. 39. Time evolution of density in the rectangular multiphase explosion problem (P <sup>1</sup> solution) .....	142
Fig. 40. Schematic of the pure gas (left) and dusty gas (right) 2-D compression corner problems.....	143
Fig. 41. Validation of pure gas case (Isopycnics for single Mach reflection: $M_s=2.03$ and $\theta_w=27^\circ$ ) and verification of dusty gas case (A-constant flow Mach number contours, B-constant gaseous phase density contours, and C-constant dust phase spatial density).....	144
Fig. 42. Verification study: Double Mach reflection (pure gas P <sup>1</sup> solution).....	146

Fig. 43. Effects of polynomial orders on the density contours .....	148
Fig. 44. Time evolution of density contours in the compression corner (double Mach reflection) problem (P <sup>1</sup> solution) .....	149
Fig. 45. Change of the DMR structure in presence of dust particles (P <sup>1</sup> solution) .....	150
Fig. 46. Parametric study on particulate loading and particle diameter in the double Mach reflection problem (P <sup>1</sup> solution).....	152
Fig. 47 Schematic of the under-expanded jet of particle-laden gas .....	153
Fig. 48 Comparison of prediction of Mach-disc location depending on the pressure ratio for the pure gas flow with previous experimental results.....	154
Fig. 49 Shadowgraphs of the under-expanded gas-particle [143] (top) and density contours of pure gas solution (right) with dusty gas (left) jet for different particle loadings (bottom): a) $\beta= 0.0$ ; b) $\beta= 0.11$ ; c) $\beta= 0.24$ ; d) $\beta= 0.35$ ; e) $\beta= 0.64$ ; f) $\beta= 1.07$ ( $P_0 = 0.31\text{MPa}$ , $P_0/P_\infty = 29.8$ , $d = 45\mu\text{m}$ ) (P <sup>1</sup> solution) .....	155
Fig. 50 Density solutions of different flux functions for map split grid (Re=73, M=0.8)	159
Fig. 51 Density solutions of different flux functions for pave grid (Re=73, M=0.8) .....	160
Fig. 52 Density solutions of different flux functions for map split grid (Re=106, M=2.0) .....	161
Fig. 53 Density solutions of different flux functions for pave grid (Re=106, M=2.0) ....	162
Fig. 54 Concentration contours of dusty gas past NACA0012.....	163
Fig. 55 Computational domain, boundary conditions, and grid.....	168
Fig. 56 Verification of drag coefficient.....	169
Fig. 57 Effect of variation of M number for a constant Re number smaller than critical Re number. ....	170
Fig. 58 Effect of variation of M number for a constant Re number smaller than critical Re number. ....	172

Fig. 59 Snapshots of instantaneous vorticity (left) and streamlines (right) in different time steps within a shedding cycle, $Re=250$ , and $M=0.1$ . .....	173
Fig. 60 Snapshots of instantaneous vorticity (left) and streamlines (right) in different time steps within a shedding cycle, $Re=250$ , and $M=0.3$ . .....	174
Fig. 61 Snapshots of instantaneous vorticity (left) and streamlines (right) in different time steps within a shedding cycle, $Re=250$ , and $M=0.8$ . .....	175
Fig. 62 Snapshots of instantaneous vorticity (left) and streamlines (right), $Re=250$ and $M=1.2$ . .....	176
Fig. 63 Snapshots of instantaneous vorticity (left) and streamlines (right), $Re=250$ and $M=2$ . .....	176
Fig. 64 Effect of variation of $Re$ number for a constant $M$ number in transonic Mach regime .....	177
Fig. 65 Effect of variation of particulate loading ( $\beta$ ) in low $Re$ and low $M$ number flow past the triangular prism .....	179
Fig. 66 Effect of variation of particulate loading on $C_d$ in a $Re$ higher than the critical $Re$ number and Mach number below the compressibility limit ( $Re=250$ , $M=0.1$ ) .....	181
Fig. 67 Snapshots of instantaneous vorticity (left) and streamlines (right) in different time steps within a shedding cycle, $Re=250$ , and $M=0.1$ , $\beta=0.01$ . .....	182
Fig. 68 Snapshots of instantaneous vorticity (left) and streamlines (right) in different time steps within a shedding cycle, $Re=250$ , and $M=0.1$ , $\beta=0.1$ . .....	183
Fig. 69 Snapshots of instantaneous vorticity (left) and streamlines (right) in different time steps within a shedding cycle, $Re=250$ , and $M=0.1$ , $\beta=0.5$ . .....	184
Fig. 70 Snapshots of instantaneous vorticity (left) and streamlines (right) in different time steps within a shedding cycle, $Re=250$ , and $M=0.1$ , $\beta=1.0$ . .....	185

Fig. 71 Effect of variation of particulate loading ( $\beta$ ) in low Re and high M number flow past the triangular prism.....	187
Fig. 72 Effect of variation of particulate loading ( $\beta$ ) in low Re and high M number flow past the triangular prism.....	188
Fig. 73 The schematic representation of the effect of Stokes number on particle dispersion in vortices. Reprinted from [257] with permission.....	189
Fig. 74 The effect of fluid properties on particle dispersion in vortices using velocity vectors of gas (black) and particle (red) phases. ....	191
Fig. 75 Prediction of Mach disk location in comparison with experimental results.....	192
Fig. 76 Effect of variation of particulate loading and Stokes number on Mach contours in the under-expanded jet problem.....	193
Fig. 77 Effect of variation of particulate loading and Stokes number on density contours and particles streamlines in the under-expanded jet problem.....	194
Fig. 78 Instantaneous Mach contours of under-expanded jet depicting the flow instabilities for high Re flows .....	195
Fig. 79 Effect of variation of jet Reynolds number on oscillatory behavior of the impinging jet.....	197
Fig. 80 Comparison of mean schlieren image (left) and DG density solution (right) .....	198
Fig. 81 The prevailing physics in the descent phase of a Moon landing .....	201
Fig. 82 Schematic of the implemented algorithm depicting the input and output of each module.....	203
Fig. 83 The schematic of the computational domain and type of applied boundary conditions .....	204
Fig. 84 Solution of internal nozzle flow ( $P_{ref}= 141251.1542$ Pa, $T_{ref}= 2317.596567$ K, $u_{ref}= 1192.698279$ m/s, $L_{ref}=1$ m).....	205

Fig. 85 Validation of jet impingement on the surface with the experiment of [44].....	206
Fig. 86 A sample computational grid for 5m of hover altitude.....	207
Fig. 87 Comparison of pressure solution NCCR (left) and DSMC (right) solution of [48]. Hover altitude: 5m .....	208
Fig. 88 Comparison of first-order (left) and second-order (right) solutions of pressure and Mach. Hover altitude: 5m. ....	209
Fig. 89 Comparison of pressure (top) and Mach (bottom) solutions of first-order Boltzmann- based (NSF) with second-order Boltzmann-based (NCCR), Hover altitude: 5m.....	210
Fig. 90 Comparison of Rayleigh-Onsager dissipation function for NSF (left) and NCCR (right) .....	210
Fig. 91 The effect of ambient pressure on pressure (right) and Mach (left) solution of the impinging jet. ....	211
Fig. 92 Comparison of NCCR solution with DPLR and Hybrid solution of [47] .....	213
Fig. 93 Distribution of the dynamic pressure on the different distances from the surface for two hover altitude .....	214
Fig. 94 Vectors of eroded mass flux overlaid on radial velocity .....	214
Fig. 95 Comparison of first-order and second-order constitutive relationships in erosion modeling .....	215
Fig. 96 Effect of particle diameter on dust momentum vectors of the eroded particles in the vicinity of the surface overlaid on normalized density ( $P_{amb}=3$ Pa) .....	217
Fig. 97 Effect of ambient pressure on dust momentum vectors of the eroded particles in the vicinity of the surface overlaid on normalized density ( $P_{amb}=3$ Pa) .....	218
Fig. 98 Effect of particle diameter on dust momentum vectors of the eroded particles in the vicinity of the surface overlaid on normalized density ( $P_{amb}=3$ Pa, $d=30$ $\mu$ m).....	219

Fig. 99 Effect of particle diameter on dust momentum vectors of the eroded particles in the vicinity of the surface overlaid on normalized density ( $P_{amb}=3$ Pa, $d=30$ $\mu$ m).....	221
Fig. 100 Contours of local a) Kn, b) M, c) $N_\delta$ numbers and d) degree of deviation of different regions from equilibrium for Apollo descent engine at 5 m hover altitude.....	223
Fig. 101 Schematic representation of Korean Lunar lander descent module with a five-nozzle configuration. Reprinted from [263] with permission.....	224
Fig. 102 Contours of local a) Kn, b) M, c) $N_\delta$ numbers and d) degree of deviation of different regions from equilibrium for the single nozzle operation of Korean lunar lander descent engine at 5 m hover altitude.....	225
Fig. 103 3D solution of local Mach number .....	226
Fig. 104 Contours of local Kn, M, $N_\delta$ numbers and degree of deviation of different regions from equilibrium for the single nozzle operation of Korean lunar lander descent engine at 227	
Fig. 105 Dust grains overlaid upon radial velocity ( $d=30\mu$ m, $h=5$ m) .....	228
Fig. 106 Comparison of drag force of high-Re (left) and low-Re (right) jet on the surface .....	229
Fig. 107 Comparison of Mach solution achieved by application of first-order and second-order Boltzmann-based constitutive relationships .....	230
Fig. 108 Comparison of non-conserved variables solution achieved by application of first-order and second-order Boltzmann-based constitutive relationships .....	231
Fig. 109 The relative level of complexity of the implementation of challenging issues in the proposed strategy of solving Lunar landing problem. ....	235

# List of tables

Table 1 Parameters characterizing the phase interaction for different characteristics velocities and particle diameters .....	18
Table 2 Thermos-physical properties of some common gases in atmospheric conditions	20
Table 3 Classification of different flow regimes based on a combination of the order of magnitude of Reynolds number and Mach number. Reprinted from [94] with permission. .	24
Table 4 Classification of the widely used methods based on simulation perspective and their range of validity in Knudsen regime.....	30
Table 5 Popular mathematical models for simulation of particulate flows .....	49
Table 6 Eulerian versus Lagrangian.....	50
Table 7 Selection of the most efficient model based on the type of multiphase problem .	52
Table 8 Summery of zeroth to second order Boltzmann-based constitutive relationships	62
Table 9 Range of important parameters in different regions of Fig. 8.....	65
Table 10 Non-dimensional parameters and their physical interpretation .....	73
Table 11 Comparison of some the numerical schemes for viscous flux. Adapted from [206]. .....	111
Table 12 The outputs for the NCCR solvers.....	121
Table 13. Initial condition for the Sod’s shock tube problem.....	125
Table 14 Accuracy analysis for 2D entropy waves.....	135
Table 15. Initial condition for the explosion problem.....	138
Table 16. Initial condition for the single Mach reflection problem .....	143
Table 17. Initial condition for the double Mach reflection problem.....	145
Table 18 Categorization of regimes based on Reynolds and Mach numbers and investigated regimes in this work.....	167
Table 19 Four possible approaches for solving the Lunar landing problem.....	202

Table 20 Coefficient a values for different hover altitudes and particle diameters. ....	220
Table 21 List of future Lunar missions with a soft landing involved .....	240
Table 22 List of future Mars missions with a soft landing involved .....	241
Table 23 Statistical definition of macroscopic parameters .....	242

# Nomenclatures

## Greek

$\alpha$	volume fraction
$\beta$	particulate loading
$\gamma$	ratio of the specific heats
$\gamma_s$	dissipation of kinetic energy due to inelastic particle collisions
$\Delta$	excess normal stress
$\zeta, \eta, \xi$	reference coordinates
$\theta$	azimuthal angle
$\Theta$	boundary contribution vector in matrix form
$\Theta'$	source terms contribution vector in matrix form
$\kappa$	thermal conductivity
$\lambda$	molecular mean free path
$\Lambda$	dissipative term
$\mu$	viscosity
$\bar{v}$	average molecular velocity
$\rho$	bulk density
$\sigma_c$	calortropy production
$\tau_c$	mean collision time
$\tau_v$	momentum response time of the particle
$\tau_T$	thermal response time of the particle
$\varphi$	basis function
$\Psi$	high order flux term
$\hat{\Psi}$	local calortropy density
$\Omega_e$	standard element
$\Omega_h$	local element
$\Pi$	viscous stress tensor

## Latin

<b>A</b>	vector of auxiliary variables
<i>b</i>	impact parameter of two-body collision

$C$	concentration
$\mathbf{c}$	thermal velocity vector
$\bar{c}$	mean thermal velocity
$C_D$	Drag coefficient
$c_m$	specific heat of the particle material
$C_m$	The coefficient of Magnus force
$c_p$	specific heat at constant pressure
$c_v$	specific heat at constant volume
$d$	particle diameter
$D$	drag force
$e$	total energy
$Ec$	Eckert number
$F$	external force
$f$	singlet probability distribution function
$f^\theta$	equilibrium probability distribution function
$f^c$	canonical probability distribution function
$\mathbf{F}_{\text{inv}}$	inviscid flux vector
$\mathbf{F}_{\text{visc}}$	viscous flux vector
$Fr$	Froude number
$H_{\text{rot}}$	rotational Hamiltonian of the molecule
$I$	moment of inertia
$J$	Jacobian matrix
$j$	magnitude of angular momentum
$k_B$	Boltzmann constant
$Kn$	Knudsen number
$l$	particle spacing
$L$	Reference length
$M$	Mach number
$m$	molecular mass
$\dot{m}$	mass flux
$n$	number density
$N$	number of molecules
$N_\delta$	composite number of non-equilibrium quantifier
$n_d$	normalization factor
$Nu$	Nusselt number

$p$	pressure
$\mathbf{P}$	Pressure tensor
$Pr$	Prandtl number
$\mathbf{Q}$	Heat flux vector
$Q$	heat transfer between phases
$R$	gas constant
$\mathbf{r}$	Cartesian coordinate of the physical space
$Re$	Reynolds number
$s$	specific entropy
$St$	Stokes number
$T$	temperature
$t$	time
$\mathbf{u}$	stream velocity vector
$V$	volume
$\mathbf{v}$	molecular velocity vector
$z$	mass loading
$\mathbf{Z}$	kinematic term

## Abbreviation

BCF	bearing capacity failure
BGK	Bhatnagar, Gross and Krook
BR1	first method of Bassi and Rebay
BR2	second method of Bassi and Rebay
BTE	Boltzmann transport equation
CFD	computational fluid dynamics
CFL	Courant-Friedrich-Levy
CPR	correction procedure reconstruction
DCD	dust contact discontinuity
DDF	diffusion-driven flow
DDPM	dense discrete phase model
DEM	discrete element method
DG	discontinuous Galerkin
DGE	diffused gas eruption

DMR	double Mach reflection
DPM	discrete particle model
DSMC	direct simulation Monte carlo
FDM	finite difference method
FDS	flux difference splitting
FEM	finite element method
FR	flux reconstruction
FVM	finite volume method
FVS	flux vector splitting
HEM	homogenous equilibrium model
KTGF	kinetic theory of granular flows
LBM	lattice Boltzmann method
LCP	lifting collocation penalty
LDG	local discontinuous Galerkin
LLF	local Lax-Friedrichs
MD	molecular dynamics
NCCR	non-linear coupled constitutive relationships
NSF	Navier-Stokes-Fourier
PIC	particle-in-cell
SD	spectral difference
SET	standard Enskog theory
SMR	single Mach reflection
SV	spectral volume
UGKS	unified gas-kinetic scheme
VE	viscous erosion
VOF	volume of fluid

# Abstract

## **A second-order Boltzmann-based continuum model for simulation of dusty gas flows in non-equilibrium using a discontinuous Galerkin method**

Omid Ejtehad

Department of Mechanical and Aerospace Engineering  
Graduate School, Gyeongsang National University

Supervised by Prof. Rho Shin Myong

With the progressive improvements in computer science and advents of computers with gigantic computational capabilities, computational fluid dynamics (CFD) has become an inseparable part of fluid dynamics. The promising CFD outcomes has motivated investigations of more complicated physical phenomena observed in fluid dynamics. Multiphase flows and non-equilibrium thermo-fluids are two challenging fields that need extra care than what is taken in conventional CFD. In the present thesis, both of these exciting topics are partially covered. The initial motivation was providing a cost-effective solution for *Lunar landing problem* (which technically is impingement and interaction of an under-expanded jet on a dusty bed in near-vacuum condition). Due to presence of various Knudsen and Mach regimes for gas phase as well as different Stokes regime for the dust phase, the problem can be challenging. Molecular methods for both non-equilibrium and particulate flows have shown tremendous potentials. Therefore, these methods are a natural primary candidate for these types of problems. However, the huge computational costs of these methods as well as the recent promising capabilities that the continuum-based methods in prediction of non-equilibrium (rarefied and micro/nanoscale) and multiphase flows has shown motivates analyses such as the one has been made in this thesis. For this purpose second-order Boltzmann-based constitutive relations derived by the method of moments and gas kinetic theory are applied to handle the non-equilibrium effects in the gas phase. The multiphase aspect is handled by considerably low cost *Eulerian-Eulerian model* compared to the *Lagrangian* counterpart. Even though the dust phase can also be treated in a similar way to the gas phase using kinetic theory (leading

to Eulerian-granular type models), the current thesis only focuses on the simpler models for the dust phase.

Discontinuous Galerkin (DG) method has been applied as the numerical discretization method due to the distinguished features. Application of DG allows to treat the numerically problematic source terms of the *two-fluid model* in a novel way. Moreover, the high-order solutions and the so-called *h-adaptivity* is desirable in most of the studied problems in the current work.

Various benchmark problems with applications in different areas of multiphase flows with the purpose of verification and validation of developed numerical tool are investigated and results are discussed. The results in most of the cases show a good agreement with experimental results or previous numerical studies. Finally, a new strategy for prediction of impact of the jet on the Lunar surface has been put forward which is shown to be able to provide competitive solutions in comparison with the high-cost Lagrangian methods.

# Abstract in Korean

## A second-order Boltzmann-based continuum model for simulation of dusty gas flows in non-equilibrium using a discontinuous Galerkin

오미드 에즈태하디

경상대학교 공과대학

기계항공공학부 항공우주공학 전공

지도교수: 명 노 신

컴퓨터 전산 능력의 진보와 막대한 계산 성능을 갖춘 컴퓨터의 등장으로 전산 유체 역학(CFD)은 이미 유체 역학의 매우 중요한 부분이 되고 있다. CFD의 유익한 결과물은 유체역학에서 관찰되는 보다 복잡한 물리 현상을 탐구하는데 있어 많은 동기를 부여하고 있다. 다상 유동과 비평형 열유체는 기존의 CFD에서 다룬 것보다 보다 더 세심한 주의가 요구되는 중요한 문제들이다. 본 논문에서는 이러한 흥미로운 두가지 주제에 관하여 다루고 있다. 동기 부여의 시작점은 달 착륙 문제와 관련하여 비용 측면에서 효율적인 해석 기법을 제공하고자 하는 것이다. (기술적으로 거의 진공 상태에 있는 달 표면의 먼지와 과소팽창 제트 기류의 충돌 및 상호 작용 문제) 가스 상태에 대한 다양한 Knudsen 조건 및 Mach 영역과 먼지의 상태에 대한 다양한 Stokes 조건에 의해 매우 도전적인 문제가 된다. 비평형 및 입자 유동에 대한 분자 운동 기법은 엄청난 잠재력을 보여주었다. 따라서 분자 운동 기법은 이러한 유형의 문제에 있어 매우 유리하다. 그러나 막대한 전산 자원 뿐만 아니라, 비평형 (희박 및 마이크로 나노 스케일)

및 다상 유동의 연속체 기반 기법의 가능성으로 인해 이 논문에서 제시된 것과 같은 시뮬레이션 기법이 장점을 갖게 되었다. 모멘트 기법과 기체 동역학 이론에 의해 유도된 2 차 Boltzmann 기반의 구성 방정식을 기체 상태의 비평형 효과를 분석하는데 적용하였다. 다상 특성은 Lagrangian 모델에 비해 상당한 저비용의 Eulerian-Eulerian 모델로 처리하였다. 비록 먼지 상태는 기체의 상태(Eulerian-Granular 유형 모델로 유도)와 유사한 방식으로 처리 될 수도 있지만, 본 논문은 먼지의 상태에 대한 간단한 모델에 초점을 맞추었다.

또한 수치적 이산 방법으로 DG(Discontinuous Galerkin) 기법을 적용하였다. DG 기법 적용을 통해 Two-Fluid 모델의 Source 항에 관련된 수치 문제를 극복하였다. 한편 고차원 해법 그리고 소위 “h-adaptivity”는 이미 연구 되어진 대부분의 문제에 있어 바람직하다.

개발된 수치 도구의 검증 및 유효성을 확인하기 위해 다상 유동의 여러 벤치마킹 문제를 해석하고 그 결과를 분석하였다. 대부분의 경우, 결과는 실험과 또는 이전의 수치적인 연구 결과와 잘 일치하는 것을 확인하였다. 결론적으로 높은 비용의 Lagrangian 기법과 비교하여 경쟁력 있는 답을 제공할 수 있고 달표면에 대한 제트 충돌 예측에 적용이 가능한 새로운 전략을 제시하였다.

# Chapter 1. Introduction

## 1.1 Motivation

The wide range of fluid dynamics applications in which dusty gas plays a significant role (from natural geophysical phenomena to industrial processes) has motivated various researchers to investigate the dynamics of dusty gas flows, known significantly different from the pure gas counterparts [1]. Furthermore, in applications where non-equilibrium effects are significant, the conventional computational fluid dynamics (CFD) models based on the first-order Navier-Stokes-Fourier constitutive laws fail to provide a correct prediction of the flow; therefore, development of the higher-order models beyond the first-order linear laws based on kinetic theory of gases is necessary [2-4].

An interesting case where the effects of rarefaction and presence of dust particles are of equal importance is the interaction of the descent engine plume of a lunar lander with loosely packed regolith of the Moon. In the early Moon explorations programs such as Surveyors I and III, the existence of a granular medium near the Moon's surface has been reported and was further confirmed by observations gathered from Apollo program. Moreover, the observations gathered from the Apollo missions confirmed the importance of dust particles during landing due to the continuous interaction of the descent module engine on the lunar surface in distances just a few meters above the surface [5]. Achieving a tool by which a detailed prediction and interpretation of the effect of descent engine plume impingement and consequently erosion of dust and large debris into the flow field is necessary. On the other hand, the recent planetary investigations which include soft landing of various explorers by major space organizations, i.e., NASA, ESA, JAXA, CNSA, and ISRO make the plume-dust interaction problem a critical issue. Examples of such programs include: the Indian Space Research Organization (ISRO) plan for the first lunar

landing in 2018, the Chang'E-4 lunar lander of China National Space Administration (CNSA) by the end of 2018, and NASA's InSight (Interior Exploration using Seismic Investigations, Geodesy and Heat Transport) Mars lander in November of 2018. A list of future Moon and Mars missions with a soft landing is provided in Appendix A.

One of the most challenging issues (maybe the most significant challenge) in the Lunar missions is reported by the astronauts who walked on the Moon to be electrically charged dust particles [6]. Gaier [7] categorized the dust effects into nine groups: vision obscuration, false instrument readings, dust coating and contamination, loss of traction, clogging of mechanisms, abrasion, thermal control problems, seal failures, and inhalation and irritation. Thus, understanding the physical nature of the interaction of plume and dusty surface in details is a crucial step in the design phase of Lunar/Martian missions.

It must be noted that providing the experimental setup in which a rocket engine is fired into a dusty bed (with many unknown characteristics) while the vacuum condition and low gravity is maintained if not impossible is a daunting task. This fact makes computational fluid dynamics a valuable tool for prediction of this type of flow regimes. The conventional method for simulation of rarefied multiphase flows formed in the descent phase of the lander is direct simulation Monte Carlo (DSMC) method or a hybrid (CFD-DSMC) method as in [8-10] which are proved to provide accurate results for highly non-equilibrium flows. As the DSMC method is applied in a Lagrangian formulation, the dust phase can be handled with minor modifications to the general algorithm. However, the multiscale nature of the problem in which various Knudsen and Mach regimes coexist makes the application of DSMC method computationally inefficient, in particular, in case of simulation of the whole transient phase of the flow. Furthermore, this approach may not be appropriate for a case where particles are present in the continuum solver domain. One example of this condition is when simulation of liquid hydrocarbon fuels is studied. In this case, the incomplete

combustion due to insufficient mixing of oxidizer and fuel lead to carbon soot formation. Therefore, the flow can be two-phase inside the nozzle where DSMC solvers are extremely inefficient due to characteristics of the flow. Another case which may be problematic for hybrid solvers is simulation of flow very close to the Moon surface and before the engine shut down where the chances of presence of the eroded particles in the continuum region is high.

These considerations motivated developing a unified multiphase solver, which can cover a wide range of Knudsen and Mach regimes. For this purpose, a two-fluid model is adapted to take into account the multiphase effects. Conservation laws along with the Boltzmann-based constitutive models are solved for both phases. For the gas phase, in order to handle the rarefaction effects, the second-order Boltzmann-based model (also known as NCCR) is applied [2, 3]. The solver is first verified and validated for zero-order Euler and first-order Navier-Stokes-Fourier equations in single phase and multiphase problems. Then, the problem of jet impingement on a surface in the presence of dust particles is simulated. Effects of parameters such as the exit to ambient pressure ratio, rarefaction degree, and dust particulate loading are investigated in detail.

The developed method can be used in other areas where dust particles are present in non-equilibrium gas condition as well. An example can be an estimation of the effect of micro-dust in heat transfer properties of micro/nano channels such as in computers cheapsets or hard disk drives. Another application is the simulation of supersonic impactors (also known as pressure impactors) which are used in the classification of nanoparticles and their working principle is based on rarefaction effects [11-14].

## **1.2 Background**

While the purpose of this thesis is to provide a general framework for handling different categories of flows in which dust particles are present in a non-equilibrium (as well as

equilibrium) gas, we focus on the lunar landing problem as the starting motivation of this work. In this section, some of the notable works on analysis of the problem of lunar landing are reviewed.

As the problem is multi-physics, it can be investigated from various viewpoints. The first challenge for simulation of the Lunar landing problem is providing a proper model capable of handling the rarefied condition on the lunar surface. Next comes selection of a model to simulate the multiphase nature of the flow successfully. Finally, selection of an erosion model which can best predict the rate of eroded particles is the other issue to be taken into account. Moreover, the existence of different types of flow regimes which have remarkably diverse nature such as boundary layers, shock waves, continuous plume core, expansion to vacuum and interaction of these fields with each other are some of the other complexities of the problem. These challenging problems can be each investigated as a separate topic in details. However, to provide a systematic study of the previous relevant works which are mainly related to the Lunar landing, the literature review is divided into three main categories. The first category contains works regarding simulation of plume and plume impingement. Next, some of the essential works regarding erosion prediction are outlined, and in the end, some of the works which directly deal with simulation of lunar landing or impingement of a jet on a dusty surface are reviewed.

### **1.2.1 Review of important works regarding ‘plume and plume impingement simulation’**

Simulation of plume and plume impingement on a surface is the primary interest in various applications in aerospace industry which spans from thrust vectoring systems and vertical and/or short take-off and landing (V/STOL) aircrafts to launching systems and lunar landing modules.

The complexity associated with the interaction of shock and expansion waves, the presence of strong shear layers and co-existence of subsonic and supersonic regions makes the jet impingement problem a challenging one. The problem has been investigated from various points of view and with various techniques. Therefore a general review of the all previous works would include a variety of topics. Here, we focus only on a few of the works which can be directly related to the topic of this thesis.

It is worth to notice that the structure of the impinging jet into a surface in vacuum condition is substantially different from when non-zero but small ambient pressure exists. In the latter, a shock wave lies near the jet boundary and extends towards the axis as a normal shock wave in a Mach-disk configuration. The aforementioned shock wave is emerged due to coalescence of compression waves produced as the result of the interactions of the expansion waves from the nozzle lip with the under-expanded jet boundary. For a same exit plane jet properties, the jet flow interior to the shock is not affected by the ambient pressure, and hence it is identical with the case when the ambient pressure is equal to zero [15].

Some experimental works have been reported for the jet impingement problem. Most of these experimental studies [16-21] are limited to surface pressure measurement with the variation of pressure ratio, flat plate inclination angle, and nozzle-plate distance. The range of pressure ratio in these problems is also limited to lower pressure ratios. However, Nakai *et al.* [20] performed experiments with a much more broad range of pressure ratios, nozzle-plate distances, and plate angles. It was found that the distance from the nozzle lip to the point where the jet shock first impinges on the plate is the critical parameter in changing the flow pattern. Another compelling case is impinging jets with high Reynolds number where the problem of sound-producing oscillations [22] arises. These oscillations lead to “lift loss” phenomena during the landing of V/STOL airframes [23]. The lift lost

phenomena is experienced as a suck-down force by the airframe due to the entrainment flow associated with the lifting jets which induce low surface pressures. Powell [22] provide a formulation in order to explain the feedback loop of the self-sustained oscillations in terms of tone frequency. Recent experimental works have contributed mainly to achieve a basic understanding of the governing physics of the problem via schlieren visualizations [24-28].

Khasawneh *et al.* [29] provided analytical relations for highly rarefied (in the collision-less limit) jets impinging on a flat surface. These results were compared with DSMC solutions for the purpose of verification. Later, Cai [30] generalized these solutions for the case of inclined plates. Cai *et al.* [31] also provided analytical relations for studying rarefaction effects on jet impingement loads. In their work, surface load formulas are compared with DSMC solutions from continuum to collision-less flow regimes to check the validity of solution in the case of low Knudsen number flows.

The problem has been investigated using numerical tools as well. Most of the works in which rarefaction effects are taken into account has utilized DSMC method [32-37]. Wu *et al.* [38] provided DSMC solutions for under-expanded jets with Kn number corresponding to a range from the transition to the near-continuum regime. Gimelshein *et al.* [33] presented simulation results for two-phase plume flow from a small aluminized propellant side thruster interacting with rarefied atmosphere using DSMC method. A decoupled CFD/DSMC [39] methodology was used to study the plume flow field characteristics of the plume in the descent phase and its interaction with the ascent stage vehicle as well as plume heating influence on the descent module. Tosh *et al.* [40] numerically analyzed the impingement of hypersonic rocket exhaust plume on the surface in the rarefied Lunar environment. A hybrid continuum-rarefied flow simulation method (with the first-order

accuracy in space) was applied, and the simulation results were shown to be in good agreement with available experiments.

### **1.2.2 Review of important works regarding ‘erosion modeling’**

One of the most valuable efforts in the estimation of erosion due to impinging jets in rarefied condition is the works of Roberts [41, 42]. The model is based on the first principle assumption that the erosion occurs only when the gas-phase shear stress is larger than the soil shear strength. Roberts’ erosion model has limitations such as considering erosion a merely shear process, not including the fundamentally different Lunar condition and, failure of correct prediction of erosion rate below a critical hover altitude. Hutton [43] compared the scaled cold gas jet experimental results of Land and Clark [44] with Roberts’ theory and concluded that erosion depths could be accurate within a factor of two and four, 43 and 87 percent of the time, respectively. Later on, Metzger and his colleagues [45, 46] modified the theory by scrutinizing the assumptions made by Roberts. The previously unrecognized diffusion-driven mechanism was incorporated into the new model. More fundamental investigations are necessary in order to provide advanced models which can take into account the complex phenomenological processes of surface erosion. However, depending on the simulation purpose, the existing models are capable of explaining large-scale phenomena to an acceptable level. Morris et al. [10, 47, 48] examined the Roberts erosion model extensively and showed that despite various reality-inconsistent assumptions, Roberts’ theory is a capable tool which can be a sufficient model depending upon the purpose of simulation.

### **1.2.3 Review of important works regarding ‘rarefied multiphase flow’**

There are few works in which the interaction of plume impingement and presence of particles due to either erosion or other sources (for example soot formation in solid propellants rockets) are considered numerically. Burt and Boyd [49] extended the DSMC

approach proposed by Gallis *et al.* [50] for simulating the transport of spherical particles in a rarefied gas flow in such a way that two-way coupling effect was taken into account. In a similar work but with a different approach Gimelshein *et al.* [33] developed a two-way combined continuum-DSMC algorithm and applied the method to two-phase plume flow from a small aluminized propellant side thruster interacting with the rarefied atmosphere. Liu *et al.* [51] developed a numerical approach by adopting discrete element method (DEM) for simulation of single dust particle ejection. These particles are then overlaid in the flow field obtained by DSMC and gas kinetic BGK method. However, due to deterministic nature of the DEM method, this approach can be computationally very costly. He *et al.* [8] applied the DSMC method to the problem of Lunar landing. In their work molecule–molecule, molecule–particle and particle–particle collisions were all taken into account. Morris *et al.* [9, 47] applied loosely coupled CFD/DSMC method to simulate the problem. The DPLR (NASA's continuum flow solver [52]) is applied for calculation of the nozzle core flow. The DSMC method is applied for calculation of the rarefied region and solid phase. Promising results were achieved, and the work was later extended to three-dimensional problems as well [10, 48].

#### **1.2.4 Other important works regarding the Lunar landing problem**

There exists a number of other works which contributed significantly to understanding of the governing physics of the problem of Lunar landing. Analytical works pioneered by Roberts *et al.* [41, 42, 53] has made a big impact in formulation and understanding of the problem. Roberts [41] analyzed the problem by suggesting formulation describing the action of hypersonic jet on a granular bed in vacuum whose axis is normal to the surface. Roddy *et al.* [54] took into account the effect of pore gases on the penetration of the jet on the densely and loosely packed dusty bed in both air and vacuum conditions. Scott and Ko [55] considered isothermal transient gas flow of Surveyor spacecraft engine in soil (porous

medium) numerically. Lane *et al.* [56] applied CFD and DSMC to produce an input for a trajectory simulation of lunar dust particles influxed during the descend and ascent phases. As mentioned earlier, due to complexity and importance of the Lunar landing problem there exist variety of other works in which the problem has been investigated from a different perspective or approaches other than numerical modeling (i.e, experimental investigations) has been applied. However, comprehensive review of all the related works is out of scope of the present thesis and only most relevant references are reviewed.

### **1.3 Outline**

This thesis can be divided into two parts. The first part including the first five chapters discusses the theory. In the next four chapters, the results achieved during this research are provided and discussed.

In Chapter 2, the fundamentals of multiphase are briefly introduced. Chapter 3 discusses the fundamentals of the kinetic theory of gases. A modified version of the method of moments, which is the preferred method for derivation of the constitutive models is also introduced in details. In Chapter 4, the mathematical modeling of particle-gas flows as well as discussions for erosion modeling are provided and in Chapter 5 discontinuous Galerkin method as the numerical approach for solving the mathematical models is outlined.

Chapters 6, 7, and, 8 are devoted to providing the results achieved by zeroth-order (Euler), first-order (Navier-Stokes-Fourier) and second-order (NCCR) Boltzmann-based constitutive equations. Finally, in Chapter 9 conclusions are made, and the possible directions for future works are briefly pointed out.

# Chapter 2. Multiphase Flows

In the context of fluid mechanics, the terms *multiphase flow* and *multicomponent flow* implies on any fluid flow consisting of more than one phase/component or have some level of phase separation at a scale well above the molecular level. The terms component and phase refer to a chemical species and a state of the matter, respectively. Multiphase flows are vastly observed in different geophysical flow conditions and technological applications. Biological flows like blood as well as most of the liquids we deal with on a daily basis such as milk and paints are examples of liquid bases containing suspensions. Preparation of coffee in a percolator needs steam and hot water to pass through coffee beans and is another example of multiphase flows which we may encounter on a daily basis. In this chapter, various types of multiphase flow are introduced. We then focus on gas-particle flows and the fundamental definitions that are necessary for the next chapters will be provided.

## 2.1 A general categorization of multiphase flows

Multiphase flows can be categorized into four general categories based on the combination of the states that are present in the flow.

### 2.1.1 Gas-liquid or liquid-liquid flows

A classification of this type of multiphase flows is based upon the superficial velocities of gas and liquid phases as shown in Fig. 1 for vertical flow in a pipe. It should be noted that other physical parameters such as densities, viscosities, and surface tension can also affect the flow regimes which are not taken into account in this classification. In a more general categorization based on the level of diffusion of the phases, gas-liquid or liquid-liquid flows can be classified as dispersed flows (such as the motion of gas bubbles in a liquid or liquid droplets in gas flow), mixed or transitional flows and separated (also known

as free surface or stratified) flows. Examples include ocean waves, blood flow, liquid propellant rockets and internal combustion engines, to name a few.

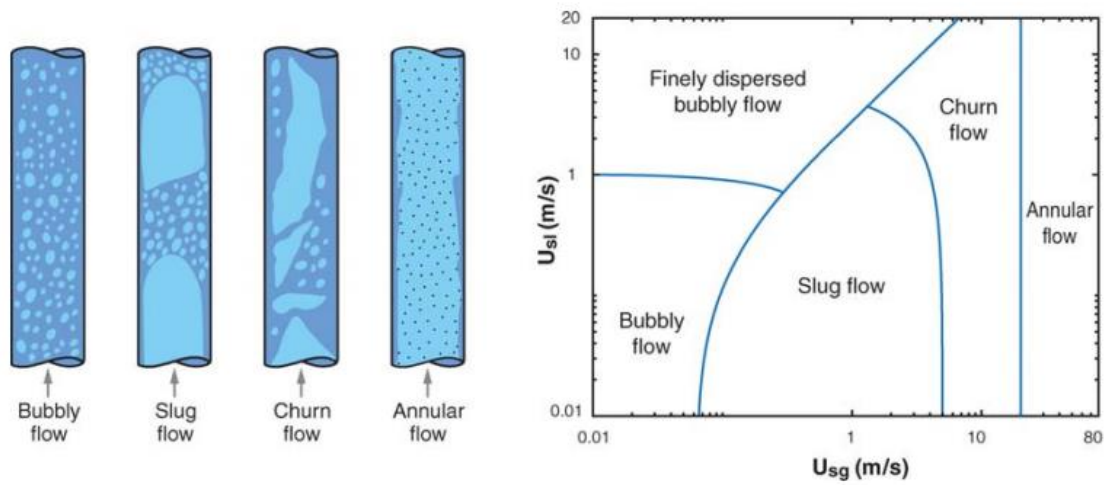


*Fig. 1 Flow patterns (right) and flow pattern map (left) for vertical pipe flow of air and water. Reprinted from [57] with permission.*

## 2.1.2 Gas-solid flows

This class of flows is identified by the presence of solid particles (particulate phase) in a gas (carrier) phase. Most of the applications in this category fall into the following sub-categories:

- gas-particle flows or particle-laden flows (sandstorms, volcanoes)
- pneumatic transport (pneumatic conveyers)
- fluidized beds

The gas-solid flow is considered a granular flow when the particle-particle or wall-particle interactions are more dominant compared to the interstitial forces. Moreover, if the particles become motionless the viscous force on the particle surface is the primary parameter to govern the physics, and the problem is known as flow through a porous medium.

### **2.1.3 Liquid-solid flows**

Liquid-solid flows are identified by the transport of solid particles in liquids. Following categories fall into the liquid-solid flows: Slurry flows, which are defined as a thin sloppy fluid mixture of a pulverized solid in a liquid with a broad range of application in industry and sediment transport which includes the transport of solid matter (sediments) as a result of gravity force and/or movement of the fluid in which the sediment is entrained. Examples include natural phenomena of sediment transport in rivers and sea, soil erosion due to rain and storms or slurry transportation, fluidized beds and waterjet cutting in industrial processes.

### **2.1.4 Three-phase flows**

As the name implies, these type of flows are identified by simultaneous presence of three phases. Mostly they can be distinguished as a combination of two of the above categories. Examples include: bubbles in a slurry flow and simultaneous presence of droplets and particles in gaseous flows.

## **2.2 Gas particulate flows**

Among the various categories of the multiphase flows, the gas-solid group makes up a significant portion of applications. A class of multi-phase flows, composed of compressible gases carrying a substantial amount of small particles like dust or droplets, has emerged as an exciting topic in recent years. The interest is largely driven by the increasing need to understand technological processes (e.g., explosions in coal mines [58], the separation of particulate matter from fluids [59], and the interaction of rocket plumes and lunar dust [60]) and natural geophysical phenomena (e.g., volcanic eruptions [61], cosmic explosions [62], and star formation [63]), as summarized in Fig. 2.

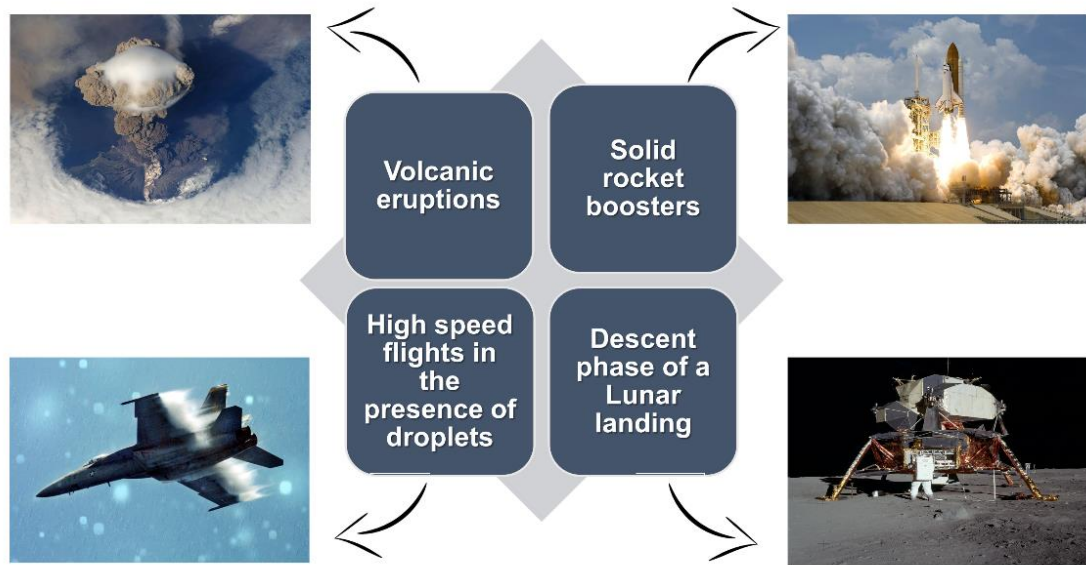


***Fig. 2 Various applications of dusty gas flows***

The dynamics of dusty gas flows is known to be significantly different from those of pure gas flows. This difference is mainly caused by the mass, momentum and heat exchange that occurs between the two phases. In dusty gas flows with shock waves, such as coal mine explosions or the interaction of the lunar lander's rocket plume with the dusty surface of the moon during the descent phase, there is a transition region where the velocity of the shock wave continuously changes due to the inertia and the heat capacity of the particles. Moreover, the mass exchange effects as a result of phase change or chemical reactions are essential in many applications [64]. Such complexities have motivated various theoretical [65, 66] and experimental [67, 68] studies. However, most of these studies have mainly focused on the one-dimensional shock tube problem in order to obtain a comprehensive physical understanding of the dusty gas flows, and consequently the development of proper mathematical models.

From a theoretical point of view, there are two prevailing approaches for predicting the dispersed flows: the trajectory (discrete or Lagrangian) and two-fluid (Eulerian-Eulerian) models [69]. In the trajectory model, the dispersed phase is described in the Lagrangian framework, while in the two-fluid model the dispersed phase is treated as a continuum. In

the present study, the two-fluid model is preferred over the trajectory model, since it is not only applicable to a wide spectrum of particulate loading in multi-phase regimes but also incur a less computational cost, compared to the Lagrangian counterpart. The model is, however, not efficient when the distribution of particle size is the main interest since a separate set of equations should be solved for each diameter size.

While most of the theoretical research has been limited to the one-dimensional numerical problem [70-74], many recent studies have focused on developing multi-dimensional numerical tools with the capability of handling unstructured grids. Saito [75], [76] developed a two-dimensional numerical tool to solve the two systems of conservation laws using the finite volume method. Igra *et al.* [77] investigated shock wave reflection from a wedge in a dusty gas flow by using a second-order accurate scheme in a finite difference framework based on the generalized Riemann problem and dimensional splitting. Moreover, they conducted an extensive parametric study on particle size and mass loading in two different time steps. In another attempt, Igra *et al.* [78] extensively studied shock wave reflection from a wedge placed in various suspensions by using a finite volume method of a two-fluid model.

On the other hand, Volkov *et al.* [79] solved the viscous two-phase gas-particle flow over a blunt body using an Eulerian-Lagrangian approach and investigated the effects of inter-particle collisions and two-way coupling. Pelanti and LeVeque [80] developed the fractional step method in the finite volume framework and applied the method to the one-dimensional shock tube and two-dimensional volcanic eruption problems. Gurriss *et al.* [81] solved the two-fluid model of dusty gas flows with a high-resolution finite element method along with a TVD type limiter, and Douglas-Rachford splitting method to handle the source terms. Recently, Carcano *et al.* [82] solved the problem of jet decomposition in both two and three dimensions using a second-order accurate semi-implicit finite volume method.

In another work, Carcano *et al.* [83] extensively investigated the grain-size distribution on the dynamics of under-expanded volcanic jets. Vié *et al.* [84] analyzed the capability of the Eulerian moment method for solving two-way coupled particle-laden turbulent flow systems.

## 2.3 Fundamental definitions of gas-particle flows

Before describing the details of the model, some necessary multiphase flow parameters are defined. The level of interaction of phases is assessed by the volume fraction of the dispersed phase ( $\alpha_s$ ) and the mass loading ( $\beta$ ). Small values of  $\alpha_s$  and  $\beta$  implies that the carrier phase is not affected by the dispersed phase and the one-way coupling is satisfactory. In cases where the masses of both phases are comparable, to take both phases into account, the two-way coupling is necessary. For larger  $\alpha_s$ , the particle-particle interactions such as collision, agglomeration, and break-up may not be ignored, requiring a four-way coupling. The other important parameter to quantify how the phases can equilibrate is the Stokes number, defined as the ratio of the aerodynamic response time of the particle ( $\tau_s$ ) to some characteristic time of the carrier phase ( $t_{ref}$ ). Useful discussions regarding basic multiphase parameters can be found in [1].

### 2.3.1 The volume fraction

In our considered multiphase gas-solid system, the solid phase is defined as small separate grains in such a way that the volume of each particle is small compared to the overall volume of the solid material. The volume fraction of solid (dispersed) phase is then defined as,

$$\alpha_s = \lim_{V \rightarrow V_0} \frac{V_s}{V}. \quad (1)$$

Here  $V_s$  and  $V$  are the volumes occupied by the solid and the total volume, respectively. The limiting volume,  $V_0$  is the volume in which flow properties do not vary significantly

from point to point. Equivalently, the volume fraction of the gas (continuous) phase can be defined as:

$$\alpha_g = \lim_{V \rightarrow V_0} \frac{V_g}{V}, \quad (2)$$

where  $V_g$  is the volume of the gas phase in the total volume which is referred to as the void fraction in some literature. The sum of the volume fractions must be unity (axiom of continuity).

$$\alpha_s + \alpha_g = 1. \quad (3)$$

### 2.3.2 Particle spacing

Another parameter which plays a vital role in characterizing the mechanics of a dispersed phase flow is the particle (or droplet) spacing and is defined as the average distance between the dispersed phase elements. This parameter can be used to determine if a particle can be treated as an isolated system or not. The relation between particle spacing and volume fraction is as follows

$$\frac{l}{d} = \left( \frac{\pi}{6\alpha_s} \right)^{\frac{1}{3}}. \quad (4)$$

Here  $d$  is the particle diameter. For  $l \gg d$ , the particles can be treated as isolated and when  $l \sim 1$  the interaction between particles cannot be neglected.

### 2.3.3 Response times

The momentum (velocity) and thermal response times ( $\tau_v$  and  $\tau_T$ ) are essential parameters in establishing non-dimensionalize parameters to characterize the flow. These parameters are an indicator of how the particles react towards the velocity and temperature changes in the flow and are defined as

$$\tau_V = \frac{\rho_s d^2}{18\mu_g} \quad \tau_T = \frac{\rho_s c_m d^2}{12\kappa_g} \quad (5)$$

where  $\rho_s$  and  $c_m$  are solid phase bulk density and specific heat of the particle material.  $\mu_g$  and  $\kappa_g$  represent gas viscosity and thermal conductivity, respectively.

### 2.3.4 Concentration and loading

The ratio of the mass of the dispersed phase to that of the continuous phase in the multiphase mixture is defined as dispersed phase mass concentration or as the particle mass ratio. It should be noted that in some literature the volume fraction of the dispersed phase is considered as concentration.

$$C = \frac{\bar{\rho}_s}{\bar{\rho}_g} = \frac{\alpha_s \rho_s}{\alpha_g \rho_g}. \quad (6)$$

Another parameter important to the definition of the particulate flows is loading, which can be defined as the ratio of particulate mass flux to that of the continuous phase. The terms loading, mass loading, and particulate loading have also been used to denote the concentration.

$$z = \frac{\dot{m}_s}{\dot{m}_g}. \quad (7)$$

### 2.3.5 Stokes number

A crucial parameter in fluid-particle flows to characterize the response rate of the particles to changes in fluid motion or, to evaluate the kinetic equilibrium of the particles with the carrier gas, is the Stokes number, defined as

$$St = \frac{\tau_V}{t_{ref}}. \quad (8)$$

$St \ll 1$  implies that the response time of the particles is much less than the characteristic time of the flow. In this case, the particles have enough time to equilibrate with the carrier

phase leading to nearly equal velocities. These types of flows can be safely simulated with a one-way coupled model. On the other extreme, when  $St \gg 1$ , the response time of the particles is much more than that of the career phase. Consequently, particle velocity is little affected by the fluid velocity change. A two-way coupling algorithm should thus take into account the back-influence of the particle phase on the career fluid.

With the same methodology, a thermal Stokes number can be defined as the ratio of the thermal response time to the characteristic time of the flow to provide an understanding about the response rate of the particles towards temporal changes in the flow.

In Table 1, an estimate on relaxation times and Stokes number for particle diameters used in the present thesis simulations is given for two different characteristics time scale of the flow based on two different reference Mach numbers.

**Table 1 Parameters characterizing the phase interaction for different characteristics velocities and particle diameters**

$M_{ref}$	$d$	$L$	$t_{ref}$	$\tau_v$	$\tau_T$	$St$
[-]	[m]	[m]	[s]	[s]	[s]	[-]
1.0	5.00E-07	1.29E-03	3.89E-06	2.02E-06	1.55E-06	0.52
	1.00E-06	2.58E-03	7.79E-06	8.09E-06	6.21E-06	1.04
	5.00E-06	1.29E-02	3.89E-05	2.02E-04	1.55E-04	5.20
	1.00E-05	2.58E-02	7.79E-05	8.09E-04	6.21E-04	10.39
	4.50E-05	1.16E-01	3.50E-04	1.64E-02	1.26E-02	46.77
3.0	5.00E-07	1.29E-03	1.30E-06	2.02E-06	1.55E-06	1.56
	1.00E-06	2.58E-03	2.60E-06	8.09E-06	6.21E-06	3.12
	5.00E-06	1.29E-02	1.30E-05	2.02E-04	1.55E-04	15.59
	1.00E-05	2.58E-02	2.60E-05	8.09E-04	6.21E-04	31.18
	4.50E-05	1.16E-01	1.17E-04	1.64E-02	1.26E-02	140.3

$\mu=1.716 \times 10^{-5}$  [Pa.s],  $\kappa=2.41 \times 10^{-2}$  [W/(m.K)],  $\rho_s=2500$  [Kg/m<sup>3</sup>],  $C_m=718.0$  [J/(kg.K)]

## Chapter 3. Kinetic theory of gases

The historical development of the kinetic theory of gases dates back to 50 BCE when a Roman philosopher, Titus Lucretius Carus, proposed the composition of static macroscopic bodies from a small scale of rapidly moving atoms which are all bouncing off each other [85]. Many famous physicists contributed to the topic. However, Ludwig Boltzmann works regarding generalizing Maxwell's achievement and formulation of the Maxwell-Boltzmann distribution as well as a statement of logarithmic connection between entropy and entropy generation was a turning point in the field. In the course of a long time, the research field was slowly developing until when the need for aerodynamic requirements to handle high altitude vehicles and vacuum technology in the fifties put an urge on the speed of development. Today, the field is well established and is being actively followed by many research groups worldwide.

### 3.1 Degree of non-equilibrium

In this section, relations for number density of molecules  $n$ , mean molecular spacing  $\delta$ , molecular diameter  $d$ , molecular mean free path  $\lambda$ , mean collision time  $\tau_c$ , and average molecular velocity  $\bar{v}$  for diluted gases are defined. The number of molecules of a mole of gas is constant and equal to Avogadro's number  $6.02252 \times 10^{23}$ . Also, the volume occupied by one mole of a gas at a given temperature and pressure is constant and not a function of the gas composition. This definition leads to the perfect gas relation given as follows,

$$p = nk_B T . \tag{9}$$

In the above equation,  $p$  is the gas pressure,  $T$  is the temperature,  $n$  is the number density of the gas, and  $k_B$  is the Boltzmann constant. The ideal gas law is valid for dilute gases for all pressures (higher than saturation pressure and less than critical point pressure). As a result, for the most applications, we can obtain the number density of molecules at a given

temperature and pressure using this equation. At atmospheric pressure and zero degree Celsius, the number density is equal to  $2.69 \times 10^{25}$ . If we assume that all molecules are uniformly distributed, the mean molecular spacing can be obtained as follows:

$$\delta \propto n^{-1/3} \quad (10)$$

Under the standard conditions, the mean molecular spacing is equal to  $3.3 \times 10^{-9} m$ .

The mean molecular spacing of the typical gases based on the viscosity coefficient and Chapman-Enskog theory is assumed to be from the order of  $10^{-10}$  with the hard sphere assumption [86]. Table 2 shows the thermo-physical properties of some common gases.

**Table 2 Thermos-physical properties of some common gases in atmospheric conditions**

	Density [kg/m <sup>3</sup> ]	Thermal conductivity [W/(mK)] ( $\times 10^{-5}$ )	Thermal diffusion [m <sup>2</sup> s]	Specific heat [J/KgK]	Mean free path [m] ( $\times 10^{-8}$ )
Argon	1.783	2.29	0.0177	515	6.44
Air	1.293	1.85	0.0261	1004.5	6.11
Nitrogen	1.251	1.8	0.026	1038.3	6.04
Carbone dioxide	1.965	1.5	0.0166	845.7	4.02
Oxygen	1.429	2.07	0.0267	916.9	6.05
Helium	0.179	2.99	0.15	5233.5	1.77

The comparison of the mean molecular spacing and typical molecular diameter  $d$  will characterize the concept of dilute gas as  $\delta/d \gg 1$ . For dilute gases, intermittent binary collisions are more common than multiple simultaneous collisions. On the other hand, in dense gases and liquids, it is the multiple collisions which complicate the modeling of inter-molecular collisions in these fluids. The assumption of the dilute gas along with the random behavior of molecules and the principles of energy equipartition leads to the derivation of the theory of the molecular kinetic energy of gases and the formulation of the Boltzmann

transport equation from the Liouville's equation. The assumptions and simplification of this derivation are given in references [87-89].

The transfer of momentum and energy in a fluid and convergence into a thermodynamic equilibrium state is made via intermolecular collisions. As a result, time and length scales regarding inter-molecular collisions are essential parameters. The distance traveled by molecules between two collisions is known as the molecular mean free path. For a simple gas with hard-sphere molecules, mean free path in the thermodynamic equilibrium is defined using the following equation,

$$\lambda = \frac{1}{\sqrt{2}\pi d^2 n} . \quad (11)$$

For example,  $\lambda$  for air in standard conditions is equal to  $5.6 \times 10^{-10}$ .

The mean thermal velocity of a gas is obtained from the following equation

$$\bar{c} = \sqrt{\frac{3p}{\rho}} = \sqrt{3RT} . \quad (12)$$

Here,  $R$  is the gas constant. For air in standard conditions, this number is  $486 \text{ m/s}$ . Given the time scale of inter-molecular collisions, and by comparing the ratio of the molecular mean free path to average molecular velocity a characteristic time can be achieved. This timescale should be compared with a characteristic time scale of the investigated problem to ensure the thermodynamic equilibrium assumption holds true.

### **3.1.1 Conventional classification of non-equilibrium regimes**

To measure the degree of non-equilibrium, the Knudsen number (Kn) is defined as the ratio of the mean free path of the gas molecules (i.e., statistically averaged distance over the billions and billions of molecules) to the characteristic length of the geometry ( $\text{Kn} = \lambda / L$ ). The Knudsen number is related to the Reynolds and Mach numbers according to the following relation:

$$\text{Kn} = \frac{\lambda}{L} = \sqrt{\frac{\gamma\pi}{2}} \frac{M}{\text{Re}}. \quad (13)$$

When the Knudsen number is sufficiently large, the gas rarefaction is the main parameter to evaluate these systems [90]. Flow regimes are also classified on the basis of the Knudsen number into: continuum ( $\text{Kn} \leq 0.01$ ), slip flow ( $0.01 < \text{Kn} < 0.1$ ), transition flow ( $0.1 < \text{Kn} < 10$ ) and free molecular ( $\text{Kn} \geq 10$ ). This classification is the most common method of characterizing of non-equilibrium regimes; however, this categorization is based on empirical information, and therefore the boundaries between different flow regimes may depend upon the geometry of the problem at hand.

### **3.1.2 Refining the conventional classification of non-equilibrium regimes**

By taking a close look at the Boltzmann equation, the Knudsen number can be perceived as the ratio of the convective term to collision terms. This rationale can, however, be questionable by the fact that microscale gas flows with high Knudsen number can be solved accurately by the linear Navier-Stokes-Fourier theory with slip boundary conditions while the same linear theory does not produce accurate results in the case of hypersonic rarefied gas flows even with low Knudsen numbers [91]. It should be noted that, in the macroscopic world, three terms are responsible for the description of the motion of the gases in the conservation law of momentum: convective, pressure, and viscous terms. Thus, two non-dimensional parameters (rather than Knudsen number alone) are necessary to classify the regimes fully. Even though this point was noted more than 70 years ago by Tsien [92], the common (but inaccurate) practice in various research papers is to take only the Kn number as the non-equilibrium quantifier. In Fig. 3(a), the classification of flow regimes based on Kn number on  $M$ - $\text{Re}$  diagram is plotted. As discussed above four regions are defined and illustrated. Fig. 3(b), shows the classification based on Tsien's parameter ( $\approx M / \sqrt{\text{Re}}$ ).

Tsien [92] defined a Kn-type parameter using the thickness of the boundary layer instead

$$\text{of a typical body dimension and showed that } \lambda / \delta \approx \begin{cases} M / \text{Re} & \text{Re} \ll 1 \\ M / \sqrt{\text{Re}} & \text{Re} \gg 1 \end{cases}$$

As can be seen, for  $\text{Re} \ll 1$ , the thickness of the boundary layer is almost the same as the body length and Tsien's parameter is equivalent to the classical Knudsen number. The range of  $0.01 \leq \lambda / \delta \leq 10$  is defined as slip regime and higher  $\lambda / \delta$  values are corresponding to free-molecular regime. The realm of fluid dynamics is shown in Fig. 3(a), from free molecular (where the collision between molecules and the collision of molecules with the wall are of equal importance) to slip regime and equilibrium condition. Macrossan [93] by comparing the DSMC and Navier-Stokes solutions showed that Tsien's parameter is a better parameter to categorize the flow regimes.

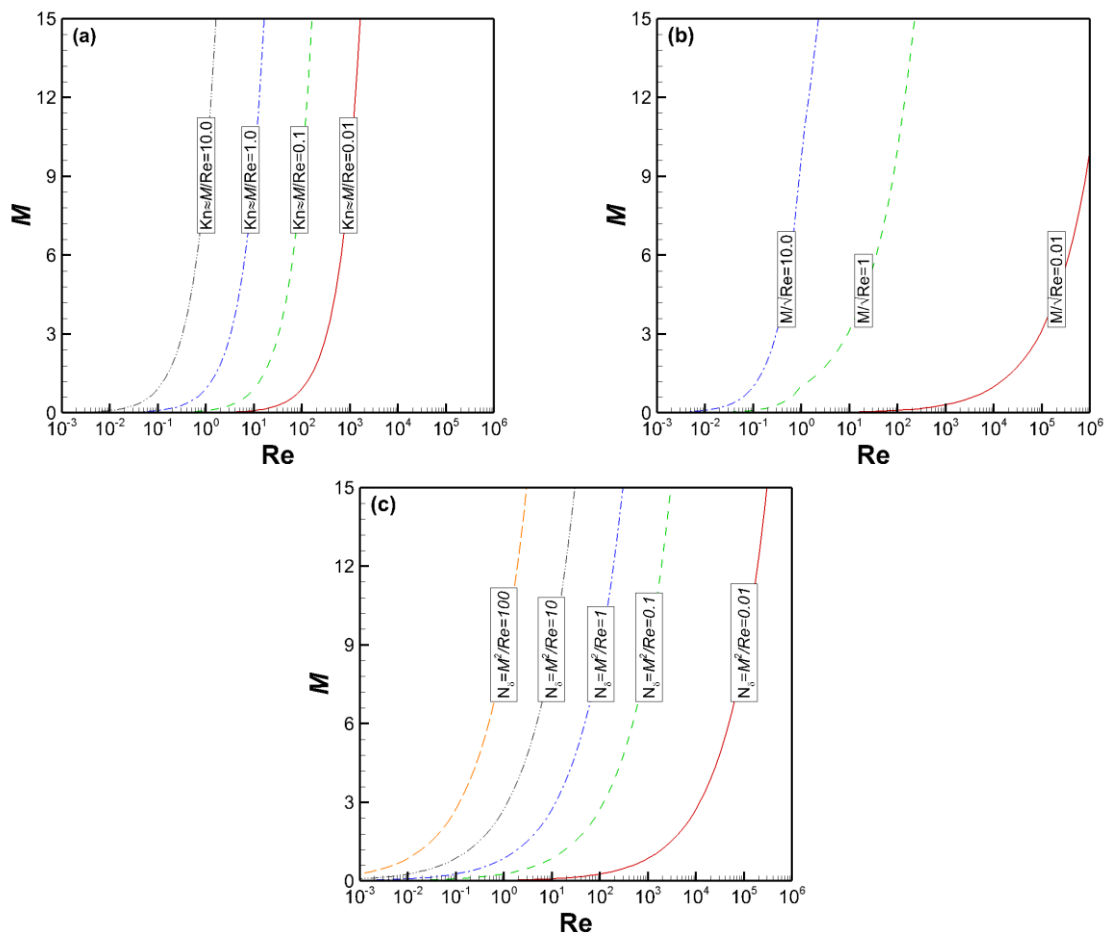


Fig. 3 The realms of fluid flow regimes according to different parameters

Another categorization of the fluids was put forward by Arkilic *et al.* [94] by defining nine independent flow regimes based on the Mach and Reynolds numbers (and their correlation with Kn). Table 3 provides useful information to estimate the basic understanding of the physics which govern the fluid motion in each regime. However, exact ranges for these regimes were not quantified in [94].

**Table 3 Classification of different flow regimes based on a combination of the order of magnitude of Reynolds number and Mach number. Reprinted from [94] with permission.**

$M$	$R$		
	$\mathcal{O}(\epsilon)$	$\mathcal{O}(1)$	$\mathcal{O}(1/\epsilon)$
$\mathcal{O}(\epsilon)$	$K = \mathcal{O}(1)$ . Creeping <i>micro</i> -flow	$K = \mathcal{O}(\epsilon)$ . Moderate <i>micro</i> -flow	$K = \mathcal{O}(\epsilon^2)$ . Low $M$ Fanno Flow
$\mathcal{O}(1)$	$K = \mathcal{O}(1/\epsilon)$ . Transonic Free-molecular flow	$K = \mathcal{O}(1)$ . Transonic <i>micro</i> -flow	$K = \mathcal{O}(\epsilon)$ . Transonic Fanno Flow
$\mathcal{O}(1/\epsilon)$	$K = \mathcal{O}(1/\epsilon^2)$ . Hypersonic Free-molecular flow	$K = \mathcal{O}(1/\epsilon)$ . Hypersonic Free-molecular flow	$K = \mathcal{O}(1)$ . Hypersonic "Fanno" (Transitional) Flow

An alternative parameter proposed by [95] is a composite parameter proportional to the ratio of viscous stress to pressure in the flow.

$$N_\delta \equiv \frac{\Pi}{p} = \frac{\mu u L}{p} \approx \frac{M^2}{\text{Re}} \approx \text{Kn} M \quad (14)$$

This parameter is shown in Fig. 3 (c) in the plane of  $M$ - $\text{Re}$ . Other parameters such as breakdown parameter of Bird [96] and Cheng's parameter [97] have also been used which are consistent with  $N_\delta$ . Each of these parameters as they consider the effect of convective, pressure and viscous terms altogether are suitable to be used to measure the degree of non-equilibrium. When these parameters are used, the limits to categorize the regimes should also be defined. In Fig. 4, the ranges of  $N_\delta$  limits are defined in such a way they are consistent with flow regimes of [94].

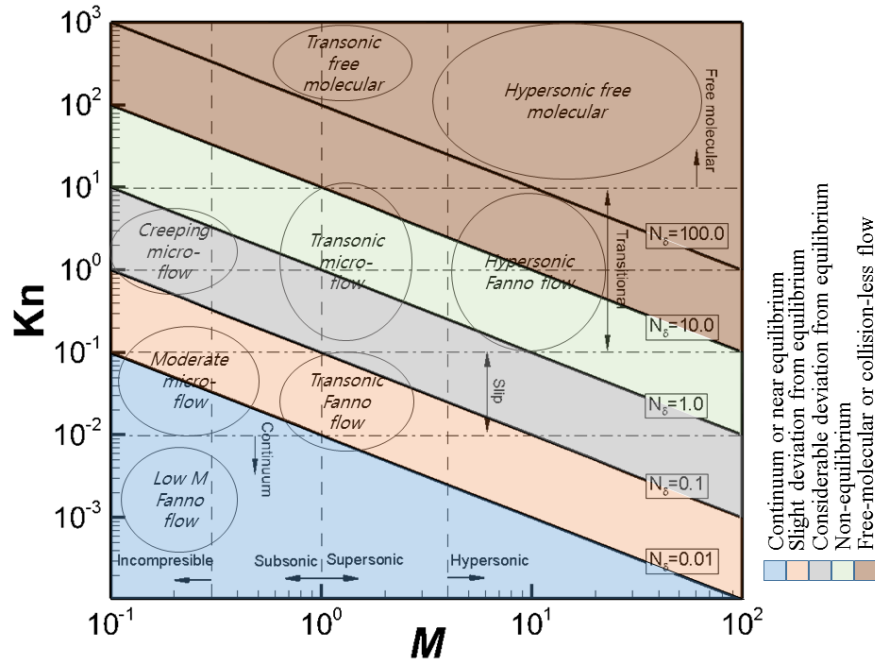


Fig. 4 Definition of the ranges of the  $N_\delta$  parameter overlaid with the classification of [94].

### 3.2 Singlet probability distribution function and macroscopic properties

Consider a dilute and non-dense gas which is composed of similar molecules. The hypothesis of dilution states that in a given volume of gas, the volume of existing molecules or the volume in which intermolecular forces are in effect is insignificant compared to the volume of gas. Achieving a mathematical relation for all molecules is then essential to describe the gas behavior. Maxwell used a velocity distribution function to describe the probability of having a specific speed at a specific location and time for the molecules. It seems that a complex velocity distribution function is required to determine the velocity of all involved molecules. However, for dilute gas, due to the randomness of molecular behavior, a velocity distribution function for molecules can be used. Let  $\mathbf{r}$  be the Cartesian coordinates of the physical space and  $\mathbf{v}$  the molecular velocity which can be stated in terms of the stream (macroscopic) velocity  $\mathbf{u}$  and thermal (peculiar) velocity  $\mathbf{c}$ . The number of molecules  $dN$  in the six-dimensional volume element  $dV = d\mathbf{v}d\mathbf{r}$  is expressed as  $dN =$

$f(t, \mathbf{r}, \mathbf{v}) d\mathbf{r} d\mathbf{v}$ . In this case,  $f$ , which is a function of the seven variables  $\mathbf{r}$ ,  $\mathbf{v}$ , and  $t$ , is called the single-particle probability distribution function of gas.

Each macroscopic quantity can be obtained using the velocity distribution function. For example, if  $\psi$  is a microscopic quantity of a molecule, the corresponding macroscopic average can be obtained by the following equation:

$$\bar{\psi} = \langle \psi f(t, \mathbf{r}, \mathbf{v}) \rangle = \int_{-\infty}^{\infty} \int_{-\infty}^{\infty} \int_{-\infty}^{\infty} \psi f(t, \mathbf{r}, \mathbf{v}) d\mathbf{v}. \quad (15)$$

Therefore, macroscopic variables such as gas density  $\rho$ , flow velocity  $\mathbf{u}$ , temperature  $T$ , pressure  $p$ , internal energy  $E$ , stress tensor  $\mathbf{\Pi}$ , heat flux vector  $\mathbf{Q}$  in position  $\mathbf{r}$  and time  $t$  according to the moments of the velocity distribution function  $f$  for a monatomic gas are as follows,

Number density:

$$n = \langle f(t, \mathbf{r}, \mathbf{v}) \rangle = \int_{-\infty}^{\infty} \int_{-\infty}^{\infty} \int_{-\infty}^{\infty} f(t, \mathbf{r}, \mathbf{v}) d\mathbf{v}. \quad (16)$$

where the  $\langle \dots \rangle$  symbol represents integration over velocity space  $\mathbf{v}$ .

Density:

$$\rho = \langle mf(t, \mathbf{r}, \mathbf{v}) \rangle = \int_{-\infty}^{\infty} \int_{-\infty}^{\infty} \int_{-\infty}^{\infty} mf(t, \mathbf{r}, \mathbf{v}) d\mathbf{v} = nm. \quad (17)$$

Velocity and momentum vectors:

$$\mathbf{u} = \langle \mathbf{v}f(t, \mathbf{r}, \mathbf{v}) \rangle = \frac{1}{n} \int_{-\infty}^{\infty} \int_{-\infty}^{\infty} \int_{-\infty}^{\infty} \mathbf{v}f(t, \mathbf{r}, \mathbf{v}) d\mathbf{v}. \quad (18)$$

$$\rho \mathbf{u} = \langle m\mathbf{v}f(t, \mathbf{r}, \mathbf{v}) \rangle = \int_{-\infty}^{\infty} \int_{-\infty}^{\infty} \int_{-\infty}^{\infty} m\mathbf{v}f(t, \mathbf{r}, \mathbf{v}) d\mathbf{v}. \quad (19)$$

Temperature and pressure:

$$RT = \left\langle \frac{1}{3} m\mathbf{c}^2 f(t, \mathbf{r}, \mathbf{v}) \right\rangle = \int_{-\infty}^{\infty} \int_{-\infty}^{\infty} \int_{-\infty}^{\infty} \frac{1}{3} m\mathbf{c}^2 f(t, \mathbf{r}, \mathbf{v}) d\mathbf{v}. \quad (20)$$

$$p = \left\langle \frac{1}{3} \mathbf{v}^2 f(t, \mathbf{r}, \mathbf{v}) \right\rangle = \frac{1}{3} \int_{-\infty}^{\infty} \int_{-\infty}^{\infty} \int_{-\infty}^{\infty} \mathbf{v}^2 f(t, \mathbf{r}, \mathbf{v}) d\mathbf{v} = \rho RT. \quad (21)$$

Total energy:

$$e = \left\langle \frac{1}{2} m \mathbf{v}^2 f(t, \mathbf{r}, \mathbf{v}) \right\rangle = \int_{-\infty}^{\infty} \int_{-\infty}^{\infty} \int_{-\infty}^{\infty} \frac{1}{2} m \mathbf{v}^2 f(t, \mathbf{r}, \mathbf{v}) d\mathbf{v} = \frac{3}{2} RT. \quad (22)$$

Pressure tensor (indicates transport of momentum by thermal velocity):

$$\mathbf{P} = \left\langle m \mathbf{c} \mathbf{c} f(t, \mathbf{r}, \mathbf{v}) \right\rangle = \int_{-\infty}^{\infty} \int_{-\infty}^{\infty} \int_{-\infty}^{\infty} m \mathbf{c} \mathbf{c} f(t, \mathbf{r}, \mathbf{v}) d\mathbf{v}. \quad (23)$$

Viscous stress tensor:

$$\mathbf{\Pi} = \left\langle m [\mathbf{c} \mathbf{c}]^2 f(t, \mathbf{r}, \mathbf{v}) \right\rangle = \int_{-\infty}^{\infty} \int_{-\infty}^{\infty} \int_{-\infty}^{\infty} m [\mathbf{c} \mathbf{c}]^2 f(t, \mathbf{r}, \mathbf{v}) d\mathbf{v}, \quad (24)$$

where,  $[\dots]^2$  denotes the traceless part of the tensor.

$$\mathbf{Q} = \left\langle \frac{1}{2} m c^2 \mathbf{c} f(t, \mathbf{r}, \mathbf{v}) \right\rangle = \int_{-\infty}^{\infty} \int_{-\infty}^{\infty} \int_{-\infty}^{\infty} \frac{1}{2} m c^2 \mathbf{c} f(t, \mathbf{r}, \mathbf{v}) d\mathbf{v}. \quad (25)$$

### 3.3 Boltzmann transport equation (BTE)

The master equation to describe the gas flow at the molecular level is the Boltzmann transport equation (BTE). The behavior of the probability distribution function can be defined via BTE as

$$\left( \frac{\partial}{\partial t} + \mathbf{v} \cdot \nabla + F \cdot \nabla_{\mathbf{v}} \right) f(t, \mathbf{r}, \mathbf{v}) = C[f, f_2], \quad (26)$$

in which  $F$  is the external force on unit mass and  $C[f, f_2]$  is called the collision integral (operator);  $\nabla = \partial / \partial \mathbf{r}$ ,  $\nabla_{\mathbf{v}} = \partial / \partial \mathbf{v}$ .

Boltzmann's transport equation illustrates the changes in the probability distribution function along a molecular pathway due to intermolecular collisions and under the presence of external force  $F$ . In fact, instead of considering the individual position and momenta of each particle in the fluid the probability distribution for the position and momentum of a

typical particle is considered. The principal assumptions in the derivation of Boltzmann equation are:

- dilute gas assumption: considering only binary collisions;
- molecular chaos assumption: uncorrelated position and velocity of each molecule;
- negligible influence of the external forces on the rate of collision.

In the absence of an intermolecular collision, collisionless Boltzmann equation can be written as:

$$\left( \frac{\partial}{\partial t} + \mathbf{v} \cdot \nabla + F \cdot \nabla_v \right) f(t, \mathbf{r}, \mathbf{v}) = 0. \quad (27)$$

However, the particles collide with each other and probability distribution function changes due to collisions. Hence,  $C[f, f_2]$  is not invariant to time reversal. The recognition of the necessity of the collision integral is Boltzmann's lasting contribution to the kinetic theory of gases. The Stosszahl ansatz proposed by Boltzmann suggests a form for this collision integral:

$$C[f_i, f_j] = \int d\mathbf{v}_j \int_0^{2\pi} d\phi \int_0^\infty db b g_{ij} \left[ f_i^*(t, \mathbf{r}, \mathbf{v}) f_j^*(t, \mathbf{r}, \mathbf{v}) - f_i(t, \mathbf{r}, \mathbf{v}) f_j(t, \mathbf{r}, \mathbf{v}) \right]. \quad (28)$$

In the above relation  $g_{ij} = |\mathbf{v}_i - \mathbf{v}_j|$  is the relative speed,  $b$  is the impact parameter of two-body collision between particles  $i$  and  $j$  and  $\phi$  is the azimuthal angle of scattering.

Some of the fundamental structural properties of the Boltzmann transport equation include:

- conservation of mass, momentum, and energy;
- the decay of entropy functional;
- Galilean invariance.

### 3.3.1 $H$ theorem

By introducing the celebrated functional  $H$  as follows,

$$H = \int f \ln f d\mathbf{v}, \quad (29)$$

Boltzmann was able to show that the solution of Boltzmann transport equation is unique. In other words, he stated that if probability distribution function  $f$  satisfies BTE, then  $H$  is a non-increasing function in time:

$$\frac{dH}{dt} \leq 0. \quad (30)$$

This statement is equivalent to the second law of thermodynamics if  $H$  is identified by the following relation:

$$H = -\frac{s}{k_B}. \quad (31)$$

where  $s$  is the entropy per unit volume. Hence, according to  $H$  theorem, the entropy never decreases. This theorem is the *formal manifestation of irreversibility* which any kinetic theory model must exhibit to confirm the correct description of the irreversible system.

### 3.3.2 Collision invariants

For a collisional invariant quantity  $\psi$ , the following relation must hold true:

$$\psi_i^* + \psi_j^* - \psi_i - \psi_j = 0. \quad (32)$$

The above relation states that the change of energy of the microscopic property  $\psi$  in a collision between two classes of molecules is zero. Classical physics state that microscopic mass, momentum, energy and any linear combination of these properties are the collisional invariants of the Boltzmann transport equation.

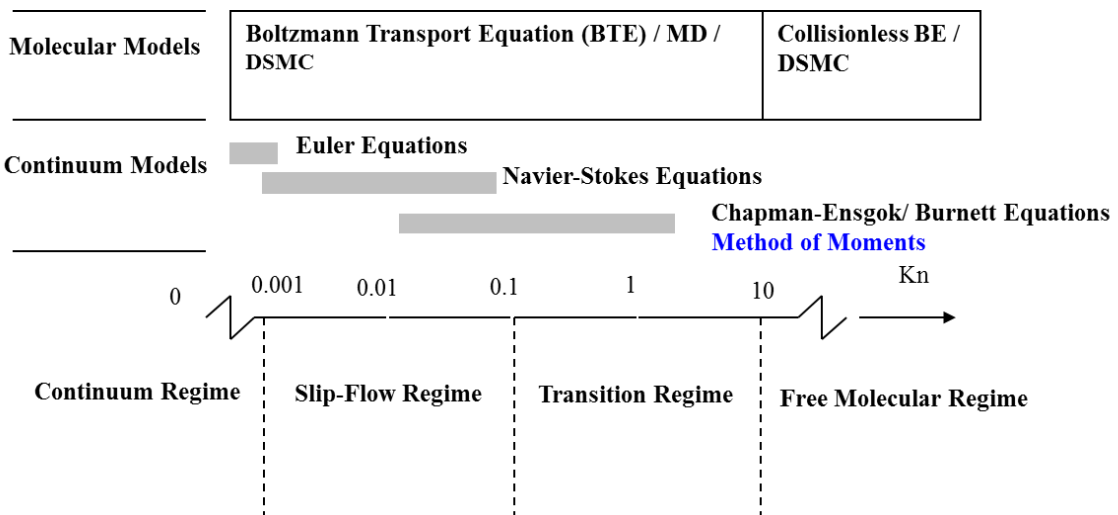
## 3.4 Theory and simulation methods

Various approaches have been introduced during the time to be applied for describing the gas behavior in different classes of problems. In this section, we briefly introduce some of the famous (and widely used/accepted) methods which deal with non-equilibrium gas

dynamics. It is clear that the existence of a plethora of methods and their subdivisions makes the introduction of all the available tools in detail a daunting task and is out of the scope of this work. Table 4 summarizes some of the mathematical/computational models from different perspectives. Two general categories include pure simulation and PDE-based approaches. Methods based on the level of physical phenomenology that is modeled can be classified as microscopic, mesoscopic and macroscopic. In what follows, each of the examples of this table is shortly introduced.

*Table 4 Classification of the widely used methods based on simulation perspective and their range of validity in Knudsen regime*

Molecular				Continuum				
Molecular				Continuum				
<b>Pure (or Semi-) Simulation</b>				<b>PDE-based Approach</b>				
MD	DSMC	Gas-Kinetic Scheme	LBM	Liouville Equation	Boltzmann and Simplified Boltzmann	Method of Moments	Chapman-Enskog and Burnett	NSF
Microscopic	Mesoscopic	Macroscopic		Microscopic	Mesoscopic		Macroscopic	



### 3.4.1 Pure (or semi-simulation) methods

#### 3.4.1.1 Molecular dynamics (MD)

One of the most formidable tools which have been used in the simulation of gas kinetic problems is the molecular dynamics (MD) method [98]. MD is a computational method for studying the physical movements of atoms and molecules by numerically solving the

classical equation of motion of a group of atoms or molecules. The method was first developed in the mid-50s [99] and found its way into different fields including theoretical physics, material science, biochemistry, and biophysics. Even though the method is capable in various aspects, the design constraints such as number of particles, time step and time duration of the physical phenomena which is being simulated can make realistic MD simulations last from several CPU-days to CPU-years.

An MD simulation usually consists of the following steps: Position and velocities of the particles are first initialized. The interatomic forces are computed based on potential functions. Atoms are next moved according to the equation of motion, and molecular geometries are restored. The desired macroscopic properties including, pressure, temperature, and energy are next calculated. The molecular positions and velocities are updated and time is advanced until the desired simulation time is reached.

#### **3.4.1.2 Direct simulation Monte Carlo (DSMC)**

DSMC is a numerical tool to solve the Boltzmann equation based on direct statistical simulation of the molecular processes described by the kinetic theory [100]. It is considered as a particle method in which particle represents a large bulk of real gas molecules. In fact, DSMC simulates particle behavior in a manner consistent with what is described by the Boltzmann equation. The primary principle of DSMC is to decouple the motion and collision of particles during one time-step. The implementation of DSMC needs breaking down the computational domain into a collection of grid cells. The cells are divided into subcells in each direction. The subcells are then utilized to facilitate the selection of collision pairs. After fulfilling all molecular movements in the domain, the collisions between molecules are simulated in each cell separately. Momentum/thermal accommodation coefficients represent a measure of the equilibrium of momentum and thermal energy of the reflected molecules with those of the wall. Full momentum

accommodation coefficient means that tangential momentum of reflected molecules is equal to the tangential momentum of the wall. Similarly, full thermal accommodation means that energy flux of reflected molecules is equal to the energy flux corresponding to the wall temperature. Accurate DSMC solution requires some constraints on the cell size, time step, and number of particles. The random selection of the particles from a cell for binary collisions requires that the cell size be a small fraction of the gas mean free path. The decoupling between the particles movement and collisions is correct if the time step is a small fraction of the mean collision time. Number of particles per cell should be high enough, around 20, to ensure that a realistic collision rate in each cell is maintained [100]. The following procedure is used to solve a stationary problem with DSMC. In the entire computational domain, an arbitrary initial state of gas particles is specified, and the desired boundary conditions are imposed at time zero. Particles movement and binary collisions are performed separately. After achieving steady flow condition, sampling of molecular properties within each cell is fulfilled during sufficient time period to avoid statistical scattering. All thermodynamic parameters such as temperature, velocity, density, and pressure are then determined from this time-averaged data. More details on DSMC algorithm are given in references [100, 101].

#### **3.4.1.3 Unified gas-kinetic scheme (UGKS)**

Gas kinetics scheme proposed by Kun Xu [102] is based on direct modeling of physical law in a control volume with limited cell resolution and should be distinguished from the direct discretization of the kinetic equations. It can be considered as a dynamic hybrid method. The method is capable of capturing multiple scale flow physics by using an explicit time evolution solution of the kinetic equation for the flux evaluation. Here, the assumption of time steps smaller than the mean collision time is not necessary as the transport and collisions steps are not split, and the method is still usable in the limit of

continuum flow regime. The main feature of the UGKS includes the use of the integral solution of the kinetic model in the flux evaluation across the cell interface.

#### **3.4.1.4 Lattice Boltzmann method (LBM)**

Contrary to conventional numerical methods which are based on the discretization of continuous macroscopic equations, and also contrary to molecular dynamics methods based on complex atomic molecular collisions, the lattice Boltzmann method (LBM) is based on both the mesoscopic kinetic equations and the microscopic models. In this method, the fluid is considered as a set of fundamental particles of a fluid element in a virtual space, which is influenced by a set of simplified laws. Although the theory looks far from reality, it has been shown that the method is capable in a specific class of applications.

The leading theory behind LBM is the creation of simplistic kinetic models that combine both mesoscopic and microscopic processes. Therefore, the macroscopic properties of LBM follow the desired macroscopic hydrodynamic laws. The basis of using these simple kinematic methods for macroscopic fluid flows is that: 1. the macroscopic dynamics of a fluid is the result of a collection of the behavior of many microscopic particles in the system, and 2. macroscopic dynamics does not take into account the details contained in the laws of microscopic physics. More details on merits and disadvantages of the method can be found in [103-108].

### **3.4.2 PDE-based approach**

#### **3.4.2.1 Classical theory (NSF)**

It should be noted that the classical system of equations of fluid dynamics can be directly derived from Boltzmann's equation as the first order contribution in a Chapman–Enskog expansion [86] or in other words conservation laws along with constitutive relations approximated by the linear assumption of Navier and Fourier. However, the classical theory precedes the kinetic theory. The classical models such as Euler and Navier-Stokes

equations are derived by applying Newton's second law of motion to each infinitesimal volume element of fluid. However, the closure models (such as the equation of state and constitutive relations) in this theory is not based on the laws governing molecular interactions. The models are primarily dependent on phenomenological or experimental/empirical data in this regard. These (mainly linear) relations are known to fail to provide a correct prediction in extreme physical processes associated with non-equilibrium (such as rarefaction and micro/nano-scales). In equilibrium condition, these relations are the most widely accepted methods and have been successfully applied to a vast spectrum of applications.

#### **3.4.2.2 Direct integration of Boltzmann equation**

The Boltzmann transport equation is a first-order nonlinear integrodifferential equation in space-time. The scale of the order of the mean free path and appearance of phase space makes this equation different from many other mathematical equations. Due to the complexity of the collision integral in BTE, providing analytical or numerical solutions for this equation are scarce but available [109, 110].

Methods of direct integration have been first introduced in [111, 112] for simple geometries. These numerical schemes were non-universal, however. More universal algorithms in order to provide conservative schemes were later proposed [113]. Approaches which combined both numerical and analytical features to estimate the collision integrals were also developed [114, 115]. The general procedure in these methods is a division of phase space into a regular network of cells on which the values of distribution function in the nodes of phase space are stored. The collision integrals are then evaluated using the Monte Carlo or the regular quadrature formulae. To evaluate the inverse collision integrals, an interpolation in velocity space (in the same velocity lattice of nodes) is performed. More details on direct numerical integrations can be found in [110].

### 3.4.2.3 Chapman-Enskog and Burnette

This class of models is based on an asymptotic expansion of velocity distribution function in the Knudsen number (or sometimes mean collision time). In general, it is assumed that the velocity distribution function is expressed in terms of the following power series

$$f = f^{(0)}(1 + a_1(\text{Kn}) + a_2(\text{Kn})^2 + \dots), \quad (33)$$

In which the coefficients  $a$  are only functions of macroscopic quantities, and  $\text{Kn}$  is the Knudsen number of the flow. The cut-off of this series to close the equations should be in a way so that the high-order moments can be calculated with the cut-off speed distribution function. The Chapman-Enskog zero-order expansion is the same as Maxwell's equilibrium distribution function.

$$f^{(0)} = \left( \frac{m}{2\pi k_B T} \right)^{3/2} \exp\left( -\frac{m\mathbf{c}^2}{2k_B T} \right) \quad (34)$$

In Maxwell expansion, the terms  $\mathbf{\Pi}$  and  $\mathbf{Q}$  are zero, and the result is Euler equations. These equations are achieved with the assumption of zero Knudsen number; therefore, they can be used (are valid) in the case of zero viscosity and heat transfer coefficient. The expansion of the first order expansion of the relation (33) is as follows:

$$f = f^{(0)}(1 + \mathbf{QC}(0.4\mathbf{C}^2 - 1) - \mathbf{\Pi CC}) \quad (35)$$

$$\mathbf{C} = \mathbf{c} / (2k_B T / m)^{1/2} \quad (36)$$

$$\mathbf{Q} = -\frac{\kappa}{p} (2k_B T / m)^{1/2} \nabla T \quad (37)$$

The range of validity of this set of relations is restricted to a set of limited problems. Higher order expansions lead to Burnett and super-Burnett equations which are ill-posed and unstable in transient flow problems. Moreover, they are not consistent with entropy inequality (second law of thermodynamics).

### 3.4.2.4 Method of moments

A popular method (alternative to the Chapman-Enskog expansion) for approaching the Boltzmann equation is the method of moments proposed by Grad [116] for the first time in the 1940s. The unknown in the Boltzmann equation as shown before is the velocity distribution function  $f$ . However, in practical applications of fluid dynamics physicists are interested in the functions of this distribution function  $f$ , from which macroscopic properties can be extracted. The method of moments is a general statistical approximation to identify these parameters based on their corresponding moments (weighted averages). As the evolution equations for the moments of a given order will contain high-order moment terms, closure models are inherent to all moment methods. These models are schemes which introduce approximations for truncation of the moment hierarchy via a representation of higher order moments in terms of lower order moments.

## 3.5 Extended moment equations

### 3.5.1 Conservation laws from Boltzmann equation

Thanks to the collisional invariant property of the microscopic properties of mass, momentum, and energy, the exact conservation laws can be derived from the Boltzmann equation without introducing any assumptions. To this end, microscopic properties corresponding collisional invariants ( $\psi = \left[ m, m\mathbf{c}, \frac{1}{2}m\mathbf{c}^2 \right]$ ) are multiplied in BTE and then integrated over the velocity space. After a series of mathematical manipulations which are summarized in Appendix B, and with keeping in mind that  $\psi$  depends only on particle position and time, the following conservation laws for monatomic gases can be achieved,

$$\frac{\partial}{\partial t} \begin{bmatrix} \rho \\ \rho\mathbf{u} \\ \rho E \end{bmatrix} + \nabla \cdot \begin{bmatrix} \rho\mathbf{u} \\ \rho\mathbf{u}\mathbf{u} + p\mathbf{I} \\ (\rho E + p)\mathbf{u} \end{bmatrix} + \nabla \cdot \begin{bmatrix} 0 \\ \mathbf{\Pi} \\ \mathbf{\Pi}\cdot\mathbf{u} + \mathbf{Q} \end{bmatrix} = 0. \quad (38)$$

As can be seen, these are the customary conservation laws which can be found in almost every fluid dynamics books. These balance equations are field equations for macroscopic variables. However, the set of equation (38) is not closed unless non-conserved variables are defined. On the other hand, these equations do not have contributions from collision integral as explained earlier. Due to the presence of non-conserved variables such as  $\mathbf{\Pi}$  and  $\mathbf{Q}$  (whose molecular definitions do not yield a collisional invariant), evolution equations for these variables should be derived which will be the aim of the next sub-section.

### 3.5.2 Boltzmann-based constitutive relationships

A similar approach to what has been used to derive conservation laws from Boltzmann equation can be applied for the derivation of evolution equation of non-conserved variables.

To yield the general evolution equation for a non-conserved variable, BTE is multiplied by  $\psi = h^{(n)}$  and integrated over velocity space, i.e.,

$$\left\langle h^{(n)} \frac{\partial f}{\partial t} \right\rangle + \left\langle h^{(n)} \mathbf{v} \cdot \nabla f \right\rangle = \left\langle h^{(n)} C[f, f_2] \right\rangle \quad (39)$$

Here, unlike what happens in the derivation of conservation laws, the collision integral term, denoted by  $\left\langle h^{(n)} C[f, f_2] \right\rangle$ , is not zero. Using the relation between molecular, stream and peculiar velocities and following mathematical operations we have,

$$\left\langle h^{(n)} \frac{\partial f}{\partial t} \right\rangle - \left\langle f \frac{d}{dt} h^{(n)} \right\rangle + \left\langle \mathbf{v} \cdot \nabla (h^{(n)}) \right\rangle - \left\langle \mathbf{v} f \cdot \nabla h^{(n)} \right\rangle = \Lambda^{(n)} \quad (40)$$

$$\left\langle \frac{\partial}{\partial t} (h^{(n)} f) \right\rangle - \left\langle f \frac{d}{dt} h^{(n)} \right\rangle + \left\langle (\mathbf{c} + \mathbf{u}) \cdot \nabla (h^{(n)} f) \right\rangle - \left\langle (\mathbf{c} + \mathbf{u}) f \cdot \nabla h^{(n)} \right\rangle = \Lambda^{(n)} \quad (41)$$

$$\begin{aligned} & \left\langle \frac{\partial}{\partial t} (h^{(n)} f) \right\rangle - \left\langle f \frac{d}{dt} h^{(n)} \right\rangle + \mathbf{u} \cdot \nabla \langle h^{(n)} f \rangle + \langle \mathbf{c} \cdot \nabla (h^{(n)} f) \rangle - \langle \mathbf{c} f \cdot \nabla h^{(n)} \rangle \\ & - \langle \mathbf{u} f \cdot \nabla h^{(n)} \rangle = \Lambda^{(n)} \end{aligned} \quad (42)$$

$$\begin{aligned} & \left\langle \frac{\partial}{\partial t} (h^{(n)} f) \right\rangle - \left\langle f \frac{d}{dt} h^{(n)} \right\rangle + \mathbf{u} \cdot \nabla \langle h^{(n)} f \rangle + \nabla \cdot \langle \mathbf{c} h^{(n)} f \rangle - \langle h^{(n)} f (\nabla \cdot \mathbf{c}) \rangle \\ & - \langle \mathbf{c} f \cdot \nabla h^{(n)} \rangle - \langle \mathbf{u} f \cdot \nabla h^{(n)} \rangle = \Lambda^{(n)} \end{aligned} \quad (43)$$

$$\begin{aligned} & \left\langle \frac{\partial}{\partial t} (h^{(n)} f) \right\rangle - \left\langle f \frac{d}{dt} h^{(n)} \right\rangle + \mathbf{u} \cdot \nabla \langle h^{(n)} f \rangle + \nabla \cdot \langle \mathbf{c} h^{(n)} f \rangle - \langle h^{(n)} f (\nabla \cdot \mathbf{u}) \rangle \\ & - \langle \mathbf{c} f \cdot \nabla h^{(n)} \rangle - \langle \mathbf{u} f \cdot \nabla h^{(n)} \rangle = \Lambda^{(n)} \end{aligned} \quad (44)$$

$$\begin{aligned} & \left( \frac{\partial}{\partial t} + \mathbf{u} \cdot \nabla \right) \langle h^{(n)} f \rangle + \langle h^{(n)} f \rangle \cdot \nabla \mathbf{u} + \nabla \cdot \langle \mathbf{c} h^{(n)} f \rangle - \left\langle f \left( \frac{\partial}{\partial t} + \mathbf{u} \cdot \nabla + \mathbf{c} \cdot \nabla \right) h^{(n)} \right\rangle \\ & = \Lambda^{(n)} \end{aligned} \quad (45)$$

With the use of material derivative notation, equation (45) can be simplified as:

$$\frac{D}{Dt} \langle h^{(n)} f \rangle + \langle h^{(n)} f \rangle \cdot \nabla \mathbf{u} + \nabla \cdot \langle \mathbf{c} h^{(n)} f \rangle - \left\langle f \left( \frac{\partial}{\partial t} + \mathbf{u} \cdot \nabla + \mathbf{c} \cdot \nabla \right) h^{(n)} \right\rangle = \Lambda^{(n)} \quad (46)$$

The above equation can be written in a way consistent with the form of other conservation laws,

$$\rho \frac{D}{Dt} \left\langle \frac{h^{(n)} f}{\rho} \right\rangle + \langle h^{(n)} f \rangle \cdot \nabla \mathbf{u} + \nabla \cdot \langle \mathbf{c} h^{(n)} f \rangle - \left\langle f \left( \frac{\partial}{\partial t} + \mathbf{u} \cdot \nabla + \mathbf{c} \cdot \nabla \right) h^{(n)} \right\rangle = \Lambda^{(n)} \quad (47)$$

The above relation with the introduction of  $\Psi^{(n)}$ ,  $\mathbf{Z}^{(n)}$ , and  $\Lambda^{(n)}$  as the flux of  $\langle h^{(n)} f \rangle$ , i.e., kinematic terms due to hydrodynamic streaming effect, and dissipation term due to energy loss associated with irreversibility can be rearranged as,

$$\rho \frac{D}{Dt} \hat{h}^{(n)} + \nabla \cdot \Psi^{(n)} - \mathbf{Z}^{(n)} = \Lambda^{(n)} \quad (48)$$

Here,

$$\begin{aligned} \hat{h}^{(n)} &= \left\langle \frac{h^{(n)}}{\rho} \right\rangle \\ \Psi^{(n)} &= \langle \mathbf{c} h^{(n)} f \rangle \\ \mathbf{Z}^{(n)} &= \left\langle f \left( \frac{D}{Dt} + \mathbf{c} \cdot \nabla \right) h^{(n)} \right\rangle \\ \Lambda^{(n)} &= \langle h^{(n)} C[f, f_2] \rangle \end{aligned} \quad (49)$$

With the molecular definitions of stress tensor and heat flux vector  $\begin{bmatrix} h^{(1)} \\ h^{(2)} \end{bmatrix} = \begin{bmatrix} m[\mathbf{cc}]^{(2)} \\ (mc^2\mathbf{c}/2) \end{bmatrix}$ ,

the following relations can be written as,

$$\begin{aligned} \rho \frac{d}{dt} \begin{bmatrix} \mathbf{\Pi}/\rho \\ \mathbf{Q}/\rho \end{bmatrix} + \nabla \cdot \begin{bmatrix} \mathbf{\Psi}^{(\Pi)} \\ \mathbf{\Psi}^{(Q)} \end{bmatrix} + \begin{bmatrix} 2[\mathbf{\Pi} \cdot \nabla \mathbf{u}]^{(2)} \\ \psi^{(P)} : \nabla \mathbf{u} + \frac{d\mathbf{u}}{dt} \cdot \mathbf{\Pi} + \mathbf{Q} \cdot \nabla \mathbf{u} + \mathbf{\Pi} \cdot C_p \nabla T \end{bmatrix} \\ + \begin{bmatrix} 2p[\nabla \mathbf{u}]^{(2)} \\ C_p p \nabla T \end{bmatrix} = \begin{bmatrix} \mathbf{\Lambda}^{(\Pi)} \\ \mathbf{\Lambda}^{(Q)} \end{bmatrix}. \end{aligned} \quad (50)$$

Here,  $\mathbf{\Psi}$  and  $\mathbf{\Lambda}$  represent kinematic high order terms and dissipation terms defined as:

$$\begin{aligned} \mathbf{\Psi}^{(\Pi)} &= \langle m\mathbf{cccf} \rangle - \langle m\text{Tr}(\mathbf{ccc})f \rangle \mathbf{I} / 3, \\ \mathbf{\Psi}^{(Q)} &= \langle mc^2\mathbf{ccf} \rangle - C_p T (p\mathbf{I} - \mathbf{\Pi}). \end{aligned} \quad (51)$$

$$\mathbf{\Lambda}^{(\Pi)} = \langle \equiv m[\mathbf{cc}]^2 C[f, f_2] \rangle. \quad (52)$$

These constitutive equations are not present in Grad's work as his 13-moment closure was already in place which explains how Eu's closure is different from Grad's closure. Explicit derivation of these equations was first provided by Eu [117].

It can be seen that these equations contain higher-order moments and the set of evolution equations is open. Proper closure methods to provide an acceptable method from both mathematics and physics point of view is necessary.

Grad introduced Hermite polynomial expansions. The collision integral with the assumption of Maxwellian molecule was then greatly simplified. However, the Maxwellian molecule assumption violates the generality of Grad's theory.

The following derivation was motivated by the fact that the calortropy production (physically known as the seat of energy dissipation) is originating from molecular collisions (therefore collision integral in BTE) which gives rise to the dissipative evolution of nonconserved macroscopic fluxes (moments). The balance equation for the calortropy (nonequilibrium entropy) can be written as

$$\rho \hat{\Psi}(\mathbf{r}, t) = -k_B \left\langle \left[ \ln f^c(\mathbf{v}, \mathbf{r}, t) - 1 \right] f(\mathbf{v}, \mathbf{r}, t) \right\rangle. \quad (53)$$

Here,  $f^c$  is the non-equilibrium canonical distribution function and can be called the thermodynamics branch of the Boltzmann equation.

Differentiating the local calortropy density with time and combining it with the Boltzmann transport equation the following equation is achieved,

$$\rho \frac{d\hat{\Psi}(\mathbf{r}, t)}{dt} + \nabla \cdot \left( -k_B \left\langle \mathbf{c} (\ln f^c - 1) f \right\rangle \right) + k_B \left\langle f \left( \frac{d}{dt} + \mathbf{c} \cdot \nabla \right) \ln f^c \right\rangle = \sigma_c. \quad (54)$$

$$\sigma_c = \left( \equiv -k_B \left\langle \ln f^c C[f, f_2] \right\rangle \right). \quad (55)$$

After assuming  $f = f^c$  and defining the relative velocity  $g_{12} \equiv |\mathbf{v} - \mathbf{v}_2|$  :

$$\sigma_c = \frac{1}{4} k_B \int d\mathbf{v} \int d\mathbf{v}_2 \int_0^{2\pi} d\phi \int_0^\infty db b g_{12} \ln(f^{c*} f_2^{c*} / f^c f_2^c) (f^{c*} f_2^{c*} - f^c f_2^c) \geq 0 \quad (56)$$

In the conventional approach of Grad, the dissipation term is worked out first. However, a thermodynamically consistent form of the dissipation term  $\Lambda^{(n)}$  can be obtained if the calortropy production term  $\sigma_c$  is first unraveled and a direct relation between  $\sigma_c$  and  $\Lambda^{(n)}$  can be found.

Another critical step in the derivation of the modified moment method of Eu is the introduction of an exponential form for  $f^c$  as follows,

$$f^c = \exp \left[ -\varpi \left( \frac{1}{2} mc^2 + \sum_{n=1}^{\infty} X^{(n)} h^{(n)} - N \right) \right] \quad (57)$$

$$\exp(-\beta N) = \frac{1}{n_d} \left\langle \exp \left[ -\varpi \left( \frac{1}{2} mc^2 \sum_{n=1}^{\infty} X^{(n)} h^{(n)} \right) \right] \right\rangle, \quad \varpi \equiv \frac{1}{k_B T} \quad (58)$$

where  $N$  and  $n_d$  are the normalization factor and number density, respectively. The first term in left hand side of equation (57) is the equilibrium part leading to the Maxwellian distribution function. The second term accounts for non-equilibrium effects.  $X^{(n)}$  represents

the unknown macroscopic quantities and is associated with conjugate variables to the molecular expressions for moment,  $h^{(n)}$ .

The polynomial Hermite expansion used in Grad's theory may yield negative values in high non-equilibrium conditions which is the inherent limitation of the method. We note that the upper limit of the summation operator in Eu's theory is infinite on the contrary to all other previous methods in which a finite estimation had been made. This issue is a critical difference which sets the Eu's theory in a better position compared to previous counterparts.

In summary, the exponential form is advantageous as:

- it is consistent with the additive property of the calortropy and calortropy production from a physics point of view
- it assures the non-negativity of the distribution function regardless of the level of approximation from the mathematics point of view

With denoting the term  $\varpi \left( \sum_{n=1}^{\infty} X^{(n)} h^{(n)} - N \right)$  as  $x$ , and dropping the superscript  $c$  for the

sake of simplicity, the distribution function can be written as,

$$f = f^{(0)} \exp(-x) \tag{59}$$

A set of notations and dimensionless variables are further defined:

$$\begin{aligned} x_{12} &= x_1 + x_2, y_{12} = y_1 + y_2 = x_{12}^*, \\ \bar{\sigma}_c &= \frac{\sigma_c}{k_B / g}, g \equiv \frac{1}{n^2 d^2} \sqrt{\frac{m}{2k_B T}}, \\ \bar{b} &= \frac{b}{d}, \bar{g}_{12} = g_{12} \sqrt{\frac{m}{2k_B T}}, \end{aligned} \tag{60}$$

$$\begin{aligned}
\mathbf{w} &= c \sqrt{\frac{m}{k_B T}}, \quad \omega(\mathbf{w}) \equiv \frac{1}{(2\pi)^{3/2}} \exp\left(-\frac{1}{2} \omega^2\right), \\
\omega_{12}(\mathbf{w}, \mathbf{w}_2) &\equiv \frac{1}{(2\pi)^3} \exp\left(-\frac{1}{2} \omega^2 - \frac{1}{2} \omega_2^2\right), \\
\langle A \rangle_c &\equiv \int d\hat{\Gamma}_{12} \omega_{12}(\mathbf{w}, \mathbf{w}_2) A(\mathbf{w}, \mathbf{w}_2), \\
\int d\hat{\Gamma}_{12} \omega_{12} \cdots &\equiv \int d\mathbf{w} \int d\mathbf{w}_2 \int_0^{2\pi} d\phi \int_0^\infty db \bar{b} \bar{g}_{12} \cdots, \\
\int d\Gamma_{12} \omega_{12} \cdots &\equiv \int d\mathbf{v} \int d\mathbf{v}_2 \int_0^{2\pi} d\phi \int_0^\infty db b g_{12} \cdots,
\end{aligned} \tag{61}$$

the calortropy production can be expressed as,

$$\begin{aligned}
\sigma_c &\equiv -k_B \langle \ln fC[f, f_2] \rangle = \\
&\frac{1}{T} \left\langle \left( \frac{1}{2} mc^2 + \sum_{n=1}^{\infty} X^{(n)} : h^{(n)} - N \right) C[f^{(0)} \exp(-x), f_2^{(0)} \exp(-x_2)] \right\rangle \\
&= \frac{1}{4} k_B \int d\mathbf{v} \int d\mathbf{v}_2 \int_0^{2\pi} d\phi \int_0^\infty db b g_{12} f^{(0)} f_2^{(0)} (x_{12} - y_{12}) [\exp(-y_{12}) - \exp(-x_{12})] \\
&= \frac{1}{4T} \int d\Gamma_{12} f^{(0)} f_2^{(0)} (x_{12} - y_{12}) [\exp(-y_{12}) - \exp(-x_{12})].
\end{aligned} \tag{62}$$

alternatively, we can write,

$$\bar{\sigma}_c = \frac{1}{4} \left\langle (x_{12} - y_{12}) [\exp(-y_{12}) - \exp(-x_{12})] \right\rangle_c. \tag{63}$$

This form of the mathematical equation is suitable for so-called cumulant expansion, i.e.,

$$\bar{\sigma}_c = \kappa_1^2 q(\kappa_1^{(\pm)}, \kappa_2^{(\pm)}, \dots), \tag{64}$$

where  $\kappa_1 \equiv \frac{1}{4} \left\{ \left\langle (x_{12} - y_{12})^2 \right\rangle_c \right\}^{1/2}$ .

$$q(\kappa_1^{(\pm)}, \kappa_2^{(\pm)}, \dots) \equiv \frac{1}{2\kappa_1} \left\{ \exp \left[ \sum_{l=1}^{\infty} \frac{(-1)^l}{l!} \kappa_l^{(+)} \right] - \exp \left[ \sum_{l=1}^{\infty} \frac{(-1)^l}{l!} \kappa_l^{(-)} \right] \right\}. \tag{65}$$

With the insertion of the definition of the distribution function (59) into calortropy production, the relation between the dissipation term and calortropy production manifests,

$$\begin{aligned}
\sigma_c &\equiv -k_B \langle \ln f C[f, f_2] \rangle = -k_B \left\langle \varpi \sum_{n=1}^{\infty} X^{(n)} h^{(n)} C[f, f_2] \right\rangle \\
&= \frac{1}{T} \sum_{n=1}^{\infty} X^{(n)} \langle h^{(n)} C[f, f_2] \rangle = \frac{1}{T} \sum_{n=1}^{\infty} X^{(n)} \Lambda^{(n)}
\end{aligned} \tag{66}$$

Calculation of the first reduced collision integral  $\kappa_l$  in terms of  $X^{(n)}$  yields the explicit form of the dissipation term. Defining  $\Delta h^{(n)} = h^{(n)} - h^{(n)*}$  and reminding

$$x \equiv \varpi \left( \sum_{n=1}^{\infty} X^{(n)} h^{(n)} - N \right),$$

$\kappa_1^2$  may be expressed as a quadratic form of  $X$  and  $X_2$  as follows,

$$\kappa_1^2 = \frac{1}{4} \sum_{n,l}^{\infty} \left\langle \left( X^{(n)} \Delta h^{(n)} + X_2^{(n)} \Delta h_2^{(n)} \right) \left( X^{(l)} \Delta h^{(l)} + X_2^{(l)} \Delta h_2^{(l)} \right) \right\rangle_c. \tag{67}$$

It can alternatively be arranged as,

$$\kappa_1^2 = \sum_{n,l}^{\infty} X^{(n)} R_{12}^{(nl)} X_2^{(l)} \tag{68}$$

where  $R_{12}^{(nl)}$  are the scalar coefficients made up of collision bracket integrals of  $h^{(n)}$  and  $h_2^{(l)}$  for an isotropic system of dilute gases. After comparing (65), (66), and (68), the following dissipation term can be derived as follows,

$$\bar{\sigma}_c = \kappa_1^2 q(\kappa_1^{(\pm)}, \kappa_2^{(\pm)}, \dots) = \varpi g \sum_{n=1}^{\infty} X^{(n)} \Lambda^{(n)} = \sum_{n,l}^{\infty} X^{(n)} R_{12}^{(nl)} X_2^{(l)} q(\kappa_1^{(\pm)}, \kappa_2^{(\pm)}, \dots), \tag{69}$$

$$\Lambda^{(n)} = \frac{1}{\varpi g} \sum_{n,l}^{\infty} R_{12}^{(nl)} X_2^{(l)} q(\kappa_1^{(\pm)}, \kappa_2^{(\pm)}, \dots). \tag{70}$$

The unknown conjugate variables  $X^{(n)}$  are achieved by generalizing the equilibrium Gibbs ensemble theory to nonequilibrium processes detailed in [117] as follows,

$$\langle h^{(n)} f \rangle / \rho = -k_B T \left( \frac{\partial}{\partial X^{(n)}} \ln Z \right), \tag{71}$$

$$\text{where } Z \equiv \frac{1}{n_d} \left\langle \exp \left[ -\frac{1}{k_B T} \left( \frac{1}{2} m c^2 + \sum_{n=1}^{\infty} X^{(n)} h^{(n)} \right) \right] \right\rangle.$$

$$X^{(1)} = -\frac{\mathbf{\Pi}}{2p}, X^{(2)} = -\frac{\mathbf{Q}}{pC_p T}. \quad (72)$$

Therefore, the moment equation of non-conserved variables for general type of molecules can be written as

$$\begin{aligned} & \rho \frac{d(\mathbf{\Pi}/\rho)}{dt} + \nabla \cdot \mathbf{\Psi}^{(\Pi)} + 2[\mathbf{\Pi} \cdot \nabla \mathbf{u}]^{(2)} + 2p[\nabla \mathbf{u}]^{(2)} \\ &= \frac{1}{\varpi g} \sum_l^{\infty} R_{12}^{(1l)} X_2^{(l)} q(\kappa_1^{(\pm)}, \kappa_2^{(\pm)}, \dots). \end{aligned} \quad (73)$$

$$\begin{aligned} & \rho \frac{d(\mathbf{Q}/\rho)}{dt} + \nabla \cdot \mathbf{\Psi}^{(Q)} + \mathbf{Q} \cdot \nabla \mathbf{u} + \mathbf{\Pi} \cdot C_p \nabla T + C_p p \nabla T \\ &= \frac{1}{\varpi g} \sum_l^{\infty} R_{12}^{(2l)} X_2^{(l)} q(\kappa_1^{(\pm)}, \kappa_2^{(\pm)}, \dots). \end{aligned} \quad (74)$$

The concept of *balanced closure* [4] implies that the kinematic high order term in the left-hand side,  $\nabla \cdot \mathbf{\Psi}^{(\Pi)}$ , and the dissipation term in the right-hand side,  $\sum_l^{\infty} R_{12}^{(2l)} X_2^{(l)} q(\kappa_1^{(\pm)}, \kappa_2^{(\pm)}, \dots)$  should be treated in a balanced manner, i.e., same order of approximation should be applied to both terms.

The variation of constitutive relations via balanced closure will be provided in Chapter 4. The extension of these equations to a more general case of diatomic and linear polytropic molecules will be discussed in the next sub-section.

### 3.5.3 Extension to diatomic and polyatomic

When modeling of diatomic and polyatomic gases is of interest, the concept of bulk viscosity becomes essential. In such gases, in addition to translational mode, rotational modes are also in effect. It is well known that the bulk viscosity of the gas flow which is associated with the relaxation of internal, rotational and vibrational, modes of molecules becomes zero for monatomic gases. However, for polyatomic gases, this parameter plays a significant role. In what follows, the incorporation of the rotational contribution of bulk

viscosity in the mathematical model via considering Boltzmann-Curtiss equation is explained.

### 3.4.3.2 Boltzmann-Curtiss equation

The Boltzmann-Curtiss transport (kinetic) equation extends the Boltzmann transport equation to take into account the effect of molecular rotation by adding extra terms in this regard. The equation for a diatomic molecule and in the absence of external forces reads as follows,

$$\left( \frac{\partial}{\partial t} + \mathbf{v} \cdot \nabla + \frac{j}{I} \frac{\partial}{\partial \theta} \right) f(\mathbf{v}, \mathbf{r}, t) = 0 \quad (75)$$

In the above equation  $j$ ,  $I$ , and  $\theta$  are the magnitude of the angular momentum, moment of inertia and azimuthal angle.

### 3.5.3.1 Conservation laws from Boltzmann-Curtiss equation

Similar to what has been done in section (3.4.1) microscopic properties corresponding to collisional invariants ( $\psi = \left[ m, m\mathbf{c}, \frac{1}{2}m\mathbf{c}^2 + H_{rot} \right]$ ) are multiplied in BTE and then integrated over the velocity space. The following conservation laws for monatomic gases can be achieved,

$$\frac{\partial}{\partial t} \begin{bmatrix} \rho \\ \rho \mathbf{u} \\ \rho E \end{bmatrix} + \nabla \cdot \begin{bmatrix} \rho \mathbf{u} \\ \rho \mathbf{u} \mathbf{u} + p \mathbf{I} \\ (\rho E + p) \mathbf{u} \end{bmatrix} + \nabla \cdot \begin{bmatrix} 0 \\ \mathbf{\Pi} + \Delta \mathbf{I} \\ (\mathbf{\Pi} + \Delta \mathbf{I}) \cdot \mathbf{u} + \mathbf{Q} \end{bmatrix} = 0. \quad (76)$$

Here  $\Delta$  is the excess stress vector defined as,

$$\Delta = \frac{1}{3} \text{Tr}(\mathbf{P}) - p. \quad (77)$$

The statistical definition of  $\Delta$  reads as,

$$\Delta = \left\langle \frac{1}{3} m \text{Tr}(\mathbf{cc}) f(t, \mathbf{r}, \mathbf{v}) \right\rangle = \int_{-\infty}^{\infty} \int_{-\infty}^{\infty} \int_{-\infty}^{\infty} \frac{1}{3} m \text{Tr}(\mathbf{cc}) f(t, \mathbf{r}, \mathbf{v}) d\mathbf{v}. \quad (78)$$

### 3.5.3.2 Boltzmann-Curtiss-based constitutive relationships

The essential steps in the process of extension of the derivation of Boltzmann-based constitutive relationships to Boltzmann-Curtiss-based relations is summarized in this section.

$$\left\langle h^{(n)} \frac{\partial f}{\partial t} \right\rangle + \left\langle h^{(n)} \mathbf{v} \cdot \nabla f \right\rangle + \left\langle h^{(n)} \frac{j}{I} \frac{\partial}{\partial \theta} \right\rangle = \left\langle h^{(n)} C[f, f_2] \right\rangle, \quad (79)$$

$$\begin{aligned} & \left\langle h^{(n)} \frac{\partial f}{\partial t} \right\rangle - \left\langle f \frac{d}{dt} h^{(n)} \right\rangle + \left\langle \mathbf{v} \cdot \nabla (h^{(n)}) \right\rangle - \left\langle \mathbf{v} f \cdot \nabla h^{(n)} \right\rangle + \left\langle \frac{j}{I} \frac{\partial}{\partial \theta} (h^{(n)} f) \right\rangle \\ & - \left\langle f \frac{j}{I} \frac{\partial}{\partial \theta} h^{(n)} \right\rangle = \Lambda^{(n)}, \end{aligned} \quad (80)$$

$$\begin{aligned} & \left\langle \frac{\partial}{\partial t} (h^{(n)} f) \right\rangle - \left\langle f \frac{d}{dt} h^{(n)} \right\rangle + \left\langle (\mathbf{c} + \mathbf{u}) \cdot \nabla (h^{(n)} f) \right\rangle - \left\langle (\mathbf{c} + \mathbf{u}) f \cdot \nabla h^{(n)} \right\rangle \\ & + \left\langle \frac{j}{I} \frac{\partial}{\partial \theta} (h^{(n)} f) \right\rangle - \left\langle f \frac{j}{I} \frac{\partial}{\partial \theta} h^{(n)} \right\rangle = \Lambda^{(n)}, \end{aligned} \quad (81)$$

$$\begin{aligned} & \left\langle \frac{\partial}{\partial t} (h^{(n)} f) \right\rangle - \left\langle f \frac{d}{dt} h^{(n)} \right\rangle + \mathbf{u} \cdot \nabla \langle h^{(n)} f \rangle + \left\langle \mathbf{c} \cdot \nabla (h^{(n)} f) \right\rangle - \left\langle \mathbf{c} f \cdot \nabla h^{(n)} \right\rangle \\ & - \left\langle \mathbf{u} f \cdot \nabla h^{(n)} \right\rangle - \left\langle f \frac{j}{I} \frac{\partial}{\partial \theta} h^{(n)} \right\rangle = \Lambda^{(n)}, \end{aligned} \quad (82)$$

$$\begin{aligned} & \left\langle \frac{\partial}{\partial t} (h^{(n)} f) \right\rangle - \left\langle f \frac{d}{dt} h^{(n)} \right\rangle + \mathbf{u} \cdot \nabla \langle h^{(n)} f \rangle + \nabla \cdot \langle \mathbf{c} h^{(n)} f \rangle - \langle h^{(n)} f (\nabla \cdot \mathbf{c}) \rangle \\ & - \left\langle \mathbf{c} f \cdot \nabla h^{(n)} \right\rangle - \left\langle \mathbf{u} f \cdot \nabla h^{(n)} \right\rangle - \left\langle f \frac{j}{I} \frac{\partial}{\partial \theta} h^{(n)} \right\rangle = \Lambda^{(n)}, \end{aligned} \quad (83)$$

$$\begin{aligned} & \left\langle \frac{\partial}{\partial t} (h^{(n)} f) \right\rangle - \left\langle f \frac{d}{dt} h^{(n)} \right\rangle + \mathbf{u} \cdot \nabla \langle h^{(n)} f \rangle + \nabla \cdot \langle \mathbf{c} h^{(n)} f \rangle - \langle h^{(n)} f (\nabla \cdot \mathbf{u}) \rangle \\ & - \left\langle \mathbf{c} f \cdot \nabla h^{(n)} \right\rangle - \left\langle \mathbf{u} f \cdot \nabla h^{(n)} \right\rangle - \left\langle f \frac{j}{I} \frac{\partial}{\partial \theta} h^{(n)} \right\rangle = \Lambda^{(n)}, \end{aligned} \quad (84)$$

$$\begin{aligned} & \left( \frac{\partial}{\partial t} + \mathbf{u} \cdot \nabla \right) \langle h^{(n)} f \rangle + \langle h^{(n)} f \rangle \cdot \nabla \mathbf{u} + \nabla \cdot \langle \mathbf{c} h^{(n)} f \rangle \\ & - \left\langle f \left( \frac{\partial}{\partial t} + \mathbf{u} \cdot \nabla + \mathbf{c} \cdot \nabla + \frac{j}{I} \frac{\partial}{\partial \theta} \right) h^{(n)} \right\rangle = \Lambda^{(n)}. \end{aligned} \quad (85)$$

The molecular definitions of stress tensor, excess normal stress, and heat flux vector for diatomic molecules are defined as,

$$\begin{bmatrix} h^{(1)} \\ h^{(2)} \\ h^{(3)} \end{bmatrix} = \begin{bmatrix} m[\mathbf{c}\mathbf{c}]^{(2)} \\ \frac{1}{3}mc^2 - \frac{p}{n} \\ (mc^2/2 + H_{rot} - m\hat{h})\mathbf{c} \end{bmatrix}. \quad (86)$$

Here,  $H_{rot}$  and  $\hat{h}$  denote rotational Hamiltonian of the molecule and enthalpy density, respectively.

$$\hat{h} = \frac{5}{2m}k_B T + \bar{E}_{rot}. \quad (87)$$

where the relation between average rotational energy density  $\bar{E}_{rot}$  and  $H_{rot}$  reads as,

$$\rho \bar{E}_{rot} = \langle H_{rot} f(t, \mathbf{r}, \mathbf{v}) \rangle. \quad (88)$$

Finally, the constitutive relation for stress tensor, excess normal stress, and heat flux can be written as,

$$\begin{aligned} \rho \frac{d}{dt} \begin{bmatrix} \Pi/\rho \\ \Delta/\rho \\ \mathbf{Q}/\rho \end{bmatrix} + \nabla \cdot \begin{bmatrix} \Psi^{(\Pi)} \\ \Psi^{(\Delta)} \\ \Psi^{(\mathcal{Q})} \end{bmatrix} + \begin{bmatrix} 2[\Pi \cdot \nabla \mathbf{u}]^{(2)} \\ 2\gamma'(\Pi + \Delta \mathbf{I}) : \nabla \mathbf{u} \\ \psi^{(P)} : \nabla \mathbf{u} + \frac{d\mathbf{u}}{dt} \cdot (\Pi + \Delta \mathbf{I}) + \mathbf{Q} \cdot \nabla \mathbf{u} + \Pi \cdot C_p \nabla T \end{bmatrix} \\ + \begin{bmatrix} 2(p + \Delta)[\nabla \mathbf{u}]^{(2)} \\ \frac{2}{3}\gamma' p \nabla \cdot \mathbf{u} \\ C_p(p + \Delta)\nabla T \end{bmatrix} = \begin{bmatrix} \Lambda^{(\Pi)} \\ \Lambda^{(\Delta)} \\ \Lambda^{(\mathcal{Q})} \end{bmatrix}. \end{aligned} \quad (89)$$

# Chapter 4. Mathematical modeling of multiphase gas-particles flows

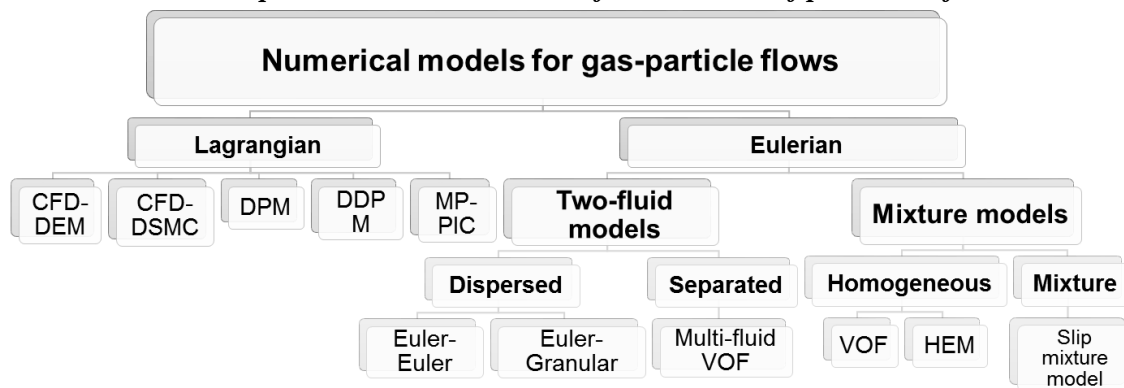
## 4.1 A general categorization of models for multiphase flows

Mathematical models for the description of dusty gas flows (generalizable to other multiphase classes) can be divided into two general categories by the assumptions made in modeling the dispersed phase: Lagrangian (where particles are considered as discrete phase) and Eulerian (where particles are considered as continuous phase) frameworks. In the Lagrangian framework (alternatively known as *trajectory*, *non-continuum* or *Eulerian-Lagrangian* model), each individual particle is tracked throughout space based upon Newton's equation of motions. The Eulerian framework (also referred to as *continuum* or *Eulerian-Eulerian* model), the particles are considered as a continuum, and a set of partial differential equations in a given coordinate system are solved to characterize the flow. A third category (or a sub-category of *Eulerian models*) can be devoted to *mixture* models, where both phases are defined by solving the continuum-based equation of a single fluid with modified properties. In the above categorization we assume that the gas phase is always characterized by an Eulerian approach; however, we need to bear in mind that the application of the Lagrangian framework in resolving the gas phase not only is feasible but also can be a more efficient strategy in specific cases.

Each category can be divided into some subcategories. The most popular models of the Lagrangian family include discrete particle model (DPM) and discrete element method (DEM). While DPM can produce fast computations compared to DEM, it is known to be appropriate only for modeling dilute particle flow (with particle volume fractions of less than 0.1). On the other hand, DEM can provide accurate solutions for a broader range of

flow regimes based upon particle concentration. The high computational demands in the aforementioned methods motivated the development of models such as the dense discrete phase model (DDPM) and multiphase particle-in-cell (MP-PIC) method in which the particle–particle, and particle–wall collisions are presented by a force function rather than being explicitly tracked. The Eulerian family in comparison with the Lagrangian counterpart, is more diverse, however. While two-fluid and mixture models are capable candidates for the solution of dispersed flows, volume of fluid (VOF) method, homogeneous equilibrium model (HEM) and two-fluid VOF method have shown desirable features in resolving separated flows or in conditions where the tracking and locating the fluid-fluid interface is of importance. This categorization is summarized in Table 5.

*Table 5 Popular mathematical models for simulation of particulate flows*



## 4.2 Model selection

The selection of a proper model is based on the investigated features of the flow under study and the capability of the model to resolve the features of interest. In fact, every computational model or scheme has its pros and cons which make the method suitable for a specific application. From a more general point of view, it is known that the Eulerian-Eulerian approaches demand less computational cost, while the Eulerian-Lagrangian (or Lagrangian-Lagrangian) methods provide solutions with better accuracy. The choice of computationally less expensive approach may allow more detailed investigation of the

whole transient phase of the flow. While the same may apply to the Lagrangian models, it may demand relatively more considerable computational cost. A comparison between the two general categories of models of simulating multiphase flows which summarizes the merits and drawbacks of each model is provided in Table 6.

*Table 6 Eulerian versus Lagrangian*

Model	Strength	Shortcoming
Eulerian	<ul style="list-style-type: none"> <li>● Easy incorporation of particle diffusion effects</li> <li>● Simple extendibility to multi-dimensional flows</li> <li>● A wide range of validity</li> </ul>	<ul style="list-style-type: none"> <li>● Numerical instabilities</li> <li>● Numerical diffusion</li> <li>● Large storage requirements for multiple particle sizes</li> <li>● Additional modeling for inter-particle interaction</li> </ul>
Lagrangian	<ul style="list-style-type: none"> <li>● Embodying the "natural" solution schemes for each phase</li> <li>● No numerical diffusion of the particulate phase</li> <li>● No excessive storage requirements for multiple particle sizes</li> </ul>	<ul style="list-style-type: none"> <li>● Need for empirical diffusion velocity or more expensive Monte Carlo methods</li> <li>● Complexity for coupling with Eulerian phase</li> <li>● Computationally expensive in high particulate loadings</li> </ul>

As the table indicates, each model should be applied based on its merit and according to the specific requirement of the simulation. The selection of model can be based upon the regime defined by the particulate loading of the flow which is demonstrated in the Fig. 5.

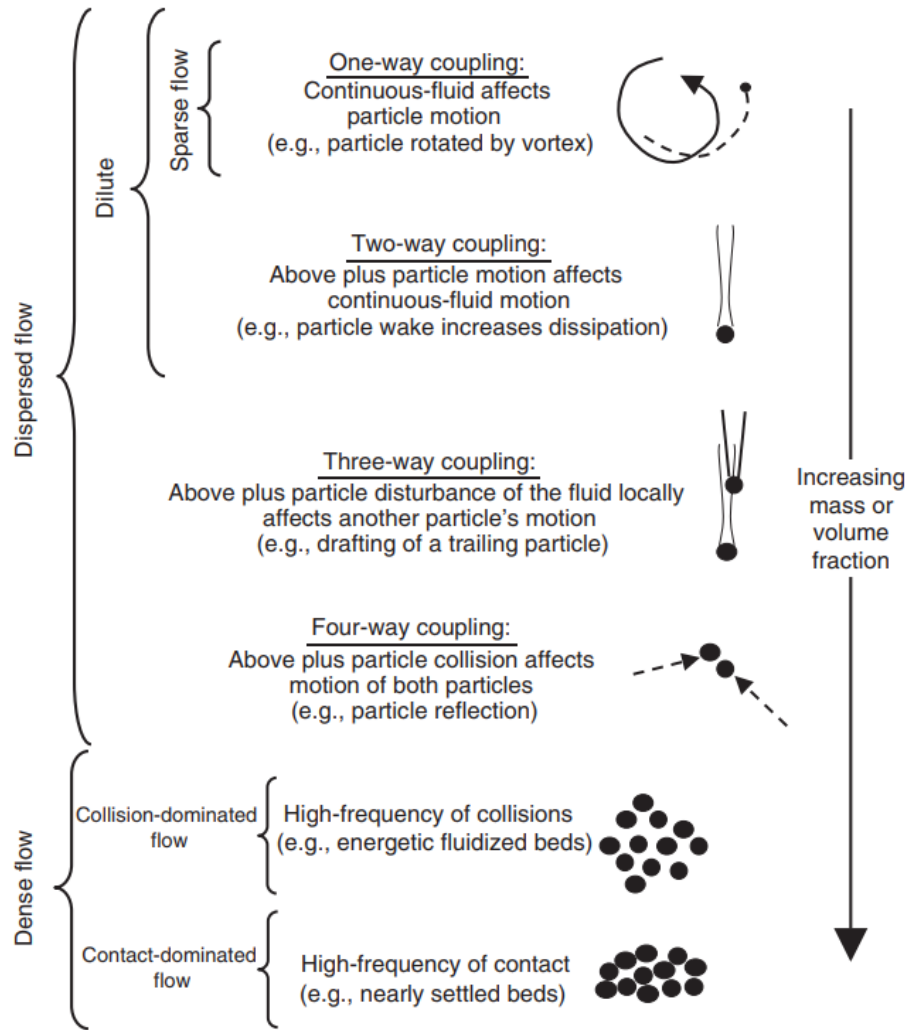
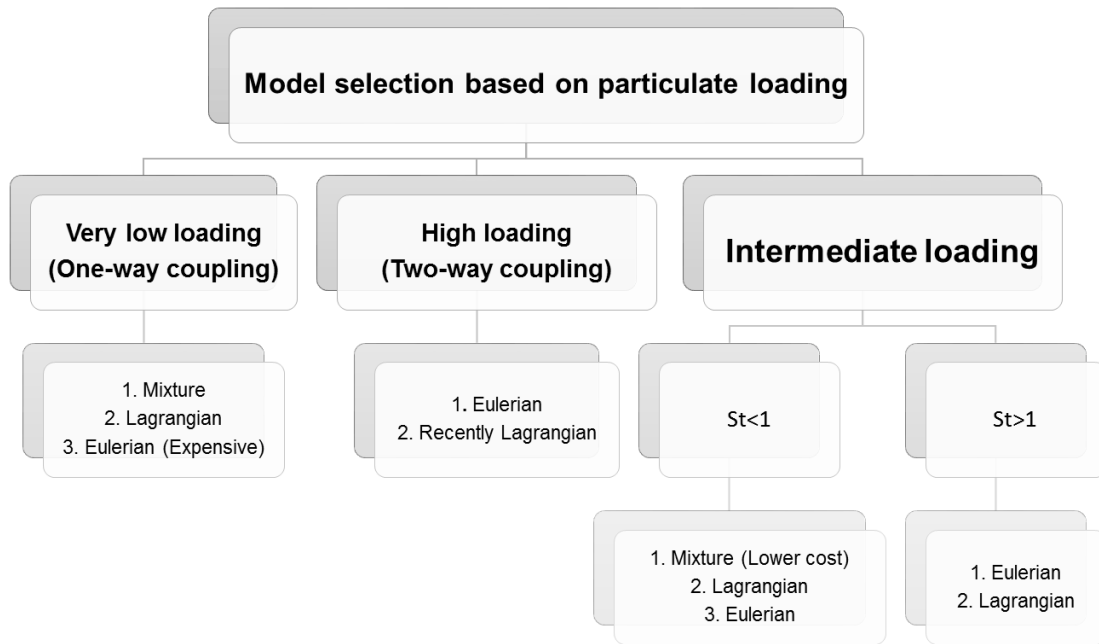


**Fig. 5 Classification of multiphase flows and the coupling effects based on particulate loading. Reprinted from [118] with permission.**

The particulate flows (including dusty gas flows) can be categorized into dispersed and dense. For particulate loadings higher than  $10^{-3}$ , the regime is categorized as dense, where high-frequency particle-particle collisions and contacts influence the flow structure. Particulate loading of  $10^{-1}$  marks the boundary of collision dominated and contact dominated flows. The other extreme, i.e., particulate loadings of less than  $10^{-3}$  corresponds to the dispersed flow regime. When the particulate loading is less than  $10^{-6}$  (or  $10^{-4}$  in some literature), the flow is called sparse, and only a one-way coupled modeling can provide satisfactory solutions. In Table 7, the suitable mathematical model based on the loading level is illustrated.

**Table 7 Selection of the most efficient model based on the type of multiphase problem**



In the problem of Lunar landing which has been the central motif of this dissertation, a wide range of particulate loadings may exist. Moreover, the Eulerian models can provide acceptable results in a wide range of applications— especially when the volume fraction of the two phases is comparable or when the interaction of the phases signifies the hydrodynamics of the flow as shown in Table 7. In Fig. 6, categorization of flow regimes based on the volume fraction of particles, number density, and particle diameter is provided. Moreover, the regime of interest (marked by a circle) is determined based on the approximate values of the aforementioned parameters in a typical Lunar landing obtained from previously published results for Apollo descent engine. Thus, the two-fluid Eulerian model can be considered as a suitable/efficient tool and has been applied as the modeling approach of this dissertation. In the Lunar landing problem as well as the other investigated problems in this dissertation, the interface shape and location is not essential. Thus dispersed Eulerian models are sufficient for the purposes has been followed during this research.

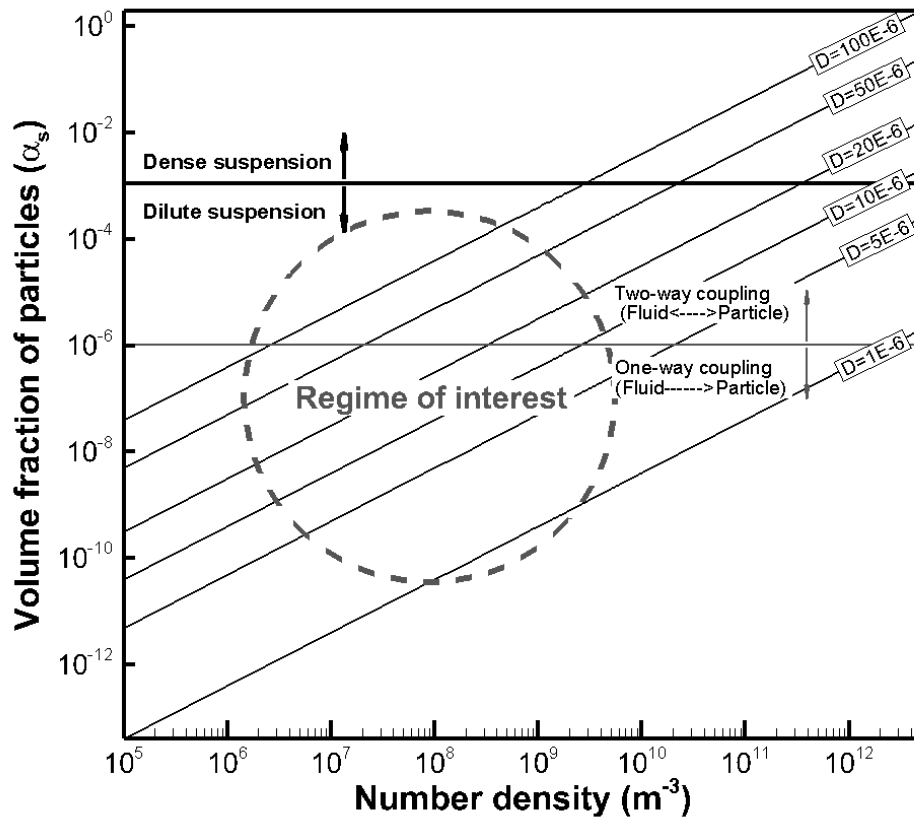


**Fig. 6** The range of encountered regimes in the Lunar landing problem overlaid on the classification of the particulate flows based on number density and particles volume fraction

It is worth to note that both dusty gas flows and gas-droplet flows are a sub-division of gas-particle flows. They are distinguished by the fact that mass transfer does not occur in the former but occurs in the latter. Thus the above discussions are extendable to gas-droplet flows as well.

The rest of this chapter is devoted to the introduction of the generic form of the two-fluid model which is the focus of current work. Furthermore, variants of the models for different types of problems are discussed, and constitutive relations of non-conserved variables which are the primary source of the deviation of models are introduced.

### **4.3 Balanced laws (for the generic two-fluid model)**

The two-fluid model is formulated by considering two separate sets of conservation equations which govern the balance of mass, momentum, and energy for each phase of the two-phase system. The interaction of the two phases is then taken into account via source terms, i.e., by momentum and heat transfer exchange between the gas and particles. Other interfacial effects including lift and gravity can be neglected since they are small compared to drag and heat transfer. In cases where the interface tracking is of interest, solving an additional face tracking model is necessary. However, in most of the dispersed solid-gas multiphase flows, the evolution and growth of interface if not unimportant, it is of secondary importance. In this section, the conventional assumptions made for computation of dusty gas flows are introduced. Then the general form of the conservation laws is provided, and the constitutive equations necessary to close the equations (the essence of the present work) are introduced in the subsequent subsections. Finally, we provide the normalized form of these equations and briefly explain the significance and role of the non-dimensional parameters that appear in the mathematical model.

#### **4.3.1 Assumptions of two-fluid dusty gas model**

A number of assumptions, conventional in the pioneering and previous literature are introduced in order to simplify the computations. These assumptions might be further refined for specific purpose applications in order to resolve the governing physical phenomena which are significant in that specific problem. These general assumptions in the majority of the works which considered dusty gas flows are as follows

- the gas phase is considered as compressible which follows the perfect-gas law;
- the solid phase is considered as incompressible;
- the particles have a constant density (constant microscopic density);
- the thermal and Brownian motion of particles are neglected;

- the number density of the particles should be large enough not to violate the continuum assumption;
- particles are assumed to be uniform sized spheres with a constant diameter;
- the inter-particle collisions are neglected (and thus no pressure term in the solid phase conservation law);
- specific heat of the particles material is constant, and the temperature is uniform within each particle;
- the particles are considered as inert;
- the gravitational and buoyant forces are negligible;
- the volume occupied by the solid phase is negligible compared to that of gas;
- the gas is considered as inviscid. Therefore, viscous and heat-conduction effects are solely considered between the gas and particles;
- the turbulence effects of gas and particles are neglected
- the effect of particles' wake is neglected.

While some of the assumptions introduced above are consequent of fundamental characteristics of the model which cannot be ignored, there is room for modifying some of the other assumptions which have been used in the previous literature in order to provide solutions closer to reality specific to the problem under investigation. For example, the effect of gravity (which finds importance in problems such as volcanic eruptions) can be quickly taken into account by additional source terms without disturbing any fundamental assumptions [82, 119, 120]. The models for inter-particle collisions has been also proposed [121-123]. The viscous effects in the gas phase can also be considered. Kinetic theory approaches have also been considered for continuum modeling of the dispersed phase [124].

### 4.3.2 Conservation laws

In this section, a simplified but general two-fluid model of dusty gas flows will be explained briefly. In what follows, the carrier phase (gas) and the dispersed phase (solid dust) are indicated by the subscripts  $g$  and  $s$ .

Under the conditions above, the conservation law can be written as follows:

For the gas phase,

$$\partial_t \mathbf{U}_g + \nabla \cdot \mathbf{F}_g = \mathbf{S}, \quad (90)$$

$$\mathbf{U}_g = \begin{bmatrix} \alpha_g \rho_g \\ \alpha_g \rho_g \mathbf{u}_g \\ \alpha_g \rho_g E_g \end{bmatrix}, \quad \mathbf{F}_g = \begin{bmatrix} \alpha_g \rho_g \mathbf{u}_g \\ \alpha_g \rho_g \mathbf{u}_g \mathbf{u}_g + p \mathbf{I} + \mathbf{\Pi}_g \\ (\alpha_g \rho_g E_g + p) \mathbf{u}_g + \mathbf{\Pi}_g \cdot \mathbf{u}_g + \mathbf{Q}_g \end{bmatrix}, \quad (91)$$

$$\mathbf{S} = \begin{bmatrix} 0 \\ D_{g,s} (\mathbf{u}_s - \mathbf{u}_g) \\ D_{g,s} (\mathbf{u}_s - \mathbf{u}_g) \mathbf{u}_s + Q_{g,s} (T_s - T_g) \end{bmatrix},$$

moreover, for the solid phase,

$$\partial_t \mathbf{U}_s + \nabla \cdot \mathbf{F}_s = -\mathbf{S}, \quad (92)$$

$$\mathbf{U}_s = \begin{bmatrix} \alpha_s \rho_s \\ \alpha_s \rho_s \mathbf{u}_s \\ \alpha_s \rho_s E_s \end{bmatrix}, \quad \mathbf{F}_s = \begin{bmatrix} \alpha_s \rho_s \mathbf{u}_s \\ \alpha_s \rho_s \mathbf{u}_s \mathbf{u}_s + \mathbf{\Pi}_s \\ (\alpha_s \rho_s E_s) \mathbf{u}_s + \mathbf{\Pi}_s \cdot \mathbf{u}_s + \mathbf{Q}_s \end{bmatrix}, \quad (93)$$

Here the  $\mathbf{U}$ ,  $\mathbf{F}$ , and  $\mathbf{S}$  are the vectors of conservative variables, fluxes, and source terms, respectively. The variables  $t$ ,  $\alpha$ ,  $\rho$ ,  $\mathbf{u}$ ,  $E$ ,  $p$ ,  $T$ ,  $\mathbf{\Pi}$ , and  $\mathbf{Q}$  represent time, volume fraction, density, velocity vector, total energy, pressure, temperature, stress tensor and heat flux vector. Further,  $D$  and  $Q$  show interphase drag and heat flux, respectively. The dust density  $\rho_s$  is assumed to be constant.

### 4.3.3 Three-dimensional conservation laws with axial symmetry

The above system of equations were written in a general form and can be easily re-written for one to three-dimensional flows. However, a particular case is the three-

dimensional flows with axial symmetry. A two-dimensional formulation in the two space variables  $(x, r)$  can be achieved by rewriting the equations in cylindrical coordinates  $(x, r, \theta)$ . Axisymmetric flow equations for the inviscid gas phase are provided in here as they are the governing equation in most of the cases of this thesis. Extension of this system of equation for viscous flows and as well as for the dust phase is trivial.

$$\frac{\partial}{\partial t}(\mathbf{U}_g) + \frac{\partial}{\partial x}\mathbf{F}_g(\mathbf{U}_g) + \frac{\partial}{\partial r}\mathbf{G}_g(\mathbf{U}_g) = \mathbf{S}_1 + \mathbf{S}_2 \quad (94)$$

$$\mathbf{U}_g = \begin{bmatrix} \alpha_g \rho_g \\ \alpha_g \rho_g u_g \\ \alpha_g \rho_g v_g \\ \alpha_g \rho_g E_g \end{bmatrix}, \quad \mathbf{F}_g = \begin{bmatrix} \alpha_g \rho_g u_g \\ \alpha_g \rho_g u_g^2 + p \\ \alpha_g \rho_g u_g v_g \\ (\alpha_g \rho_g E_g + p)u_g \end{bmatrix}, \quad \mathbf{G}_g = \begin{bmatrix} \alpha_g \rho_g v_g \\ \alpha_g \rho_g u_g v_g \\ \alpha_g \rho_g v_g^2 + p \\ (\alpha_g \rho_g E_g + p)v_g \end{bmatrix}$$

$$\mathbf{S}_1 = \begin{bmatrix} 0 \\ D_{g,s}(u_s - u_g) \\ D_{g,s}(v_s - v_g) \\ D_{g,s}((u_s - u_g)u_s + (v_s - v_g)v_s) + Q_g(T_s - T_g) \end{bmatrix}, \quad (95)$$

$$\mathbf{S}_2 = \frac{1}{r} \begin{bmatrix} \alpha_g \rho_g v_g \\ \alpha_g \rho_g u_g v_g \\ \alpha_g \rho_g v_g^2 \\ (\alpha_g \rho_g E_g + p)v_g \end{bmatrix}.$$

In the above relation,  $x$  and  $r$  are the axial and radial directions;  $u$  and  $v$  are the corresponding velocities.  $\mathbf{F}$  and  $\mathbf{G}$  are the inviscid flux in axial and radial directions.  $\mathbf{S}_1$  and  $\mathbf{S}_2$  are source terms responsible for phase interactions and axisymmetric geometry.

## 4.4 Constitutive relations

A set of closure relationships are required to complete the mathematical model introduced in the previous section. These constitutive relations are introduced in this section. Application of different constitutive relations for the non-conserved variables leads to variants of the generic model which will also be discussed here.

#### 4.4.1 Volume fraction closure

This closure is an indication that the phases are treated as interpenetrating continua, defined as

$$\begin{aligned} 0 \leq \alpha_g \leq 1, \quad 0 \leq \alpha_s \leq 1, \\ \alpha_g + \alpha_s = 1. \end{aligned} \quad (96)$$

#### 4.4.2 Equation of state

The equation of state expresses the gas pressure in terms of other gas properties:

$$p = \rho_g RT_g, \quad (97)$$

where  $R$  is the gas constant.

The equation of state for the solid phase is not needed since it is treated as incompressible.

The total specific energy of the gas and particulate phases are defined as

$$E_g = c_v T_g + \frac{1}{2} |\mathbf{u}_g|^2, \quad (98)$$

$$E_s = c_m T_p + \frac{1}{2} |\mathbf{u}_s|^2, \quad (99)$$

where  $c_v$  and  $c_m$  are the specific heat capacity of the gas at constant volume and the specific heat of the particle material.

#### 4.4.3 Drag forces on spherical particles

According to Miura and Glass [70], the drag force that solid particles exert on the gas phase can be expressed as,

$$D_{g,s} = \frac{3}{4} C_D \frac{\alpha_s \rho_g}{d} |\mathbf{u}_g - \mathbf{u}_s|, \quad (100)$$

in which  $d$  is the particle diameter and  $C_D$  is the drag coefficient computed as a function of the Reynolds number based on the particle diameter and relative velocity of the particle to

the gas (i.e.  $Re_d = \frac{\rho_g d |\mathbf{u}_g - \mathbf{u}_s|}{\mu_g}$ ). Based on experimental studies of Morsi and Alexander

[125], drag coefficient on a particle can be defined as a function of Reynolds number as follows

$$C_D = a_0 + \frac{a_1}{Re_p} + \frac{a_2}{Re_p^2}. \quad (101)$$

where  $a_0$ ,  $a_1$  and  $a_2$  are empirical coefficients which differ for different Reynolds numbers.

The other expression for  $C_D$ , which is widely used is provided by Durst *et al.* [126]

$$C_D = \frac{24}{Re_p} (1 + 0.15 Re_p^{0.687}). \quad (102)$$

A better estimate is the following well-established semi-empirical correlation [119],

$$C_D = \begin{cases} \frac{24}{Re_d} (1 + 0.15 Re_d^{0.687}), & \text{if } Re_d < 1000 \\ 0.44, & \text{if } Re_d > 1000 \end{cases} \quad (103)$$

Other drag coefficient models are also evaluated in the literature [127] including the early models by Newton, Stokes and Oseen defined as

Newton	$C_D = 0.44$	$1000 \leq Re_d \leq 2 \sim 4 \cdot 10^5$
Stokes	$C_D = \frac{24}{Re_d}$	$Re_d \leq 1$
Oseen	$C_D = \frac{24}{Re_d} \left( 1 + \frac{3}{16} Re \right)$	$Re_d \leq 1$

(104)

Later, a variety of other models with an improved range of validity were proposed, such as:

Klychko [128]	$C_D = \frac{24}{Re_d} \left( 1 + \frac{(Re)^{2/3}}{6} \right)$	$Re_d \leq 1000$
---------------	---	------------------

(105)

Gilbert [129]  $C_D = 0.48 + 28(\text{Re})^{-0.85}$   $\text{Re}_d \leq 2 \sim 4.10^5$

Clift [130]

$$C_D = \begin{cases} \frac{24}{\text{Re}_d} (1 + 0.15 \text{Re}_d^{0.687}), & \text{if } 0 < \text{Re}_d < 800 \\ \frac{24}{\text{Re}_d} (1 + 0.15 \text{Re}_d^{0.687}) + \frac{0.42}{1 + 42500(\text{Re})^{-1.16}}, & \text{if } 800 < \text{Re}_d < 3.10^5 \end{cases}$$

Models, which consider the Mach number (compressibility) effects, have also been proposed by Henderson [131].

$$C_D = \begin{cases} \frac{24}{\text{Re}_d + S \left\{ 4.33 + \frac{3.65 - 1.53\Theta/T}{1 + 0.353\Theta/T} \exp\left(-0.247 \frac{\text{Re}}{S}\right) \right\}} \\ + \exp\left(-0.5 \frac{M}{\sqrt{\text{Re}}}\right) \left\{ \frac{4.5 + 0.38(0.3\text{Re} + 0.48\sqrt{\text{Re}})}{1 + 0.03\text{Re} + 0.48\sqrt{\text{Re}}} 0.1M^2 + 0.2M^8 \right\} \\ + 0.6S \left\{ 1 - \exp\left(-\frac{M}{\text{Re}}\right) \right\}, & \text{if } M < 1.0 \\ C_D|_{M=1.0} + \frac{4}{3}(M - 1.0)(C_D|_{M=1.75} - C_D|_{M=1.0}) & \text{if } 1.0 < M < 1.75 \\ \frac{0.9 + \frac{0.34}{M^2} + 1.86\sqrt{\frac{M}{\text{Re}}} \left( 2 + \frac{2}{S^2} + \frac{1.058}{S} \sqrt{\Theta/T} - \frac{1}{S^4} \right)}{1 + 1.86\sqrt{M/\text{Re}}}, & \text{if } M \geq 1.75 \end{cases} \quad (106)$$

where,

$$S = M \sqrt{\frac{\gamma}{2}}. \quad (107)$$

Knudsen number dependent drag coefficients are also available in the literature [132],

$$C_D = A(24/\text{Re})(1 + 0.25\text{Re}^{0.687}) \text{ where } A = 1/[1 + \text{Kn}(3.83 + 1.28\exp(-1/\text{Kn}))].$$

Some studies on the application of proper drag models in dusty gas flows are available in the literature. An example of such studies can be found in [76]. The comparison of models indicates that all models tested can produce similar results, except for Stokes and

Oseen which are only valid for very small Reynolds numbers ( $Re < 1$ ). Moreover, the variation of the numerical results is minimal. Therefore, a wise selection suggests a model with less complexity. Regarding the Mach number effects, as mentioned in [133], the application of incompressible drag coefficients for Mach numbers in the early supersonic regime is sufficient. Therefore, despite the fact that most of the flow problems under investigation in this work are compressible flows simple piecewise functions such as the one provided in (103) is used. This selection is mainly for keeping consistent with previous studies [75, 80, 81] as well as considering the computational efficiency. We note that the drag coefficients are algebraic equations that can be easily plugged into the numerical code without interfering the generality of the method. When an intermediate solution for the problem under study is achieved, the effects of drag model can be further investigated.

The heat transfer, which is proportional to temperature difference, can be expressed as a function of the Nusselt number [134],

$$Q_{g,s} = \frac{6Nu\kappa_g}{d^2} \alpha_s (T_g - T_s), \quad (108)$$

$$Nu = 2 + 0.65 Re_d^{\frac{1}{2}} Pr^{\frac{1}{3}}, \quad Pr = \frac{c_p \mu_g}{\kappa_g}. \quad (109)$$

Here  $\mu_g$  and  $\kappa_g$  represent the viscosity and thermal conductivity of the gas, respectively. Other relations for Nu number can be found in [135-137].

#### 4.4.4 Non-conserved variable of the gas phase

The primary challenge in modeling the of the majority of the particulate-gas flows is the establishment of an accurate hydrodynamic description of particulate phase [138]. However, in the Lunar landing problem this is not the case, i.e., the establishment of the accurate model is as important as or even more critical than modeling of the dust phase. As explained in Chapter 3, the conservation laws can be directly extracted from the Boltzmann

equation. With the same approach detailed in subsection 3.5, a set of equations for the non-conservative variables can be derived. The zeroth and first-order approximation of high order terms in this relation would recover the Euler and Navier-Stokes classical relationships. However, by a second order approximation (equipped with the concept of balanced closure) a non-linear coupled constitutive relationship (NCCR) can be achieved. When the viscous effects become significant, the validity of classical relationships are questionable, and application of second-order Boltzmann-based relationships are necessary. These relations are introduced in this section.

The constitutive relations from zero-order to second order based on the balanced closure of Myong [4] are provided in the Table 8.

**Table 8 Summary of zeroth to second order Boltzmann-based constitutive relationships**

Zeroth-order Boltzmann based (Euler-type) constitutive models
$\begin{aligned}\mathbf{\Pi}_g &= 0, \\ \Delta_g &= 0, \\ \mathbf{Q}_g &= 0.\end{aligned}$
First-order Boltzmann based (NF type) constitutive models
$\begin{aligned}\mathbf{\Pi}_g &= -2\mu_g [\nabla \mathbf{u}_g]^{(2)}, \\ \Delta_g &= -\mu_b \nabla \cdot \mathbf{u}_g, \\ \mathbf{Q}_g &= -\kappa_g \nabla T_g.\end{aligned}$
Second-order Boltzmann based (NCCR type) constitutive models
$\begin{aligned}(2p_g + \Delta_g)[\nabla \mathbf{u}_g]^{(2)} + 2[\mathbf{\Pi}_g \cdot \nabla \mathbf{u}_g]^{(2)} &= -\frac{p_g}{\mu_g} \mathbf{\Pi}_{g2nd}(\kappa_1), \\ 2\gamma'_g (\mathbf{\Pi}_g + \Delta_g \mathbf{I}) : \nabla \mathbf{u}_g + \frac{2}{3} \gamma'_g p_g \nabla \cdot \mathbf{u}_g &= -\frac{2}{3} \gamma'_g \frac{p_g}{\mu_b} \Delta q_{g2nd}(\kappa_1), \\ (p_g + \Delta_g) C_p \nabla T_g + \mathbf{\Pi}_g \cdot C_p \nabla T_g + \mathbf{Q}_g \cdot \nabla \mathbf{u}_g &= -\frac{p_g C_p}{\kappa_g} \mathbf{Q}_g q_{2nd}(\kappa_1).\end{aligned}$

The bulk viscosity, shear viscosity, and second coefficient viscosity are related according to the following relation,

$$\mu_b = \lambda + \frac{2}{3}\mu. \quad (110)$$

Here, a distinction should be made regarding Navier-Fourier (NF) and Navier-Stokes-Fourier (NSF) terms. In the latter, the Stokes hypothesis ( $\mu_b = 0$ ) implies  $\lambda = -\frac{2}{3}\mu$ .

#### 4.4.5 Non-conserved variables of the solid phase

The majority of the previous works which considered dusty gas flows by two-fluid model, have applied Euler-type relations ( $\mathbf{\Pi}_s=0$  and  $\mathbf{Q}_s=0$ ) [64, 66, 70, 71, 78, 80, 133, 139-143] capable of describing the *hydrodynamics* behavior of the particle phase adequately. As the collision term scales with the square of particle phase volume fraction, the pressure and stress tensor of solid phase tends to zero in dilute limit which makes the pressureless gas assumption valid in this regime. However, this leads to a shortcoming of the two fluid model due to appearance of delta-shocks and advent of intense particle segregation. Moreover, when the role of particle-particle collisions in the description of the solid phase is not negligible, the closures models for the solid stress tensor would play a significant role in the modeling. The closure models are the chief factor that makes the two-fluid models differ from each other significantly [138]. According to Castellanos *et al.* [144], four different granular regimes can be defined as depicted in Fig. 7. These are plastic, inertial, fluidized, and entrained regimes which are characterized by the tightly packed granular bed, inter-particle collisions, interstitial effects, and large mean free paths, respectively. The latter, also known as rapid granular flow, is of central importance when the simulation of erosion and consequent entrainment of the particles into flow field due to impingement of descent engine plume of a Lunar lander is of interest. Prior to simulation, the existing regimes should be distinguished to select the proper mathematical model. A

rough but sensible estimate of the regimes can be done by defining three regions in nozzle proximity as shown in Fig. 8. The particulate loading and the Stokes number can be used to characterize the flow. Region 1, just beneath the nozzle, is the onset of erosion. Here the gas flow after experiencing the powerful stand-off shock wave would stagnate due to a confrontation with the surface. In this area, the gas static pressure is maximum, and the gas velocity is minimum. In the second region, the fictitious passage formed by the stand-off shock and the surface acts as a converging-diverging passage accelerating the gas to reach supersonic velocities. The maximum erosion happens in this area. In region 3, both the particles and gas molecules expand further into Moon semi-vacuum atmosphere and undergo free traveling with high velocities. The data range of the simulation results by previous studies indicates that the granular flows in the limits of suspensions and early fluidized bed may appear depending on the erosion rate.

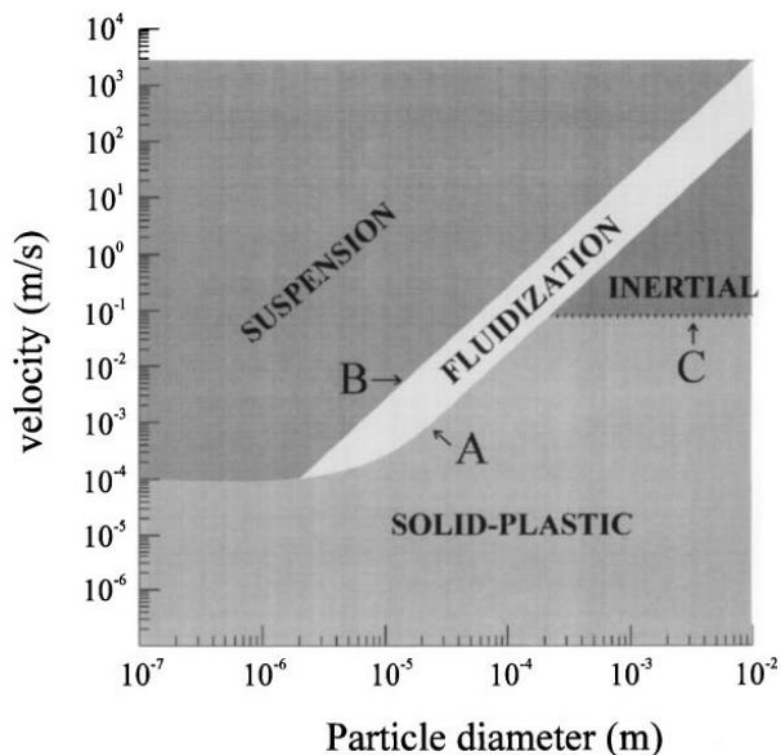


**Fig. 7** A typical phase diagram determining the transition between granular flow regimes as a function of particle diameter. Reprinted from [144] with permission.

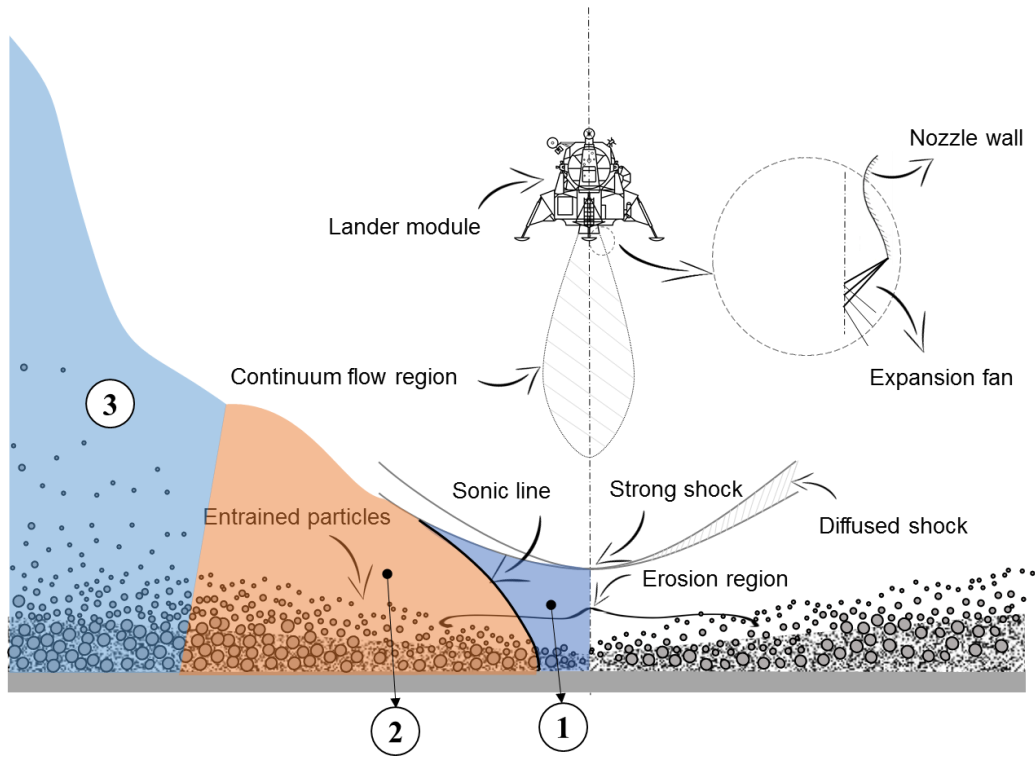


**Fig. 8 Graphical categorization of different regions with various specifications. Regions 1-3 are quantified in the Table 9.**

Table 9 summarizes the characteristics of different regions of Fig. 8.

**Table 9 Range of important parameters in different regions of Fig. 8**

	Region 1	Region 2	Region 3
$u_g$	Very low	High	High
$u_s$	0	Low	High
$\rho_g$	$O(10^{-3})$	$O(10^{-4})$	$\geq O(10^{-4})$
$\rho_s$	Constant	Constant	Constant
$\alpha_s$	Very low	High	Intermediate
$\alpha_g$	$\approx 1$	Low	Intermediate
$\beta$	$\approx 0$	Intermediate	High
$St$	$\ll 1$	$< 1$	$\approx 1$

Three approaches to define the solid stress tensor (solid viscosity, more specifically) are available. In the early models of [145-147], experiments are used to define the dependence

of solid phase pressure on the particle volume fraction and also an empirical constant is used to define viscosity. These models are known as *constant viscosity models* (CVM). The other class of models, by the analogy from the gas phase, defined a particle turbulent viscosity. These models are however restricted to dilute dusty gas flows as the effect of particle-particle collision is not included. Moreover, some has tried to develop relations based on kinetic theory of the gases and considering a similar analogy with rarefied gas flows, leading to the so-called *kinetic theory of granular flows* (KTGF), class of closure models for kinetic-collisional stresses [124, 148-151]. Such an approach can provide a link between the microscopic and macroscopic descriptions of the granular flow. These models have been mostly applied in fluidized beds and moving beds, however, they can be used (with a reasonable level of approximation) in various other applications when the particle-particle interactions (through binary and frictional contacts) modeling is crucial. One must keep in mind that the granular flow of particles is significantly different from the molecular gas flows. The main differences are due to 1. elastic collisions in gases versus elastic-plastic deformation and surface friction in particles and, 2. conservation of kinetic energy in an isothermal system for gases versus inexistence of an equilibrium state in granular systems without external energy sources [138]. Schneiderbauer *et al.* [151] demonstrated that the model could provide substantial improvement compared to the DEM simulations. Two-fluid models based on KTGF has shown desirable capability in providing the particle pressure, viscosity and other transport coefficients; besides, less *ad hoc* adjustments are required, compared to the previously discussed models. However, the method has limitations as well [150] and is under development. An alternative model for the models above is the application of higher-order constitutive relations which can be derived with a similar approach applied for the gas phase, detailed in Chapter 3 of this thesis. The KTGF models are known to provide promising results when the volume fraction of particles  $\alpha_s$ ,

is less than 40% (where the assumption of binary collisions holds true). Had the solid volume fraction been higher, the solid phase would undergo multiple particle-particle frictional contacts leading to failure of kinetic theory in explaining the physics of dense granular media.

As the basics of the kinetic theory have been discussed in detail in Chapter 3, we refuse to repeat those discussions. However, the procedure and the final constitutive relations are briefly provided for completeness.

In what follows the procedure to formulate the KTGF constitutive relations is summarized. The time evolution of the granular temperature can be given by KTGF as,

$$\frac{3}{2} \left[ \frac{\partial}{\partial t} (\alpha_s \rho_s T_s) + \nabla \cdot (\alpha_s \rho_s T_s \mathbf{u}_s) \right] = - (p_s \mathbf{I} + \mathbf{\Pi}_s) : \nabla \mathbf{u}_s - \nabla \cdot \mathbf{Q}_s - 3\beta \mathbf{T}_s - \gamma_s, \quad (111)$$

where  $\beta$  and  $\gamma_s$  are the momentum exchange coefficient and the dissipation of kinetic energy due to inelastic particle collisions, respectively. Moreover,

$$\mathbf{P}_s = \langle m \mathbf{c} \mathbf{c} f(t, \mathbf{r}, \mathbf{v}) \rangle = \int_{-\infty}^{\infty} \int_{-\infty}^{\infty} \int_{-\infty}^{\infty} m \mathbf{c} \mathbf{c} f_s(t, \mathbf{r}, \mathbf{v}) d\mathbf{v}, \quad (112)$$

$$\mathbf{Q}_s = \left\langle \frac{1}{2} m c^2 \mathbf{c} f_s(t, \mathbf{r}, \mathbf{v}) \right\rangle = \int_{-\infty}^{\infty} \int_{-\infty}^{\infty} \int_{-\infty}^{\infty} \frac{1}{2} m c^2 \mathbf{c} f_s(t, \mathbf{r}, \mathbf{v}) d\mathbf{v}. \quad (113)$$

In KTGF, to achieve explicit expressions for the above variables, the distribution function is expanded about the equilibrium distribution function to second order (via the Chapman-Enskog expansion) to yield the following expansion

$$\mathbf{P}_s = p_s \mathbf{I} + \mathbf{\Pi}_s, \quad (114)$$

$$\mathbf{Q}_s = -\kappa_s \nabla T_s. \quad (115)$$

Thus,

$$\mathbf{\Pi}_s = -\mu_s \left[ (\nabla \mathbf{u}_s) + (\nabla \mathbf{u}_s)^T \right] - \left( \lambda_s - \frac{2}{3} \mu_s \right) [(\nabla \cdot \mathbf{u}_s) \mathbf{I}]. \quad (116)$$

The unknown parameters in the above relations, viz.,  $\kappa_s$ ,  $\lambda_s$ ,  $\mu_s$ , and  $p_s$ , can be calculated if the collision integral of the Boltzmann equation for the solid particles are known. A simple BGK model will not provide desirable results for particle phase as it does not contain the description of particle-particle interactions. Thus, after introducing a joint probability function  $f_s^{(2)}$  in terms of solid distribution function  $f_s$  and pair distribution function  $g$  (which itself is dependant upon the distance  $r_{12} = |\mathbf{r}_2 - \mathbf{r}_1|$  and the solid fraction), the collision integral of the solid phase can be estimated resulting in explicit expressions for pressure, shear viscosity, and thermal conductivity:

$$\mu_s = \frac{5}{96} \pi \rho_s d \sqrt{\frac{T_s}{\pi}} \quad (117)$$

$$\kappa_s = \frac{75}{384} \pi \rho_s d \sqrt{\frac{T_s}{\pi}} \quad (118)$$

$$p_s = \alpha_s \rho_s T_s \quad (119)$$

The above expressions are derived for sufficiently low particle density ( $g = 1$ ) and can be applied to the limit of dilute flow. The assumption of  $g = 1$  is not valid for high densities. According to Chapman and Cowling [86], the shear viscosity and thermal conductivity of standard Enskog theory (SET) can be defined as

$$\mu_s^{SET} = c_1 \mu_s \left( \frac{1}{\chi b \rho_s} + \frac{4}{5} + \frac{4}{25} \left( 1 + \frac{12}{\pi c_2} \right) \chi b \rho_s \right) b \rho_s, \quad (120)$$

$$\kappa_s^{SET} = c_1 \kappa_s \left( \frac{1}{\chi b \rho_s} + \frac{4}{5} + \frac{4}{25} \left( 1 + \frac{12}{\pi c_2} \right) \chi b \rho_s \right) b \rho_s, \quad (121)$$

with  $c_1 = c_2 = 1.016$ , the relations (120) and (121) can be simplified to,

$$\mu_s^{SET} = \mu_s \left( \frac{1}{\chi b \rho_s} + \frac{4}{5} + 0.7614 \chi b \rho_s \right) b \rho_s, \quad (122)$$

$$\kappa_s^{SET} = \kappa_s \left( \frac{1}{\chi b \rho_s} + \frac{4}{5} + 0.7614 \chi b \rho_s \right) b \rho_s. \quad (123)$$

In most expressions in literature including [124],  $c_1 = c_2 = 1.016$  which gives the slightly different coefficient 0.771, compared to 0.7614.

Moreover, the pressure of a dense system is given by [152]

$$p_s^{SET} = p_s (1 + y^{SET}). \quad (124)$$

where  $y^{SET}$  is the excess compressibility of the elastic hard-sphere system given by

$$y^{SET} = \chi b \rho_s = 4 \chi \alpha_s. \quad (125)$$

The generic form of  $y^{SET}$  can be written as a function of  $\alpha_s$

$$y^{SET}(\alpha_s) = \frac{\sum_{n=0} c_n (4\alpha_s)^{n+1}}{\left(1 - (\alpha_s / \alpha_{cp})^a\right)^b}. \quad (126)$$

The comparison of the parameters in the above equation provided in [153-155] with MD simulations of [156, 157] is provided in reference [138] and is illustrated in Fig. 9 for completeness. It can be seen that the expressions of [154, 155] provide a better agreement with MD data compared to that of the [153].

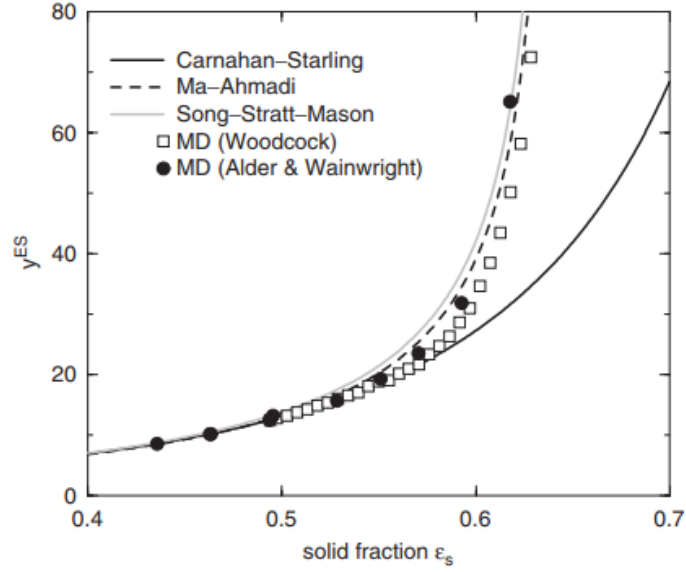


*Fig. 9 Comparison of the expressions from equation (126) with data from MD simulations. Adapted from [138] with permission.*

An analogous and synchronous numerical scheme will be used to solve the mathematical model equations for both phases, which will be introduced in next chapter.

## 4.5 Dimensionless form of the governing equations

The following dimensionless variables and parameters are used to derive the non-dimensional governing system of equations. Here the dimensionless parameters are superscripted by \*, and the subscript *ref* denotes the reference values,

$$\begin{aligned}
 \mathbf{x}^* &= \frac{\mathbf{x}}{L}, & t^* &= \frac{t}{t_{ref}}, & \mathbf{u}^* &= \frac{\mathbf{u}}{u_{ref}}, & T^* &= \frac{T}{T_{ref}}, & \rho^* &= \frac{\rho}{\rho_{ref}}, & p^* &= \frac{p}{P_{ref}}, \\
 E^* &= \frac{E}{E_{ref}}, & Q^* &= \frac{Q}{Q_{ref}}, & \mu^* &= \frac{\mu}{\mu_{ref}}, & \kappa^* &= \frac{\kappa}{\kappa_{ref}}, \\
 c_p^* &= \frac{c_p}{c_{p_{ref}}}, & c_v^* &= \frac{c_v}{c_{v_{ref}}}.
 \end{aligned} \tag{127}$$

In the above relations,  $\mathbf{x}$  and  $c_p$  are the spatial coordinates and the specific heat capacity at constant pressure, respectively. We then define the references and non-dimensional parameters as follows:

$$\begin{aligned}
t_{ref} &= \frac{L}{u_{ref}}, \quad \tau_s = \frac{\rho_s d_s^2}{18\mu_{ref}} \quad E_{ref} = u_{ref}^2, \quad Q_{ref} = \frac{\kappa_{ref} \Delta T_{ref}}{L}, \\
M &= \frac{u_{ref}}{a_{ref}}, \quad Re = \frac{\rho_{ref} u_{ref} L}{\mu_{ref}}, \quad Pr = \frac{\mu_{ref} C_{p_{ref}}}{\kappa_{ref}}, \quad Pe = Re Pr, \\
\gamma &= \frac{C_{p_{ref}}}{C_{v_{ref}}}, \quad \frac{1}{N_\delta Re} = \frac{p_{ref}}{\rho_{ref} u_{ref}^2}, \\
N_\delta &= \frac{\mu_{ref} u_{ref}}{p_{ref} L}, \quad \frac{1}{Re Pr Ec} = \frac{1}{Pe} \frac{C_{p_{ref}} T_{ref}}{u_{ref}^2}, \\
St &= \frac{\rho_{ref} u_{ref}}{D_{g,s} L}, \quad Nu = \frac{Q_s L^2}{k_{ref}}, \quad Ec = \frac{u_{ref}^2}{C_{p_{ref}} T_{ref}}.
\end{aligned} \tag{128}$$

After applying these to equations (90) and (93), the following non-dimensional system of equations can be derived:

$$\begin{aligned}
\partial_t \mathbf{U}_g + \nabla \cdot \mathbf{F}_g &= \mathbf{S}, \\
\mathbf{U}_g &= \begin{bmatrix} \alpha_g \rho_g \\ \alpha_g \rho_g \mathbf{u}_g \\ \alpha_g \rho_g E_g \end{bmatrix}, \\
\mathbf{F}_g &= \begin{bmatrix} \alpha_g \rho_g \mathbf{u}_g \\ \alpha_g \rho_g \mathbf{u}_g \mathbf{u}_g + \frac{1}{N_\delta Re} p \mathbf{I} + \frac{1}{Re} \mathbf{\Pi}_g \\ (\alpha_g \rho_g E_g + \frac{1}{N_\delta Re} p) \mathbf{u}_g + \frac{1}{Re} \mathbf{\Pi}_g \cdot \mathbf{u}_g + \frac{1}{Ec Pr Re} \mathbf{Q}_g \end{bmatrix}, \\
\mathbf{S} &= \begin{bmatrix} 0 \\ \frac{1}{St} (\mathbf{u}_s - \mathbf{u}_g) \\ \frac{1}{St} (\mathbf{u}_s - \mathbf{u}_g) \cdot \mathbf{u}_s + \frac{Nu}{Ec Pe} (T_s - T_g) \end{bmatrix}. \\
\partial_t \mathbf{U}_s + \nabla \cdot \mathbf{F}_s &= -\mathbf{S}, \\
\mathbf{U}_s &= \begin{bmatrix} \alpha_s \rho_s \\ \alpha_s \rho_s \mathbf{u}_s \\ \alpha_s \rho_s E_s \end{bmatrix}, \quad \mathbf{F}_s = \begin{bmatrix} \alpha_s \rho_s \mathbf{u}_s \\ \alpha_s \rho_s \mathbf{u}_s \mathbf{u}_s \\ (\alpha_s \rho_s E_s) \mathbf{u}_s \end{bmatrix}.
\end{aligned} \tag{129}$$

Here the superscript \* has been omitted for the sake of simplicity. The reference values for the length, pressure, temperature, and velocity are defined for each test case depending upon the problem of under investigation.

#### **4.5.1 The physical interpretation of non-dimensional parameters**

The non-dimensional parameters defined above will become handy in the identification of the physical regimes and recognition of physical features which are essential in each investigated problem. These parameters are tabulated in Table 10.

The Reynolds number represents the ratio of inertial forces to viscous forces. High Reynolds number implies the dominance of inertial forces. Therefore, the viscous effects are negligible, and inviscid Euler equations can adequately model this flow regime. The other extreme, i.e.,  $Re \ll 1$ , includes a class of flow regimes called Stokes or creeping flow that can be modeled by Stokes equation (linearized Navier-Stokes).

The Mach number is the ratio of fluid velocity to the speed of sound in the medium and can be used to characterize the compressibility effects.  $M=0.3$  is the limit of incompressible flow where the variation of density is negligible. For higher Mach numbers density variation should be taken into account.

The Prandtl number is the ratio of momentum dissipation to thermal conduction.  $Pr \gg 1$  implies on the dominance of momentum diffusivity and  $Pr \ll 1$  represents the dominance of thermal diffusivity.

The Eckert number characterizing the heat dissipation in high speed flows for which dominance of viscous effects is considerable, is defined as the ratio of kinetic energy to enthalpy (or heat dissipation to advective transport). When  $Ec \ll 1$ , viscous dissipation, pressure changes and body forces in the energy equation are negligible.

The Peclet number, defined as the ratio of advective transport rate to diffusive transport rate. When  $Pe \rightarrow \infty$ , the heat diffusion can be neglected due to the small time scale of the advection compared to the large time scale of the thermal diffusion.

The Nusselt number represents the ratio of convective to conductive heat transfer.  $Nu \approx 1$  is known as slug flow. When  $Nu$  is large, conductive heat transfer (diffusion) is negligible.

Stokes number can be applied to characterize the response rate of the particles to changes in fluid motion. When  $St \ll 1$ , particles can follow the carrier phase (one-way coupling) and when  $St \gg 1$ , particles are little affected by carrier phase (two-way coupling).

Froude number compares flow inertia to the external field. The external field in the most application is the gravitational forces.  $Fr \rightarrow \infty$  corresponds to a high-velocity flow in which gravitational force cannot affect the fluid motion.

*Table 10 Non-dimensional parameters and their physical interpretation*

Non-dimensional number	Definition	Mathematical equation
Reynolds number	<u>Inertial forces</u> Viscous forces	$Re = \frac{\rho_{ref} u_{ref} L}{\mu_{ref}}$
Mach number	<u>Inertial forces</u> Compressibility forces	$M = \frac{u_{ref}}{a_{ref}}$
Prandtl number	<u>Dissipation</u> Conduction	$Pr = \frac{\mu_{ref} C_{p,ref}}{\kappa_{ref}}$
Eckert number	<u>Kinetic energy</u> Enthalpy	$Ec = \frac{u_{ref}^2}{C_{p,ref} T_{ref}}$
Peclet number	<u>Advection</u> Diffusion	$Pe = \frac{L u_{ref}}{\kappa_{ref}}$
Nusselt number	<u>Convective heat transfer</u> Conductive heat transfer	$Nu = \frac{h_{ref} L}{\kappa_{ref}}$
Stokes number	<u>Particle response time</u> Fluid characteristic time	$St = \frac{\tau_s}{t_{ref}}$
Froude number	<u>Inertial forces</u> Gravitational forces	$Fr = \frac{u_{ref}}{\sqrt{gL}}$

## **4.6 Erosion Modeling**

The last important challenge in the proposed strategy for simulation of multiphase effects in lunar descent is surface erosion and consequent particle influx into the flow field. A practical erosion model must provide information regarding location and time at which erosion starts as well as the rate and direction at which particles are lofted from the surface and in-fluxed into the computational domain. Due to the erosion of surface, craters might be formed and change the initial shape of the surface. This phenomenon might change the final solution. However, the effect is not intense. In this work, it is assumed the effect of surface variation are negligible similar to what has been assumed in [48]. In case such effects are of interest the strategy of the simulation may be modified by applying Eulerian multiphase models in which the interface between solid and gas phases is modeled by solving another equation as in volume of fluid or level set models. The more accurate approach (considering microscopic scales) can be the application of Lagrangian models; however, it should be noted that the computational cost would become much larger compared to the Eulerian counterpart. In this section, first, the erosion mechanisms are put forward. Next, some of the popular erosion models which have been applied in solving the Lunar landing problem are introduced, the limitation of each model is discussed, and the applied model is described.

### **4.6.1 Stationary particle on the sediment bed**

The immobile particle on a sediment bed can experience several forces including shear, pressure, interparticle and body forces. In case the moments produced by aerodynamic forces about point P exceed the momentum imposed by gravitational and interparticle forces, the particle may be mobilized. A schematic of the forces acting on an immobile particle are provided in Fig. 10.

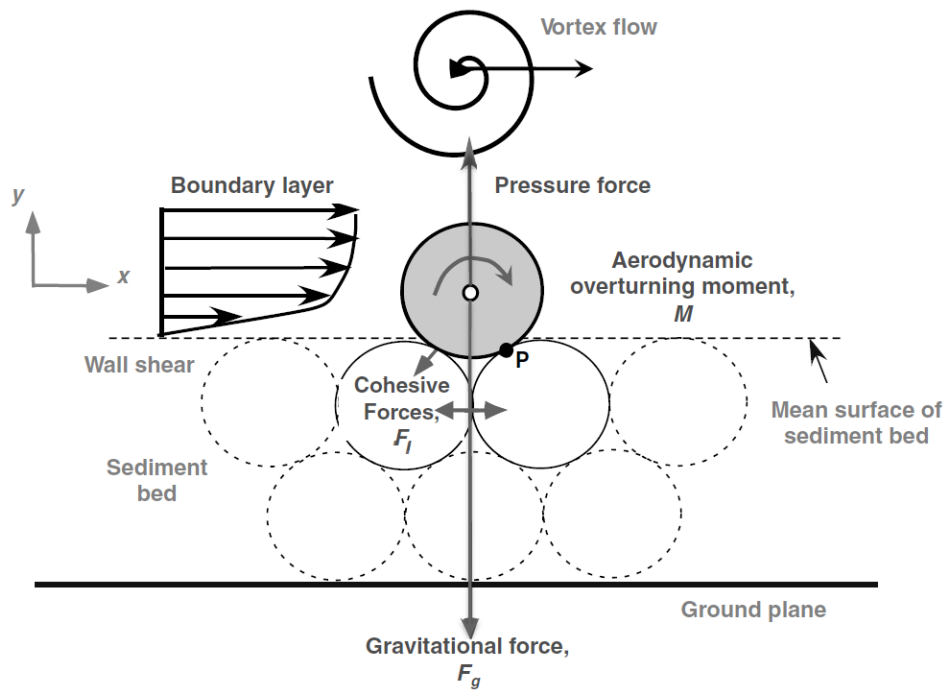


**Fig. 10** The various forces acting on particles on a sediment bed under the action of an external flow. Reprinted from [158] with permission.

#### 4.6.2 Forces on an entrained particle

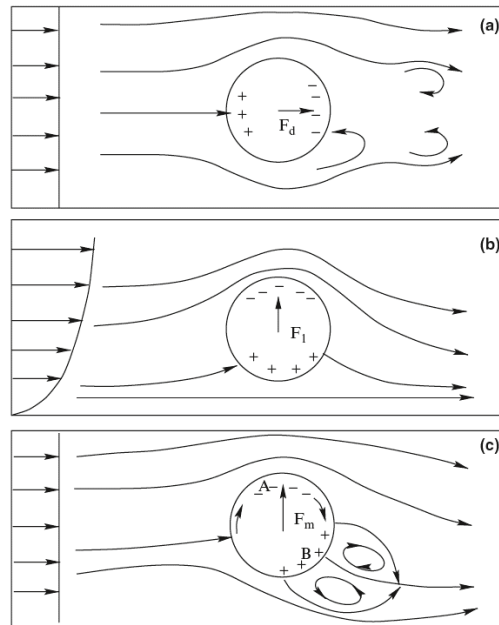
The motion of a lofted particle can be affected by various forces including the aerodynamic drag  $\mathbf{F}_d$ , aerodynamic lift  $\mathbf{F}_l$ , the gravity force  $\mathbf{F}_g$ , the Magnus force due to the rotation  $\mathbf{F}_m$ , and the electric force  $\mathbf{F}_E$ . The effect of buoyancy upon the particle is negligible due to large density ratio defined as the ratio of particle density to air density. The gravitational force only acts on the vertical direction and is set equal to  $-mg$ , with  $m$  as particle mass, and  $g$  is the acceleration of gravity.

Fig. 11 depicts the physical mechanism by which aerodynamic drag is generated. Once the particle travels relative to the surrounding fluid, it will experience a force opposed to the relative velocity by the fluid. This force is the well-known drag which is caused by the pressure difference in front of the particle and the wake behind it, as well as the viscous effects in which the momentum is transferred from fluid to the particle via molecular

movements. The integration of total momentum flux (or total stress) over the particle surface is equal to the exerted force.

$$F_{di} = -\int_S p n_i dS + \int_S \sigma_{ij} n_j dS \quad (130)$$

The momentum transfer to the particle by the pressure forces (the first right-hand side term of the equation (130)) is independent of fluid viscosity. However, the second term is associated with fluid viscosity and is known as the frictional drag.



**Fig. 11 The physical mechanism of a) aerodynamic drag force, b) aerodynamic lift force and c) Magnus force on a spinning particle. Reprinted from [159] with permission.**

Due to the difficulty in measuring of  $p$  and  $\sigma_{ij}$  distribution over the particle surface, equation (130) is not appropriate for aerodynamic drag expression. As an alternative, it is shown that the drag force is proportional to particle-to-fluid relative velocity  $\mathbf{u}_r$  ;

$$\mathbf{F}_d = -\frac{1}{2} C_D \rho A \mathbf{u}_r U_r \quad (131)$$

In the above relation, the aerodynamic drag coefficient is indicated by  $C_D$ . The particle cross-section in direction of flow is denoted by  $A$  and for spherical particles, is equal to

$\pi d^2/4$ .  $U_r$  is the magnitude of  $\mathbf{u}_r$ . Moreover,  $u_{pi}$  and  $u_i$  are the  $i$ th particle velocity and fluid velocity components, respectively, and the  $i$ th component of  $\mathbf{u}_r$  is as follows,

$$u_{ri} = u_{pi} - u_i. \quad (132)$$

Thus,  $U_r$  can be defined by

$$U_r = (u_{r1}^2 + u_{r2}^2 + u_{r3}^2)^{1/2}. \quad (133)$$

As the aerodynamic drag coefficient is a function of particle Reynolds number  $Re_p = U_r d / \nu$ , the magnitude of the drag force is dependant upon the flow pattern. This function,  $C_D(Re_p)$ , has been widely investigated by various experimental works for different flow patterns. Fig. 12 illustrates a summary on dependance of drag coefficient on Reynolds number and flow patterns.

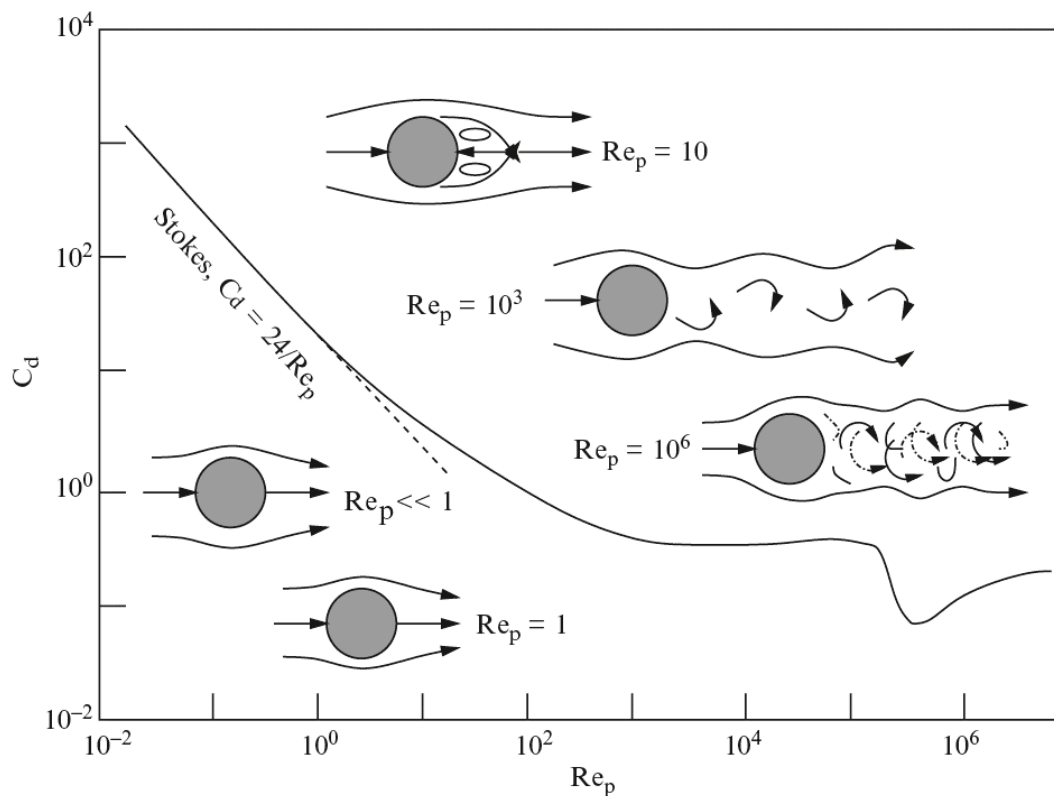


**Fig. 12 Aerodynamic drag coefficient for different flow regime in terms of Reynolds number. Reprinted from [159] with permission.**

The Reynolds regimes shown in Fig. 12 can be characterized as follows:

$Re_p \ll 1$  (known as Stokes region) corresponds to high viscous effects and negligible fluid inertia. The pressure and viscous stresses on the particle surface in this region were first determined analytically to be  $C_D = 24/Re_p$  [160] for Reynolds numbers smaller than 10. When  $10^3 < Re_p < 3 \times 10^5$ , the drag coefficient is close to 0.5 and relatively independent of Reynolds number. Moreover, viscous drag is negligible compared to pressure-induced drag. Finally, for  $Re_p > 3 \times 10^5$ , a significant decrement of drag coefficient from about 0.5 to approximately 0.1 can be seen owing to the variation of pressure distribution over the particle surface, and a transition of the laminar boundary layer to turbulent boundary layer on the particle can be observed. In section 4.4.3, various relations for drag coefficients were provided.

The Bernoulli equation explains the aerodynamic lift mechanism shown in Fig. 11(b). This equation states that the total head produced by velocity head, pressure head and gravity head along the streamline, is constant and can be derived from motion equations for inviscid barotropic flow in a steady-state condition.

$$\frac{1}{2}u^2 + \frac{p}{\rho} + gh = const. \quad (134)$$

$u$  and  $h$  are the velocity of flow along the streamline and the height of streamline corresponding to reference level, respectively. The aerodynamic lift phenomenon is the result of pressure gradient caused by shear in the flow. This pressure gradient is normal to the shear and in the direction of decreasing velocity. In other words, the faster-flow region over the upper surface induces lower pressure compared to the lower surface which is exposed to lower velocity and higher pressure. The aerodynamic lift can be expressed by

$$\mathbf{F}_l = \frac{1}{2}C_l\rho A(\nabla U^2)d. \quad (135)$$

In the above equation,  $C_l$  corresponds to lift coefficient and is correlated to drag coefficient,  $C_l = 0.85C_D$  given by Chepil [161] and the gradient of  $U \equiv |\mathbf{u}|^2$  is denoted as  $\nabla U^2$ . Here, the shape of the particles plays a substantial role in defining  $\mathbf{F}_l$ . For instance, a spherical particle only when is placed in a strong shear flow can experience lift force, whereas in the case of a non-spherical particle, considerable lift force may take place even in the uniform flows due to the velocity gradient that geometry imposes, and hence the distribution of pressure on the surface.

As shown in Fig. 11(c), for a spinning particle a force perpendicular to both direction of motion and rotation is generated which is know as Magnus force. In order to explain Magnus force in terms of the Bernoulli equation, the viscous effects in relation to particle should be taken into account. The flow at the upper surface of the rotating particle (side A) undergoes pressure reduction due to an increase of the velocity which itself is a result of the same direction in rotation of particle and fluid motion (in the presence of viscous forces). It is trivial that the opposite side experiences contrary conditions. The Magnus force is proportional to  $Re_p$ , and the ratio of circumferential speed to the magnitude of relative velocity,  $v_s / U_r$  [162]. In works of [163, 164] regarding the motion of sands grains in the atmosphere, the following relation has been applied,

$$\begin{aligned} \mathbf{F}_m &= \pi \rho \frac{d^3}{8} (\boldsymbol{\Omega}_p \times \mathbf{u}_r), \quad \text{for low } Re \text{ numbers} \\ \mathbf{F}_m &= C_m \pi \rho \frac{d^3}{8} (\boldsymbol{\Omega}_p \times \mathbf{u}_r), \quad \text{for high } Re \text{ numbers} \end{aligned} \tag{136}$$

In the above equations,  $\boldsymbol{\Omega}_p$  stands for angular particle velocity and  $C_m$  is a coefficient that accounts for the Magnus force dependency on  $Re_p$  and  $v_s / U_r$ .

In the case of charged soil particles, the motion of windblown particles generates an Electric field near the surface [165]. These particles may experience an electric force  $\mathbf{F}_e$

with the strength as large as the gravity force. According to Zheng *et al.* [165], only the vertical component can define the electric field, and the horizontal component can be neglected. Accordingly, the electric force for a particle of mass  $m$  and the particle specific charge  $C_e$  (charge per unit mass) can be written as

$$\mathbf{F}_e = mC_e\mathbf{E}. \quad (137)$$

In summary, the equation of particle motion for a particle of mass  $m$  with velocity  $\mathbf{u}_s$  can be expressed by the forces detailed above:

$$m\frac{d\mathbf{u}_s}{dt} = \mathbf{F}_d + \mathbf{F}_l + \mathbf{F}_g + \mathbf{F}_m + \mathbf{F}_e. \quad (138)$$

By using the definition of the forces we have

$$\begin{aligned} m\frac{d\mathbf{u}_s}{dt} = & -\frac{1}{2}C_d\rho A\mathbf{u}_rU_r + \frac{1}{2}C_l\rho A(\nabla U^2)d + mg \\ & + \frac{1}{8}C_m\pi\rho d^3(\boldsymbol{\Omega}_p \times \mathbf{u}_r) + mC_e\mathbf{E}. \end{aligned} \quad (139)$$

In the case of a particle with the spherical shape,  $m = \pi\rho_s d^3 / 6$  and  $A = \pi d^2 / 4$ , the above equation can be written in the following form:

$$\frac{d\mathbf{u}_s}{dt} = -\frac{3}{4}\frac{C_d\rho}{\rho_s d}\mathbf{u}_rU_r + \frac{3}{4}\frac{C_l\rho}{\rho_s}\nabla U^2 + g + \frac{3}{4}\frac{C_m\rho}{\rho_s}(\boldsymbol{\Omega}_p \times \mathbf{u}_r) + C_e\mathbf{E}. \quad (140)$$

### 4.6.3 Modes of particle motion

Various modes of motion may occur during wind erosion for different particle sizes, some of which may also be applicable in the Lunar landing problem. Bagnold [166] classified the particle motion based on experimental observations into three categories: Suspension, saltation, and creep which are schematically demonstrated in Fig. 13.

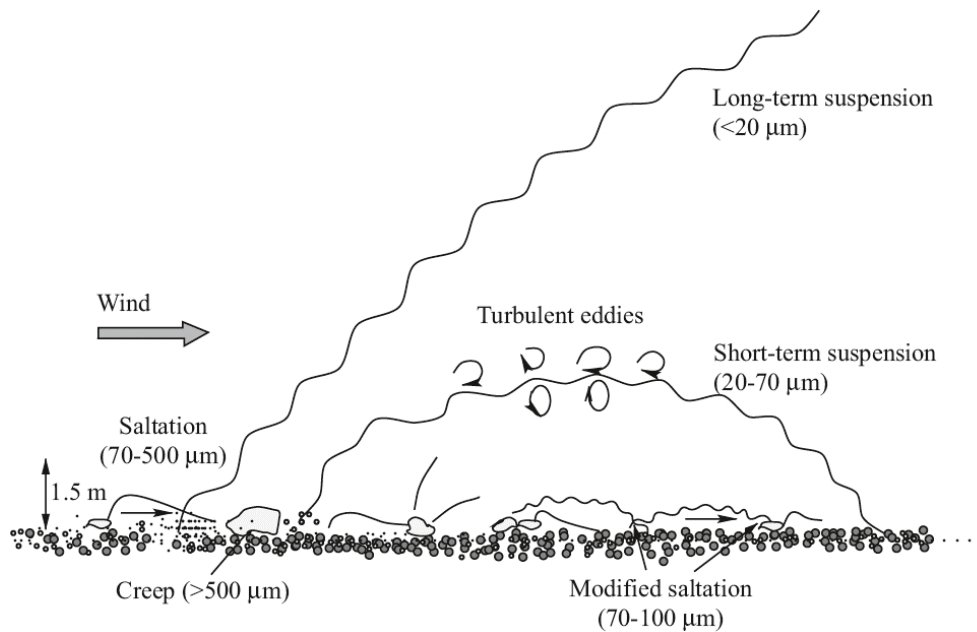


**Fig. 13** Suspension, saltation, and creep of grains during wind erosion. Reprinted from [159] with permission.

### Suspension

The dust particles are suspended in air due to small terminal velocity which by definition is the relative velocity of the particle to fluid at which the particle acceleration is negligible. The turbulence in the atmospheric boundary layer disperses the dust particles away from the surface, and the airborne grains can travel up to thousands of kilometers by means of the atmospheric circulation. Since the residence time of dust particle is proportional to terminal velocity, the suspension can be divided into long-term and short-term suspension. For the very fine particle (less than  $20\mu m$ ) they can be suspended for several days which refers to a long-term suspension. The short-term suspension is covered by the particles with a diameter between  $20$  and  $70\mu m$  that remain suspended for typically several hours. The particles in the Lunar atmosphere would mostly experience long-terms suspensions due to lower gravitational forces (compared to the earth) and less resistance from the semi-vacuum condition of the Moon.

### *Saltation*

The bouncing off action of the particles across the surface during erosion phenomena is called saltation. The particles are initially lofted off from the surface with the steep vertical ascent then traveled horizontally and eventually struck to the surface with the small impact angle. It is observed that the ascent angles are about  $55^\circ$  and the striking angles are around  $10^\circ$ .

### *Creep*

Particles with a diameter larger than  $1000\mu m$  are heavy to be entrained into flowfield under normal atmospheric condition. However, they can roll on the surface by wind or the impact of the saltation particles. This phenomenon is known as creep.

## **4.6.4 Phenomenology of soil erosion on the Lunar surface**

The soil erosion is a complex phenomenon which has been studied via various theoretical, computational and experimental investigations from different viewpoints. The unique properties of lunar environment and regolith make the issue even more complicated. Replicating the lunar environment for conducting experiments is almost impossible. Therefore experimental investigations are not sufficiently reliable. Theoretical and numerical studies are still in the development stage, and even with the significant effort which has been put in previous research studies [41, 42, 45, 46, 53, 60, 167, 168], a comprehensive model which can explain physics of the erosion even terrestrially is not available to date. These observations make one of the most critical shortcomings of solving the problem of Lunar landing from a theoretical point of view. Before selecting erosion model, it is beneficial to know about the erosion mechanisms.

Four possible erosion mechanism to form craters have been identified by Metzger *et al.* [60] which are summarized as follows:

#### **4.6.4.1 Viscous erosion (VE)**

Viscous erosion takes place when the shear stress on the surface overcomes the critical cohesive strength of the soil and causes the solid particles to creep along the surface. The rolled particles elevate the possibility of particle-particle collision; accordingly, these collisions can lead to scattering of the particles into the flow field.

#### **4.6.4.2 Diffused gas eruption (DGE)**

The diffused gas eruption occurs when the gas penetrates into a porous media and loosens the porous soil such that the soil layer could be fluidized. Therefore, it can be erupted at any location and cause the solid particles to be suspended along with it.

#### **4.6.4.3 Bearing capacity failure (BCF)**

When the pressure becomes higher than bearing capacity of the soil, a narrow cup shape is created which has unstable circumstances and can easily collapse under the gravity force. Consequently, many solid particles would entrain to flow field.

#### **4.6.4.4 Diffusion-driven flow (DDF)**

The drag force of fluid jet through the pore spaces of the soil reacts against the grains posing a distributed body force in the bulk of the soil which can shear the material.

The dominant erosion mechanism on the lunar surface is viscous erosion. Due to the existence of a semi-vacuum, the soil layers are tightly packed therefore DGE, and DDF mechanisms are not in effect during the Lunar surface erosion. Besides, bearing capacity failure mechanism is negligible because of high packing density and bearing capacity of the Lunar regolith. However, some simulations results [36], which may represent the existence of this mechanism make this assumption subject to further investigations.

Viscous erosion is associated with:

- aerodynamic entrainment in which aerodynamic forces are dominant compared to gravitational forces;
- saltation bombardment in which high-energy particles dislodge other particles by colliding;

- aggregate disintegration in which particles get together due to thermal cycling and cohesion, then break apart when a significant force is exerted [159]. The contents above are summarized in Fig. 14.

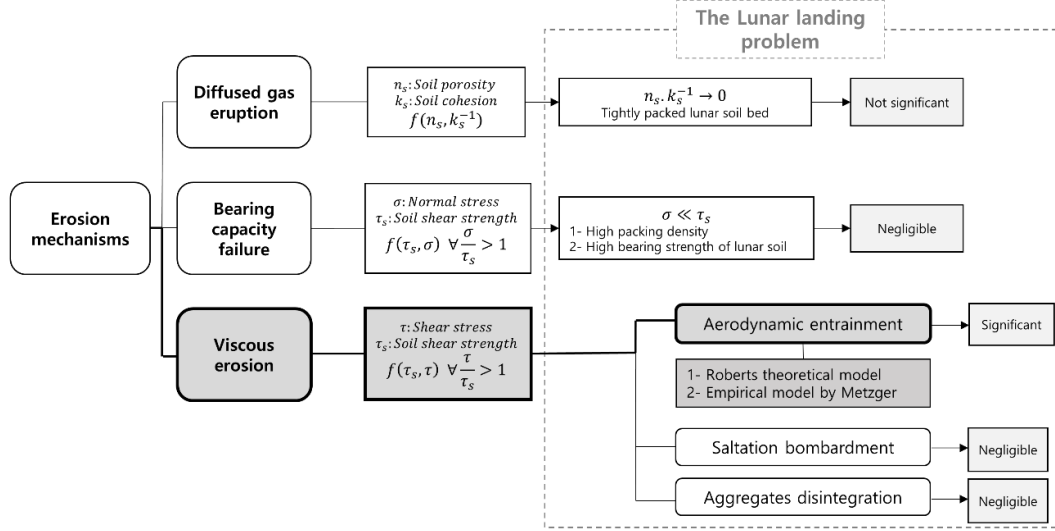


**Fig. 14. Erosion mechanisms and their importance in lunar landing problem**

A simplified yet potent model to simulate erosion on the surface is the Roberts' erosion model. According to Roberts [42], when the induced shear stress on the ground exceeds the threshold stress, erosion with a mass flux proportional to the excess shear will occur:

$$\frac{1}{2} au \phi = \tau - \tau_c \quad (141)$$

In the above equations,  $\phi$  is erosion rate (mass flux),  $au$  is the fraction of gas velocity that the particles can obtain,  $\tau$  is shear stress on the surface, and  $\tau_c$  indicates the threshold stress below which erosion does not occur defined as

$$\tau_c = C + P \tan \varphi. \quad (142)$$

Here,  $C, P$  and  $\varphi$  are cohesive stress, gas static pressure on surface and friction angle, respectively. The coefficient  $a$  is

$$a = \left[ \frac{1}{2} + \sqrt{\frac{1}{4} + \frac{1}{\zeta}} \right]^{-1}, \quad (143)$$

where,

$$\zeta = \frac{18\mu_c h}{\rho_s \sqrt{RT_c (4+k_h)}} \left[ \frac{1}{d^2} + \frac{1}{d} \frac{(4+k_h) C_D F}{72e \sqrt{2RT_c \mu_c}} \right]. \quad (144)$$

From the above relations, it is clear that the coefficient  $a$  is dependent on various parameters. In the equation (144),  $\mu_c$  and  $T_c$  are the engine chamber viscosity and temperature,  $h$  is the hover altitude,  $\rho_s$  and  $D$  are particle density and the particle diameter of regolith,  $k_h$  is the hypersonic factor which is defined by  $\gamma(\gamma-1)M_n^2$ , where  $\gamma$  is the ratio of specific heats and the Mach number at nozzle exit plane is specified by  $M_n$ . Further,  $\zeta$  in the above equation is related to  $R$  gas constant as well as drag coefficient,  $C_D$  (set equal to the constant value of 0.2 by Roberts) and engine thrust,  $F$ .

Less sophisticated models can be derived by an analogy from sediment beds research area. More sophisticated models based on wind erosion are also available; However, the dependency of these models on regolith properties which are mostly unknown (or at best, limited) makes the use of these models impractical. Moreover, empirical relationships to take into account the particle density, diameter and gas density and velocity, and gravity are provided by [46, 167, 168].

# Chapter 5. Numerical approach

## 5.1 Fundamentals of numerical simulation

When an initial mathematical model with a proper level of approximation for the physical problem to be solved is selected, the next step is the choice of discretization method. It is essential to select the efficient method among the various available numerical methods for the solution of the specific system of equations. Important factors which affect this selection are the accuracy of the solution and computational expense (or power), and a compromise between these two should be taken into account. The discretization method involves two steps: space discretization and equation discretization. Space discretization is the introduction of a mesh to approximate the continuum space into a finite number of grids or points in which the solution values has to be determined. Equation discretization, on the other hand, implies the transformation of differential or integral equations to discrete algebraic relations to yield the unknown values.

### 5.1.1 Discretization methods

The most favorite discretization techniques in computational fluid dynamics (CFD) are finite difference method (FDM), finite element method (FEM) and finite volume method (FVM). The structure of a numerical method is depicted in Fig. 15.

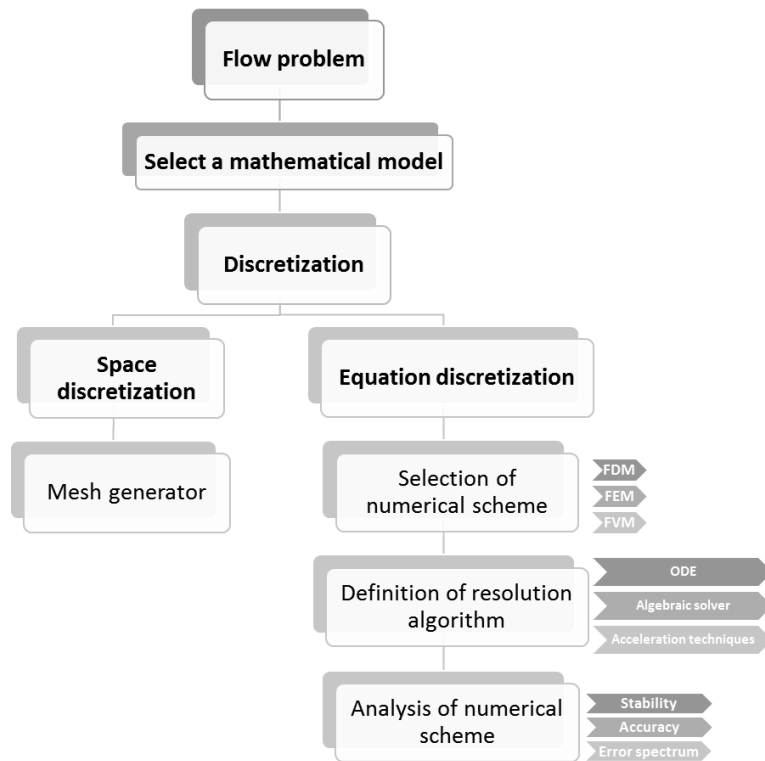


**Fig. 15 Structure of a numerical simulation. Reproduced based on [169].**

The finite difference method is the simplest discretization method which is based on the properties of Taylor expansions. The FDM formulas can be defined in a general manner for first and higher order derivatives. While FDM is easy to code, capable of providing high-order accurate solutions and can be benefitted from *hp*-additivity, it cannot be used in complex geometries and unstructured grids. Another widely used discretization method is the finite element method, which was originated from the field of structural analysis. The method was first applied in fluid dynamics problem in the late 70's and continued its development till date. It is based on variational methods, can reach any order of accuracy and is applicable on an unstructured grid. In FEM the reconstruction data are employed from within the element. One of the main drawbacks of the FEM method is the inability of providing explicit semi-discrete form. In other words, the method is inherently implicit; However, it can be explicit with major modifications. The final category is the finite volume method which solves the integral formulation of the conservation laws directly in the physical space. Besides the arbitrary mesh handling capability, the methods of

evaluation of the fluxes on the surfaces of the control volumes make the FVM a very flexible tool. The main weakness of the FVM is the difficulty associated with computation of high order solutions especially on unstructured grids which makes finite volume method limited to second-order accuracy in most applications.

### **5.1.2 High order methods**

Another class of discretization methods which are gaining popularity in fluid dynamics field from fundamental fluid mechanics problems to more sophisticated wave-based problems of computational electromagnetics are the so-called high order —higher than second-order—spectral methods. The primary goal here is to provide a high-order conservative scheme that has a compact formulation and can handle complex geometries in a computationally efficient manner. In these methods, high order solution is achieved by increasing the polynomial order, and some of the popular subcategories include spectral difference (SD), spectral volume (SV), and flux reconstruction/correction procedure via reconstruction (FR/CPR) and discontinuous Galerkin (DG) method. In spectral (finite) volume method each spectral volume is further subdivided into control volumes depending on the desired order of accuracy, and the high-order reconstruction is based on cell-averaged state variables from these control volumes [170]. In spectral difference method, the concept of discontinuous and high-order local representations is used to achieve conservation and high accuracy in a manner similar to the DG and SV methods. The difference is the application of the simpler finite-difference formulation to increase efficiency [171]. Flux reconstruction approach applies the differential form of the equation same as what is done in SD. However, in FR method the reconstruction of flux polynomial is achieved via a more general scheme compared to the interpolation procedure used by SD. By such general reconstruction, other schemes (DG, SD, and SV) can be recovered. The extension of FR approach [172] to simplex elements provided lifting collocation

penalty (LCP) framework [173]. The FR and LCP schemes are later renamed to CPR by their creators as both the methods provide a same final formulation. Interested readers are referred to the review papers of Ekaterinaris [174] and Wang [175] for more details regarding the comparison of high-order spectral methods.

In discontinuous Galerkin formulation in comparison with continuous counterpart, discontinuous basis functions are applied (local elemental mass matrix of the finite element formulation versus globally coupled mass matrix of continuous finite element method). The discontinuous feature of the basis functions makes DG method more flexible. For example, arbitrary triangulation with hanging nodes can be allowed.  $P$  adaptivity can be achieved as the polynomial degree, or even the basis functions can be defined for individual elements independent from neighbor elements. Embarrassingly high parallel efficiency is also achievable due to extremely local data structure [176].

These type of methods are known to benefit from the advantages of FVM and FDM at the same time. In the current thesis, a DG discretization is applied due to high order capability of the method which is desirable in most of the investigated problems, as well as the consistency of the selected mathematical model with some inherent features of the scheme which will be discussed in the following sections.

## **5.2 A numerical framework based on a modal unstructured discontinuous Galerkin method**

### **5.2.1 Review of literature**

First introduced by Reed and Hill [177] and further developed by [178-180], the DG method has become a prominent tool for solving the fluid dynamics governing equations. While the DG method has been successfully applied to various classes of problems such as compressible and incompressible flows, aeroacoustics, magneto-hydrodynamics, and

many more [181], it has recently also found its way into the multiphase problem. This application is driven by the improvement of the method, as well as recent advances in computer resources, which make the DG method a feasible tool for a more substantial number of industrial applications.

Sun and Wheeler [182] used primal DG with an interior penalty to solve the coupled system of flow and reactive transport in porous media. Klieber and Rivière [183] presented adaptive techniques in space and time and showed that the proposed DG schemes on heterogeneous media are robust. Franquet and Perrier [184] developed a robust high order DG method for compressible multiphase flows based on the Baer and Nunziato type systems and reported good agreement with experimental results. They also extended the method to reactive multiphase flows [185]. Owkes and Desjardins [186] applied the DG method to conservative level set equations for interphase capturing in multiphase flows. Lu *et al.* [187] presented a Runge-Kutta DG method together with the front tracking method for solving two-medium gas-gas and gas-liquid flows. They proved that the method has the capability of enhancing the resolution near discontinuities in the single medium and material interfacial vicinities. de Frahan *et al.* [188] obtained the DG solution for multiphase flows using the Mie-Grüneisen family of equations of state. They also show analytically that solving the non-conservative weak form of the equations and limiting of a suitable variable can prevent spurious oscillations. Recently, Dumbser and Loubère [189] proposed an accurate nonlinear a posteriori stabilization of the DG method and applied the method to the Baer-Nunziato model in two-dimensional space. Moortgat and Firoozabadi [190] developed a vertex-based DG method of multiphase compositional flow on 3D unstructured grids. Diehl *et al.* [191] obtained the solutions of the Navier-Stokes-Korteweg equations for compressible liquid-vapor multiphase flow with phase transition using the

local discontinuous Galerkin (LDG) method. It was shown that the approach is reliable and efficient in two and three space dimension.

Although these recent studies demonstrated the capability of the DG method for very diverse problems, few mathematical models pertaining to multiphase flow categories or regimes have been investigated using the DG method. *To the best knowledge of the author, there is no previous work on applications of a high order DG method to solve a two-fluid model of dusty gas flows.* Further, in flow problems with strong discontinuities and the presence of stiff source terms due to the coupling effects in the two-fluid model, the mere application of high-order methods without proper treatment of numerical artifacts or without proper handling of the non-homogeneous part of the partial differential equation will generally lead to divergence, an oscillatory solution or in the best scenario a huge computational penalty, caused by small time steps.

The equations of the dusty gas flows described in the previous section are discretized using a modal discontinuous Galerkin (DG) method. The essential parts of the modal unstructured DG method developed in the present work—in particular, high order accuracy and positivity/monotonicity preserving property—are summarized in this section. For a more detailed discussion on general DG methods, readers are referred to [178-181], for DG implementations, and [192-195] for limiter-related issues.

### **5.2.2 A modal DG formulation for inviscid (convection dominated) flows**

The mathematical model of interest in the present work can be written in a compact form;

$$\partial_t \mathbf{U} + \nabla \cdot \mathbf{F}_{\text{inv}}(\mathbf{U}) = \mathbf{S}(\mathbf{U}) \quad \text{in } \left[ (t, \Omega) \mid t \in (0, \infty), \Omega \subset \mathbb{R} \right], \quad (145)$$

where  $\Omega$  denotes a bounded domain, and  $\mathbf{U}$ ,  $\mathbf{F}_{\text{inv}}$ ,  $\mathbf{S}$  are conservative variables vector, inviscid flux vector, and source terms vector, respectively. The solution domain can be decomposed by a group of non-overlapping elements,  $\Omega = \Omega_1 \cup \Omega_2 \cup \dots \cup \Omega_{ne}$ , in which  $ne$  is the number of elements. The partial differential equation of (145) cannot allow for solutions with discontinuities. By multiplying a weighting function  $\phi_i$  into the conservative laws (145) and integrating over the control volume for each element, the following formulation can be derived:

$$\int_{\Omega_k} [\partial_t \mathbf{U} \phi(\mathbf{x}) + \nabla \cdot \mathbf{F}_{\text{inv}}(\mathbf{U}) \phi(\mathbf{x}) - \mathbf{S}(\mathbf{U}) \phi(\mathbf{x})] d\Omega = 0. \quad (146)$$

In order to construct a discretized system of the conservation laws, the global spatial domain  $\Omega$  can be approximated by  $\Omega_h$  where  $\Omega_h \rightarrow \Omega$  as  $h \rightarrow 0$ . The approximated domain, which is a tessellation of the space by bounded elementary control volumes,  $\mathcal{T}_h = \{\Omega_k\}$ , is filled with  $ne$  number of the non-overlapping elements  $\Omega_k \in \mathcal{T}_h$ . The exact solution of the governing equations can be approximated by the numerical solution in every local element as

$$\mathbf{U}(\mathbf{x}, t) \approx \mathbf{U}_h = \sum_{e=1}^{ne} \mathbf{U}_h^e(\mathbf{x}, t) \equiv \mathbf{U}_h^1 + \dots + \mathbf{U}_h^n. \quad (147)$$

By splitting the integral over  $\Omega_h$  into series of the integrals over the sub-elements and applying the integration by part as well as divergence theorem to the equation (146)(146), the elemental formulation reads as

$$\begin{aligned} & \int_{\Omega_k} \partial_t \mathbf{U}_h \phi_i(\mathbf{x}) d\Omega_k + \oint_{\partial\Omega_k} \phi_i(\mathbf{x}) \mathbf{F}_{\text{inv}}(\mathbf{U}_h) \cdot \hat{n} d\sigma - \int_{\Omega_k} \nabla \phi_i(\mathbf{x}) \cdot \mathbf{F}_{\text{inv}}(\mathbf{U}_h) d\Omega_k \\ & = \int_{\Omega_k} \phi_i(\mathbf{x}) \mathbf{S}(\mathbf{U}_h) d\Omega_k, \end{aligned} \quad (148)$$

where  $\hat{n}$  is the outward normal vector of the element interface and  $\mathbf{U}_h$  is the  $p$ -exact polynomial approximated solutions of the  $\mathbf{U}$  on the discretized domain of  $\Omega_h$ .  $\mathbf{U}_h$  can be

expressed as the polynomial field that sums the multiplication of local degree of freedom with the corresponding smooth polynomials of degree  $P$  in the standard element:

$$\mathbf{U}_h = \sum_i^P U_i(t) \phi_i(\mathbf{x}). \quad (149)$$

Here  $U_i(t)$  and  $\phi(\mathbf{x})$  denote the local degree of freedom and the basis function, which can be chosen to be any continuous polynomial function, respectively.

In the one-dimensional case, the orthogonal scaled Legendre functions were selected as basis functions, while a linear mapping function was used for mapping from the physical space to the standard element. In the two-dimensional case, the PDK polynomials [196] were selected as basis functions, while a collapsed coordinate transformation was used to transfer the triangles in the physical domain to the standard square elements,  $\Omega_e$ , in which the coordinates  $(a, b)$  are bound by constant limits

$$\mathcal{R} = \{(a, b) \mid -1 \leq a, b \leq 1\}. \quad (150)$$

Another transformation was introduced to transfer the triangle in the physical space into the computational space where the new local coordinates have independent bounds, as depicted in Fig. 16. A suitable coordinate system, which describes the triangular region between constant independent limits, can be defined by the following inverse transformation:

$$r = \frac{(1+a)(1-b)}{2} - 1, \quad w = b. \quad (151)$$

New local coordinates  $(r, w)$  can then define the standard triangular region as follows:

$$\mathcal{T} = \{(r, w) \mid -1 \leq r, w; r + w \leq 0\}. \quad (152)$$

For more details on the various transformations used in the DG method, readers are referred to subsections 5.3-5.10 and the text book [197].

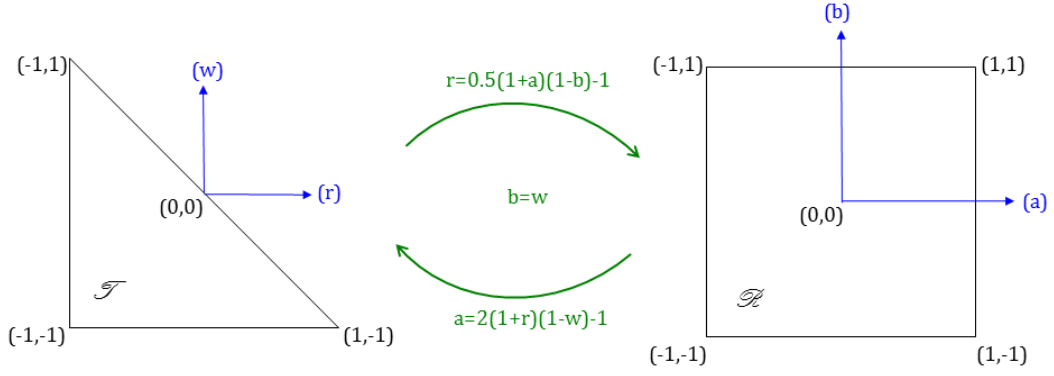


**Fig. 16 Coordinate transformation**

The simple and efficient local Lax-Friedrichs (LLF) flux function, commonly used in the DG method, is applied to all the multiphase test cases in the present study. Despite the dissipative nature of the numerical flux, it improves the linear stability of the DG numerical approximation. The dimensionless form of the LLF flux is defined as

$$\mathbf{F}_{\text{inv}}(\mathbf{U}_h) \approx \hat{\mathbf{f}}_{i,\text{inv}}(\mathbf{U}_h^-, \mathbf{U}_h^+) = \frac{1}{2} \left[ \mathbf{F}_{i,\text{inv}}(\mathbf{U}_h^-) + \mathbf{F}_{i,\text{inv}}(\mathbf{U}_h^+) - C(\mathbf{U}_h^+ - \mathbf{U}_h^-) \right], \quad (153)$$

where  $C$  is the maximum modulus of the eigenvalues of the Jacobian matrix,

$$\max_{\min(U^-, U^+) \leq U \leq \max(U^-, U^+)} |F'_{i,\text{inv}}(U)|, \quad \text{and for convex fluxes, it reads as}$$

$C = \max(|v^-| + a_s^-, |v^+| + a_s^+)$ . Here  $a_s = \sqrt{T}/M$  is the speed of sound at an elemental interface, and the superscripts (+) and (-) denote the inside and outside of an elemental interface, respectively.

Moreover, a third-order accurate, three-stage total-variation-diminishing Runge-Kutta method was employed for time integration, owing to its simplicity, efficiency, and robustness. In order to minimize the temporal discretization error, the time step was set in such a way that the Courant-Friedrich-Levy (CFL) criterion is always satisfied. The Gauss-Legendre quadrature rule was used to calculate the volume and surface integrals in (148), which are proved to be  $2P$  and  $2P+1$  order accurate, respectively.

### 5.2.3 A modal DG formulation for viscous (convection-diffusion problems) flows

The mathematical model of interest in the present work can be written in a compact form;

$$\partial_t \mathbf{U} + \nabla \cdot \mathbf{F}_{\text{inv}}(\mathbf{U}) + \nabla \cdot \mathbf{F}_{\text{vis}}(\mathbf{U}, \nabla \mathbf{U}) = \mathbf{S}(\mathbf{U}) \quad \text{in } \left[ (t, \Omega) \mid t \in (0, \infty), \Omega \subset \mathbb{R} \right], \quad (154)$$

As can be seen in (154), when the solution of viscous flows is of interest, an approach for estimation of the derivatives of the conserved variable which appear in the viscous flux terms should be applied. In this regard. These first-order derivatives will change into second-order derivatives when the viscous fluxes are evaluated. These terms cannot be accommodated directly in a weak variational formulation using a discontinuous space function. One possible approach is the addition of a set of separate equations to regard the gradient of the conservative variables as an auxiliary set of unknowns, as proposed by Bassi and Rebay [198]. In this work  $\mathbf{A}$  is chosen to be the derivatives of the conserved variables  $\mathbf{U}$ , i.e.,  $\mathbf{A} = \nabla \mathbf{U}$ . This approach is known as mixed DG formulation and will result in a coupled system

$$\begin{aligned} \mathbf{A} - \nabla \mathbf{U} &= 0, \\ \partial_t \mathbf{U} + \nabla \cdot \mathbf{F}_{\text{inv}}(\mathbf{U}) + \nabla \cdot \mathbf{F}_{\text{vis}}(\mathbf{U}, \nabla \mathbf{U}) &= \mathbf{S}(\mathbf{U}). \end{aligned} \quad (155)$$

In a similar way to (149) we can write,

$$\mathbf{U}_h = \sum_i^P U_i(t) \varphi_i(\mathbf{x}) \quad \text{and} \quad \mathbf{A}_h = \sum_i^P A_i(t) \varphi_i(\mathbf{x}). \quad (156)$$

where  $A_i(t)$  denotes the local degree of freedom for the auxiliary variable. By following the similar procedure outlined in section 5.2.2 for an inviscid system of equations,

$$\int_{\Omega_k} [\mathbf{A} \varphi(\mathbf{x}) - \nabla \mathbf{U} \varphi(\mathbf{x})] d\Omega = 0 \quad (157)$$

$$\int_{\Omega_k} [\partial_t \mathbf{U} \varphi(\mathbf{x}) + \nabla \cdot \mathbf{F}_{\text{inv}}(\mathbf{U}) \varphi(\mathbf{x}) + \nabla \cdot \mathbf{F}_{\text{vis}}(\mathbf{U}) \varphi(\mathbf{x}) - \mathbf{S}(\mathbf{U}) \varphi(\mathbf{x})] d\Omega = 0 \quad (158)$$

$$\int_{\Omega_k} \varphi_i(\mathbf{x}) A_h d\Omega_k - \oint_{\partial\Omega_k} \varphi_i(\mathbf{x}) \mathbf{U}_h \cdot \hat{\mathbf{n}} d\sigma + \int_{\Omega_k} \nabla \varphi_i(\mathbf{x}) \cdot \mathbf{U}_h d\Omega_k = 0, \quad (159)$$

$$\begin{aligned} & \int_{\Omega_k} \partial_t \mathbf{U}_h \varphi_i(\mathbf{x}) d\Omega_k + \oint_{\partial\Omega_k} \varphi_i(\mathbf{x}) \mathbf{F}_{\text{inv}}(\mathbf{U}_h) \cdot \hat{\mathbf{n}} d\sigma - \int_{\Omega_k} \nabla \varphi_i(\mathbf{x}) \cdot \mathbf{F}_{\text{inv}}(\mathbf{U}_h) d\Omega_k \\ & + \oint_{\partial\Omega_k} \varphi_i(\mathbf{x}) \mathbf{F}_{\text{vis}}(\mathbf{U}_h) \cdot \hat{\mathbf{n}} d\sigma - \int_{\Omega_k} \nabla \varphi_i(\mathbf{x}) \cdot \mathbf{F}_{\text{vis}}(\mathbf{U}_h) d\Omega_k = \int_{\Omega_k} \varphi_i(\mathbf{x}) \mathbf{S}(\mathbf{U}_h) d\Omega_k, \end{aligned} \quad (160)$$

The process of estimation of surface and volume integrals are analogous to the inviscid system procedure. However, for the auxiliary terms, a central flux splitting scheme is applied.

$$\begin{aligned} \mathbf{F}_{\text{vis}}(\mathbf{U}_h) & \approx \hat{\mathbf{f}}_{i,\text{vis}}(\mathbf{U}_h^-, \mathbf{A}_h^-, \mathbf{U}_h^+, \mathbf{A}_h^+) = \frac{1}{2} \left[ \mathbf{F}_{i,\text{vis}}(\mathbf{U}_h^-, \mathbf{A}_h^-) + \mathbf{F}_{i,\text{vis}}(\mathbf{U}_h^+, \mathbf{A}_h^+) \right] \\ \mathbf{U} & \approx \hat{\mathbf{f}}_{i,\text{aux}}(\mathbf{U}_h^-, \mathbf{U}_h^+) = \frac{1}{2} \left[ \mathbf{U}_h^- + \mathbf{U}_h^+ \right] \end{aligned} \quad (161)$$

The formulations outlined in sections 5.2.2 and 5.2.3 present a sample formulations that can be applied for convection dominated and convection-diffusion dominated systems, respectively. However, some of the features (for example the numerical fluxes) can be chosen based on the properties that each specific scheme suggests.

## 5.3 Elemental transformation

In order to perform the numerical integrations appear in (160), i.e., surface and volume integrations that involve basis functions, it is beneficial to define the bases over the standard elements.

### 5.3.1 One-dimensional elemental transformation

In the case of one-dimensional problems, the local element  $\Omega_h$  in space coordinate  $x$  is transferred to standard element  $\Omega_e$  through the following sub-parametric mapping.

$$\eta = 2 \frac{x - x_i}{x_{i+1} - x_i} - 1 \quad \forall \eta \in \Omega_h \quad (162)$$

with the inverse transformation as,

$$x = \frac{1-\eta}{2} x_i + \frac{1+\eta}{2} x_{i+1} \quad \forall x \in \Omega_e \quad (163)$$

The master element, in the one-dimensional case, is defined in the range of  $(\eta) \in [-1, 1]$ , as shown in Fig. 17.

The transfer Jacobians will be,

$$\mathbf{J}_{x \rightarrow \eta} = \frac{\partial x}{\partial \eta} = \Delta x, \quad \mathbf{J}_{\eta \rightarrow x} = \frac{\partial \eta}{\partial x} = \Delta x / 2. \quad (164)$$

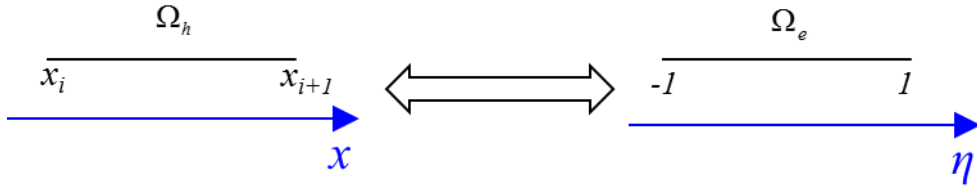


*Fig. 17 Schematic diagram of the linear mapping of the 1D element.*

### 5.3.2 Two-dimensional elemental transformation

#### *Quadrilateral elements*

A mapping shown in is used to transfer the physical element in Cartesian coordinate  $(x, y)$  to a standard quadrilateral element  $(\eta_1, \eta_2) \in [-1, 1]$  as follows,

$$\begin{aligned} x &= \frac{(1-\eta_1)(1-\eta_2)}{4} x_1 + \frac{(1+\eta_1)(1-\eta_2)}{4} x_2 + \frac{(1+\eta_1)(1+\eta_2)}{4} x_3 + \frac{(1-\eta_1)(1+\eta_2)}{4} x_4 \\ y &= \frac{(1-\eta_1)(1-\eta_2)}{4} y_1 + \frac{(1+\eta_1)(1-\eta_2)}{4} y_2 + \frac{(1+\eta_1)(1+\eta_2)}{4} y_3 + \frac{(1-\eta_1)(1+\eta_2)}{4} y_4 \end{aligned} \quad (165)$$

The transfer Jacobian from  $xy$ -coordinate to  $\eta_1\eta_2$ -coordinate reads as follows,

$$\mathbf{J}_{xy \rightarrow \eta_1\eta_2} = \frac{\partial(x, y)}{\partial(\eta_1, \eta_2)} = \begin{bmatrix} \frac{\partial x}{\partial \eta_1} & \frac{\partial x}{\partial \eta_2} \\ \frac{\partial y}{\partial \eta_1} & \frac{\partial y}{\partial \eta_2} \end{bmatrix} \quad (166)$$

where,

$$\begin{aligned}
\frac{\partial x}{\partial \eta_1} &= \frac{1}{4} [(1-\eta_2)(x_2-x_1) + (1+\eta_2)(x_3-x_4)] \\
\frac{\partial y}{\partial \eta_1} &= \frac{1}{4} [(1-\eta_2)(y_2-y_1) + (1+\eta_2)(y_3-y_4)] \\
\frac{\partial x}{\partial \eta_2} &= \frac{1}{4} [(1-\eta_1)(x_4-x_1) + (1+\eta_1)(x_3-x_2)] \\
\frac{\partial y}{\partial \eta_2} &= \frac{1}{4} [(1-\eta_1)(y_4-y_1) + (1+\eta_1)(y_3-y_2)]
\end{aligned} \tag{167}$$

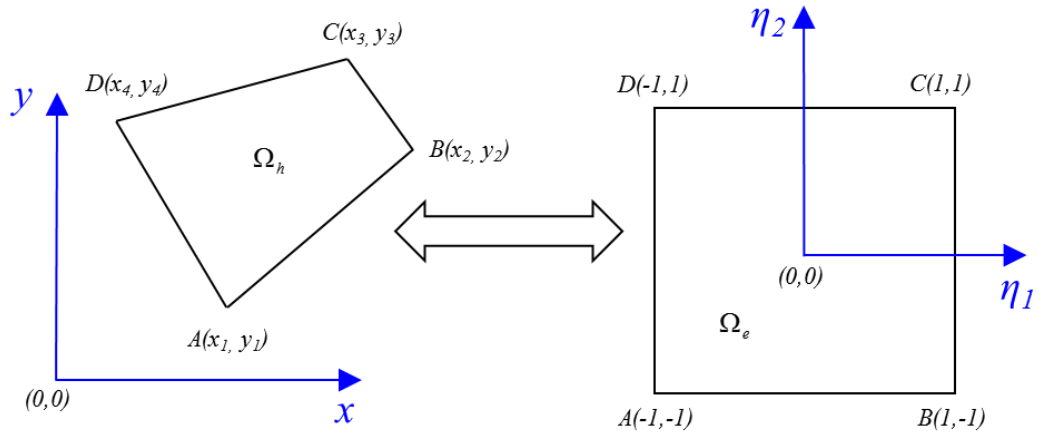


**Fig. 18 Schematic diagram of the linear mapping of the 2D quadrilateral element.**

### Triangular elements

For triangular elements, more care is required in the process of transformation of a physical element to the standard one. Here, a special coordinate mapping the so-called *collapsed coordinate* is used to fulfill the transformation. The two-step transformation, depicted in Fig. 19 includes:

1. Transformation of an arbitrary triangle into the canonical (right triangle) element by the following,

$$\begin{aligned}
x &= -\left(\frac{\xi_1 + \xi_2}{2}\right)x_1 + \left(\frac{1 + \xi_1}{2}\right)x_2 + \left(\frac{1 + \xi_2}{2}\right)x_3 \\
y &= -\left(\frac{\xi_1 + \xi_2}{2}\right)y_1 + \left(\frac{1 + \xi_1}{2}\right)y_2 + \left(\frac{1 + \xi_2}{2}\right)y_3
\end{aligned} \tag{168}$$

Here,

$$J_{xy \rightarrow \xi_1 \xi_2} = \frac{\partial(x, y)}{\partial(\xi_1, \xi_2)} = \begin{bmatrix} \frac{\partial x}{\partial \xi_1} & \frac{\partial x}{\partial \xi_2} \\ \frac{\partial y}{\partial \xi_1} & \frac{\partial y}{\partial \xi_2} \end{bmatrix} = \frac{1}{2} \begin{bmatrix} x_2 - x_1 & x_3 - x_1 \\ y_2 - y_1 & y_2 - y_1 \end{bmatrix} = \text{Area} / 2 \quad (169)$$

2. Mapping of the right triangle element  $\Omega'_e$  the standard square element  $\Omega_e$  by the following transformation

$$\eta_1 = 2 \frac{1 + \xi_1}{1 - \xi_2} - 1, \quad \eta_2 = \xi_2. \quad (170)$$

for which,

$$J_{\xi_1 \xi_2 \rightarrow \eta_1 \eta_2} = \frac{\partial(\xi_1, \xi_2)}{\partial(\eta_1, \eta_2)} = \begin{bmatrix} \frac{\partial \xi_1}{\partial \eta_1} & \frac{\partial \xi_1}{\partial \eta_2} \\ \frac{\partial \xi_2}{\partial \eta_1} & \frac{\partial \xi_2}{\partial \eta_2} \end{bmatrix} = \frac{1 - \eta_2}{2} \quad (171)$$

In order to perform collapsed coordinate transformation, the master triangular and quadrilateral elements should be considered as follows,

$$\begin{aligned} \Omega'_e &= \{(\eta_1, \eta_2) | -1 \leq \eta_1, \eta_2; \eta_1 + \eta_2 \leq 0\}, \\ \Omega_e^q &= \{(\xi_1, \xi_2) | -1 \leq \xi_1, -1 \leq \xi_2\}. \end{aligned} \quad (172)$$

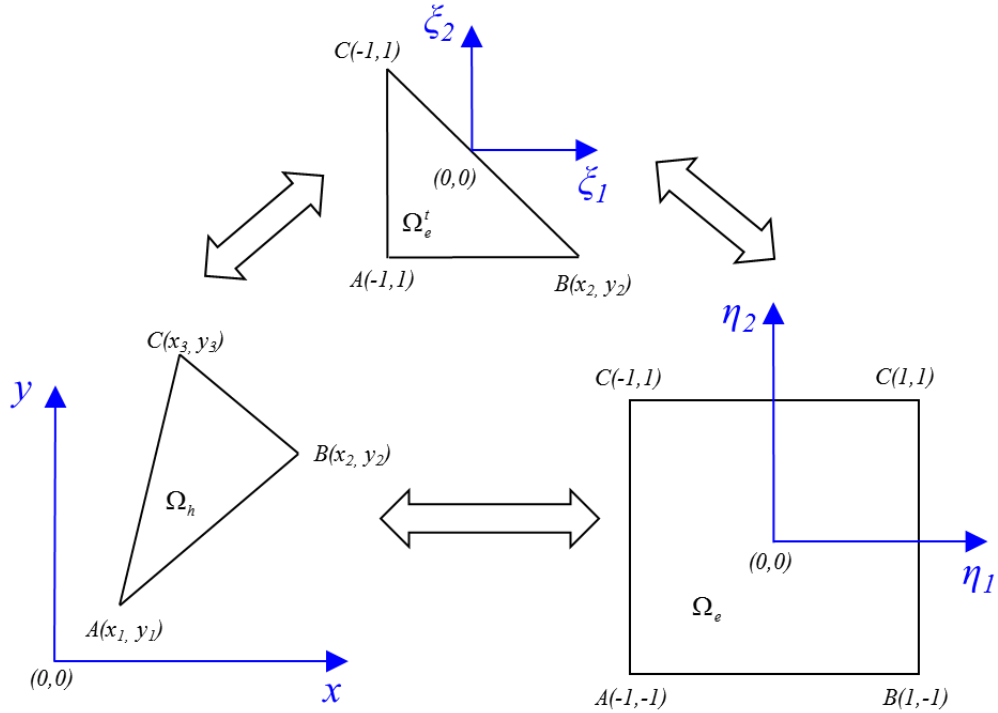


**Fig. 19 Schematic diagram of the linear mappings of the 2D triangular element.**

### 5.3.3 Three-dimensional elemental transformation

For mapping of the tetrahedron elements in physical space to the canonical master element

$\Omega_e^c = \{(\eta_1, \eta_2, \eta_3) | 0 \leq \eta_1 \leq 1; 0 \leq \eta_2 \leq 1 - \eta_1; 0 \leq \eta_3 \leq 1 - \eta_1 - \eta_2\}$  (depicted in Fig. 20), the

following linear transformation is applied,

$$\begin{aligned}
 x &= (1 - \eta_1 - \eta_2 - \eta_3)x_1 + \eta_1x_2 + \eta_2x_3 + \eta_3x_4 \\
 y &= (1 - \eta_1 - \eta_2 - \eta_3)y_1 + \eta_1y_2 + \eta_2y_3 + \eta_3y_4 \\
 z &= (1 - \eta_1 - \eta_2 - \eta_3)z_1 + \eta_1z_2 + \eta_2z_3 + \eta_3z_4
 \end{aligned} \tag{173}$$

$$J_{xyz \rightarrow \eta_1\eta_2\eta_3} = \begin{bmatrix} \frac{\partial x}{\partial \eta_1} & \frac{\partial x}{\partial \eta_2} & \frac{\partial x}{\partial \eta_3} \\ \frac{\partial y}{\partial \eta_1} & \frac{\partial y}{\partial \eta_2} & \frac{\partial y}{\partial \eta_3} \\ \frac{\partial z}{\partial \eta_1} & \frac{\partial z}{\partial \eta_2} & \frac{\partial z}{\partial \eta_3} \end{bmatrix} = 6 \times \text{Volume} \tag{174}$$

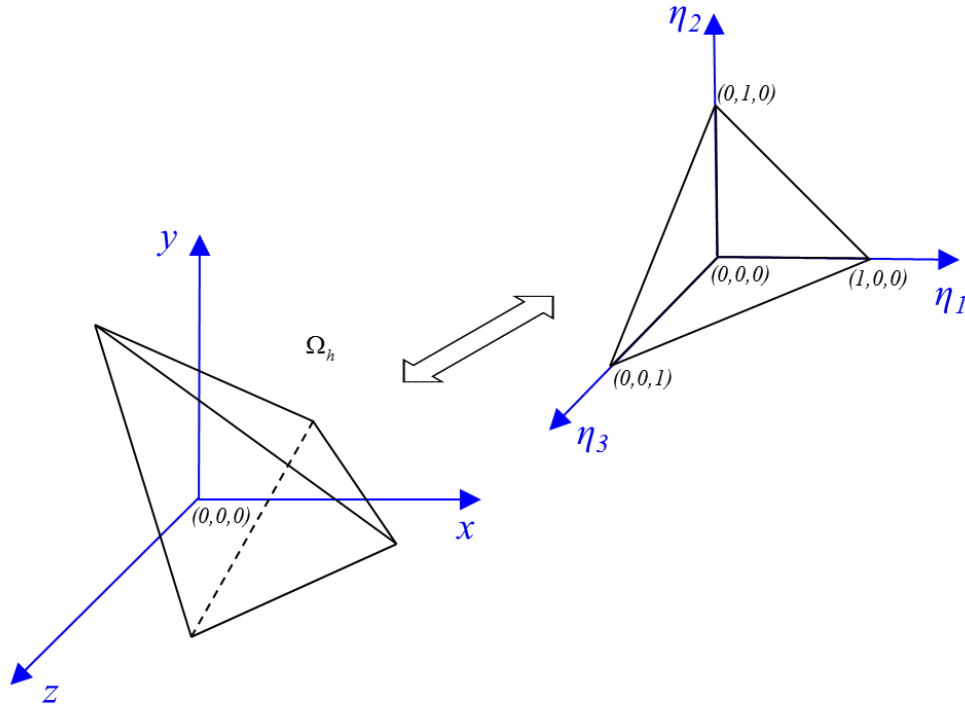


*Fig. 20 Schematic diagram of the linear mapping of the 3D tetrahedron element*

## 5.4 Basis functions

In this section, we introduce functions in order to construct a polynomial basis for polynomials of degree  $P$  on standard reference elements which were introduced in the previous chapter. These are local functions restricted to an element and are the heart of the discontinuous Galerkin methods. Two popular class of polynomials are frequently used in discontinuous finite element methods: Lagrange polynomial and Legendre polynomial. The former is a non-hierarchical basis while the latter is a hierarchical basis. The Lagrange polynomials (eigenfunctions of a particular Sturm-Liouville problem) are particularly useful as an interpolation basis. The Legendre polynomials are a particular form of orthogonal Jacobi polynomials. The orthogonality property leads to helpful features such as block matrices which can be solved efficiently. This remarkable property will be useful in handling the source terms which will be discussed in section 5.10 in details. The use of the *nodal* basis will indicate a non-hierarchical expansion associated with a set of nodes;

however, the *modal* basis will typically represent a hierarchical expansion. These bases are called modal because the unknowns are the coefficients of the expansion functions (also known as modes).

A schematic of the mass matrices computed by Lagrange and Legendre basis is shown in Fig. 21.

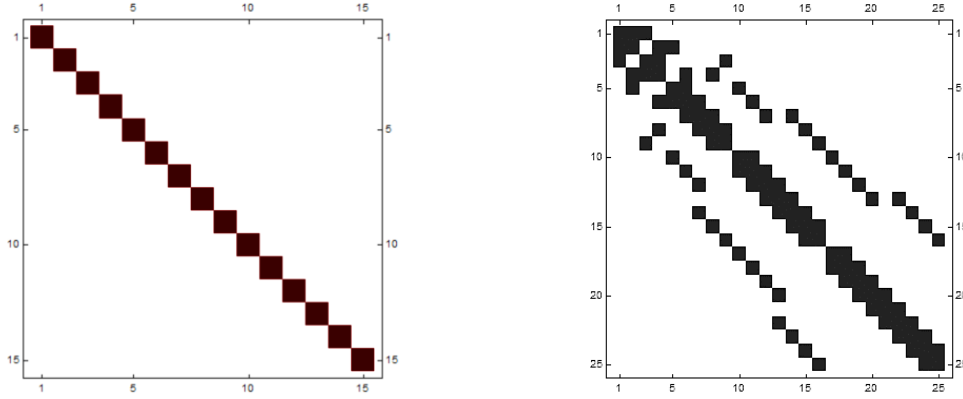


**Fig. 21 Comparison of typical mass matrices corresponding to Lagrange (right) and Legendre (left) bases**

Due to favorable properties such as recursion and orthogonality, the Legendre polynomials are used as basis functions in this work which will be introduced for one, two, and three-dimensional space in the following subsections. These functions are solutions to the Legendre differential equation. The  $n^{\text{th}}$ -order Jacobi- polynomial  $P_n^{\alpha,\beta}(x)$  is given by

$$P_n^{\alpha,\beta}(x) = \frac{(-1)^n}{2^n n!} (1-x)^{-\alpha} (1+x)^{-\beta} \frac{d^n}{dx^n} \left[ (1-x)^{\alpha+n} (1+x)^{\beta+n} \right] \quad \alpha, \beta > 1 \quad (175)$$

### 5.4.1 Basis functions for one-dimensional space

In one-dimensional space, the Legendre polynomials (also known as Legendre functions) are denoted as  $P_n(\eta)$  and can be achieved by Rodrigue's formula,

$$P_n(\eta) = \frac{1}{2^n n!} \frac{d^n}{d\eta^n} (\eta^2 - 1)^n. \quad (176)$$

The orthogonality property of Legendre polynomials implies:

$$\int_{-1}^1 P_i(\eta)P_j(\eta)d\eta = \begin{cases} 0 & \text{if } i \neq j \\ C_{mm} & \text{if } i = j \end{cases} \quad (177)$$

The first few Legendre polynomials, which are the basis functions to provide a 6<sup>th</sup> order accurate estimation are:

$$\begin{aligned} \varphi_0(\eta) &= P_0(\eta) = 1 \\ \varphi_1(\eta) &= P_1(\eta) = \eta \\ \varphi_2(\eta) &= P_2(\eta) = \frac{1}{2}(3\eta^2 - 1) \\ \varphi_3(\eta) &= P_3(\eta) = \frac{1}{2}(5\eta^3 - 3\eta) \\ \varphi_4(\eta) &= P_4(\eta) = \frac{1}{8}(35\eta^4 - 30\eta^2 + 3) \\ \varphi_5(\eta) &= P_5(\eta) = \frac{1}{8}(63\eta^5 - 70\eta^3 + 15\eta) \end{aligned} \quad (178)$$

Scaled Legendre polynomials are defined as:  $\wp_n(\eta) = \frac{2^n (n!)^2}{(2n)!} P_n(\eta)$

$$\begin{aligned} \varphi_0(\eta) &= \wp_0(\eta) = 1 \\ \varphi_1(\eta) &= \wp_1(\eta) = \eta \\ \varphi_2(\eta) &= \wp_2(\eta) = \eta^2 - \frac{1}{3} \\ \varphi_3(\eta) &= \wp_3(\eta) = \eta^3 - \frac{3}{5}\eta^2 \\ \varphi_4(\eta) &= \wp_4(\eta) = \eta^4 - \frac{6}{7}\eta^2 + \frac{3}{35} \\ \varphi_5(\eta) &= \wp_5(\eta) = \eta^5 - \frac{10}{9}\eta^3 + \frac{5}{21}\eta \end{aligned} \quad (179)$$

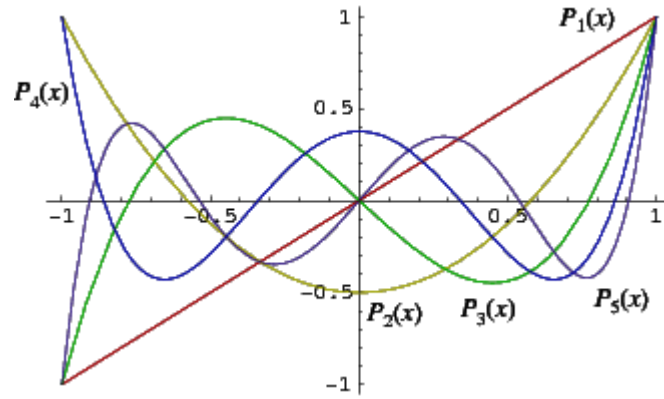


*Fig. 22 Legendre polynomial space*

## 5.4.2 Basis functions for two-dimensional space

### *Rectangular basis*

Basis functions can be constructed by tensorial product of the Legendre polynomials (principal functions) in each coordinate direction. The polynomial function of order  $N$ , is defined as  $\varphi_k(\eta_1, \eta_2) = L_p(\eta_1) \cdot L_q(\eta_2)$  with:  $k = p + q(N + 1)$ ;  $0 \leq p; q \leq N$ .

where,  $\varphi_k$  is the single indexed multidimensional basis which sorts all the modes of the principal functions ( $P$  and  $Q$ ). It should be noted that these polynomials on rectangular elements would not yield a diagonal mass matrix due to the applied bilinear mapping [197].

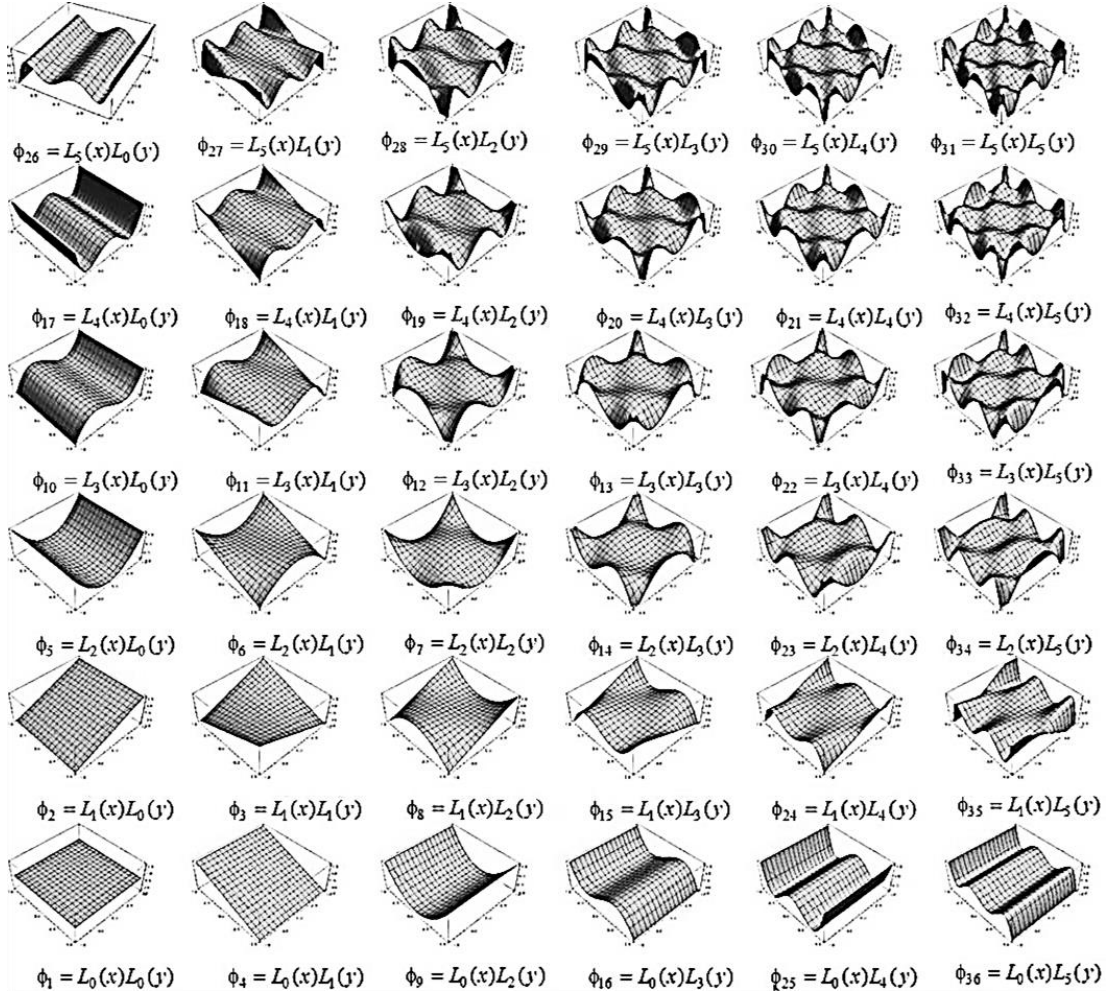


**Fig. 23 Polynomial space in terms of the Pascal's triangle of the full tensor product for rectangular elements (up to polynomial order of  $P=6$ ).**

### Triangular basis

Orthogonal basis functions can be constructed over  $\Omega_e^t$  by tensorial product of the Legendre polynomials (principal functions) in the region  $\Omega_e^q$ .

$$\varphi_k(\xi_1, \xi_2) = P_p^{0,0}(\eta_1) \left( \frac{1-\eta_2}{2} \right)^p P_q^{2p+1,0}(\eta_2) \quad (180)$$

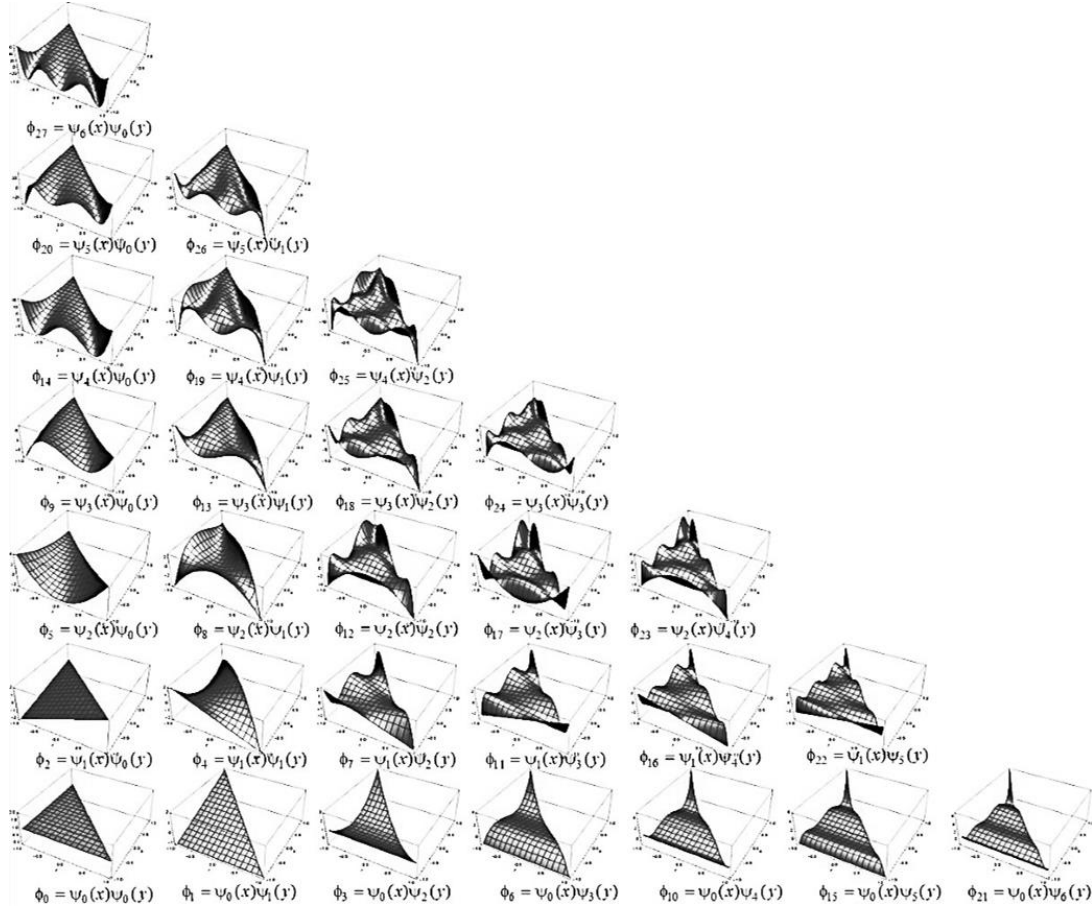


*Fig. 24 Polynomial space in terms of the Pascal's triangle of the full tensor product for triangular elements (up to polynomial order of  $P=6$ ).*

### 5.4.3 Basis functions for two-dimensional space

Orthogonal basis functions can be constructed over  $\Omega_e$  by tensorial product of the Legendre polynomials (principal functions) in the region  $\Omega_e^c$ .

$$\varphi_k(\eta_1, \eta_2, \eta_2) = P_p^{0,0} \left( \frac{2\eta_3}{1-\eta_1-\eta_2} - 1 \right) \left( -\frac{4\eta_1}{1-\eta_2} \right)^p P_q^{2p+1,0} (1-\eta_2)^{p+q} P_r^{2p+2q+2,0} (2\eta_2 - 1). \quad (181)$$

In this case, the mass matrix is orthogonal.

## 5.5 Numerical integration

In order to compute the volume and surface integrals of the discrete local weak form of the governing equations, a numerical integration method may be applied. One of the

various possible algorithms, known as numerical quadrature (in 1D and sometimes as a general term) or cubature (in 2D or 3D) rules in which a formula to approximate the definite integral of a function via a weighted sum of function evaluations, is widely used in finite element and discontinuous Galerkin. The choice of an in-exact integration rule leads to aliasing instabilities where strong discontinuities or turbulence effects are present. In this dissertation Gauss-Legendre quadrature as a particular class of Gauss quadrature technique is applied. The Gauss-Legendre quadrature is defined for the limits of integration of -1 to 1. Therefore transformation of physical elements to standard ones is necessary. In Fig. 25 and Fig. 26, the integration approximation and the graphical illustration of the quadrature, depicting position and number of required quadrature points are summarized for 1D /2D and 3D respectively.

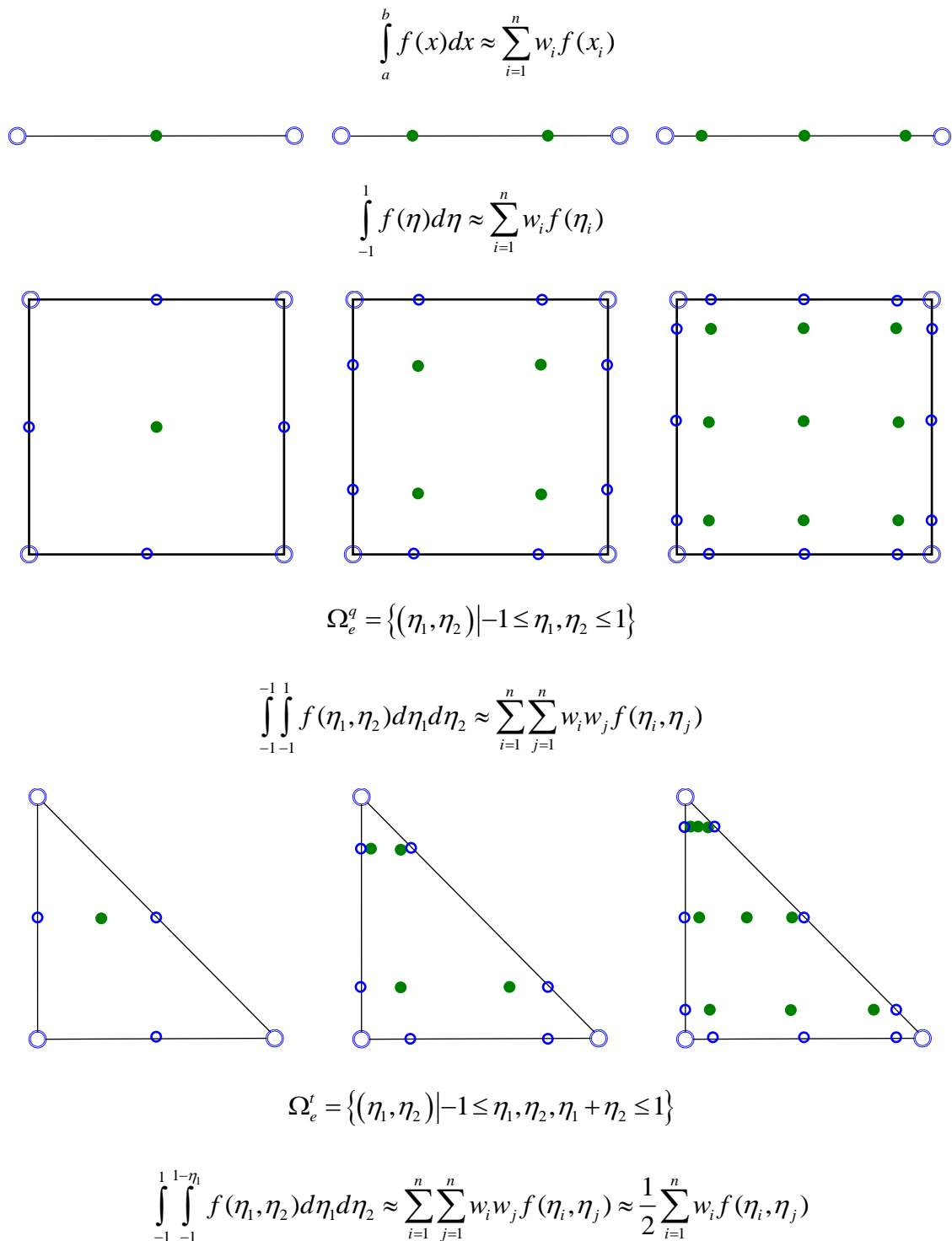
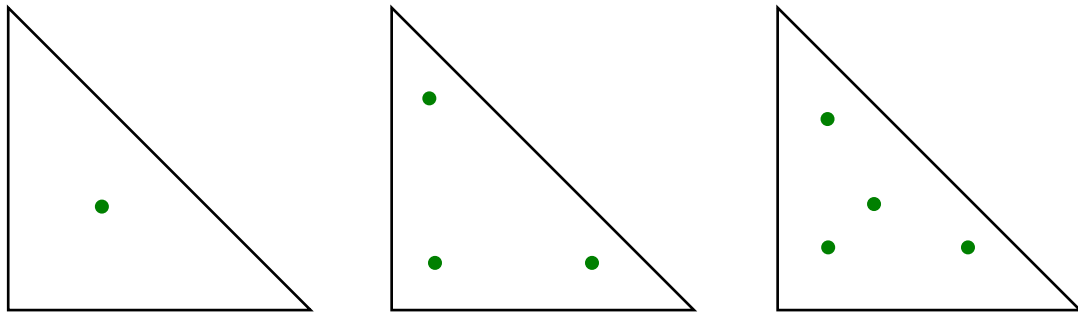
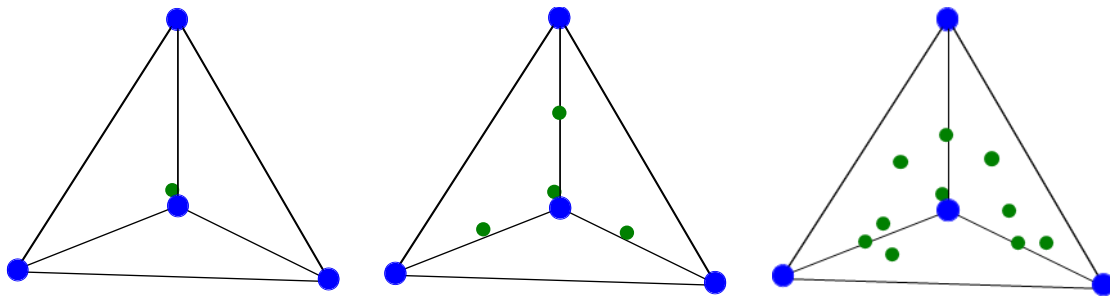


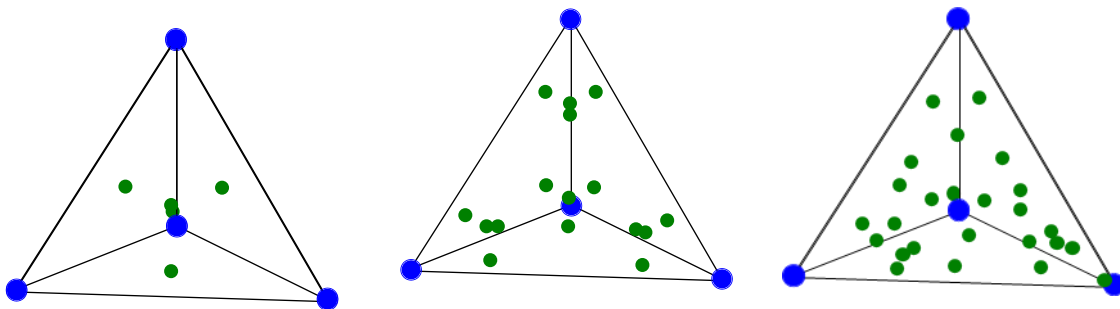
**Fig. 25 Schematic representation of number and location of required quadrature points used in numerical integration for (a) 1D elements, (b) 2D quadrilateral elements, (c) 2D triangular elements**



(a) Surface quadrature points



(b) Volume quadrature points



(c) Surface and volume quadrature points together

$$\Omega_e^c = \{(\eta_1, \eta_2, \eta_3) | 0 \leq \eta_1, \eta_2, \eta_1 + \eta_2 + \eta_3 \leq 1\}$$

$$\int_{-1}^1 \int_{-1}^{1-\eta_1} \int_{-1}^{1-\eta_1-\eta_2} f(\eta_1, \eta_2, \eta_3) d\eta_1 d\eta_2 d\eta_3 \approx \frac{1}{6} \sum_{i=1}^n w_i f(\eta_i, \eta_j, \eta_k)$$

**Fig. 26 Schematic representation of number and location of required quadrature points used in numerical integration in a 3D tetrahedron element**

## 5.6 Inviscid and viscous numerical flux functions

The choice of the numerical flux can determine the stability, and the accuracy of the numerical method. In order to obtain a stable scheme the numerical flux should be

consistent as well as conservative. Consistency implies an identical solution of the numerical flux to the analytic flux function for smooth continuous inter-element boundary values. Moreover, conservativity requires single-valued flux on the inter-element boundaries. Two general class of inviscid numerical flux functions are categorized as flux difference splitting (FDS) methods and flux vector splitting (FVS) methods. These numerical schemes are based on the upwind direction identification approaches which are referred to as *Riemann approach* or *Boltzmann approach*. These approaches are extensively introduced in the classical review paper of Harten *et al.* [199] and various textbooks [169, 200-202]. It is well known that the FVS method leads to more straightforward and more efficient compared to Godunov-type methods of FDS class. In this work Rusanov [203] (or local Lax-Friedrichs) and Rotated-RHLL [204] fluxes which are both known to be simple and carbuncle-free are implemented and applied depending on the investigated problem. The implementation of the inviscid numerical flux is exactly analogous to the well-established FVM procedure, and the details of the implementation is skipped.

The viscous numerical flux implementation in DG framework is not as straightforward as the inviscid flux is. Rigorous mathematical derivation and presentation of these numerical flux functions for pure elliptical equations (Laplace problem) can be found in [205, 206]. The unified representation of some numerical schemes suggested by [206] is summarized in Table 11. The operators  $\{ \}$  and  $\{ \}$  for scalar variable  $s$  and vector quantity  $\vec{v}$  is defined as follows

$$\begin{aligned}
s &= s^+ \bar{n}^+ + s^- \bar{n}^- = \bar{n} (s^+ - s^-) \\
\{s\} &= \frac{1}{2} (s^+ + s^-) \\
\bar{v} &= \bar{v}^+ \bar{n}^+ + \bar{v}^- \bar{n}^- = \bar{n} (\bar{v}^+ - \bar{v}^-) \\
\{\bar{v}\} &= \frac{1}{2} (\bar{v}^+ + \bar{v}^-)
\end{aligned} \tag{182}$$

**Table 11 Comparison of some the numerical schemes for viscous flux. Adapted from [206].**

Method	$\hat{u}$	$\hat{\sigma}$
Bassi and Rebay [198] (BR1)	$\{u_h\}$	$\{\sigma_h\}$
Brezzi <i>et al.</i> [207]	$\{u_h\}$	$\{\sigma_h\} - \alpha_r (u_h)$
Cockburn and Shu [208] (LDG)	$\{u_h\} - \beta \cdot [u_h]$	$\{\sigma_h\} + \beta \sigma_h - \alpha_j (u_h)$
Douglas and Dupont [209] (IP)	$\{u_h\}$	$\{\nabla_h u_h\} - \alpha_j (u_h)$
Bassi <i>et al.</i> [210] (BR2)	$\{u_h\}$	$\{\nabla_h u_h\} - \alpha_r (u_h)$

The functional operators of  $\alpha_r$  and  $\alpha_j$ , the so-called penalty terms are defined as

$$\begin{aligned}
\alpha_j(\varphi) &= \mu\varphi = \eta_e h_e^{-1} \varphi, \\
\alpha_r(\varphi) &= -\eta_e \{r_e(\varphi)\},
\end{aligned} \tag{183}$$

where,  $\eta_e$  is a positive number and  $h_e$  is an indicator of element size (e.g., circumscribed

circle radius of the element), and  $\int_{\Omega} r_e(\varphi) \cdot \tau dx = -\int_e \varphi \cdot \{\tau\} ds$ .

In most of the computations in this thesis, BR1 and LDG methods are applied unless otherwise is mentioned. In the BR1 scheme, central discretization is used for both auxiliary and viscous fluxes. This method which is extensively used by the DG community is shown to have a convergence order of only  $P$  (polynomial degree) for odd ansatz [208]. Moreover, the stencil is known to be spread. These deficiencies motivated application of LDG method in which one-sided fluxes in opposite directions for the auxiliary and viscous fluxes are utilized. In this thesis,  $\beta$  is set equal to zero when LDG flux is used leading to an *upwind-downwind* (also known as *alternating flux*) scheme.

## 5.7 Positivity preserving scheme

High order conservative schemes, including the DG scheme introduced in the previous section, usually suffer from the non-physical negative density or pressure. This situation leads to the ill-posedness of the system and numerical breakdowns in consequence. On the other hand, in the case of conservation laws with source terms which are added to account for chemical reactions, gravity or the interaction of phases, as in the present case, the possibility of encountering negative density or pressure during numerical simulation increases. Therefore, the application of an efficient positivity preserving schemes is necessary to prevent the numerical breakdown. In the present work, the positivity preserving scheme of Zhang and Shu [211] for compressible Euler equations was applied to ensure the positivity of density and pressure fields, while maintaining the higher order accuracy. The general implementation of the scheme can be outlined as follows.

Limiting the higher order coefficients for density was achieved first by computing the minimum value of the density amongst all quadrature points,  $\rho_{\min}$ . The coefficients for the density expansion were then modified as  $\tilde{a}_i^\rho = \theta_i a_i^\rho$  with  $\theta_i = \min(\frac{a_0^\rho - \varepsilon}{a_0^\rho - \rho_{\min}}, 1)$ . Here the  $i$  index accounts for all the bases, and the zero index represents the mean solution. Also, the value  $\varepsilon$  is determined by  $\varepsilon = \min(10^{-13}, a_0^\rho, \bar{p})$  where  $\bar{p}$  denotes the mean element pressure.

For the modification of pressure, the following procedures were used. First, we set  $\mathbf{s}$  as

$$\mathbf{s} = (1-t)\bar{\mathbf{w}} + \beta\bar{\mathbf{q}}, \quad (184)$$

where  $\bar{\mathbf{w}}$  and  $\bar{\mathbf{q}}$  are the cell average and conservative variables, respectively.  $\beta$  can be calculated as follows

$$\beta = \begin{cases} 1 & \text{if } p(\mathbf{q}) \geq \varepsilon \\ \text{the solution of } p(\mathbf{s}) = \varepsilon, & \text{if } p(\mathbf{q}) < \varepsilon \end{cases} \quad (185)$$

Finally, the coefficients are modified by  $\tilde{a}_i^p = \theta_2 a_i^p$  with  $\theta_2 = \min(\beta, 1)$ .

The application of this limiter was proved to provide stable schemes for unstructured triangular meshes with favorable results [195]. We report the first application of this type of limiter to the two-fluid model of dusty gas flows. Our numerical experiments on all the test cases show that application of a positivity preserving limiter is necessary to obtain converged solutions without compromising the accuracy of the solution.

## 5.8 Monotonicity preserving scheme

Our numerical investigations show that simple application of the positivity preserving scheme is not enough to develop a stable scheme, especially in the presence of strong shock waves. The situation deteriorates when the multiphase system with source terms is being solved. In the present study, the limiter of Zhang and Shu [212] for one-dimensional cases and the limiter of Barth and Jespersen [192] which was initially devised for the finite volume framework are applied. It is important to note that any TVD/MUSCL type scheme can degrade the order of accuracy in the smooth regions of the solution unless a pragmatic shock detection scheme is introduced.

According to Barth and Jespersen [192], the limiting procedure of slopes should be done in a way that the solution at the integration points is confined to the range spanned by the neighboring solution averages. The limited solution can then be written as

$$U(\mathbf{x}, t) = a_0(t)\varphi_0(\mathbf{x}) + \lambda_{\min} \sum_{i>0}^p a_i \varphi_i(\mathbf{x}), \quad (186)$$

where  $\lambda_{\min} = \min \max(\lambda_1, 0)$ ,

$$\lambda_1 = \begin{cases} \min(1, \frac{U_{\max} - U_i}{\Delta_2}), & \text{if } \Delta_2 > 0 \\ \max(1, \frac{U_{\min} - U_i}{\Delta_2}), & \text{if } \Delta_2 < 0 \\ 1, & \text{otherwise} \end{cases} \quad (187)$$

Here  $\Delta_2 = U_j(\mathbf{x}_i^*) - U_j$  and  $U_{\max}$  and  $U_{\min}$  are the maximum and minimum solution averages on the elements sharing edges, respectively.

## 5.9 Boundary conditions

The implementation of boundary conditions in two-fluid or multi-fluid systems requires a different set of conditions for each phase. The benchmark problems considered in this paper are free from boundary effects, except the compression corner test case, in which an adiabatic, impermeable, inviscid wall boundary condition is applied for both phases (Kim and Chang [142]). Other boundary conditions choices like the adherence condition or reflection conditions are also viable for the solid phase [213]. When the viscous system of conservation laws (e.g., Navier-Stokes-Fourier) is considered, it is necessary to use a non-slip boundary condition for the gas phase and a slip boundary condition for the solid phase.

## 5.10 Novel source terms treatment

It was well-known that the stiff relaxation terms in balance laws (i.e., strictly hyperbolic systems with source terms) lead to disparate relaxation times, which in turn results in severe numerical difficulties. In the case of the two-fluid model, in addition to the time scale related to the convection, a much smaller relaxation time scale exists that inevitably imposes smaller time steps on the numerical solver. The use of a slower time scale in such problems can cause severe numerical instability.

The most well-known methods for removing this limitation are the operator splitting and zero-relaxation limit; however, as reported in Béreux [214], the range of validity of

each method is very limited, to the product of relaxation time and the acoustic wave pulsation. Moreover, spurious solutions may arise when the effects of the source terms are not properly resolved [215]. Finally, it is well established that the convergence rate of the first-order finite difference methods for conservation laws will be no better than  $O(h^{1/2})$  [216]. Here we demonstrate that the inherent feature of the new DG scheme bypasses the need to apply such inefficient treatments in conventional methods.

For a single variable  $u_h$ , the elemental formulation (148) reduces to

$$\begin{aligned} & \frac{d}{dt} \int_{\Omega_k} u_h \varphi_i(\mathbf{x}) d\Omega_k + \oint_{\partial\Omega_k} F(u_h) \cdot \hat{n} \varphi_i(\mathbf{x}) d\sigma - \int_{\Omega_k} F(u_h) \cdot \nabla \varphi_i(\mathbf{x}) d\Omega_k \\ & = \int_{\Omega_k} S(u_h) \varphi_i(\mathbf{x}) d\Omega_k. \end{aligned} \quad (188)$$

Taking  $\mathbf{U}$  as the global vector of degrees of freedom, this equation can be written in a matrix form:

$$\begin{aligned} & \mathbf{M} \frac{d\mathbf{U}}{dt} - \mathbf{K}\mathbf{U} + \widehat{F}(u_h)\boldsymbol{\Theta} - S(u_h)\boldsymbol{\Theta}' = 0 \\ & \frac{d\mathbf{U}}{dt} - \mathbf{M}^{-1}\mathbf{K}\mathbf{U} + \widehat{F}(u_h)\mathbf{M}^{-1}\boldsymbol{\Theta} - S(u_h)\mathbf{M}^{-1}\boldsymbol{\Theta}' = 0 \\ & \frac{d\mathbf{U}}{dt} = L(\mathbf{U}) \\ & \mathbf{U} = (U^{(1)}, U^{(2)}, \dots, U^{(N)})^T \\ & L(\mathbf{U}) = \mathbf{M}^{-1}\mathbf{K}\mathbf{U} - \widehat{F}(u_h)\mathbf{M}^{-1}\boldsymbol{\Theta} + S(u_h)\mathbf{M}^{-1}\boldsymbol{\Theta}' \end{aligned} \quad (189)$$

Here,  $\mathbf{M}$  and  $\mathbf{K}$  are the mass and stiffness matrixes, and  $\boldsymbol{\Theta}$  and  $\boldsymbol{\Theta}'$  are the vectors that incorporate the contributions of the boundary and source terms, respectively. The matrixes are defined as follows:

$$\begin{aligned} & \mathbf{M} = \int_{\Omega_k} \varphi_i(\mathbf{x}) \varphi_j(\mathbf{x}) d\Omega_k \quad \forall \quad 1 \leq i \leq j \leq n \\ & = \begin{bmatrix} \int_{\Omega_k} \varphi_1(\mathbf{x}) \varphi_1(\mathbf{x}) d\Omega_k & \int_{\Omega_k} \varphi_1(\mathbf{x}) \varphi_2(\mathbf{x}) d\Omega_k & \dots & \int_{\Omega_k} \varphi_1(\mathbf{x}) \varphi_n(\mathbf{x}) d\Omega_k \\ \int_{\Omega_k} \varphi_2(\mathbf{x}) \varphi_1(\mathbf{x}) d\Omega_k & \int_{\Omega_k} \varphi_2(\mathbf{x}) \varphi_2(\mathbf{x}) d\Omega_k & \dots & \int_{\Omega_k} \varphi_2(\mathbf{x}) \varphi_n(\mathbf{x}) d\Omega_k \\ \vdots & \vdots & \ddots & \vdots \\ \int_{\Omega_k} \varphi_n(\mathbf{x}) \varphi_1(\mathbf{x}) d\Omega_k & \int_{\Omega_k} \varphi_n(\mathbf{x}) \varphi_2(\mathbf{x}) d\Omega_k & \dots & \int_{\Omega_k} \varphi_n(\mathbf{x}) \varphi_n(\mathbf{x}) d\Omega_k \end{bmatrix}, \end{aligned} \quad (190)$$

Owing to the orthogonal property of the basis functions,  $\mathbf{M} = \begin{cases} C_{ij} & i = j \\ 0 & i \neq j \end{cases}$

$$\mathbf{K} = \int_{\Omega_k} \nabla \varphi_i(\mathbf{x}) \varphi_i(\mathbf{x}) d\Omega_k$$

$$= \begin{bmatrix} \int_{\Omega_k} \nabla \varphi_1(\mathbf{x}) \varphi_1(\mathbf{x}) d\Omega_k & \int_{\Omega_k} \nabla \varphi_1(\mathbf{x}) \varphi_2(\mathbf{x}) d\Omega_k & \dots & \int_{\Omega_k} \nabla \varphi_1(\mathbf{x}) \varphi_n(\mathbf{x}) d\Omega_k \\ \int_{\Omega_k} \nabla \varphi_2(\mathbf{x}) \varphi_1(\mathbf{x}) d\Omega_k & \int_{\Omega_k} \nabla \varphi_2(\mathbf{x}) \varphi_2(\mathbf{x}) d\Omega_k & \dots & \int_{\Omega_k} \nabla \varphi_2(\mathbf{x}) \varphi_n(\mathbf{x}) d\Omega_k \\ \vdots & \vdots & \ddots & \vdots \\ \int_{\Omega_k} \nabla \varphi_n(\mathbf{x}) \varphi_1(\mathbf{x}) d\Omega_k & \int_{\Omega_k} \nabla \varphi_n(\mathbf{x}) \varphi_2(\mathbf{x}) d\Omega_k & \dots & \int_{\Omega_k} \nabla \varphi_n(\mathbf{x}) \varphi_n(\mathbf{x}) d\Omega_k \end{bmatrix}, \quad (191)$$

$$\Theta = \begin{bmatrix} \int_{\Omega_e} \varphi_1(\mathbf{x}) |J| d\Omega_e \\ \int_{\Omega_e} \varphi_2(\mathbf{x}) |J| d\Omega_e \\ \vdots \\ \int_{\Omega_e} \varphi_n(\mathbf{x}) |J| d\Omega_e \end{bmatrix}, \quad (192)$$

$$\Theta' = \begin{bmatrix} \int_{\Omega_e} \varphi_1(\mathbf{x}) |J'| d\Omega_e \\ \int_{\Omega_e} \varphi_2(\mathbf{x}) |J'| d\Omega_e \\ \vdots \\ \int_{\Omega_e} \varphi_n(\mathbf{x}) |J'| d\Omega_e \end{bmatrix}. \quad (193)$$

The choice of orthogonal basis functions greatly simplifies the contribution of the high order moments of the polynomial approximate solution to the source-term related vector  $\Theta'$  in equation (30). Once the basis functions (Legendre polynomials),  $\varphi_n(\mathbf{x})$ , are multiplied by the transformation Jacobian ( $|J'| = (1-b)/2$ ), the integration in the interval  $[-1, 1]$  will vanish for all the terms except the first term, due to the orthogonal property of the basis functions and a coincidental relation  $\varphi_1(\mathbf{x}) = 1$ ; that is,

$$\Theta' = \begin{bmatrix} \int_{\Omega_e} \varphi_1(\mathbf{x}) |J'| d\Omega_e \\ \int_{\Omega_e} \varphi_2(\mathbf{x}) |J'| d\Omega_e \\ \vdots \\ \int_{\Omega_e} \varphi_n(\mathbf{x}) |J'| d\Omega_e \end{bmatrix} = \begin{bmatrix} 2 \\ 0 \\ \vdots \\ \vdots \\ 0 \end{bmatrix}. \quad (194)$$

Note that, in this novel method, the source term treatment is greatly simplified, exactly the same as the first-order ( $P^0$ ) case. In other words, the contribution of the cell average solutions is dominant in the source terms in the DG framework, although the left-hand side of equations (148) and (25) is calculated by the high order polynomial approximation.

## 5.11 The numerical algorithm for solving constitutive equations

The nonlinear algebraic system of constitutive relations provided in \*\* can be recast in a reduced form as follows [2]

$$\begin{aligned} \hat{\Pi}q(c\hat{R}) &= (1 + f_b \hat{\Delta}) \hat{\Pi}_0 + [\hat{\Pi} \cdot \nabla \hat{\mathbf{u}}]^{(2)}, \\ \hat{\Delta}q(c\hat{R}) &= \hat{\Delta}_0 + \frac{3}{2} f_b (\hat{\Pi} + f_b \hat{\Delta} \mathbf{I}) : \nabla \hat{\mathbf{u}}, \\ \hat{\mathbf{Q}}q(c\hat{R}) &= (1 + f_b \hat{\Delta}) \hat{\mathbf{Q}}_0 + \hat{\Pi} \cdot \hat{\mathbf{Q}}_0 + \frac{1}{2 \text{Pr}} \hat{\mathbf{Q}} \cdot \nabla \hat{\mathbf{u}} \end{aligned} \quad (195)$$

Here the caret ^ over a symbol represents a quantity with the dimension of the ratio of the stress to the pressure. The subscript 0 stands for first-order Boltzmann-based constitutive equations which are determined by the Newtonian law of shear, bulk viscosity and Fourier law of heat conduction as follows

$$\hat{\Pi}_0 = -2\mu [\nabla \mathbf{u}]^{(2)}, \quad \hat{\Delta}_0 = -2\mu_b \nabla \cdot \mathbf{u}, \quad \hat{\mathbf{Q}}_0 = -k \nabla \ln T \quad (196)$$

The following definitions are necessary in order to have complete definition of the above relations

$$\begin{aligned}\hat{\Pi} &\equiv \frac{N_\delta}{p} \Pi, \quad \hat{\Delta} \equiv \frac{N_\delta}{p} \Delta, \quad \hat{\mathbf{Q}} \equiv \frac{N_\delta}{p} \frac{\mathbf{Q}}{\sqrt{T/(2\varepsilon)}}, \\ \nabla \hat{\mathbf{u}} &\equiv -2\mu \frac{N_\delta}{p} \nabla \mathbf{u}, \quad \nabla \hat{T} \equiv -2\kappa \frac{N_\delta}{p} \frac{\nabla T}{\sqrt{T/(2\varepsilon)}}, \quad \varepsilon \equiv \frac{1}{Ec} \frac{1}{Pr} \frac{1}{T_r/\Delta T}.\end{aligned}\quad (197)$$

A nonlinear coupling factor  $q(c\hat{R})$  is defined as

$$\begin{aligned}q(c\hat{R}) &= \frac{\sinh(c\hat{R})}{c\hat{R}}, \\ \hat{R}^2 &= \hat{\Pi} : \hat{\Pi} + \frac{2\gamma'}{f_b} \hat{\Delta}^2 + \hat{\mathbf{Q}} \cdot \hat{\mathbf{Q}},\end{aligned}\quad (198)$$

$$c^2 = \frac{8\sqrt{2}}{5\pi} A_2(\nu) \Gamma \left[ 4 - \frac{2}{\nu-1} \right]$$

where,  $\gamma' = (5-3\gamma)/2$   $\nu$  is the exponent of the inverse power law for gas particle interaction potential, and the tabulated values of  $A_2(\nu)$  are available in the literature.

Definition of other parameters is in consistence with those introduced in Chapter 3.

The solution of these equations will provide viscous stress, excess stress, and heat flux which are essential in defining the numerical viscous flux on cell interfaces. Contrary to the classical Navier-Stokes constitutive equations where the viscous stress and heat flux are linearly proportional to the thermodynamic forces (i.e., derivatives of velocity and temperature), solving the nonlinear form of the second-order Boltzmann-based constitutive equations requires an additional algorithm.

Contrary to other the moments method in which the constitutive equations are derived in a way that the whole system is of hyperbolic type, the nonlinear algebraic constitutive equations are solved by an iterative algorithm. This solution can then be applied by the similar manner in conventional Navier-Stokes codes. The constitutive equations consist of 10 equations ( $\Pi_{xx}, \Pi_{xy}, \Pi_{xz}, \Pi_{yy}, \Pi_{yz}, \Pi_{zz}, \Delta, Q_x, Q_y, Q_z$ ) for known 14 parameters ( $p, T, \nabla u, \nabla v, \nabla w, \nabla T$ ). It has been shown that a proper numerical method for solving the

highly nonlinear equations can be developed by application of the method of iteration [2, 95, 217].

Here we present an iterative method in three-dimensional space via decomposition. In this case, the stress, excess stress and heat flux components ( $\Pi_{xx}$ ,  $\Pi_{xy}$ ,  $\Pi_{xz}$ ,  $\Delta$ ,  $Q_x$ ) on a surface can be approximated as the sum of three solvers in 3 spatial directions:

$$\begin{aligned} f_x(u_x, v_x, w_x, T_x) &= f_{1x}(u_x, 0, 0, T_x) + f_{2x}(0, v_x, 0, 0) + f_{3x}(0, 0, w_x, 0) \\ f_y(u_y, v_y, w_y, T_y) &= f_{1y}(0, v_y, 0, T_y) + f_{2y}(u_y, 0, 0, 0) + f_{3y}(0, 0, w_y, 0) \\ f_z(u_z, v_z, w_z, T_z) &= f_{1z}(0, 0, w_z, T_z) + f_{2z}(u_z, 0, 0, 0) + f_{3z}(0, 0, v_z, 0) \end{aligned} \quad (199)$$

The iterative procedures, which is proved to have a converged solution within a few iterations can be summarized as follows. In the solver on  $(u_x, 0, 0, T_x)$  which is responsible for compression-expansion of the gas, for positive  $\hat{\Pi}_{xx0}$  and  $\hat{Q}_{x0}$

$$\hat{R}_{n+1} = \frac{1}{c} \sinh^{-1} \left[ c \sqrt{Y_n} \right], \quad (200)$$

where

$$Y_n \equiv \left(1 + \hat{\Pi}_{xxn} + f_b \hat{\Delta}_n\right)^2 \hat{R}_0^2 + 4 \left(\hat{\Pi}_{xxn} + f_b \hat{\Delta}_n\right) \left[1 + 2 \left(\hat{\Pi}_{xxn} + f_b \hat{\Delta}_n\right)\right] \frac{4}{5 f_b} \hat{\Delta}_0^2, \quad (201)$$

and

$$\hat{\Pi}_{xx_{n+1}} = \frac{\left(1 + \hat{\Pi}_{xxn} + f_b \hat{\Delta}_n\right) \hat{\Pi}_{xx0}}{\sqrt{Y_n}} \hat{R}_{n+1}, \quad (202)$$

$$\hat{Q}_{x_{n+1}} = \frac{\hat{Q}_{x0}}{\hat{\Pi}_{xx0}} \hat{\Pi}_{xx_{n+1}},$$

and for negative  $\hat{\Pi}_{xx0}$  and  $\hat{Q}_{x0}$ ,

$$\hat{\Pi}_{xx_{n+1}} = \frac{\left(1 + f_b \hat{\Delta}_n\right) \hat{\Pi}_{xx0}}{q \left(c \hat{R}_n\right) - \hat{\Pi}_{xx0}}, \quad (203)$$

$$\hat{Q}_{x_{n+1}} = \frac{\hat{Q}_{x_0}}{\hat{\Pi}_{x_0}} \hat{\Pi}_{x_{n+1}}$$

Since the equations are invariant under a transformation  $\hat{Q}_x \leftrightarrow -\hat{Q}_x$ , only two cases satisfying  $\hat{\Pi}_{x_0} \hat{Q}_x > 0$  are considered. In the above expressions,  $\hat{\Pi}_{x_1}$ ,  $\hat{\Delta}_1$ , and  $\hat{Q}_{x_1}$  are given by

$$\begin{aligned} \hat{\Pi}_{x_1} &= \frac{\sinh^{-1}(c\hat{R}_0)}{c\hat{R}_0} \hat{\Pi}_{x_0}, \\ \hat{\Delta}_1 &= \frac{\sinh^{-1}(c\hat{R}_0)}{c\hat{R}_0} \hat{\Delta}_0, \\ \hat{Q}_{x_1} &= \frac{\sinh^{-1}(c\hat{R}_0)}{c\hat{R}_0} \hat{Q}_{x_0}. \end{aligned} \tag{204}$$

The outputs for these solvers are summarized in Table 12. More detailed discussions regarding the application of NCCR model in DG framework and extension to diatomic and polyatomic can be found in [218, 219].

*Table 12 The outputs for the NCCR solvers.*

	$f_1$	$f_2$	$f_3$
x	$\hat{\Pi}_{xx}$	$\hat{\Pi}_{xx}$	$\hat{\Pi}_{xx}$
	$\hat{\Pi}_{yy}$	$-0.5\hat{\Pi}_{xx}$	$-2\hat{\Pi}_{xx}$
	$\hat{\Pi}_{zz}$	$-0.5\hat{\Pi}_{xx}$	$\hat{\Pi}_{xx}$
	$\hat{\Pi}_{xy}$	0	$\hat{\Pi}_{xy}$
	$\hat{\Pi}_{xz}$	0	0
	$\hat{\Pi}_{yz}$	0	0
	$\hat{Q}_x$	$\hat{Q}_x$	0
	$\hat{Q}_y$	0	0
	$\hat{Q}_z$	0	0
	$\hat{\Delta}$	$\hat{\Delta}$	0
	y	$\hat{\Pi}_{xx}$	$-0.5\hat{\Pi}_{yy}$
$\hat{\Pi}_{yy}$		$\hat{\Pi}_{yy}$	$\hat{\Pi}_{yy}$
$\hat{\Pi}_{zz}$		$-0.5\hat{\Pi}_{yy}$	$\hat{\Pi}_{yy}$
$\hat{\Pi}_{xy}$		0	$\hat{\Pi}_{xy}$
$\hat{\Pi}_{xz}$		0	0
$\hat{\Pi}_{yz}$		0	0
$\hat{Q}_x$		0	0
$\hat{Q}_y$		$\hat{Q}_y$	0
$\hat{Q}_z$		0	0
$\hat{\Delta}$		0	0
z		$\hat{\Pi}_{xx}$	$-0.5\hat{\Pi}_{zz}$
	$\hat{\Pi}_{yy}$	$-0.5\hat{\Pi}_{zz}$	$\hat{\Pi}_{zz}$
	$\hat{\Pi}_{zz}$	$\hat{\Pi}_{zz}$	$\hat{\Pi}_{zz}$
	$\hat{\Pi}_{xy}$	0	0
	$\hat{\Pi}_{xz}$	0	$\hat{\Pi}_{xz}$
	$\hat{\Pi}_{yz}$	0	0
	$\hat{Q}_x$	0	0
	$\hat{Q}_y$	0	0
	$\hat{Q}_z$	$\hat{Q}_z$	0
	$\hat{\Delta}$	0	0

# Chapter 6. Numerical experiments on zeroth-order Euler-type systems of equation

In this chapter, we present the results for some of the well-known benchmark problems in one- and two-dimensional space. For the purpose of verifying the code and estimating the order of accuracy of the numerical scheme, we first solve a smooth problem with analytical solutions. We then investigate the widely studied Sod's shock tube problem in dusty gas flows with special emphasis on the complex wave behaviors therein. Finally, we solve two two-dimensional multiphase flows—explosion and compression corner problems—to highlight the effects of the dispersed phase (solid dust) on multi-dimensional dusty gas flow. In all test cases, the ratio of the specific heats of air ( $\gamma$ ) and the ratio of the specific heats of the two phases ( $c_m/c_v$ ) are set equal to 1.4 and 1.0, respectively. Unless otherwise mentioned, the following values are used for particle properties:

diameter,  $d=10 \mu\text{m}$ ;

mass density,  $\rho_s=2,500 \text{ kg/m}^3$ ;

specific heat,  $c_m=718 \text{ J/kg-K}$ .

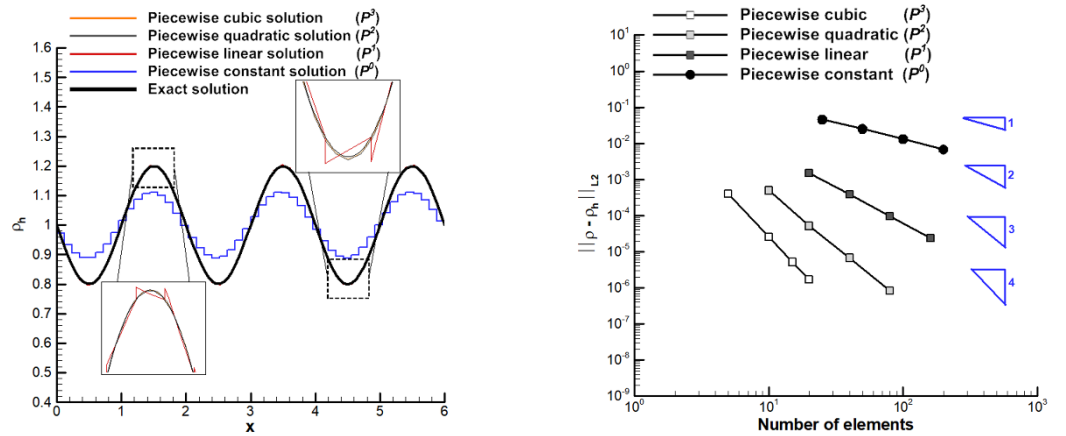
## 6.1 One-dimensional dusty gas flows

### 6.1.1 Verification study in the single-phase case (1-D)

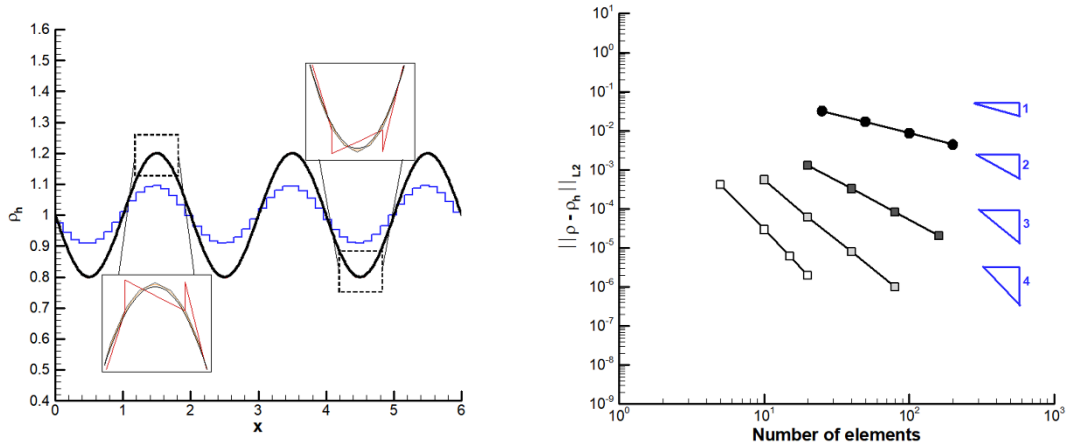
The propagation of a smooth sine wave (known as the entropy waves problem) was considered for verification of the code. The periodic boundary conditions were applied at both sides of the domain. For the following initial condition,

$$\begin{cases} u(x,0) = 1, \\ \rho(x,0) = 1.0 + 0.2\sin(\pi x), \\ p(x,0) = 1, \end{cases} \quad (205)$$

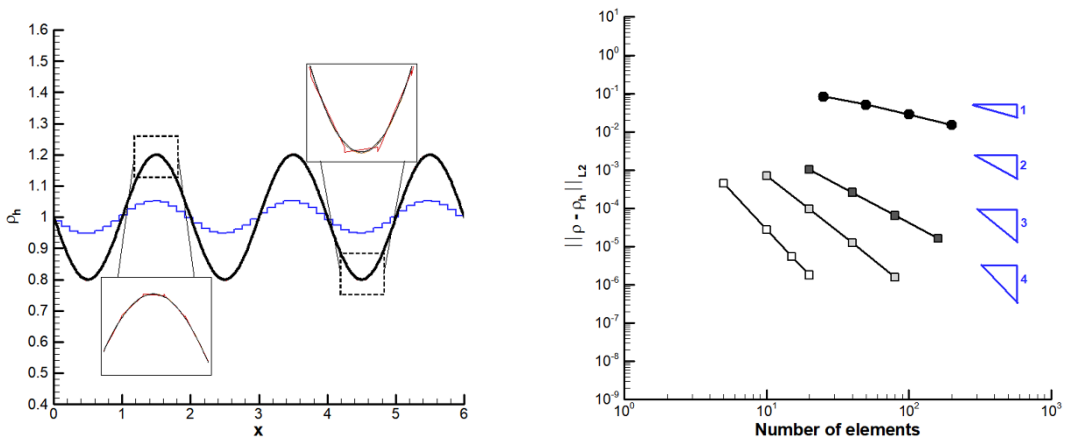
the corresponding exact solutions can be written as



**Roe flux function**



**HLL flux function**



**Rusanov (LLF) flux function**

**Fig. 27. Comparison of various numerical fluxes for smooth solution of Euler equation; (left) profile, (right) Euclidean norm of density**

$$\begin{cases} u(x,t) = 1, \\ \rho(x,t) = 1.0 + 0.2 \sin(\pi(x-t)), \\ p(x,t) = 1. \end{cases} \quad (206)$$

In order to measure the order of accuracy of the DG method for various flux functions, the density distribution of the solution was obtained for different orders of accuracy ( $P^\chi$ , with  $\chi$  indicating the polynomial order) and the results are shown in Fig. 27. It can be seen that numerical deviation from the analytical solution is large in the first-order piecewise constant case ( $P^0$ ); however, the application of more sophisticated numerical fluxes such as Roe and HLL can improve the accuracy of the piecewise constant solution.

In order to evaluate the performance of the numerical scheme in more detail, the numerical errors and the order of accuracy were calculated based on the density solution. The results were found to be consistent with the observations of Qiu *et al.* [220]. Moreover, it was confirmed that all numerical fluxes lead to the expected order of accuracy of  $P+1$ . It is worth noting that each flux function shows a different behavior in performance for different orders of polynomial function, and thus drawing a general conclusion is not possible.

### 6.1.2 Sod shock tube problem in dusty gas flows

Fig. 28 depicts the shock tube problem in single phase (pure gas) and multiphase (dusty gas). The evolution of various types of waves and discontinuities from the initial Riemann data can provide the essence of dusty gas flows; as, for example, the supersonic flows formed by the interaction of rocket plume and lunar dust. Moreover, the shock tube problem is ideal for examining the feasibility and validity of the new numerical methods, since it is free from boundary effects or other numerical complexities. The scheme tested

in the one dimension problem can also be extended to the multi-dimensional situation afterwards.

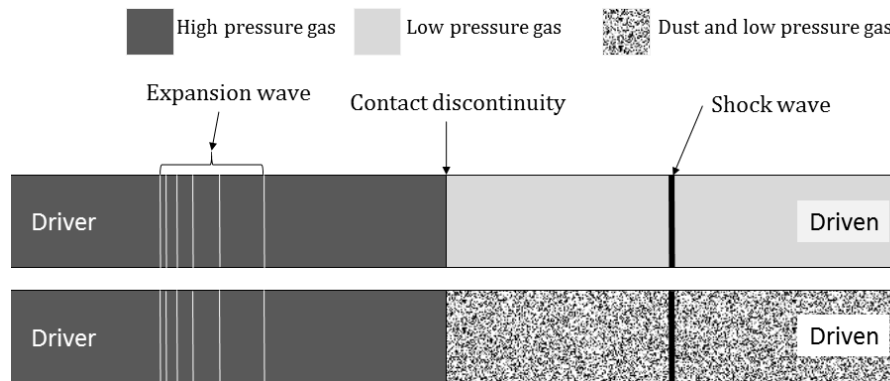


**Fig. 28. Schematic of the shock tube problem in dusty gas (pure gas versus dusty gas) (computational domain length: 100L)**

In order to obtain solutions without spurious oscillations, the positivity-preserving scheme was used in conjunction with the monotonicity-preserving limiter. It should be emphasized again that no extra effort is necessary for handling the source terms, thanks to the special feature associated with the orthogonal basis functions introduced in the new DG scheme, as explained in subsection 3.5. That is, the present DG method is immune to the artifact that may arise from splitting the source terms, or the complexity incurred by application of the fractional step approach [81, 221] or the random choice method [140] to cope with the source terms.

**Table 13. Initial condition for the Sod's shock tube problem**

Non-dimensional variable	Driver section	Driven section
Pressure	10.0	1.0
Gas density	10.0	1.0
Particle concentration	0.00001	1.0
Gas velocity	0.0	0.0
Dust velocity	0.0	0.0

The results of the dusty shock tube problem with the initial condition summarized in Table 1 are presented in Fig. 29. It can be seen that the numerical solutions of the pure gas are in good agreement with the analytical solutions of the shock tube problem. In the figures, the term ‘dusy gas’ implies the carrier gas phase. This problem has been previously investigated by Saito [75], Saito *et al.* [76] and Pelanti and LeVeque [80]. Comparison with these previous results can be used as verification of the present computational model of two-fluid dusty gas. The multiphase solutions clearly demonstrate the profound effects of the inertia of the dust particles on the flow properties. The gradual response of the dust particles to the diaphragm rupture was observed, especially in the velocity and temperature profiles. Interestingly, the strength of the right-running shock wave front was found to be much smaller than that of pure gas, which is due to the absorption of momentum and heat from the gas molecules by the dust particles. In addition, the deceleration of the shock wave front was observed from the velocity profile, inducing compression waves behind the shock wave. This phenomenon was identified in the pressure profiles as well.

### **6.1.3 Composite wave structures in the Sod problem of dusty gas flows**

In contrast to a single-phase flow, dusty gas flows can show some striking wave structures, which have no counterpart in classical theory. The physical explanation of these phenomena in dusty gas flows has rarely been addressed in the literatures. In this section, we provide a detailed discussion on the underlying physics forming these abnormal waves. Various wave structures that are formed in the shock tube problem of dusty gases are schematically illustrated using the  $x-t$  diagram in Fig. 30 (a) describes the case in which the contact discontinuity of gas and the boundary path of a particle are located at the same position, while Fig. 30 (b) describes the case in which the boundary path of a particle is located at a distance from the contact discontinuity of gas. When a shock wave impinges on a cloud of particles in dusty gas flows, it will be reflected as an expansion or shock

wave, depending on the ratio of the specific heats of the solid particle and gas, and the particulate loading of the mixture [67]. In this diagram, the case of reflected rarefaction waves was not considered, since the properties of the test case of the mixture correspond to the case of shock wave reflection. Since solid particles with non-negligible inertia cannot follow the abrupt changes of flow, a relaxation zone attached to the shock wave forms and the shock wave front decelerates until a new equilibrium condition is reached. The size of the relaxation zone is affected by the diameter of the solid particle, density, and heat capacity. As mentioned before, a finite time is required for the particles to fully attain the speed of the gas. During this period, reflected compression waves are generated from the boundary path of the particle, eventually forming a weak left-running shock wave, as illustrated in Fig. 30 (a).

For better clarification, we investigated in detail how the evolution of those waves is affected by the concentration of dust particles. We identified three abnormal behaviors based on the density profile: 1) the tail of the left-running rarefaction waves; 2) the region before the contact discontinuity; and 3) the tail of the right-running shock wave. It is well known that, after the diaphragm ruptures, a right-running compression wave and left-running rarefaction waves will start to propagate in the background medium. On the other hand, dust particles with different density ratios on each side of the diaphragm will lead to the existence of an extra contact discontinuity (in solid phase) compared to the case of pure gas. We refer to this discontinuity as the dust contact discontinuity (DCD).

The first composite wave structure, marked as number (1) in Fig. 31, was observed at the tail of the rarefaction waves in the density profile. This exotic structure should be distinguished from the numerical artifacts that may be found in high order methods when they are not treated properly. Due to the presence of dust particles, the rarefaction waves weaken and their propagation speed decreases as well. Therefore, gas will accumulate in

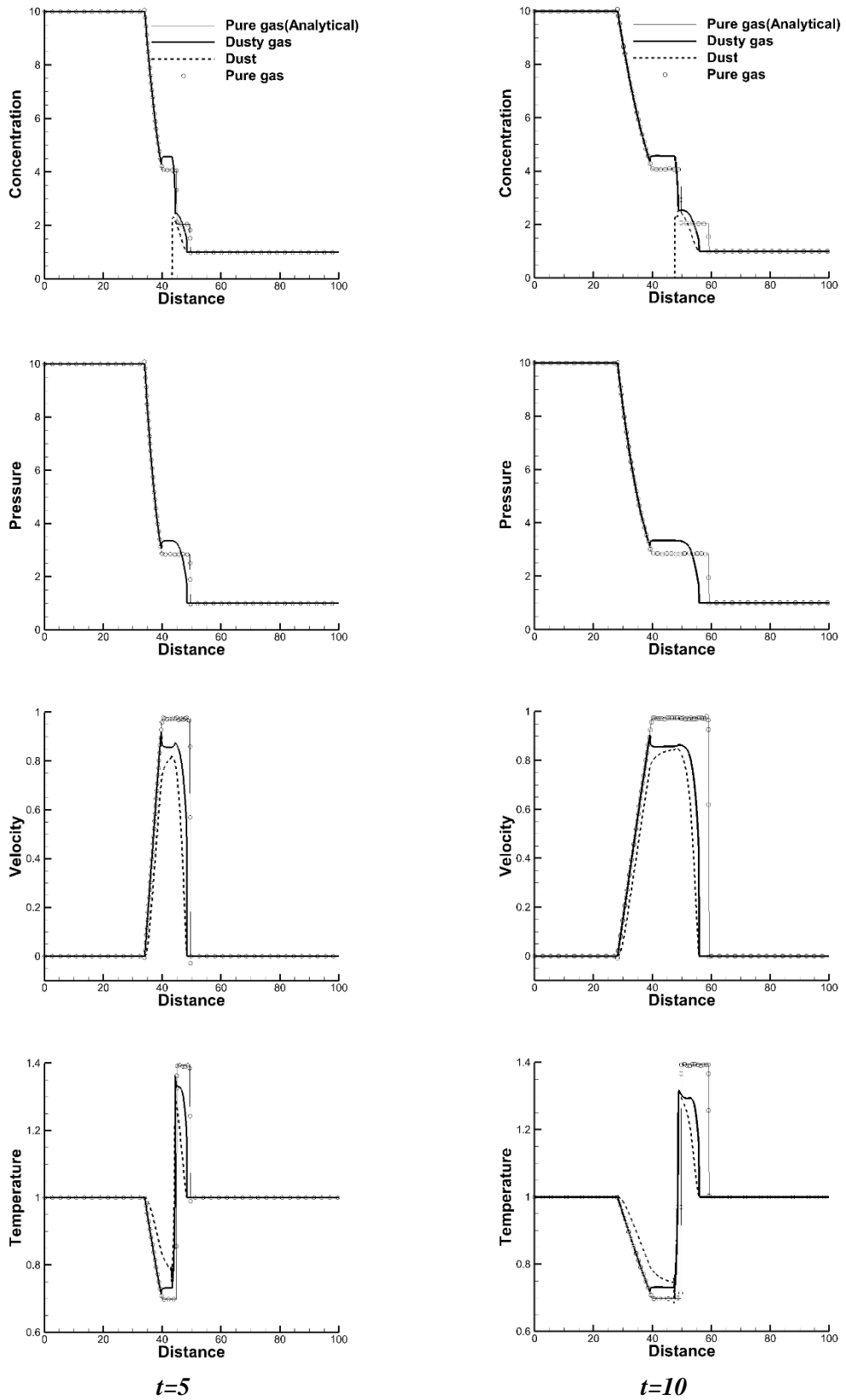


*Fig. 29. Solutions of the Sod's shock tube problem in dusty gas for two different time steps (P1 solution)*

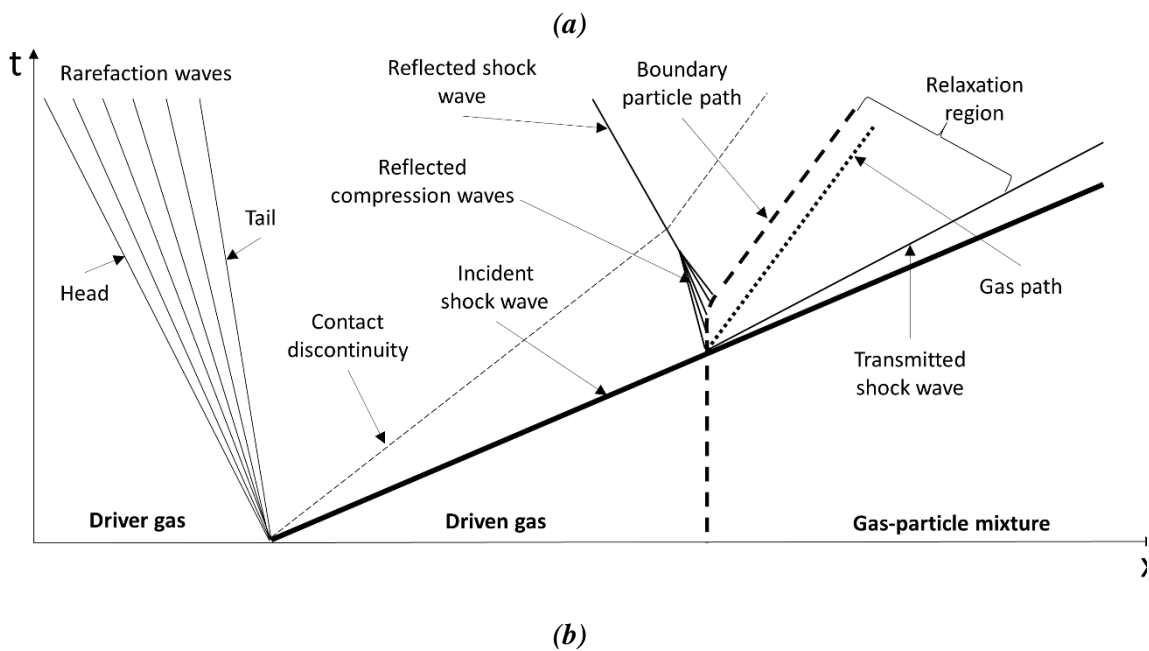
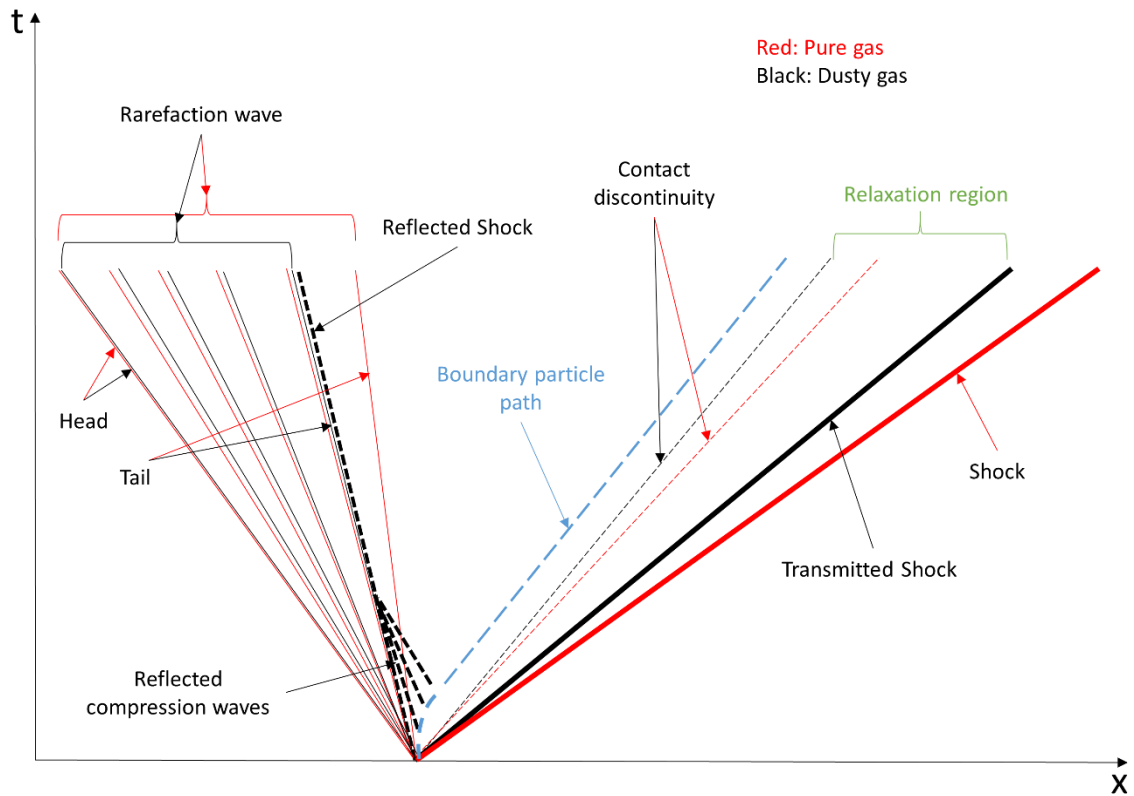


**Fig. 30. Schematic of various wave structures in the 1-D dusty gas flows: (a) The gas contact discontinuity and boundary particle path are initially located at the same position, (b) The particle boundary path is located at a distance from the gas phase contact discontinuity.**

the region close to the tail of the rarefaction waves, and the reflected compression waves generated from the boundary path of the dust particle will form a weak shock wave attached to the tail of the left-running rarefaction waves, as observed in Fig. 31 (a).

This weak shock wave is directly related to the presence of the DCD and it will be strengthened when the dust concentration increases. It will be shown in a later figure that, when there is no DCD, i.e., when both the high and low pressure sections are filled with the same dust concentration, this composite wave structure will disappear. In passing, it should be mentioned that this type of composite waves is different from the generic compound waves observed in magneto-hydrodynamics, due to the non-convexity and the non-strict hyperbolicity [222], and the present waves should be called composite waves or pseudo-compound waves, rather than compound waves.

In another region, marked number (2) in Fig. 31, the presence of dust induces an increase in pressure (and a decrease in velocity) in the middle region, leading to higher density compared to the case of pure gas. It turns out that this increase in density is dependent on dust concentration, as well as the location of the DCD.

A second composite wave structure, marked number (3) in Fig. 31, was observed at the tail of the shock wave. It consists of a right-running shock wave followed by a relaxation zone. When there is no particle, the shock wave is steep and strong as expected. When particles are present, however, the shock wave weakens substantially and the relaxation zone forms instead, due to the coupling effects between the two phases. We can clearly see that a higher particle concentration leads to a larger relaxation zone and a reduction in the propagation speed of the shock wave. It will be shown in the next figure that the location of the DCD changes the position where the shock wave forms, but does not affect the size of the relaxation zone.

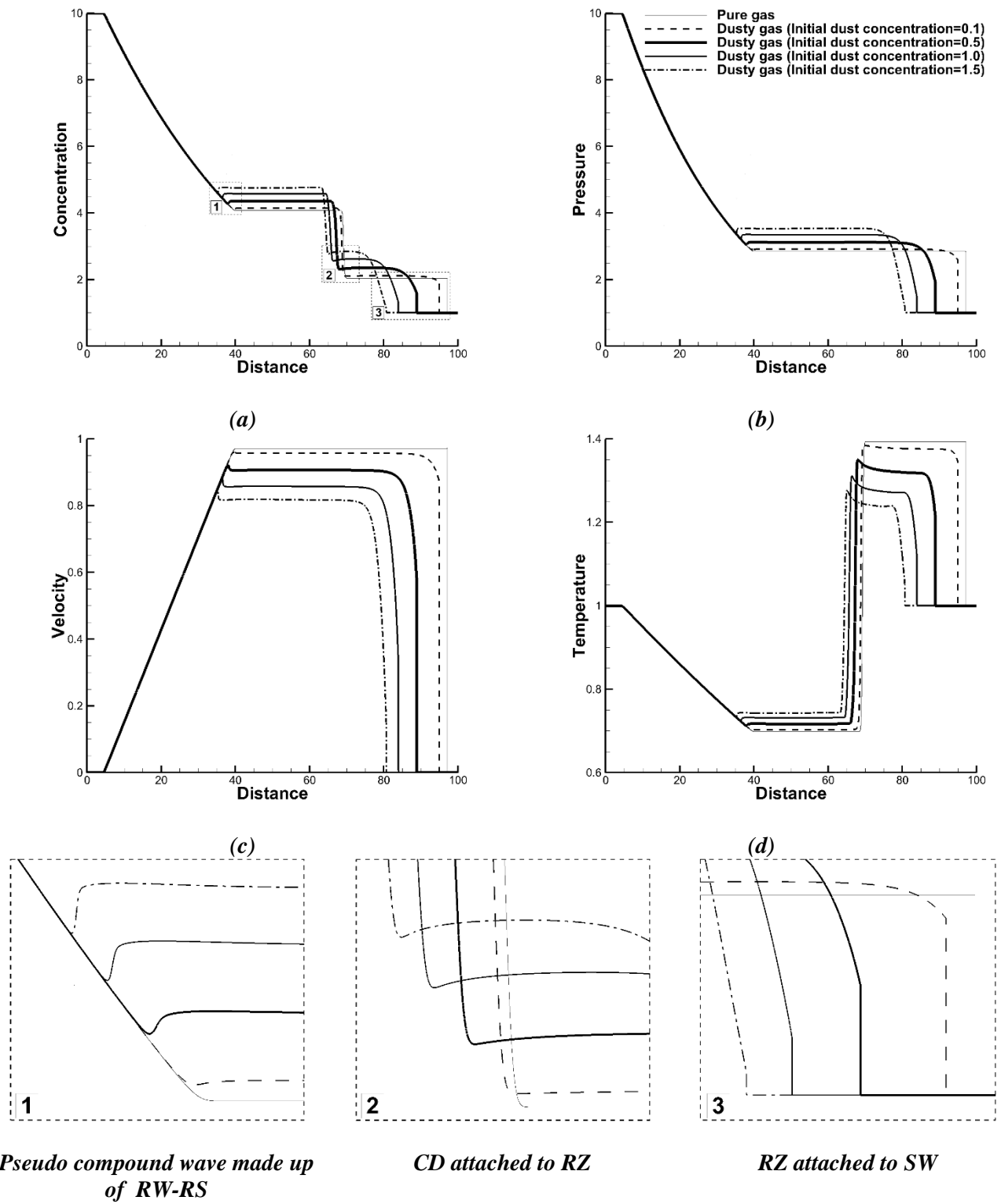
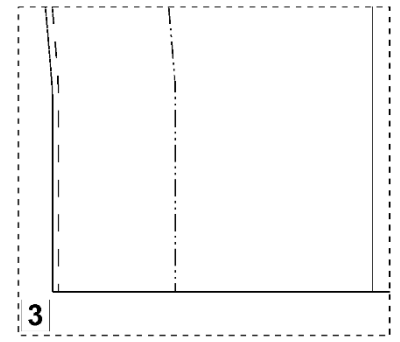
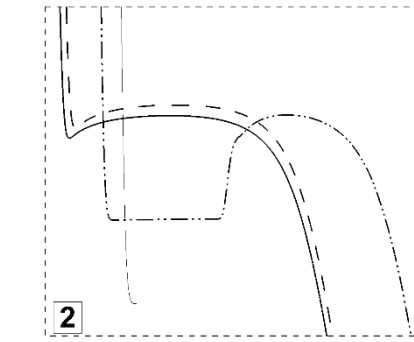
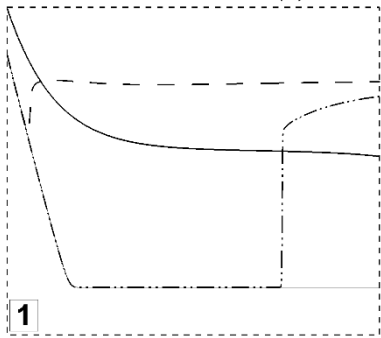
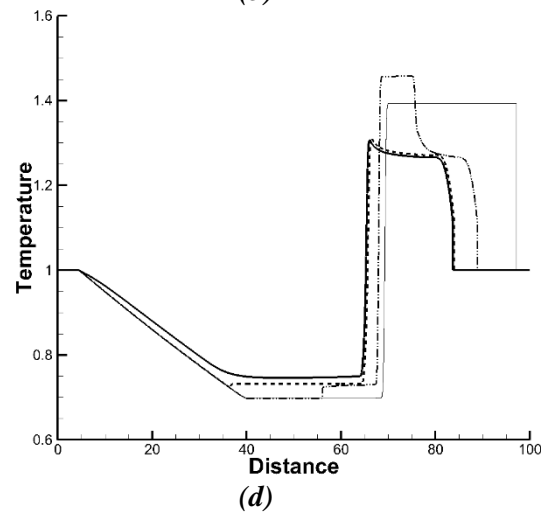
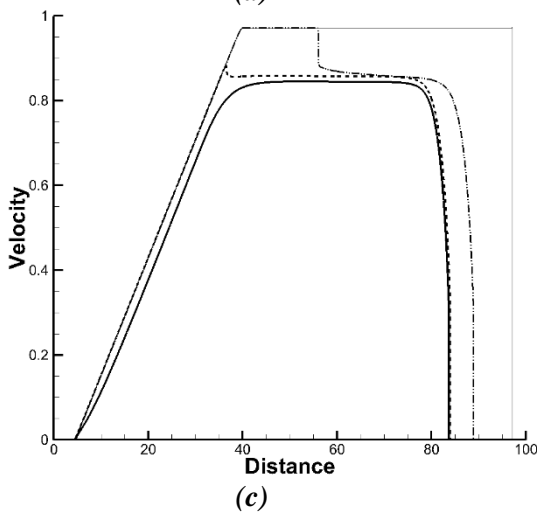
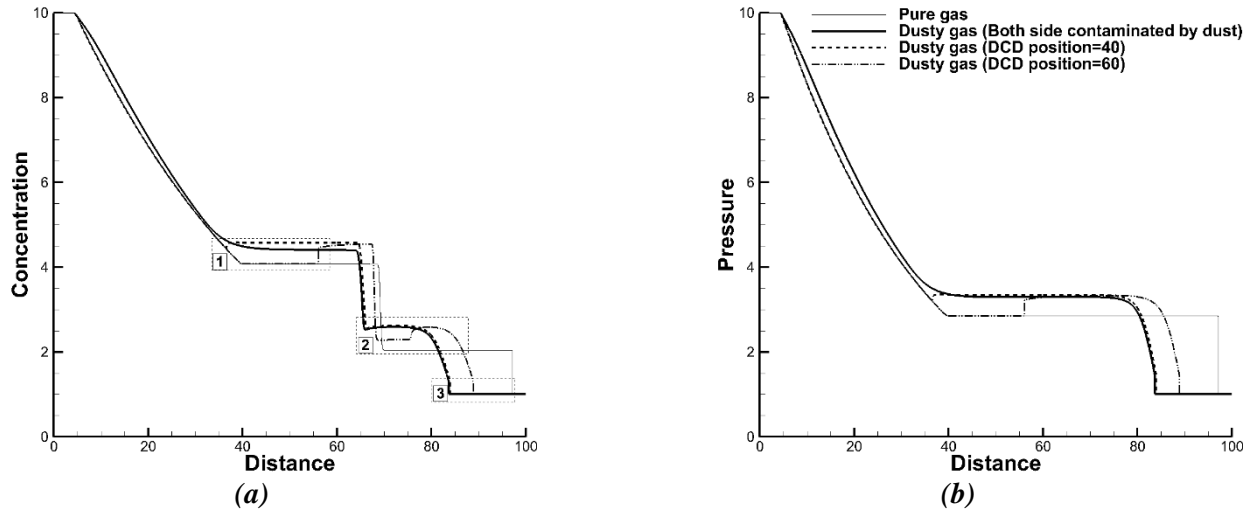


**Fig. 31. Effects of initial dust concentration on the Sod's shock tube in the dusty gas ( $P^1$  solution) (RW: rarefaction wave, RS: reflected shock, CD: contact discontinuity, RZ: relaxation zone, SW: shock wave )**



**1**  
*Pseudo compound wave made up of RW-RS*

**2**  
*CD attached/detached to/from RZ*

**3**  
*RZ attached to SW*

**Fig. 32.** Effects of location of the initial dust contact discontinuity (DCD) on the Sod's shock tube in the dusty gas at  $t=30$  ( $P^I$  solution)  
(RW: rarefaction wave, RS: reflected shock, CD: contact discontinuity, RZ: relaxation zone, SW: shock wave)

In order to investigate how the DCD would affect wave patterns in the dusty gas flows, additional cases were simulated by varying the position of the DCD (from  $x=40$  to  $x=60$ ) while maintaining the same dust concentration, as shown in Fig. 32. The other profiles in

this figure correspond to the pure gas and the dusty gas case of the previous figure. In all cases, the dust concentration is assigned with the same value ( $\alpha_0\rho_0=0.1$ ). In the region marked number (1), the weak discontinuity in density, pressure and temperature profiles discussed in Fig. 31 vanishes when there is no DCD. When the DCD is shifted towards the right end of the tube ( $x=60$ ), the discontinuity is detached from the rarefaction waves and is shifted to the right as well.

In the region marked number (2), the shifted DCD seems to produce yet another contact discontinuity (around  $x=70$ ) attached to the relaxation zone. When put together with adjacent waves, there seems to be a new composite wave structure, consisting of three waves—a contact discontinuity, the relaxation zone, and a shock wave. On the other hand, as can be seen in region number (3), the strength of the right-running shock wave and the size of the relaxation zone remain the same for all dusty gas cases, though the position of the waves is shifted as expected.

## 6.2 Two-dimensional dusty gas flows

### 6.2.1 Verification study in the single-phase case (2-D)

In order to examine the order of the accuracy of the developed method, the propagation of a smooth sine wave in a two-dimensional domain was considered. The periodic boundary conditions were applied at all sides of the square domain as shown in Fig. 33(a).

For the following initial condition,

$$\begin{cases} u(x, y, 0) = 1, \\ v(x, y, 0) = 1, \\ \rho(x, y, 0) = 1.0 + 0.2 \sin[\pi(x + y)], \\ p(x, y, 0) = 1. \end{cases} \quad (207)$$

the corresponding exact solutions can be written as

$$\begin{cases} u(x, y, 0) = 1, \\ v(x, y, 0) = 1, \\ \rho(x, y, 0) = 1.0 + 0.2 \sin[\pi(x + y - t)], \\ p(x, y, 0) = 1. \end{cases} \quad (208)$$

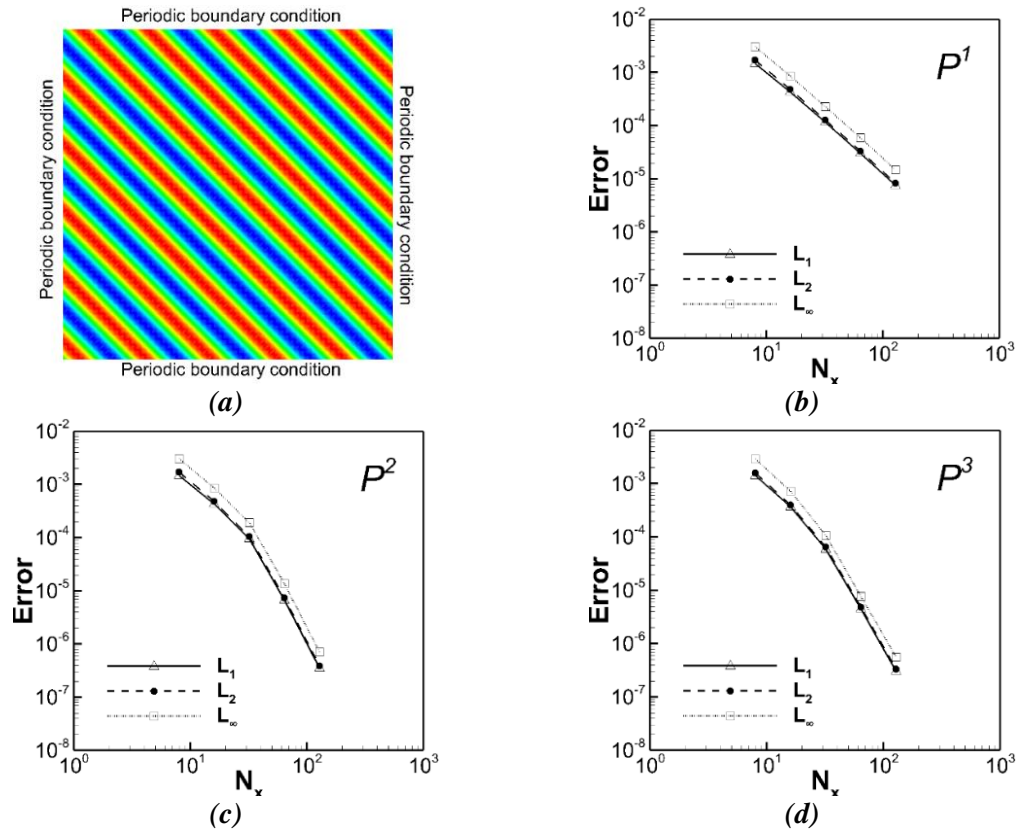


**Fig. 33** Analysis of the order of the accuracy of the two-dimensional code for a smooth sine function problem

The error norms for density solutions up to fourth-order accuracy ( $P^3$ ) are calculated and summarized in Fig. 33 (b-d) Table 14. It can be seen that the desired order of accuracy is achieved. For fine grids, the actual order is shown to be higher than the nominal order of accuracy.

**Table 14 Accuracy analysis for 2D entropy waves.**

$P^1$							
$\Delta X$	$N_x$	L <sub>1</sub> error	L <sub>2</sub> error	L <sub>∞</sub> error	L <sub>1</sub> order	L <sub>2</sub> order	L <sub>∞</sub> order
1.25	8	1.47E-03	1.72E-03	3.09E-03	-	-	-
0.625	16	4.33E-04	4.84E-04	8.65E-04	1.764	1.829	1.835
0.3125	32	1.16E-04	1.29E-04	2.30E-04	1.896	1.912	1.914
0.15625	64	3.01E-05	3.31E-05	5.92E-05	1.951	1.955	1.956
0.078125	128	7.64E-06	8.40E-06	1.50E-05	1.979	1.980	1.980
$P^2$							
$\Delta X$	$N_x$	L <sub>1</sub> error	L <sub>2</sub> error	L <sub>∞</sub> error	L <sub>1</sub> order	L <sub>2</sub> order	L <sub>∞</sub> order
1.25	8	1.47E-03	1.72E-03	3.09E-03	-	-	-
0.625	16	4.33E-04	4.84E-04	8.65E-04	1.764	1.830	1.835
0.3125	32	9.60E-05	1.06E-04	1.92E-04	2.174	2.197	2.172
0.15625	64	6.77E-06	7.44E-06	1.38E-05	3.827	3.825	3.801
0.078125	128	3.55E-07	3.91E-07	7.06E-07	4.251	4.249	4.286
$P^3$							
$\Delta X$	$N_x$	L <sub>1</sub> error	L <sub>2</sub> error	L <sub>∞</sub> error	L <sub>1</sub> order	L <sub>2</sub> order	L <sub>∞</sub> order
1.25	8	1.43E-03	1.59E-03	2.90E-03	-	-	-
0.625	16	3.69E-04	4.03E-04	7.30E-04	1.959	1.980	1.990
0.3125	32	5.90E-05	6.50E-05	1.09E-04	2.643	2.633	2.744
0.15625	64	4.47E-06	4.91E-06	7.75E-06	3.725	3.728	3.813
0.078125	128	3.06E-07	3.37E-07	5.68E-07	3.866	3.863	3.771

## 6.2.2 2-D explosion problem in dusty gas flows

As the first two-dimensional test case, we investigated the explosion problem outlined in Toro [200] for a pure gas. This problem is in essence the two-dimensional extension of the classical Sod's shock tube, as illustrated in Fig. 34.

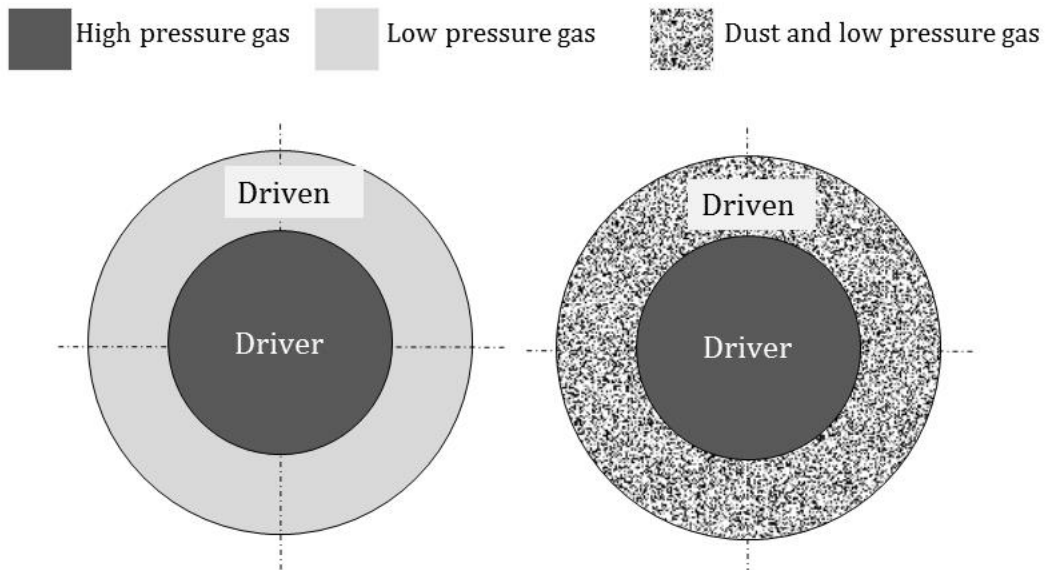


**Fig. 34. Schematic of the pure gas (left) and dusty gas (right) 2-D explosion problems (outer radius:  $L$ )**

The initial conditions for the single-phase and multiphase cases are summarized in Table 2.

A study on grid independency is presented in Fig. 35 where five different grids with mesh sizes of  $h=1/20$ ,  $1/40$ ,  $1/80$ ,  $1/120$  and  $1/160$  are considered, where  $h$  is the characteristic size of grid. A grid resolution with  $h=1/120$  was found to provide almost identical results with  $h=1/160$ , and hence this grid was used for the rest of simulations.

In the next step, the effects of the polynomial order of the DG method was examined with and without the monotonicity preserving limiter for the single-phase problem, while the positivity preserving limiter was applied for all cases. It can be seen in the left column of Fig. 36 that, without the monotonicity preserving limiter, the second- and third-order solutions exhibit severe oscillations near strong waves. The Barth-Jespersen limiter described in subsection 3.3, however, was shown to handle the non-physical oscillations effectively, as confirmed in the right column of Fig. 36. Our numerical experiments showed that such oscillations lead to a breakdown of the numerical code, in the case of high CFL numbers, or when multiphase problems are solved without proper monotonicity preserving limiters. The judicious use of limiters specially developed for the DG method, along with

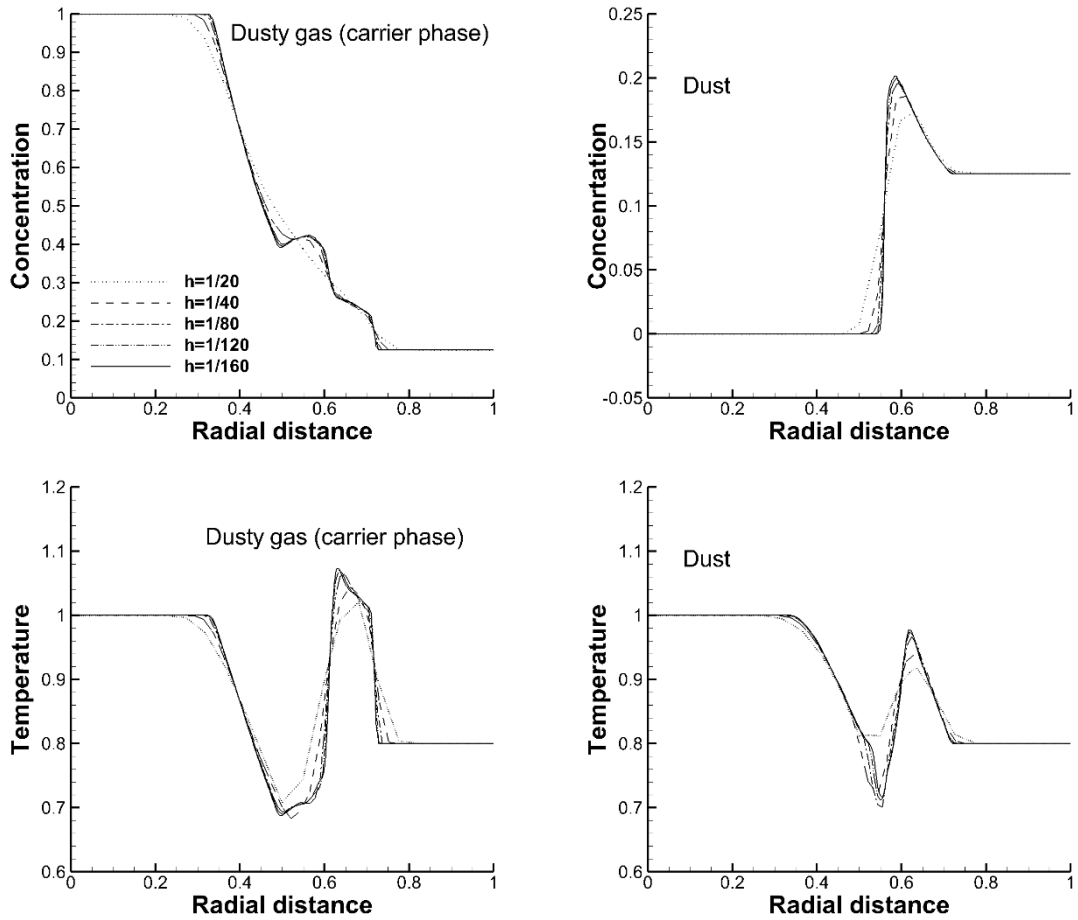


**Fig. 35. Grid independency test for the explosion test case (P<sup>1</sup> solution)**

the discontinuity detection scheme, is believed to be key factors in the successful shock capture with a minimum penalty in accuracy.

In addition, we investigated the evolution of the gas and solid phase concentrations, as summarized in Fig. 37 and Fig. 38. The initial conditions for this multiphase case are given in Table 15. The physical justifications obtained from the one-dimensional Sod's shock tube in dusty gas flows hold true here. That is, the presence of dust particles leads to a weakened shock wave whose front is cut by the relaxation zone. Moreover, for the same reason, the shock wave front decelerates substantially as time elapses.

*Table 15. Initial condition for the explosion problem*

Non-dimensional variable	Driver section	Driven section
Pressure	1.0	0.1
Gas density	1.0	0.125
Particle concentration	0.00001	0.1
Gas velocity	0.0	0.0
Dust velocity	0.0	0.0

### **6.2.3 Asymmetric explosion problem in dusty gas flows**

With the same initial data applied to the 2-D explosion problem in dusty gas flows in the previous section and with specifying a square area in the low-pressure section the problem will be asymmetric explosion problem. The solutions will be more complicated when there is no radial symmetry, such as the rectangular case shown in Fig. 15. This non-radial symmetrical multiphase explosion problem was suggested by Saito [75], primarily to examine the ability of the numerical method to capture more complicated flow patterns. The contours of the evolution of pure gas, dusty gas, and dust concentrations evolutions are depicted in the figure. Conclusions similar to those of the previous radial symmetrical multiphase explosion problem can be drawn.

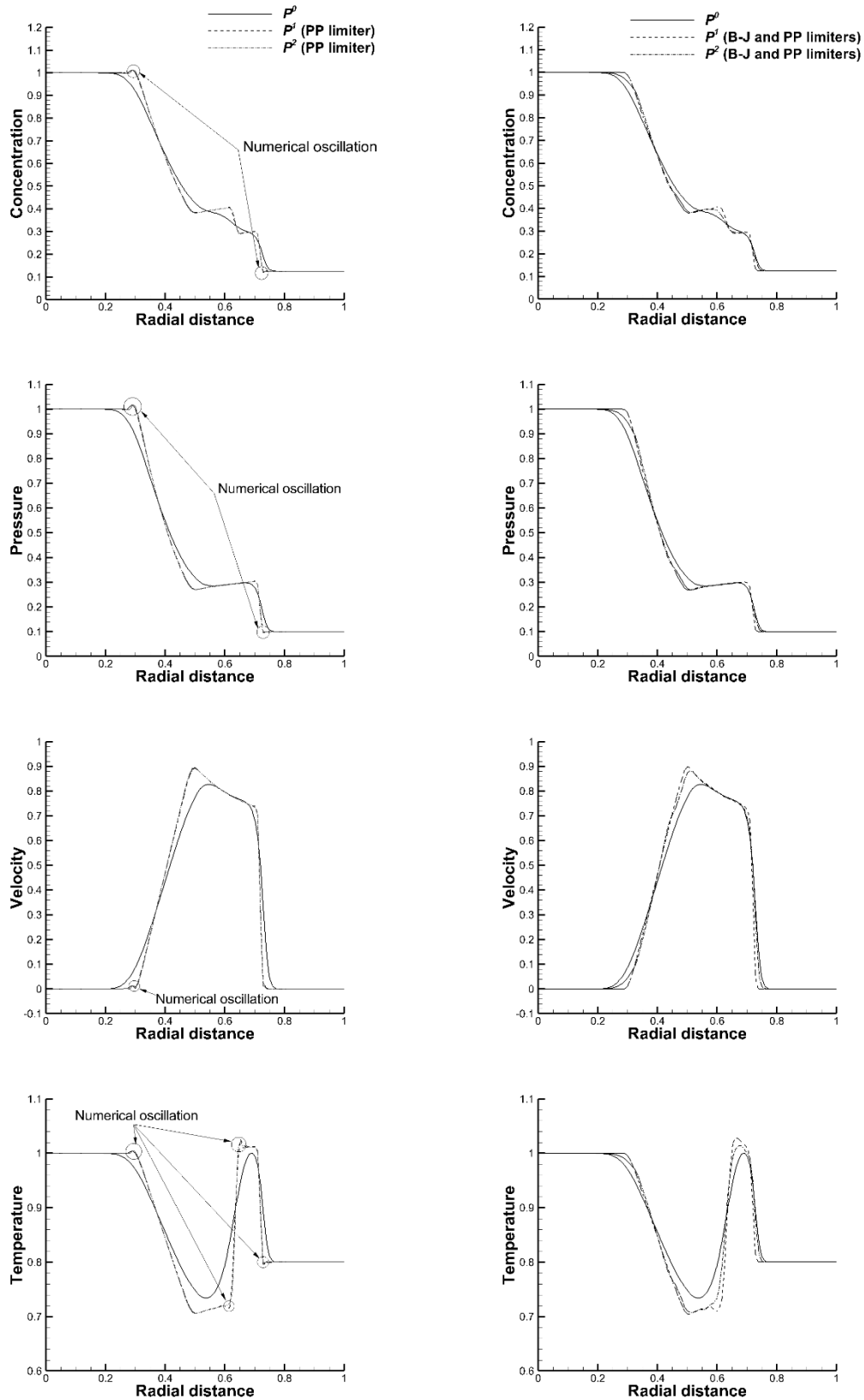


**Fig. 36. High order solutions of the explosion problem for pure gas ( $h=1/100$ ,  $t=0.2$ ) Without monotonicity preserving limiter (left); with monotonicity preserving limiter (right) ( $P^1$  solution)**

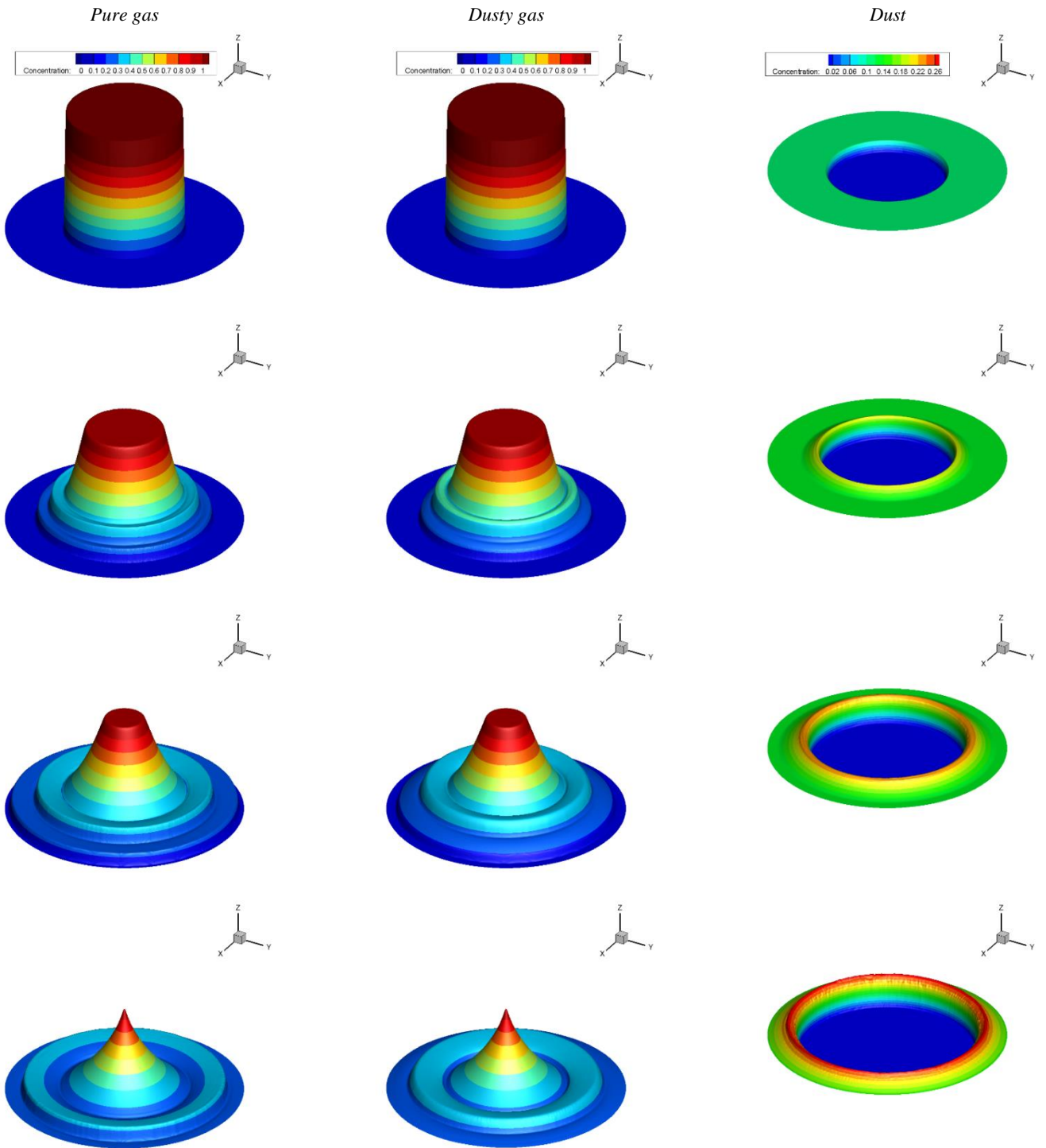
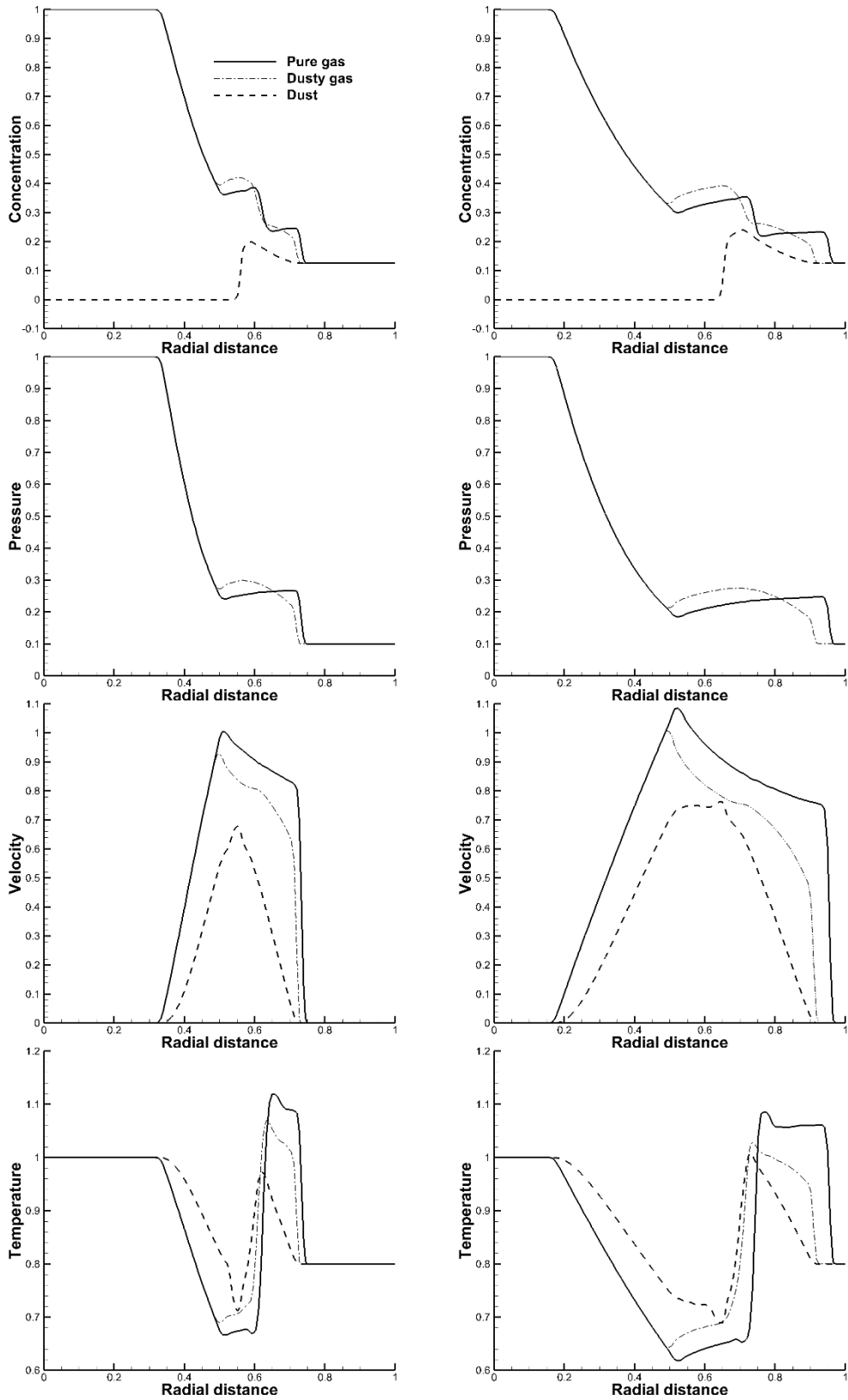


*Fig. 37. Graphical presentation of time evolution of density in the multiphase explosion problem ( $P^1$  solution)*



$t=5$

$t=10$

Fig. 38. Time evolution in the multiphase explosion problem ( $P^1$  solution)

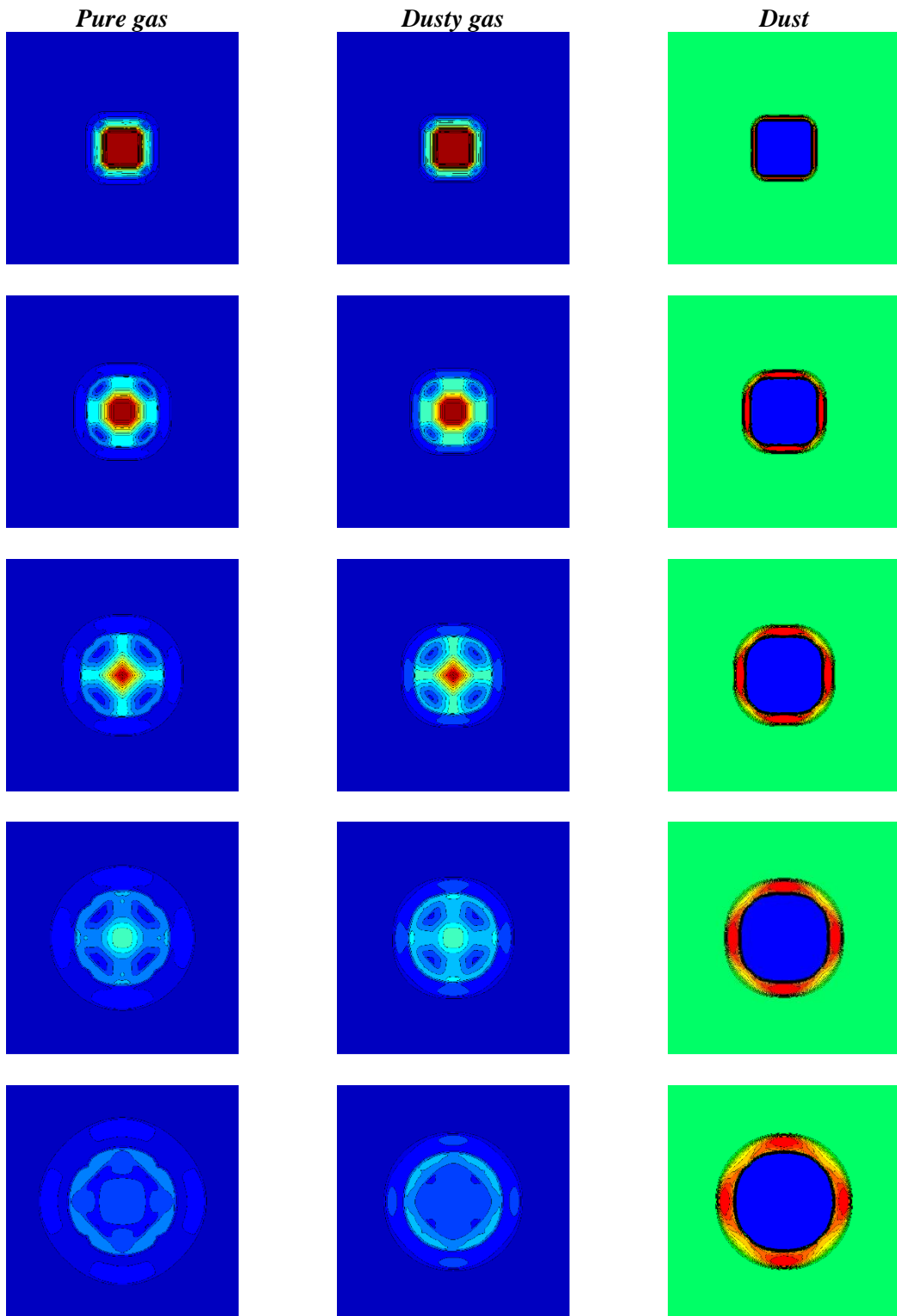


*Fig. 39. Time evolution of density in the rectangular multiphase explosion problem ( $P^I$  solution)*

### 6.2.4 2-D compression corner problem in dusty gas flow

As the second two-dimensional benchmark problem, we investigated the compression corner problem for both the single and multi-phase applications. This problem is far more complicated due to the presences of boundary effects and the intrinsic complexity of the flow. The incident shock Mach number  $M_s$ , the wall inclination angel  $\theta_w$ , and the initial condition of driven and driver sections define the governing physics of the shock-wave diffraction. The schematic of the compression corner problem is illustrated in Fig. 40.

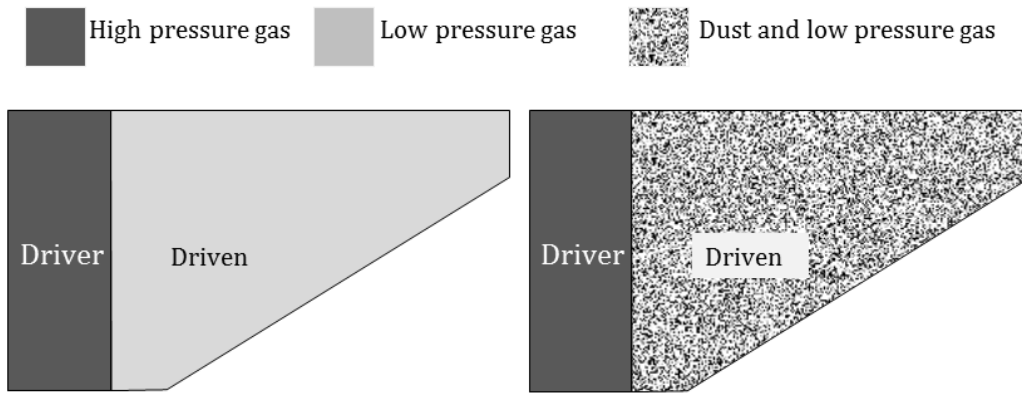
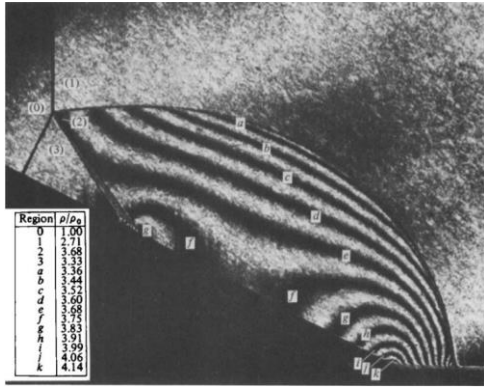


**Fig. 40. Schematic of the pure gas (left) and dusty gas (right) 2-D compression corner problems (computational domain size:  $5L \times 4L$ )**

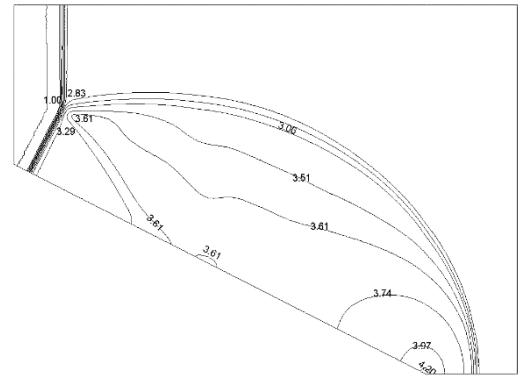
As a validation study, we compared our numerical solutions with the experimental results obtained by [139] for the case of a single Mach reflection (SMR). The initial condition are for both the single-phase and multiphase cases are provide in Table 16.

**Table 16. Initial condition for the single Mach reflection problem**

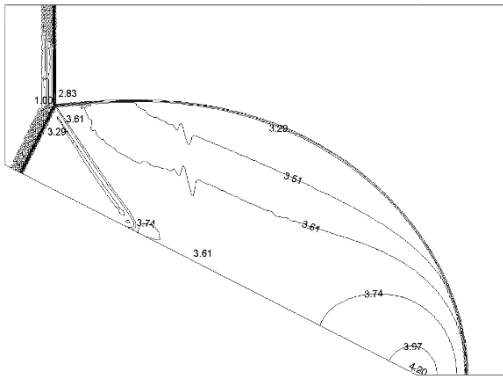
Non-dimensional variable	Driver section	Driven section
Pressure	4.64	1.0
Gas density	2.71	1.4
Particle concentration	0.1	0.1
Gas velocity ( $x$ -direction)	1.51	0.0
Gas velocity ( $y$ -direction)	0.0	0.0
Dust velocity ( $x$ and $y$ -directions)	0.0	0.0



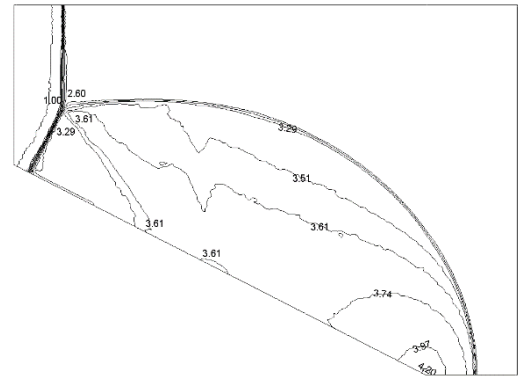
Experimental image [139]



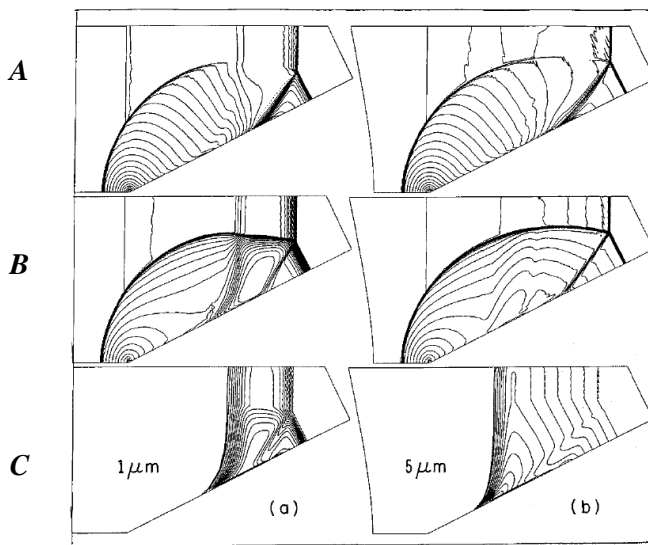
$P^0$  solution



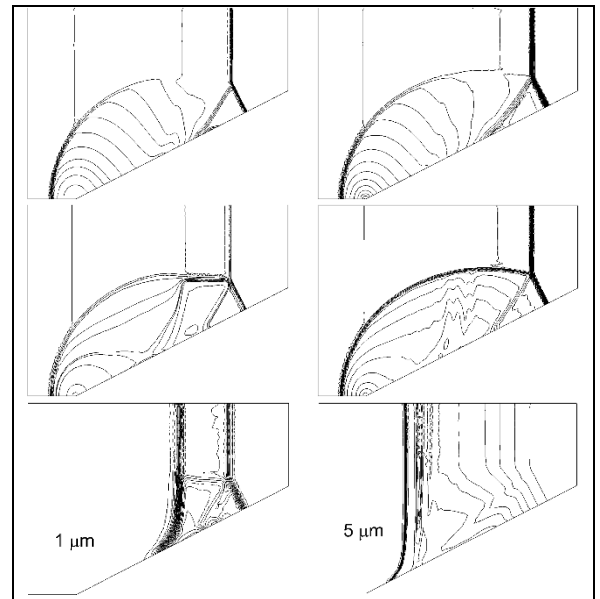
$P^1$  solution



$P^2$  solution



Ben-Dor et al. [133]



Present result ( $P^1$  solution)

Fig. 41. Validation of pure gas case (Isopycnics for single Mach reflection:  $M_s=2.03$  and  $\theta_w=27^\circ$ ) and verification of dusty gas case (A-constant flow Mach number contours, B-constant gaseous phase density contours, and C-constant dust phase spatial density)

The incident shock Mach number is set to 2.03, and the corner wedge angle is given by  $27^\circ$ . Numerical solutions, up to the third order of accuracy, were in good agreement with experimental data, as shown in Fig. 41. We confine our validation to a single-phase SMR case, since no experimental data are available in the case of dusty gas flows. The comparison shows that the solutions up to third order accuracy (P2) are in good agreement with the experimental data. Also, we verified the dusty gas results with the solutions of [133] for two particle diameters ( $1\ \mu\text{m}$  and  $5\ \mu\text{m}$ ) in the case of SMR. The comparison of Mach contours as well as isopycnic surfaces of gas and dust densities indicates a good agreement.

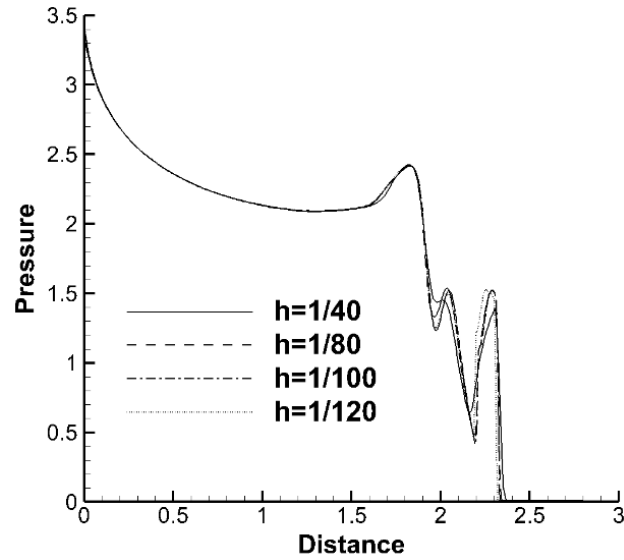
Furthermore, a very strong shock wave case studied by Woodward and Colella [223] was investigated. The problem, a strong Mach 10 shock impinging on a wall inclined at  $30^\circ$ , was known to lead to a complicated double Mach reflection (DMR). The initial conditions for both the single-phase and multiphase cases are summarized in Table 17.

*Table 17. Initial condition for the double Mach reflection problem*

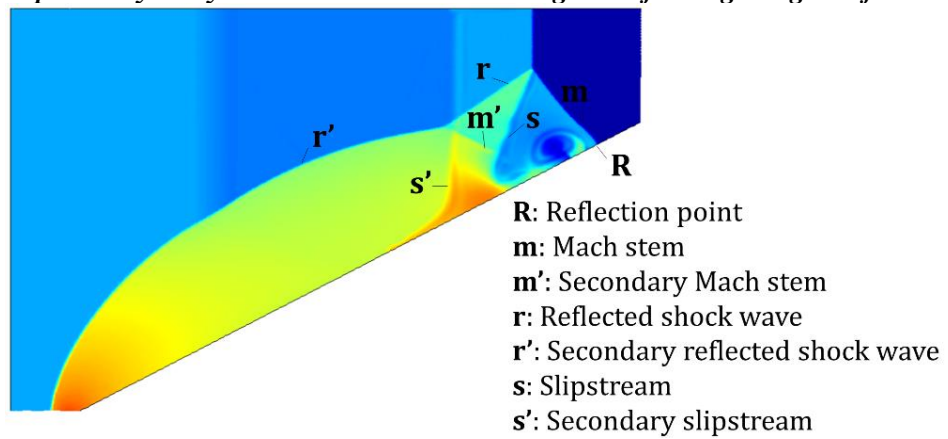
Non-dimensional variable	Driver section	Driven section
Pressure	116.5	1.0
Gas density	8.0	1.4
Particle concentration	0.1	0.1
Gas velocity ( $x$ -direction)	8.25	0.0
Gas velocity ( $y$ -direction)	0.0	0.0
Dust velocity ( $x$ and $y$ -directions)	0.0	0.0

In Fig. 42 (a), a study on grid independency was done for solutions with the second order of accuracy ( $P^1$ ). A grid resolution with  $h=1/100$  was found to provide almost identical results with  $h=1/120$ , and hence the grid with  $h=1/100$  was used throughout. The density and Mach contours at non-dimensional time  $t=200$ , as shown in Fig. 42 (b) and (c), indicated that the present DG scheme successfully resolves all the important flow features:

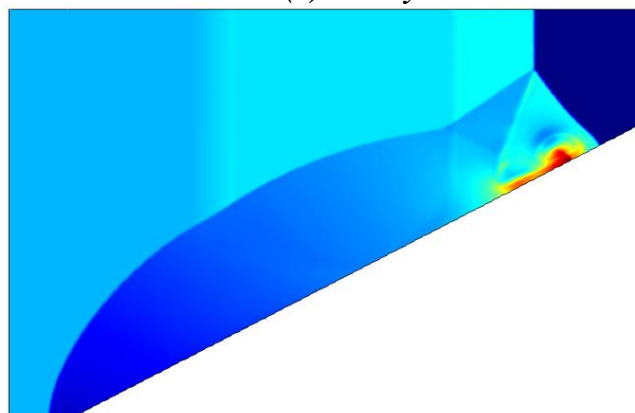
slip lines, Mach stem, secondary Mach stem, reflected shock wave, and the formation of supersonic flow in the delta region. A weak jetting effect reported in Ben-Dor *et al.* [133] was also observed.



(a) Grid independency study: Pressure distribution along the reflecting wedge surface



(b) Density contour

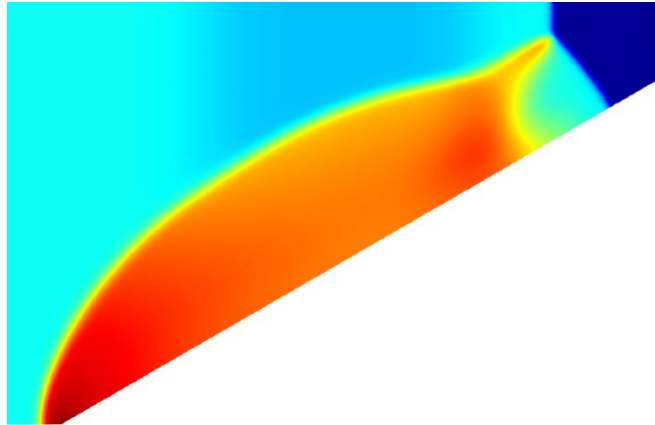


(c) Mach contour

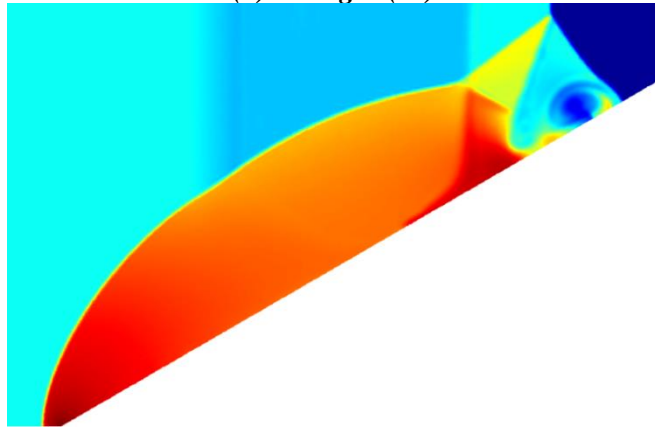
Fig. 42. Verification study: Double Mach reflection (pure gas  $P^I$  solution)

The effects of polynomial order on numerical solutions were analyzed in Fig. 43. It can be clearly seen that the first-order solution with  $h=1/100$  cannot resolve the expected flow feature properly. However, higher order solutions can provide a satisfactory resolution to accurately explain the important physical features of the flow. It can also be seen that there is no drastic change in solutions when increasing the polynomial order from one (P1) to two (P2). It should be mentioned that the application of the positivity preserving scheme is necessary to prevent numerical instabilities in this high Mach number flow.

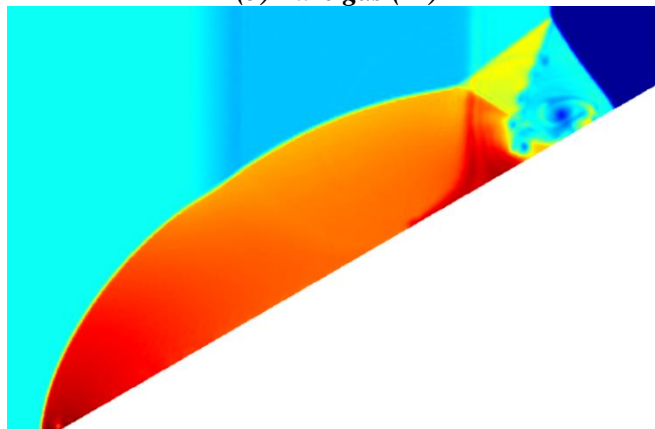
In order to understand the effects of dust particles on the time evolution of the flow, the single-phase and multiphase solutions (pure gas, dusty gas, and dust concentration) are summarized in Fig. 44 for two different time steps. One of the main features of the dusty gas flows is that the transition region in the shock waves is much thicker than that of the pure gas. In the multiphase flow, as the shock front is decelerated due to interaction with particles, a longer time is required for the shock front to reach the same location when there is no particle in the flow field. It is also evident that the presence of the particles can lead to attenuation of the incident shock wave. It should be mentioned that both the positivity and monotonicity preserving limiters were applied in the simulation of multiphase flows to prevent the numerical breakdown.



(a) *Pure gas (P<sup>0</sup>)*



(b) *Pure gas (P<sup>1</sup>)*



(c) *Pure gas (P<sup>2</sup>)*

*Fig. 43. Effects of polynomial orders on the density contours*

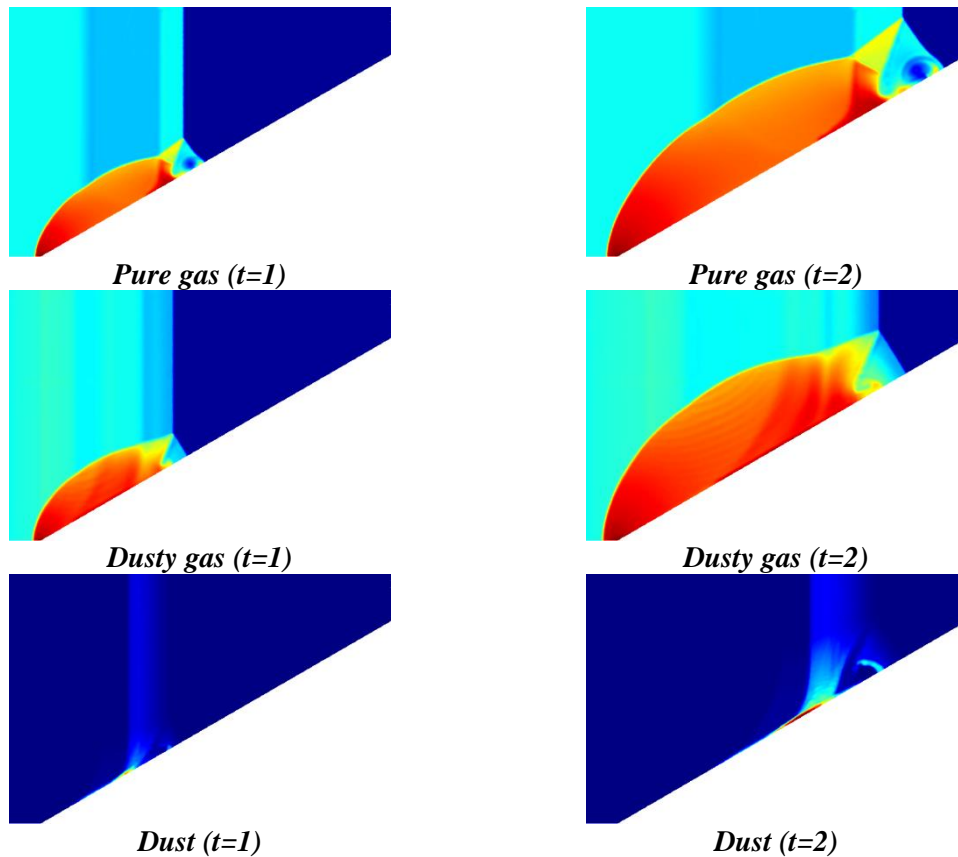
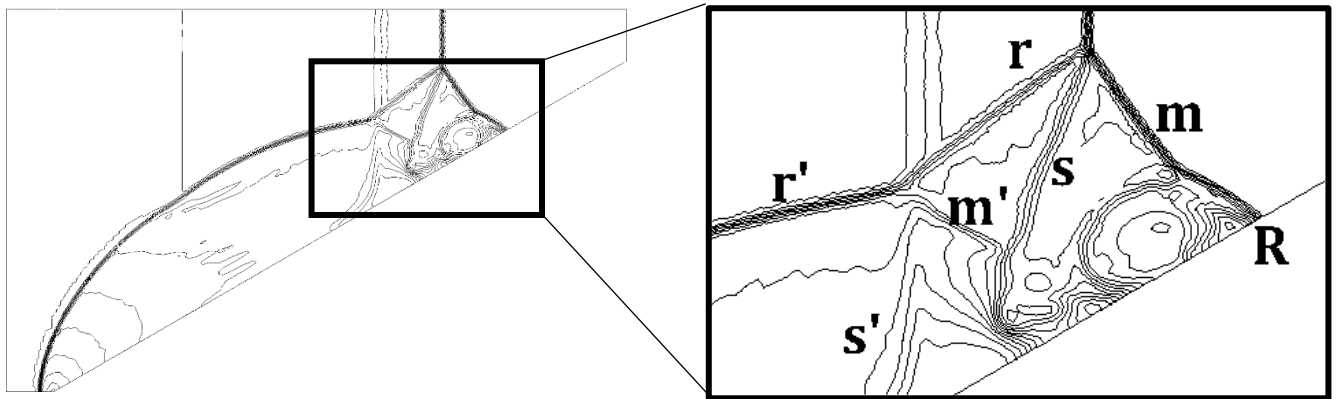
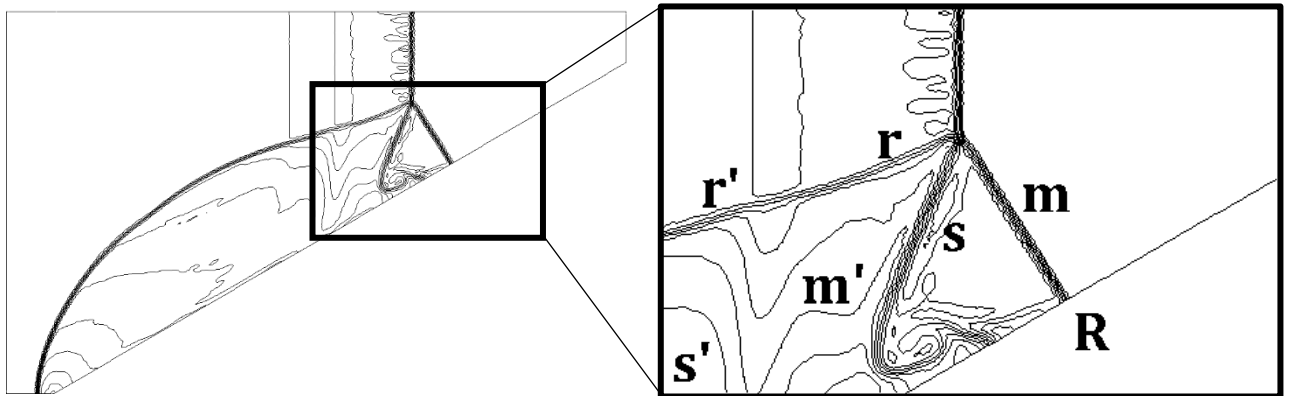


**Fig. 44. Time evolution of density contours in the compression corner (double Mach reflection) problem ( $P^I$  solution)**

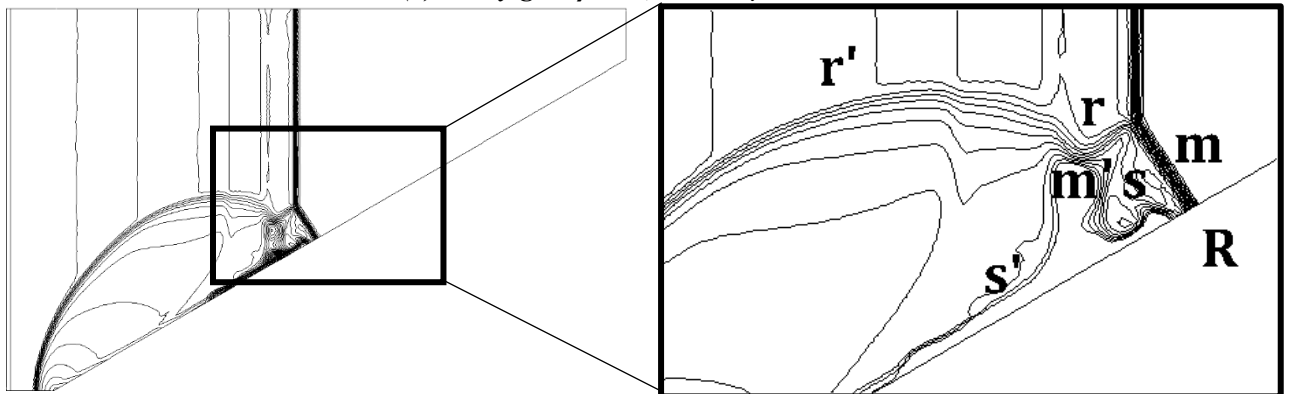
The effects of dust particles on the structure of the DMR were also investigated, as summarized in Fig. 45. The convex shape of the Mach stem in the pure gas simulation is due to the front of the curled slipstream reaching the Mach stem [224]. The presence of particles, however, decelerates the velocity of the slipstream front and does not allow the slipstream to catch up with the Mach stem, as shown in Fig. 45 (b) of the multiphase case with a particulate loading  $\beta=0.1$  and a particle diameter  $10 \mu\text{m}$ . As a result, the Mach stem forms almost perpendicular to the reflecting wall surface in the dusty gas case. The secondary reflected shock wave and slipstream are severely distorted so that they are not clearly identified. Moreover, the secondary triple point configuration, in which the secondary reflected shock wave, Mach stem and slipstream coincide undergoes a significant change so that such a point is almost indistinguishable.



(a) Pure gas



(b) Dusty gas:  $\beta=0.1$ ,  $d=10.0 \mu\text{m}$



(c) Dusty gas:  $\beta=0.5$ ,  $d=0.5 \mu\text{m}$

**Fig. 45. Change of the DMR structure in presence of dust particles ( $P^I$  solution)**

Another dusty gas case with a particulate loading  $\beta=0.5$  and a particle diameter  $0.5 \mu\text{m}$  was considered. Such a setting leads to a greater number of particles in the domain compared to the previous case. It can be seen in Fig. 45 (c) that, unlike the previous case in which only the secondary triple point is subject to major change, both the primary and

secondary triple points are affected by dust particles. Note also that the incident shock front is significantly decelerated in this case with high dust concentration.

Finally, a more detailed parametric study on the effects of particulate loading and particle diameter size was summarized in Fig. 46. Isopycnic surfaces, that is, surfaces with a constant density of gas phase in the dusty gas indicate that the particulate loading will substantially affect the configuration of the triple points. This change is more significant in the case of larger dust particles. Moreover, when the particulate loading increases, the incident shock front greatly decelerates, especially in the case of smaller dust particles. Furthermore, it can be seen that the height of the Mach stem shortens in dusty gas flows. Due to the increased momentum and thermal interactions, the height of the Mach stem shortens more in the case of a smaller dust particle. In addition, it can be observed that the particle diameter affects the curvature and slope of the secondary and primary reflected shock waves. The larger the particle diameter is the less is the curvature of the secondary reflected wave. Also the primary reflected shock gets more aligned with the secondary reflected shock as the diameter increases. In case of large particles and high mass loadings, the reflected shocks are completely distorted. Furthermore, it can be seen that the slipstreams are affected by increase of particulate loading. The slipstreams are found highly distorted in case of smaller particles. In summary, it can be inferred that the increase of particle diameter and mass loading would lead to blurrier flow patterns of reflected waves and slipstreams. The surfaces of constant density of solid phase in the dusty gas, shown in Fig. 46 (b), imply that smaller particles can follow the gas phase closely, but larger particles cannot follow the gas phase, so that the structure of isopycnic surfaces becomes drastically different from that of the corresponding gas.

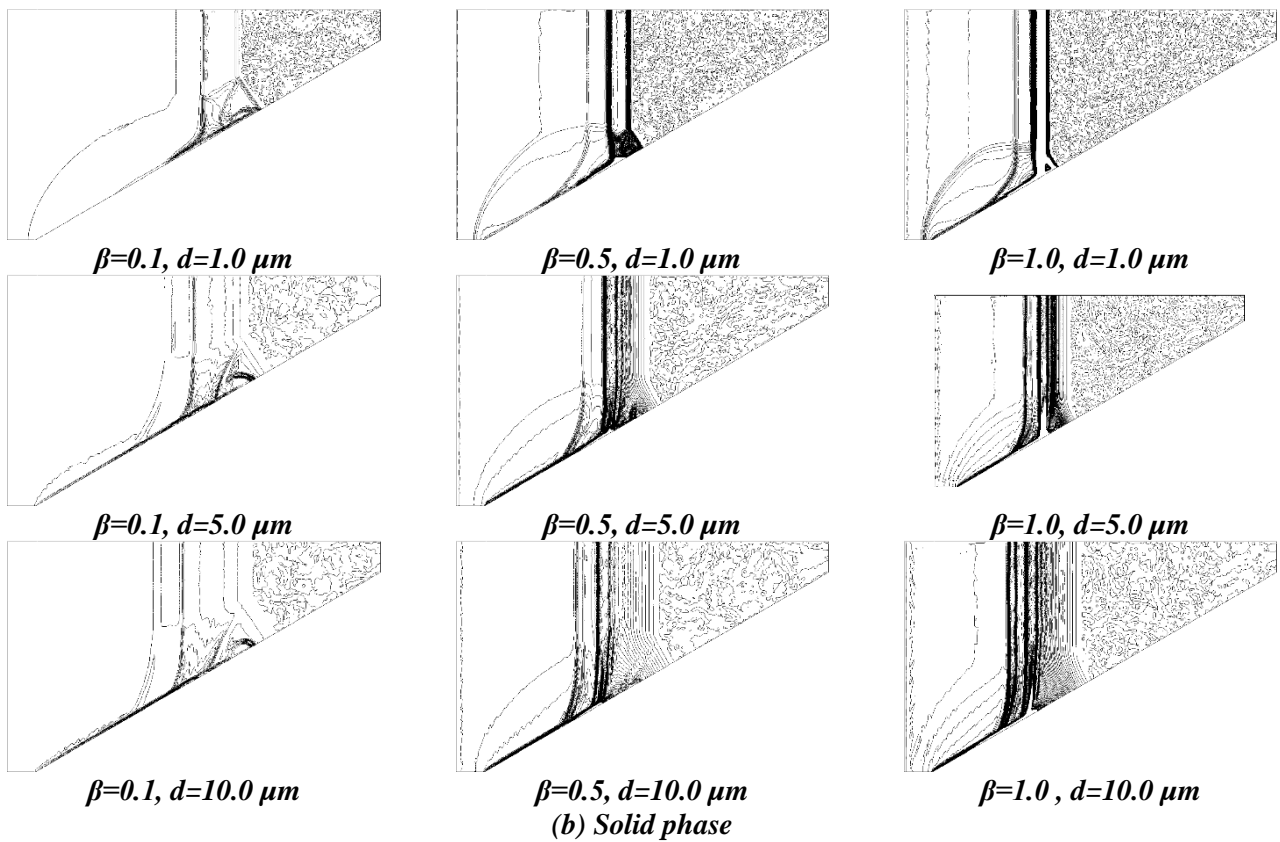
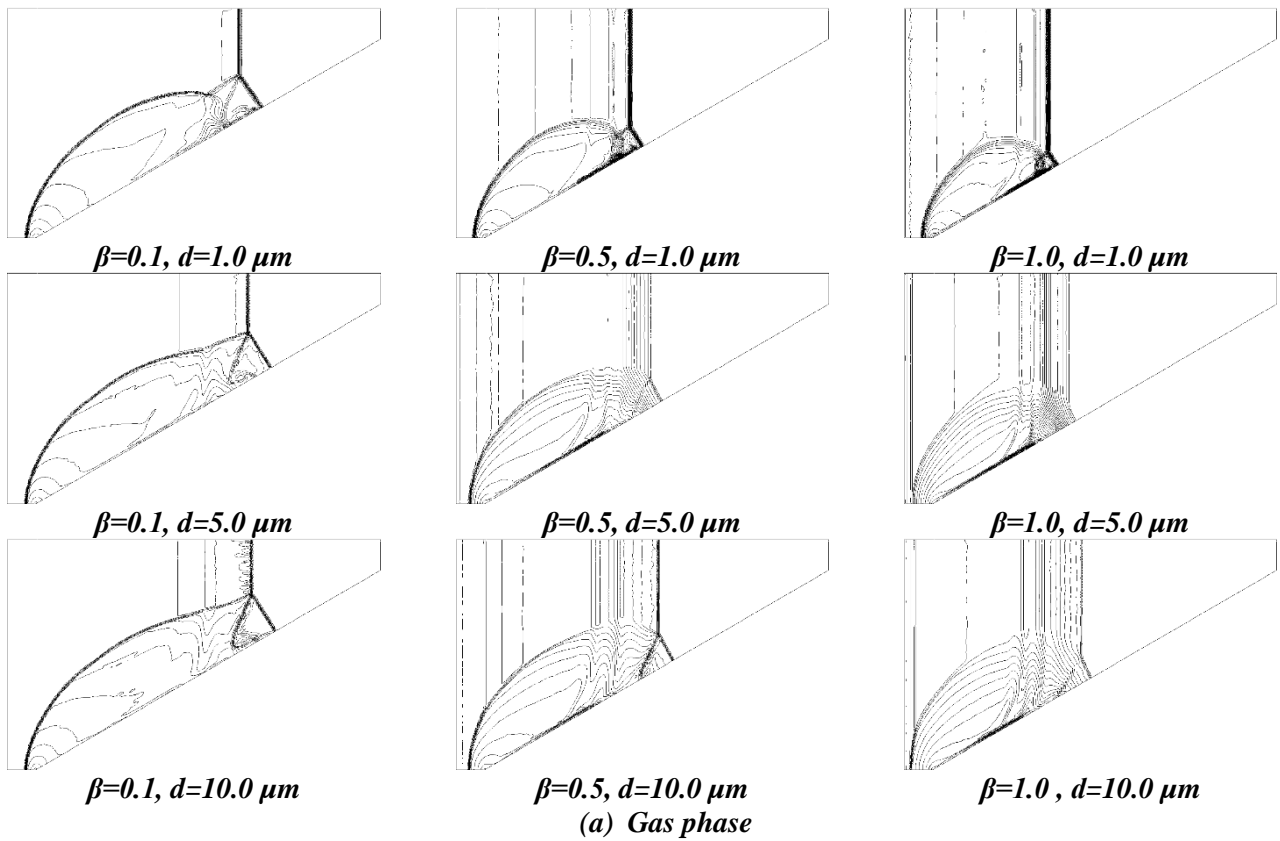
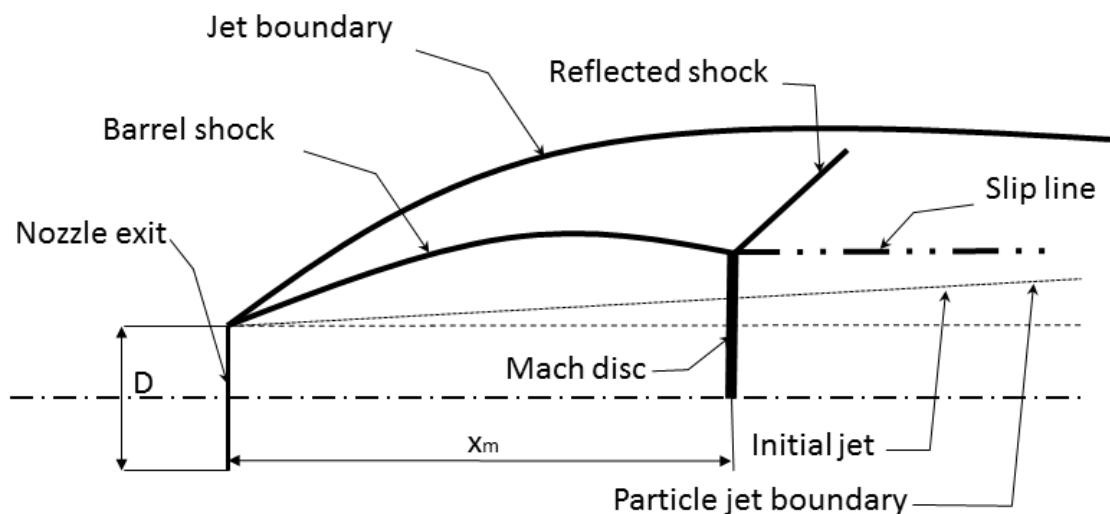


Fig. 46. Parametric study on particulate loading and particle diameter in the double Mach reflection problem ( $P^1$  solution)

## 6.2.5 Axisymmetric particle-laden under-expanded jet

One of the few experimental studies on the interaction of particles with shock waves is the case of under-expanded supersonic jets of gas and particle. In this subsection, we investigate the problem of supersonic jets of particle-laden gas [143]. In order to implement the axisymmetric formulation in the present computational framework, the source terms in the system of governing equations should be modified. The axisymmetric equations can be easily derived by following previous studies [80, 141, 143]. The problem is defined as a supersonic jet which is expanded from a high pressure chamber into a low pressure chamber, as illustrated in Fig. 47.



**Fig. 47 Schematic of the under-expanded jet of particle-laden gas (computational domain size:  $5D \times 10D$ )**

The location of Mach disk in the absence of particles is first studied for validation of the pure gas solver. This parameter has been experimentally studied by various researchers in the past [143, 225-227]. Recently, Franquet *et al.* [228] presented an extensive review on experimental works dealing with free under-expanded jets. The comparison of Mach disk location with experimental results is shown in Fig. 48. Generally, the results are in good agreement with experimental data of Avduevskii *et al.*

[227] for mid-range pressure ratios. In the case of pressure ratios of 2 and 100, our predictions are more close to the experimental results of Lewis and Carlson [225].

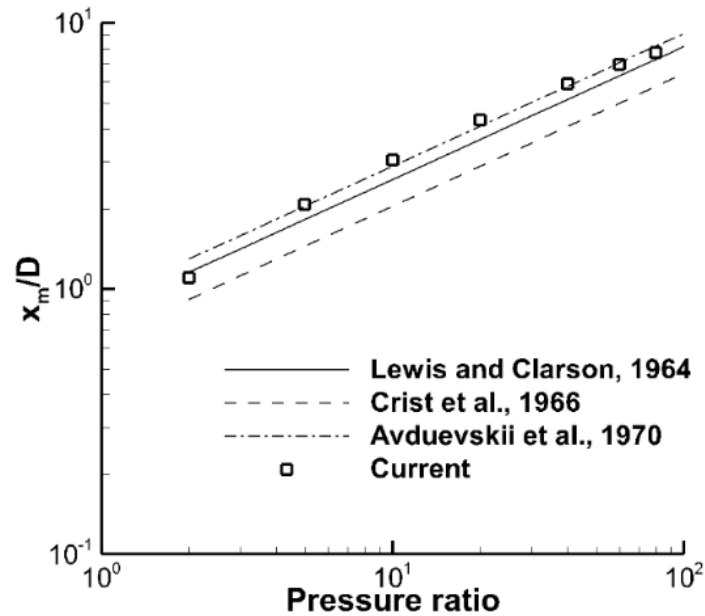


*Fig. 48 Comparison of prediction of Mach-disk location depending on the pressure ratio for the pure gas flow with previous experimental results*

Moreover, a comparison of dusty gas solutions with experiments of Sommerfeld [143] is shown in Fig. 49. Here, particle properties are set equal to the values of diameter  $45 \mu\text{m}$  and mass density  $2500 \text{ kg/m}^3$ . In this problem, one of the important flow features is the upstream movement of Mach disk as a consequence of the interaction of gas phase with particles. As reported in [143], when the particle loading increases, the Mach disk gets closer to the nozzle exit and the wave patterns observed in the downstream of the Mach disk becomes more pronounced. The phenomena of movement of Mach disk has also been reported in [229] and [230]. As can be seen in Fig. 49 (b), even though an exact match with experimental results is not achieved, a close agreement in the qualitative trend of upstream movement of the Mach disk is found. There were, nonetheless, some differences between the numerical solutions and the experimental shadowgraphs; for example, the curvature of the Mach disk and the width of the jet boundary. While experiments show that the Mach

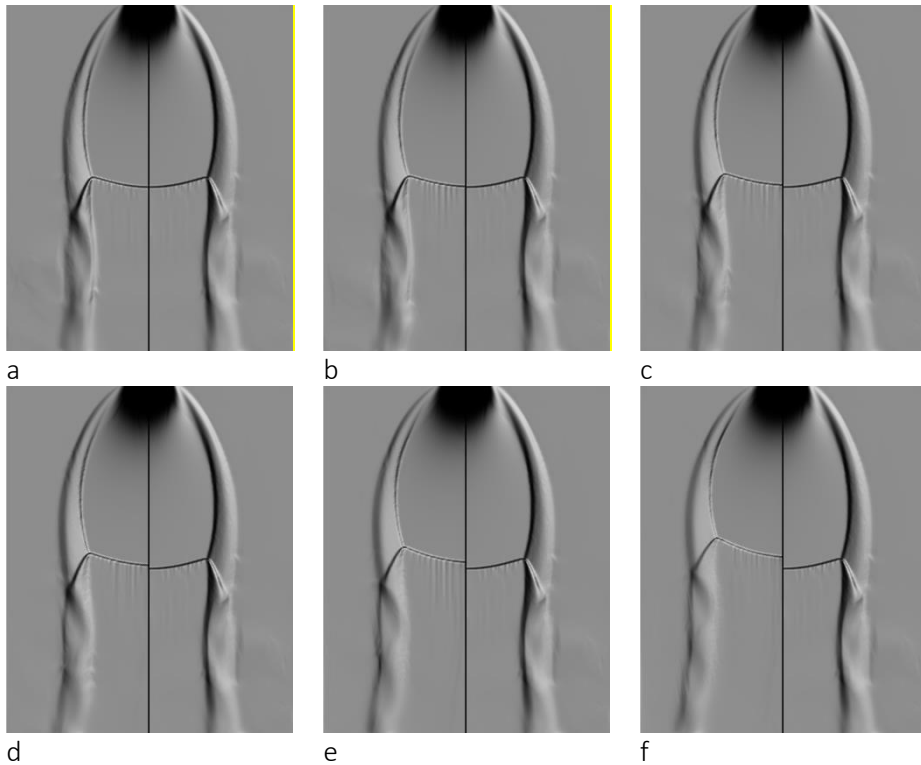
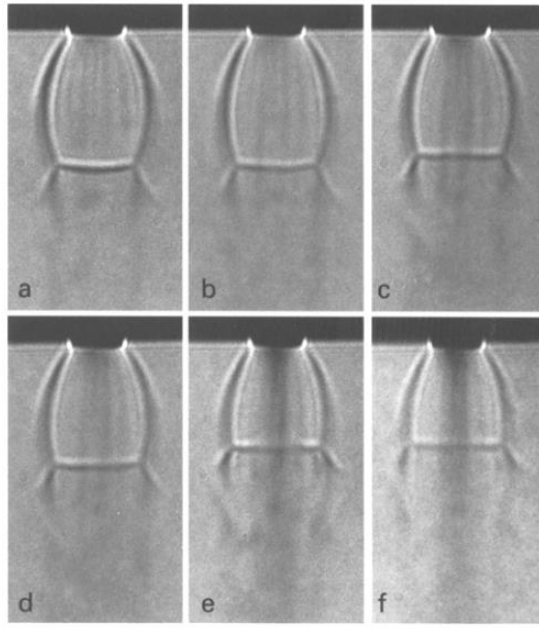


**Fig. 49** *Shadowgraphs of the under-expanded gas-particle [143] (top) and density contours of pure gas solution (right) with dusty gas (left) jet for different particle loadings (bottom): a)  $\beta = 0.0$ ; b)  $\beta = 0.11$ ; c)  $\beta = 0.24$ ; d)  $\beta = 0.35$ ; e)  $\beta = 0.64$ ; f)  $\beta = 1.07$  ( $P_0 = 0.31\text{MPa}$ ,  $P_0/P_\infty = 29.8$ ,  $d = 45\mu\text{m}$ ) ( $P^I$  solution)*

disk tends to straighten as the particle loading increases, the numerical simulation cannot predict this feature. In addition, the width of the jet boundary is over-predicted in the numerical solutions compared to experimental results. Such deviations may arise from the

difference in considering the effect of a nozzle. In the present investigation, for the sake of simplicity, the computation is set up to simulate expansion of a circular jet from a hole into ambient condition without considering a nozzle. Apparently, further in-depth investigation will be necessary for capturing all the detailed features observed in experiments.

# Chapter 7. Numerical experiments on first-order NSF-type systems of equation

In this chapter simulation results for few problems where the first-order Boltzmann-based constitutive relations (NSF) govern the flow are presented. In the investigated problems the viscous effects find importance and application of zeroth-order Boltzmann-based constitutive relations (Euler) is not sufficient for prediction of this category of problems.

## 7.1 Flow past NACA0012 airfoil

In this section, external flow over the NACA0012 airfoil for which experimental results are well documented is considered, and a series of numerical experiments have been conducted. Variety of experimental results for the investigated airfoil is available in [231] which can be used as a comprehensive reference for validation of numerical methods. The goal is to compare the solution of different numerical flux functions for both inviscid (Rotated RHLL and LLF) and viscous flux (BR1 and LDG) parts and evaluate their performance. Moreover, the effect of the polynomial order is investigated. To these ends, two types of computational grid, i.e., grids produced by *map-split* and *pave* algorithms are applied. The results for polynomial degrees corresponding to first-order ( $P^0$ ), second-order ( $P^1$ ), and third-order ( $P^2$ ) accuracy are presented. We note that here we are more interested in the numerical behavior of the flux functions rather than producing perfect matches with experimental results. Therefore, relatively coarse grids are applied to highlight the effects of the used numerical grid, flux functions, and polynomial orders. The grid size for both the applied meshes is almost identical in order to make a reasonable comparison possible. The density isolines for the subsonic flow past NACA0012 with  $M=0.8$ ,  $Re=73$  and an

angle of attack of 10 degrees is shown in Fig. 50 and Fig. 51 for map-split and pave grids, respectively. It can be seen that the solutions are almost identical with the experimental results in most cases. More oscillations in high order solutions are observed. These oscillations will diminish using a smaller CFL number. An artifact is observed when Rotated-RHLL flux is applied with LDG flux. It can also be observed that an LLF-BR1 combination can give solutions more close to experimental results. The results of a similar comparison for supersonic flow is provided in Fig. 52 and Fig. 53. Here the Mach and Reynolds numbers are set equal to 2.0 and 106, respectively. The artifacts observed in the subsonic case for Rotated-RHLL-LDG combination does not exist here. As expected, high order solutions predict a less diffused shock wave and show more oscillatory contours. These oscillations would diminish as the CFL decreases. Here, almost all the solutions are in good agreement with the experimental solution of density. Rotated-RHLL shows better performance compared with LLF in combination with any of the viscous flux functions.

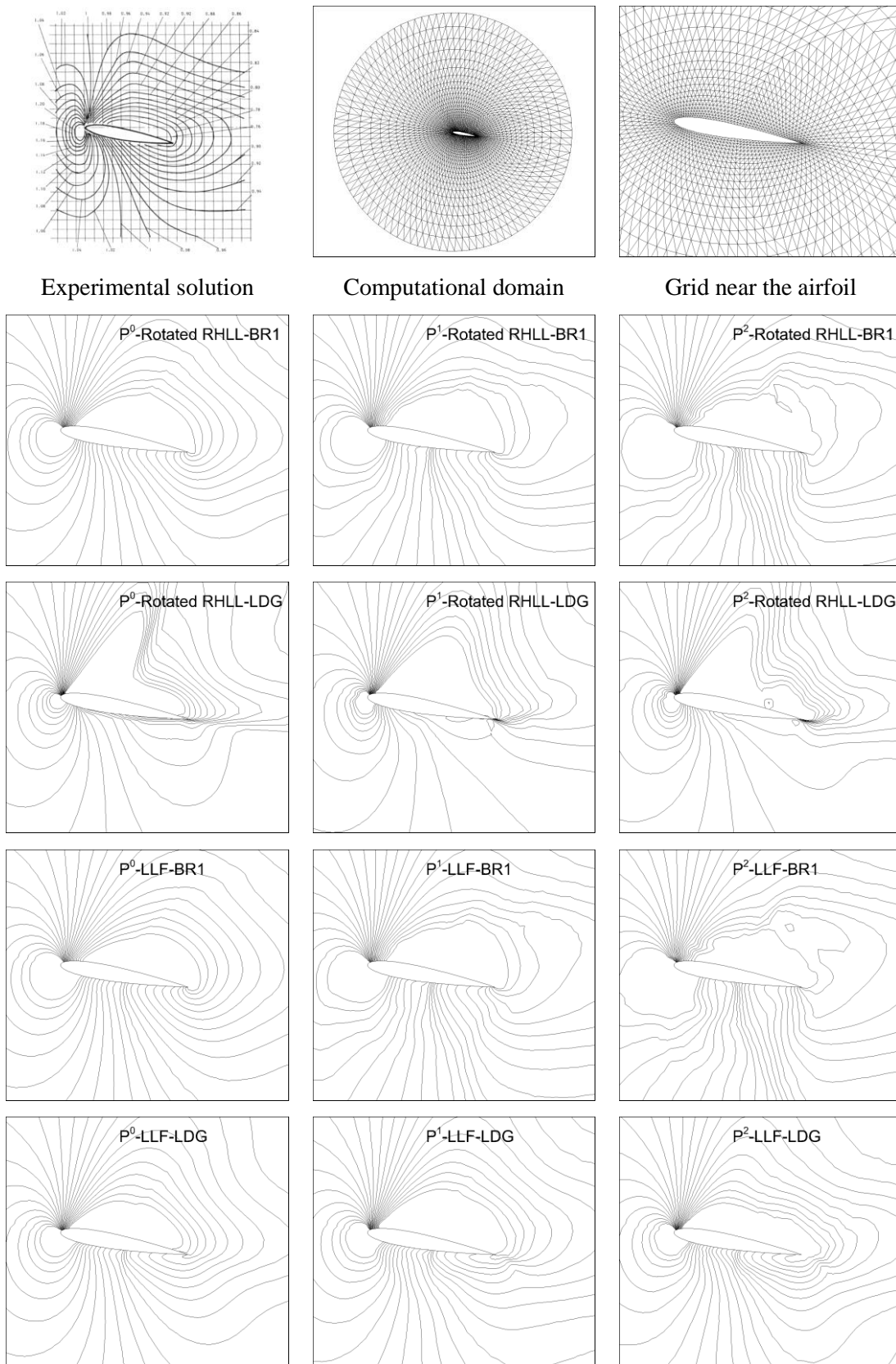


**Fig. 50** Density solutions of different flux functions for map split grid ( $Re=73$ ,  $M=0.8$ )

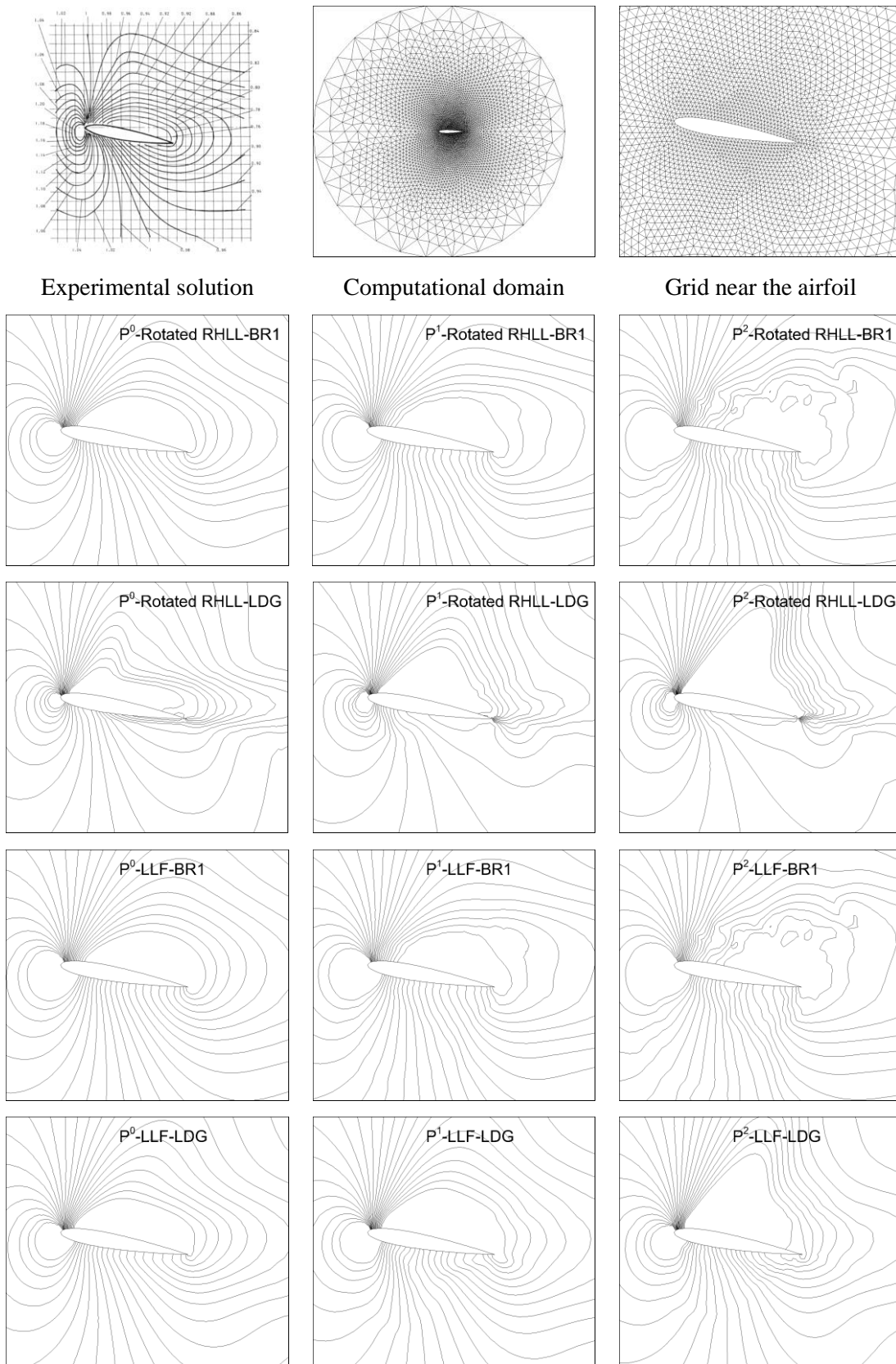


**Fig. 51** Density solutions of different flux functions for pave grid ( $Re=73$ ,  $M=0.8$ )

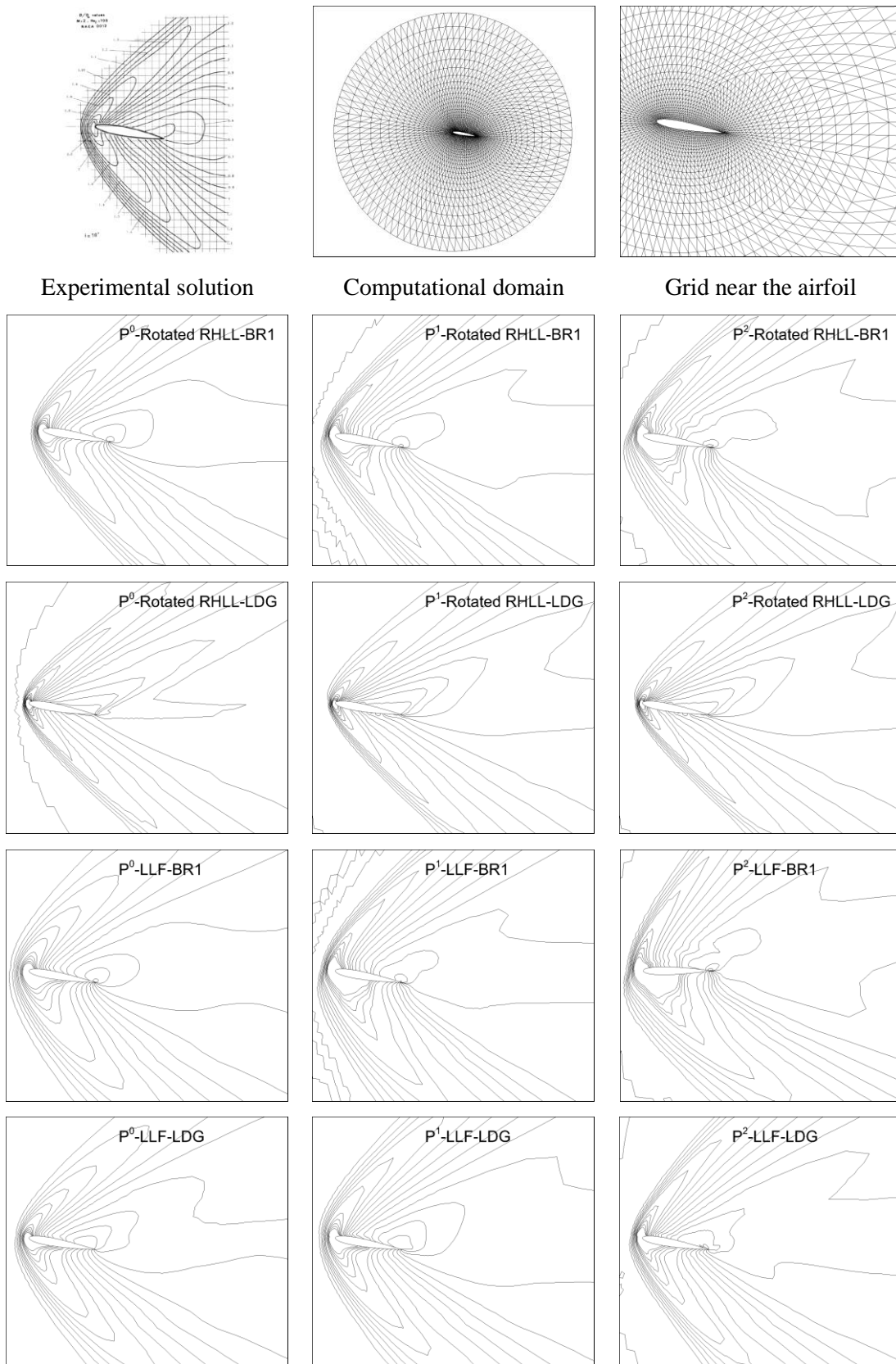


**Fig. 52** Density solutions of different flux functions for map split grid ( $Re=106$ ,  $M=2.0$ )

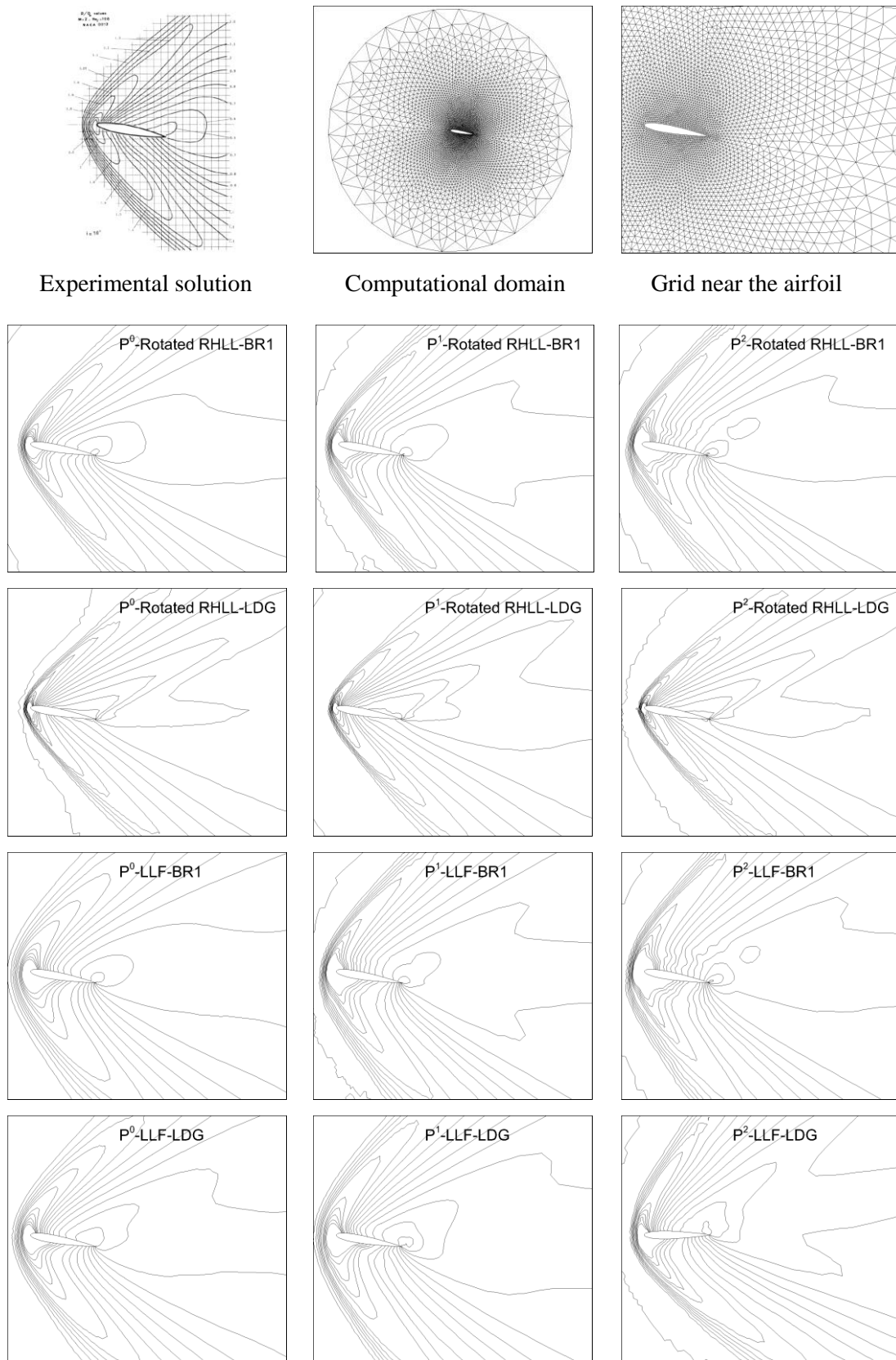


**Fig. 53** Density solutions of different flux functions for pave grid ( $Re=106$ ,  $M=2.0$ )

The preliminary results for simulation of dusty gas flow past the airfoil are also provided. Such simulations can be useful in applications including the flight through sand storms, rain and atmospheric icing to name a few. In Fig. 54, the accretion of particles for flow past NACA0012 with different flow condition and dust parameters is provided. With the knowledge that such analysis without verification and validation is not worthy of note, the preliminary results are presented to show feasibility of applications of the current model in this class of problems. It should be noted that in case of flight in rain and snow, modifications are more substantial.

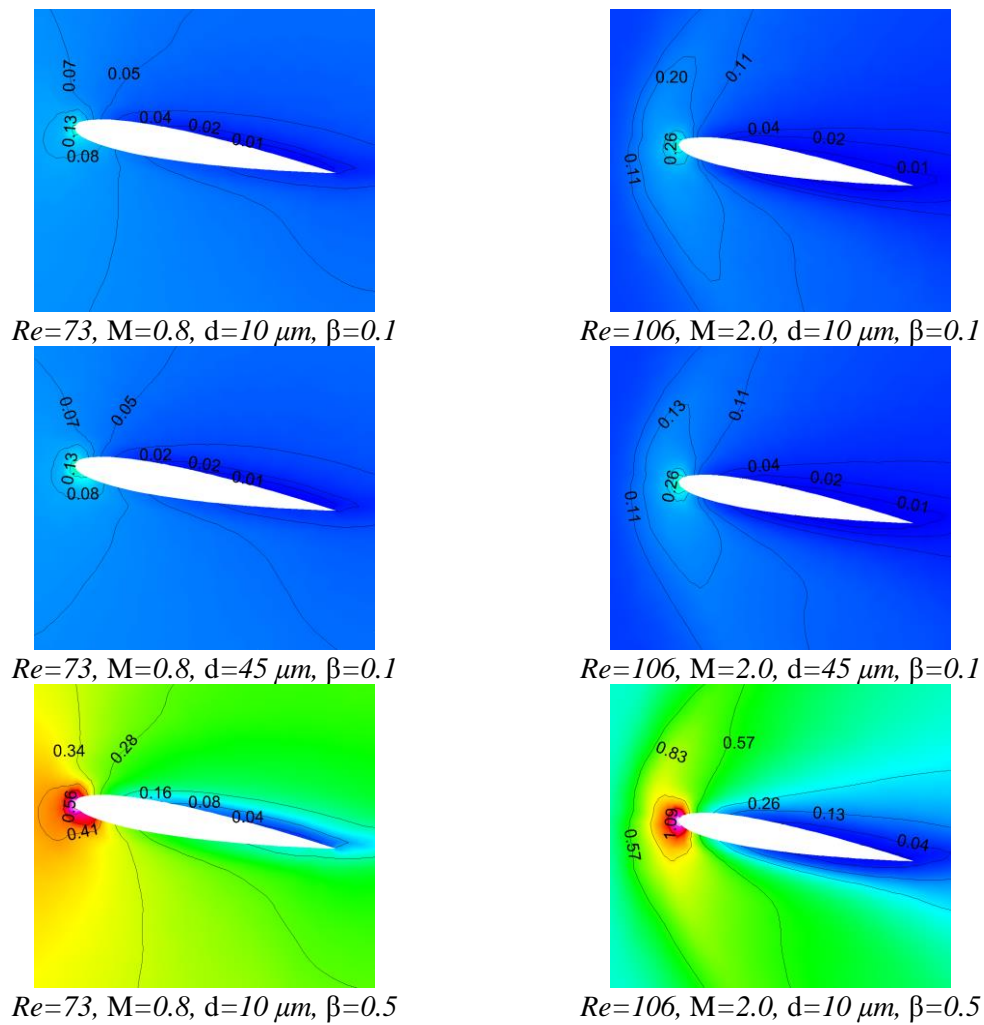


**Fig. 54 Concentration contours of dusty gas past NACA0012**

## 7.2 Flow past triangular prism

Flow past bluff bodies has been a compelling subject for researchers due to a vast area of applications including aerodynamics design of flying objects, electronic cooling, acoustic emission, heat exchangers, solar heating systems, flow dividers and many more. The shape and size of the bluff body would influence the location of separation as well as wake dynamics behind the obstacle. The location of separation on bodies with continuous surface curvatures (circular/elliptical cylinders) depends on the geometry of the body and the state of the boundary layer defined by the free stream Re number. However, on sharp edged surfaces (triangular/rectangular prisms) this parameter is only dependent on the shape of the body. Moreover, it is well known that above a certain Reynolds number (*critical Reynolds number*) the stable flow around the bluff body turns into an unstable one (the onset of *von Kármán vortex street*). The Bérnard-von Kármán instability leads to deformation of the symmetrical twin vortices (bubbles), and vortices are shed with the frequencies which are defined by Strouhal number. The vortex shedding phenomenon may be laminar or turbulent. Here, we limit our investigation to the laminar case. There are plenty of researches in which these crucial features are investigated both experimentally and numerically. The problem for circular cylinders is well reviewed and documented in [232, 233]. Also, works are abundant on square cylinders [234-240]. However, the number of researches on triangular prisms has been limited. In the previous studies, both unconfined and confined channels are investigated. Jackson [241] reported the critical Reynolds number to be 34.318 for isosceles triangles with base 1 and height 0.8. A critical Re number of 38.3 for flow past equilateral triangular prism with a blockage ratio of 1.15 was reported in a numerical investigation by [242]. The findings of Zielinska and Wesfreid [242] were further confirmed by experiments of Goujon-Durand *et al.* [243] and Wesfreid *et al.* [244]. Reynolds-averaged Navier-Stokes (RANS) turbulence model of the  $k-\varepsilon$  model

was applied by Johansson *et al.* [245] in order to investigate the turbulent flow past a triangular cylinder. Two-dimensional laminar flow past triangular cylinder was investigated by De and Dalal [246] in which a  $Re_{cr}=39.9$  was predicted. Further discussions on time-averaged drag coefficient, rms of lift and Strouhal number were also presented. Prhashanna *et al.* [247] conducted numerical investigations on the influence of power-law index on the formation of the wake and the onset of vortex shedding in flow across an equilateral triangular cylinder. Effect of variation of Reynolds number and Prandtl number on the drag coefficients and heat transfer in the steady regime has also been investigated. Furthermore, Chatterjee and Mondal [248] studied forced convection heat transfer for flow past a long heated equilateral triangular cylinder in an unconfined medium for the low Reynolds number laminar regime.

Works in which the effect of Re number in a flow regime with Mach numbers over the limit of compressible and over the limit of subsonic regimes are absent or rare. This section was initially motivated by verification of the NSF solver for unsteady incompressible subsonic Mach regime. However, as the reviewed work were all confined to the limit of the incompressible regime, in addition to verification of method some further analysis on the compressibility effects has been done.

Moreover, the influence of dust particles on viscous flows, which can be seen in many natural phenomena such as soil erosion by natural winds, volcanic eruptions or engineering applications like in petroleum industry for purification of crude oil, in gas cooling systems for enhancement of heat transfer process with the use of dust, in dust/mist/fume collators, is an interesting subject for investigation. The need for elucidating the two-way coupling effects [249] motivated conducting extensive numerical experiments in order to investigate the influence of particles on the steady and unsteady behavior of vortices.

Due to the importance of the interaction of particles with vortices in applications like combustion systems, wire and plate electrostatic precipitators, the spread of fires by firebrands [249, 250], some investigations have been done before. [251] showed that for fine dust particles ( $\tau_v < t_{ref}$ ) the addition of dust could destabilize a gas flow. However, for coarse grain particles, the dust addition leads to a stabilizing action. Damseh [252], investigated the flow of a viscous incompressible flow of gas in the presence of uniform dust particles cloud across an isothermal cylinder. Mehrizi *et al.* [253] investigated the effect of nanoparticles on natural convection heat transfer in two-dimensional horizontal internal flow in an annulus made up of a heated triangular inner cylinder and a circular outer cylinder. In a more recent work, Xu *et al.* [254] investigated the fine particle behavior in the laminar flow of air past a triangular prism experimentally and numerically. Bai and Li [255] investigated the motion and deposition of particles in supersonic flow past a wedge using a Eulerian-Lagrangian numerical model.

Here we are interested in phase coupling effects on the symmetrical vortices, the onset of unsteadiness and frequency of the shedding. A set of numerical experiments can be designed based on the Reynolds and Mach number variations. The Mach regime based on classical categorization can be divided into: low subsonic (incompressible limit,  $M < 0.3$ ), subsonic ( $0.3 < M < 0.8$ ), transonic ( $0.8 < M < 1.2$ ), supersonic ( $1.2 < M < 5.0$ ) and hypersonic ( $M > 5.0$ ) regimes. We are interested in the low Reynolds laminar flow before and after the onset of the shedding phenomena characterized by  $Re_{cr}$ . The overall outline of the investigated test cases is summarized in Table 18.

**Table 18** *Categorization of regimes based on Reynolds and Mach numbers and investigated regimes in this work*

	Re < Re <sub>cr</sub>		Re > Re <sub>cr</sub>	
	Pure gas	Dusty gas	Pure gas	Dusty gas
$M < 0.3$	✓	✓	✓	✓
$0.3 < M < 0.8$	✓		✓	
$0.8 < M < 1.2$	✓		✓	
$1.2 < M < 5.0$	✓	✓	✓	✓
$M > 5.0$				

The applied computational domain size, boundary conditions, and grid are outlined in Fig. 55. As shown in the figure, far-field and outflow boundary conditions are applied in the distance far enough from the prism. Moreover, it can be seen that the grid is finer in locations where larger gradients exist.

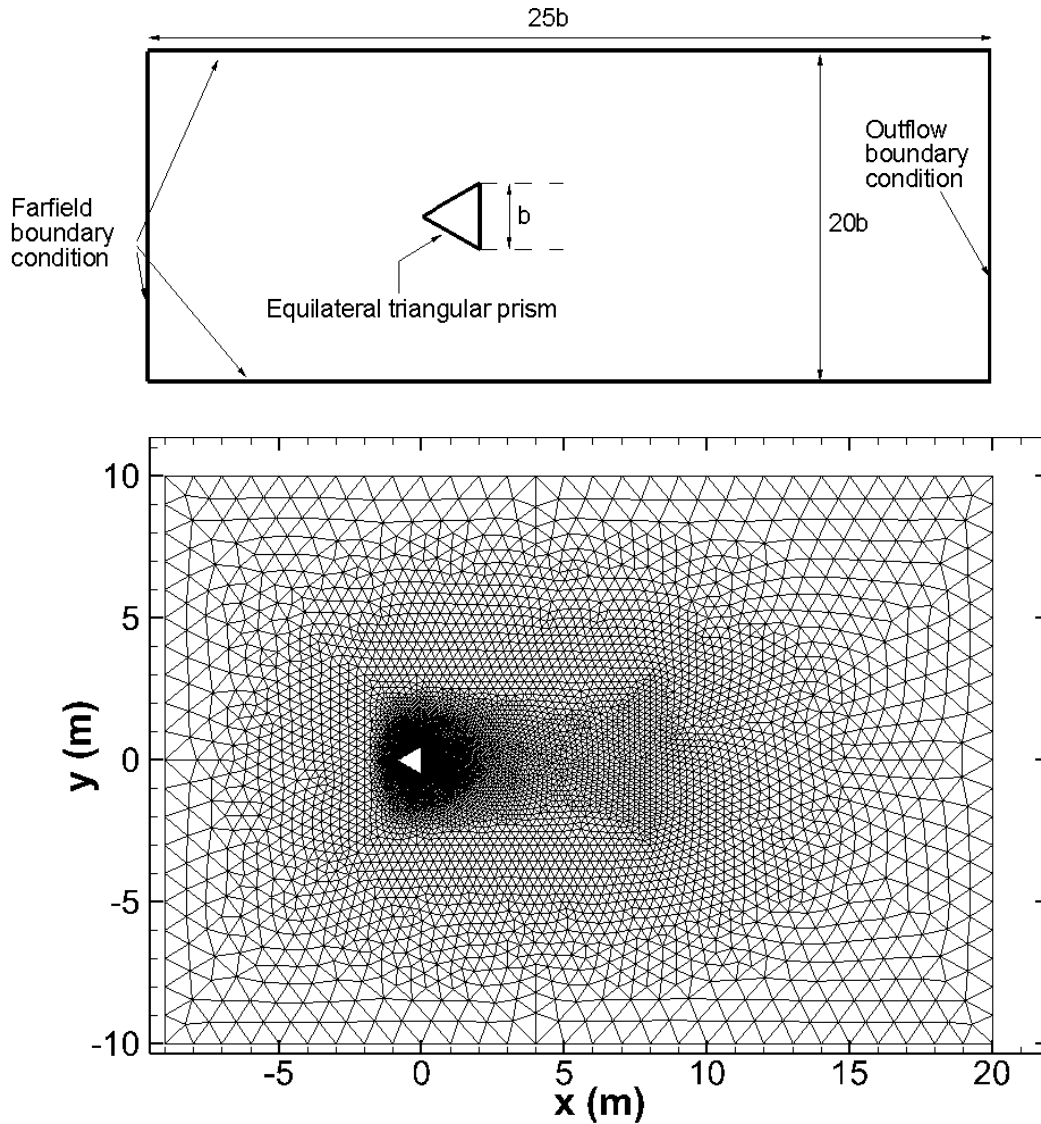
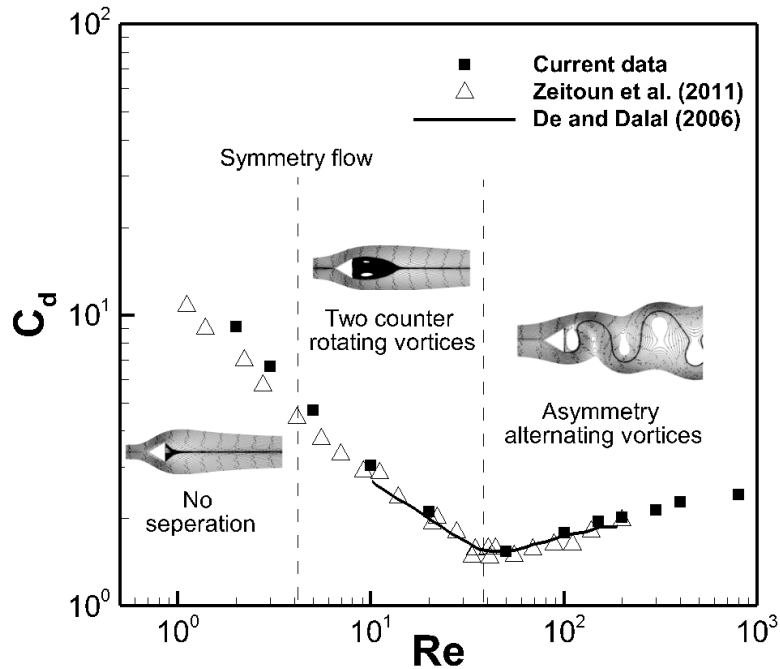


Fig. 55 Computational domain, boundary conditions, and grid.

### 7.2.1 Pure gas simulations

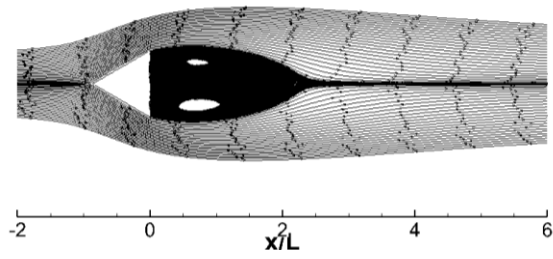
The validity of the numerical solutions are verified by comparison with previous solutions of [246, 256]. It can be seen in Fig. 56 that a good agreement with previous results is achieved. A discrepancy with the drag solution of Zeitoun *et al.* [256] for low Reynolds numbers is observed. The cause of this mismatch may be due to a different formulation (incompressible vs. compressible), numerical grid (quadrilateral vs. triangular), or used numerical schemes. However, as a third solution in this regime is not available, recognizing the more accurate solution is not possible. The magnitude of this deviation is not

considerable (<10%), however. Furthermore, it can be seen that in higher Re numbers all three solutions are in good agreement.

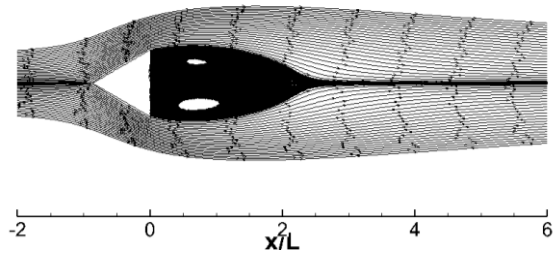


*Fig. 56 Verification of drag coefficient.*

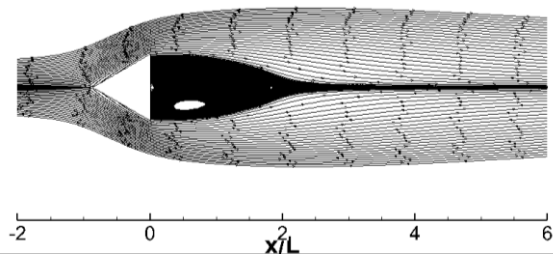
The effect of Mach number on the flows with Re numbers less than  $Re_{cr}$  is shown in Fig. 57. It can be observed that with the increase of Mach number the symmetrical vortices shrink in size. For  $M = 2$ , there is no separation, and thus no vortices can be observed.



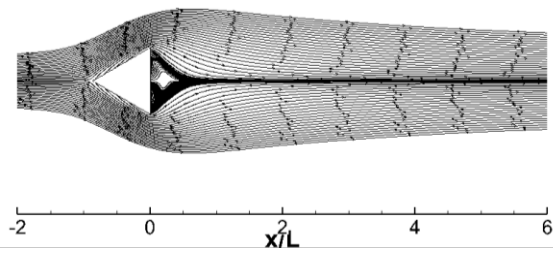
$Re=30, M=0.1$



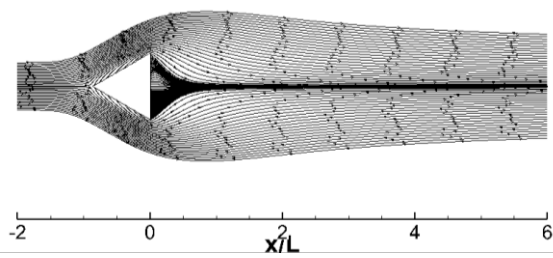
$Re=30, M=0.3$



$Re=30, M=0.8$



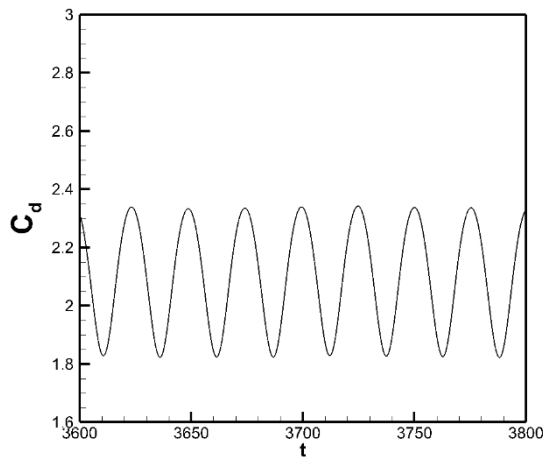
$Re=30, M=1.2$



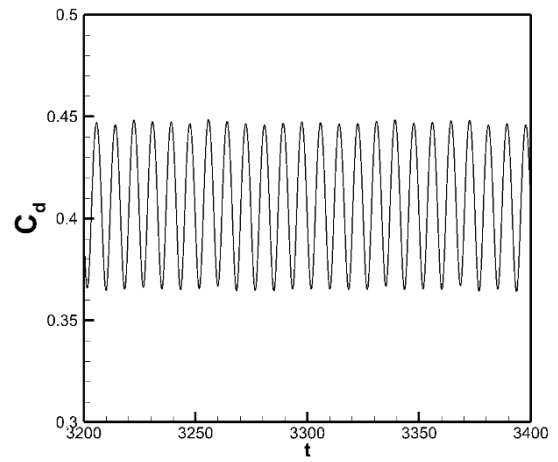
$Re=30, M=2.0$

**Fig. 57** Effect of variation of  $M$  number for a constant  $Re$  number smaller than critical  $Re$  number.

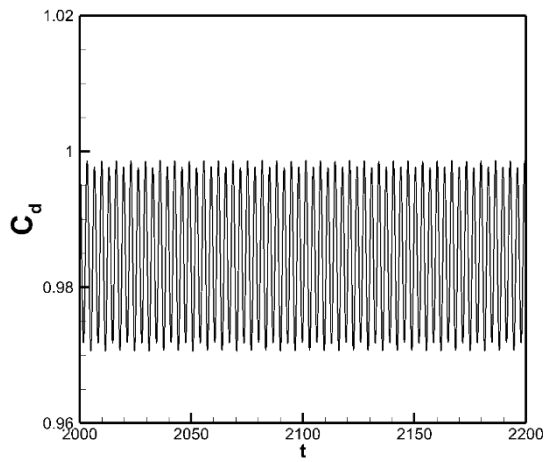
Furthermore, the effect of variation of Mach number on a flow with Re number higher than the critical Reynolds number is investigated. As can be seen in Fig. 58, an increase of  $M$  leads to a decrease in amplitude and an increase in the frequency of the drag coefficient oscillations. For high transonic regime ( $M = 1.2$ ), this oscillatory behavior has almost vanished. No oscillation in the case of the supersonic regime is observed. The snapshots of instantaneous vorticity and streamlines for the investigated Mach numbers are plotted individually in Fig. 59 to Fig. 63. Such analysis is useful in studying the transient behavior of vortices and can elaborate on how this transient behavior is influenced by variation of  $M$  number. As the drag coefficient variation implies, the increase of  $M$  number would stabilize the flow. For  $M$  numbers corresponding to supersonic regimes, the von Kármán vortex street changes into two symmetrical counter-rotating vortices (Fig. 62 and Fig. 63). The topologies of these vortices are however different from the symmetrical vortices that appear in low Re and low  $M$  number regimes.



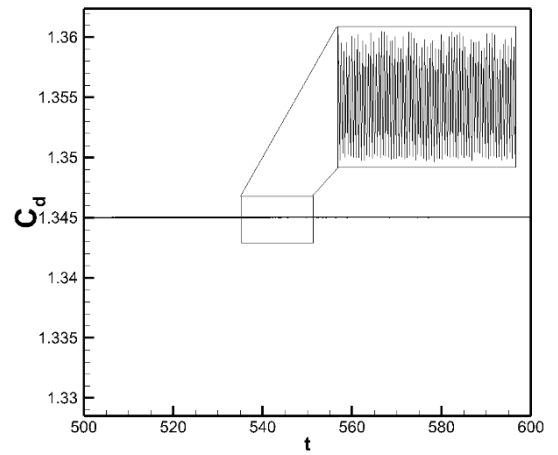
$Re=250, M=0.1$



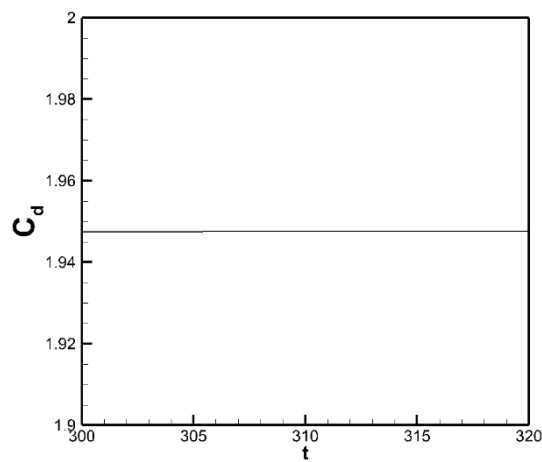
$Re=250, M=0.3$



$Re=250, M=0.8$



$Re=250, M=1.2$



$Re=250, M=2.0$

**Fig. 58 Effect of variation of  $M$  number for a constant  $Re$  number smaller than critical  $Re$  number.**

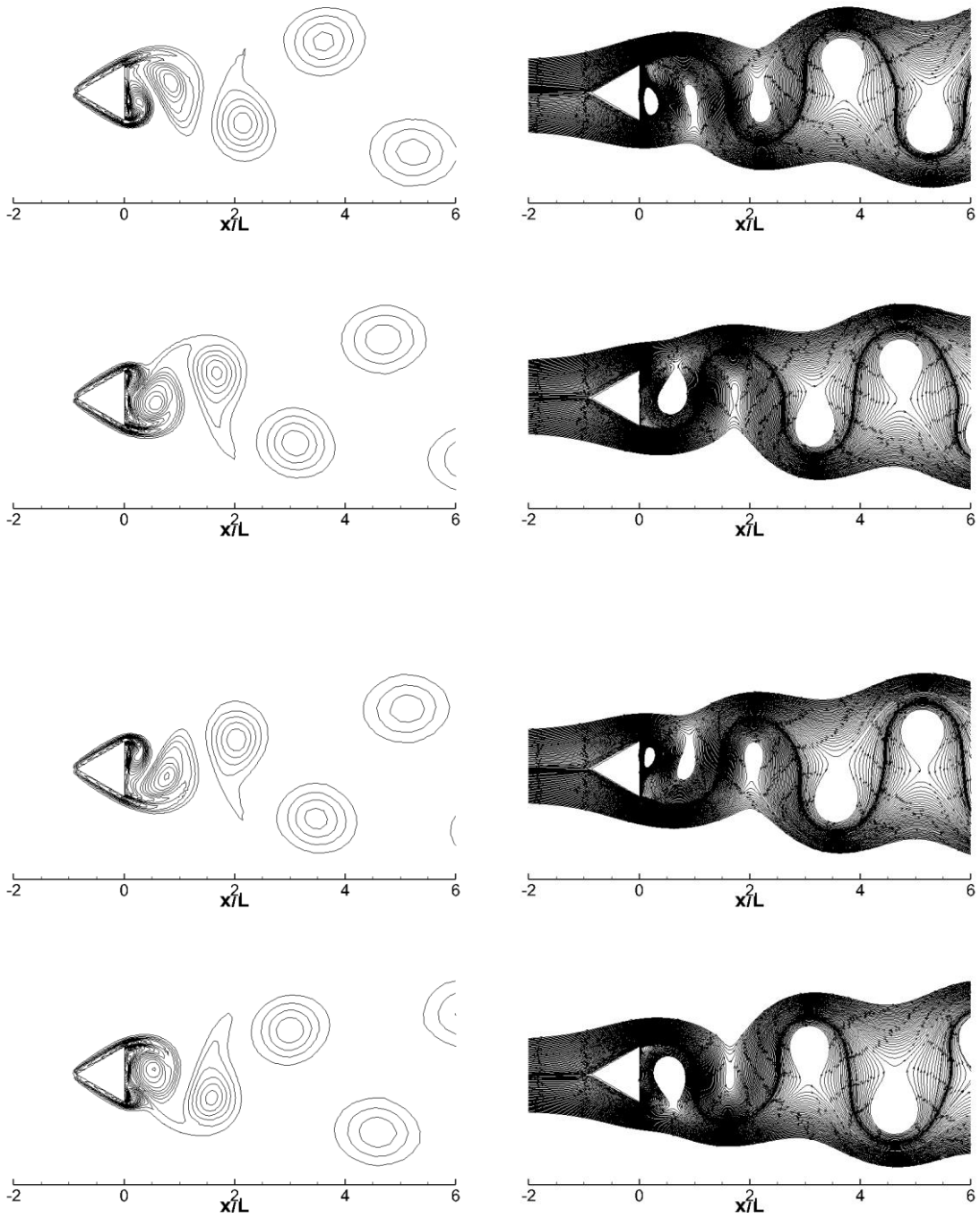


**Fig. 59** Snapshots of instantaneous vorticity (left) and streamlines (right) in different time steps within a shedding cycle,  $Re=250$ , and  $M=0.1$ .

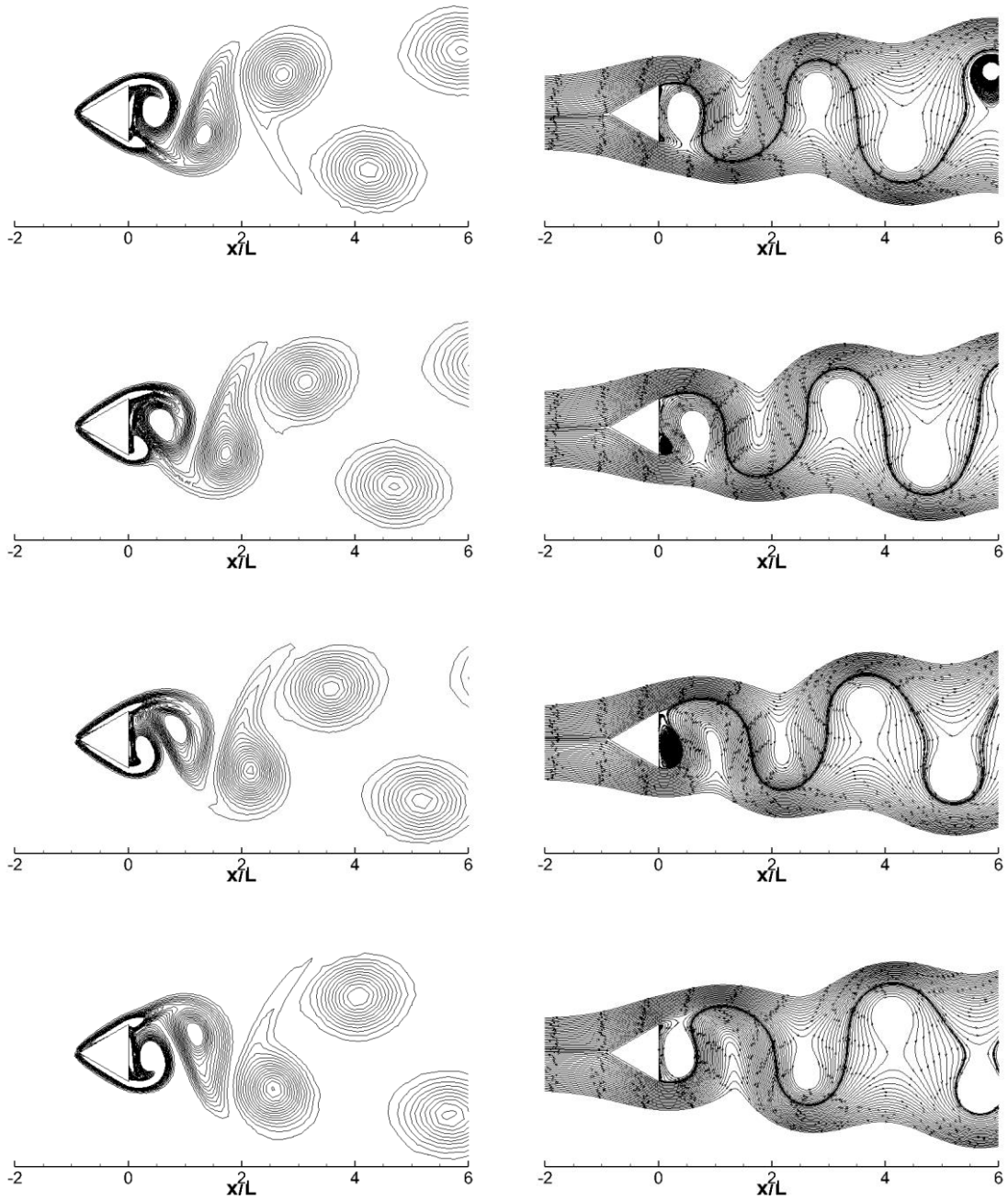


**Fig. 60** Snapshots of instantaneous vorticity (left) and streamlines (right) in different time steps within a shedding cycle,  $Re=250$ , and  $M=0.3$ .

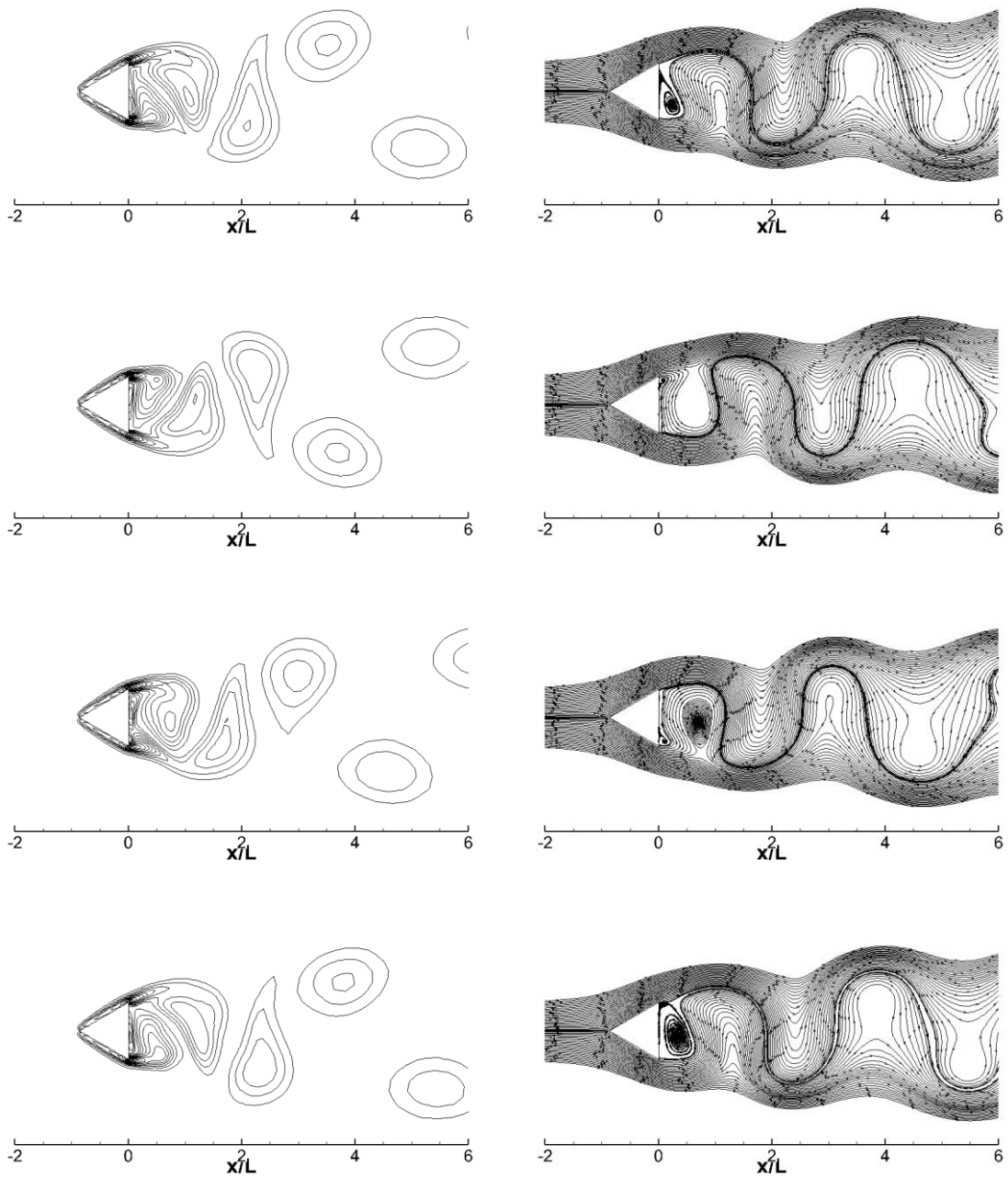


**Fig. 61** Snapshots of instantaneous vorticity (left) and streamlines (right) in different time steps within a shedding cycle,  $Re=250$ , and  $M=0.8$ .

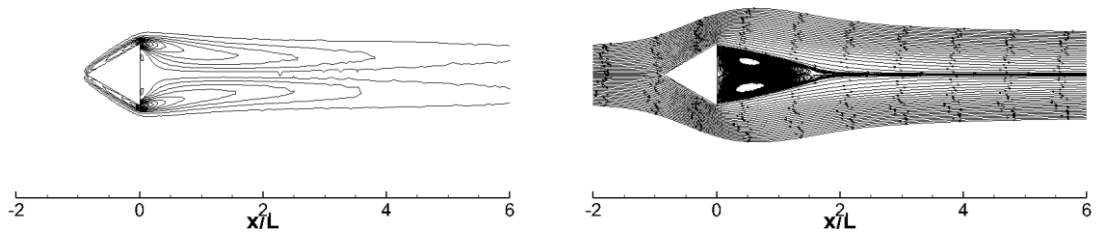


**Fig. 62 Snapshots of instantaneous vorticity (left) and streamlines (right),  $Re=250$  and  $M=1.2$ .**

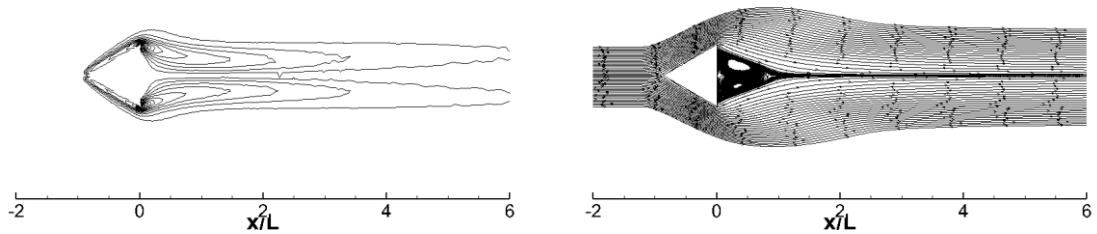


**Fig. 63 Snapshots of instantaneous vorticity (left) and streamlines (right),  $Re=250$  and  $M=2$ .**

The effect of variation of  $Re$  for a constant Mach number in the early supersonic flow regime is also investigated. The compressibility effects are dominant here. The  $Re_{cr}$  (which marks the transition from steady to unsteady flow structure) is much higher when the compressibility effects are present. As evident from Fig. 64, the increase of Mach number hinders the separation and transition processes. Even though the  $Re_{cr}$  is around 40 for the incompressible regime, no unsteady behavior is observed in this case even for a  $Re=200$  simulation.

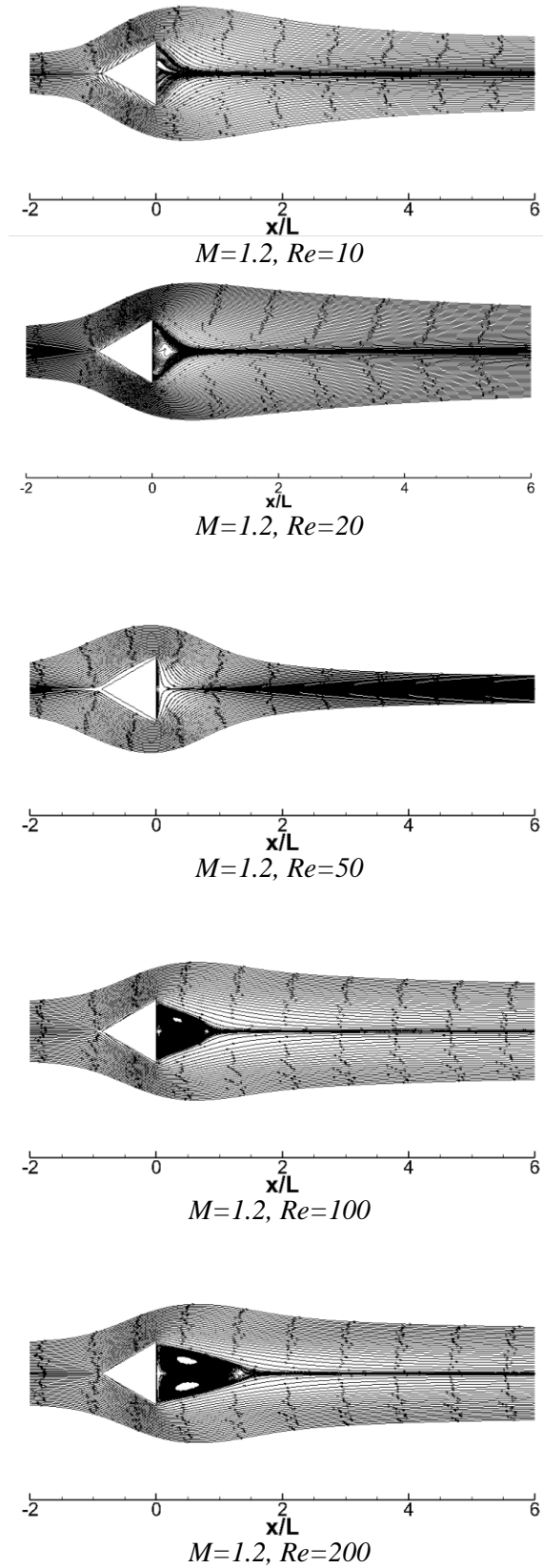
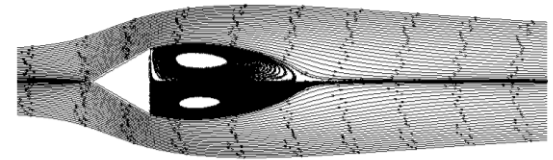


**Fig. 64** Effect of variation of  $Re$  number for a constant  $M$  number in transonic Mach regime

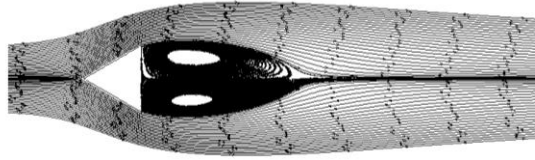
### 7.2.2 Dusty gas simulations

For some of the simulated test cases in the previous section, the effects of adding particles are investigated. Here, the properties of the simulated particles are similar to glass beads with a diameter of  $20 \mu m$ . Due to the lack of experimental data for the cases of interest in here, a validation study is not conducted, and we rely on the previous validation in Chapter 6 as well as the verification on pure gas in the previous section.

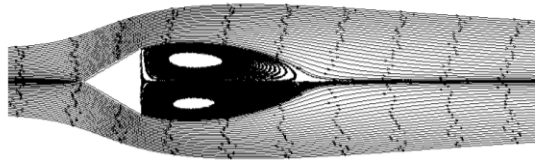
The effect of particulate loading is first investigated on a flow with  $Re=30$  and  $M=0.1$ . In the case of pure gas, as mentioned in previous works and confirmed in Fig. 57, we expect two counter-rotating vortices to form. As demonstrated in Fig. 65, the increase of particulate loading will destabilize the flow. While particles have almost no effect on the behavior of the flow and the shape of the symmetrical vortices for  $\beta < 0.1$ , in higher particulate loading simulations a transition can be observed.



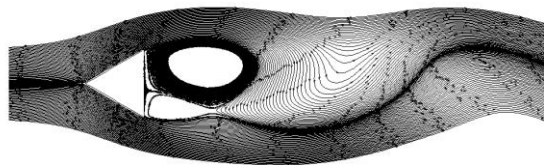
$x/L$   
 $Re=30, M=0.1, \beta=0.0$



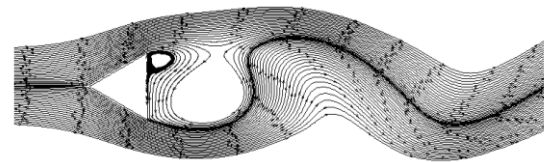
$x/L$   
 $Re=30, M=0.1, \beta=0.05$



$x/L$   
 $Re=30, M=0.1, \beta=0.1$



$x/L$   
 $Re=30, M=0.1, \beta=0.5$



$x/L$   
 $Re=30, M=0.1, \beta=1.0$

**Fig. 65** Effect of variation of particulate loading ( $\beta$ ) in low  $Re$  and low  $M$  number flow past the triangular prism

The effect of variation of particulate loading in case of low Mach number and Reynolds number higher than the critical value ( $Re=250$  and  $M=0.1$ ) is also studied. In Fig. 66, the unsteady behavior of  $C_d$  is plotted. While the drag coefficient shows a sinusoidal behavior, the increase of dust loading irregulates the shape of this behavior. However, the trend is periodic still. The more the particulate loading is, the more is the degree of disorder of  $C_d$ . The nature of the behavior of  $C_d$ , and thus the flow field for all the particulate loadings investigated here is oscillatory, however. This is primarily due to two-way coupling effects. The details of this behavior is illustrated via snapshots of vorticity and streamline in Fig. 66 to Fig. 70. These figures can help in understanding the irregular behavior of  $C_d$  which was previously discussed. Specifically vorticity snapshots plotted in Fig. 69 and Fig. 70, can explain how the non-smooth time-dependent drag profiles are generated as the vortices are deformed near the solid walls.



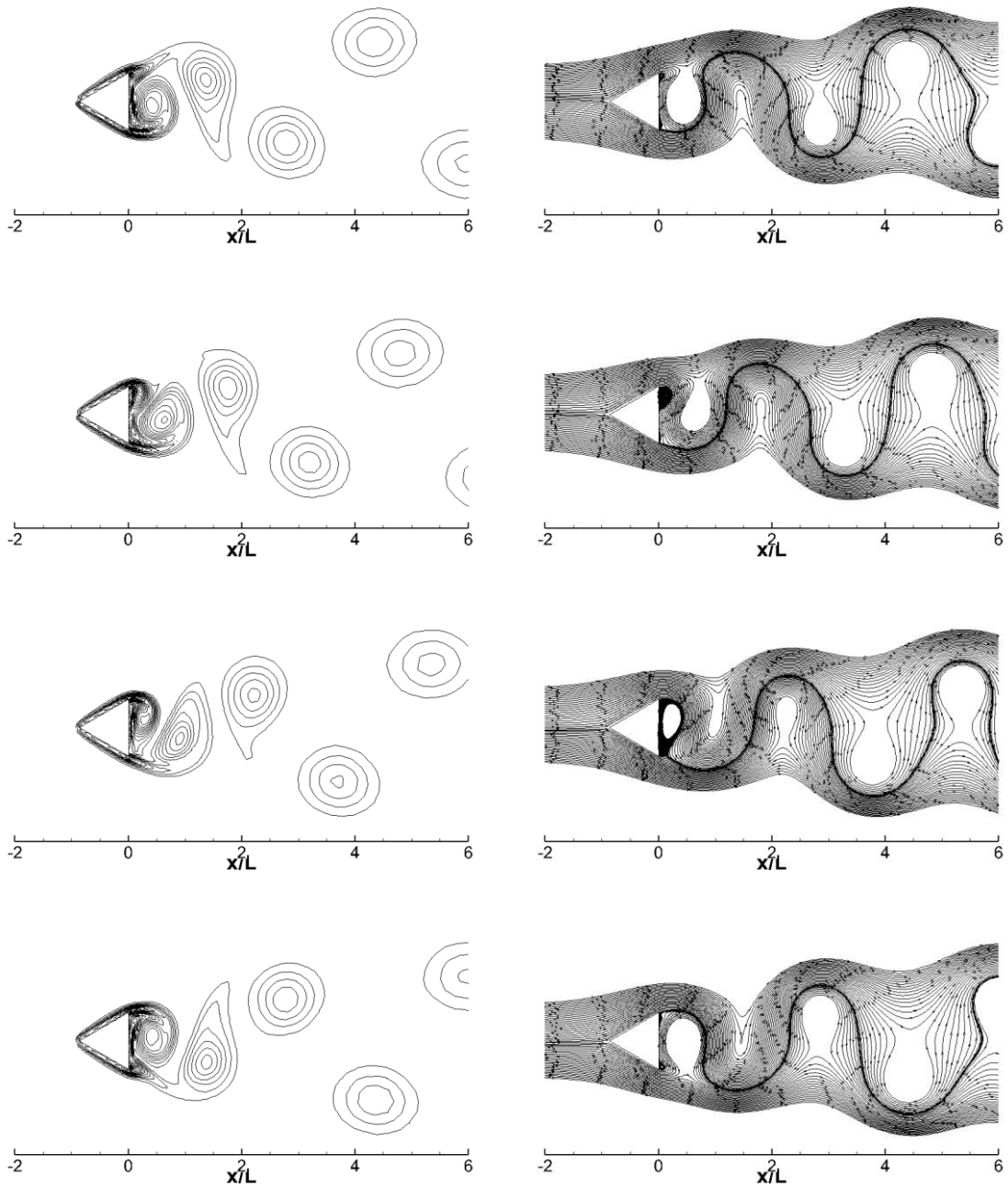


**Fig. 67** Snapshots of instantaneous vorticity (left) and streamlines (right) in different time steps within a shedding cycle,  $Re=250$ , and  $M=0.1$ ,  $\beta=0.01$ .

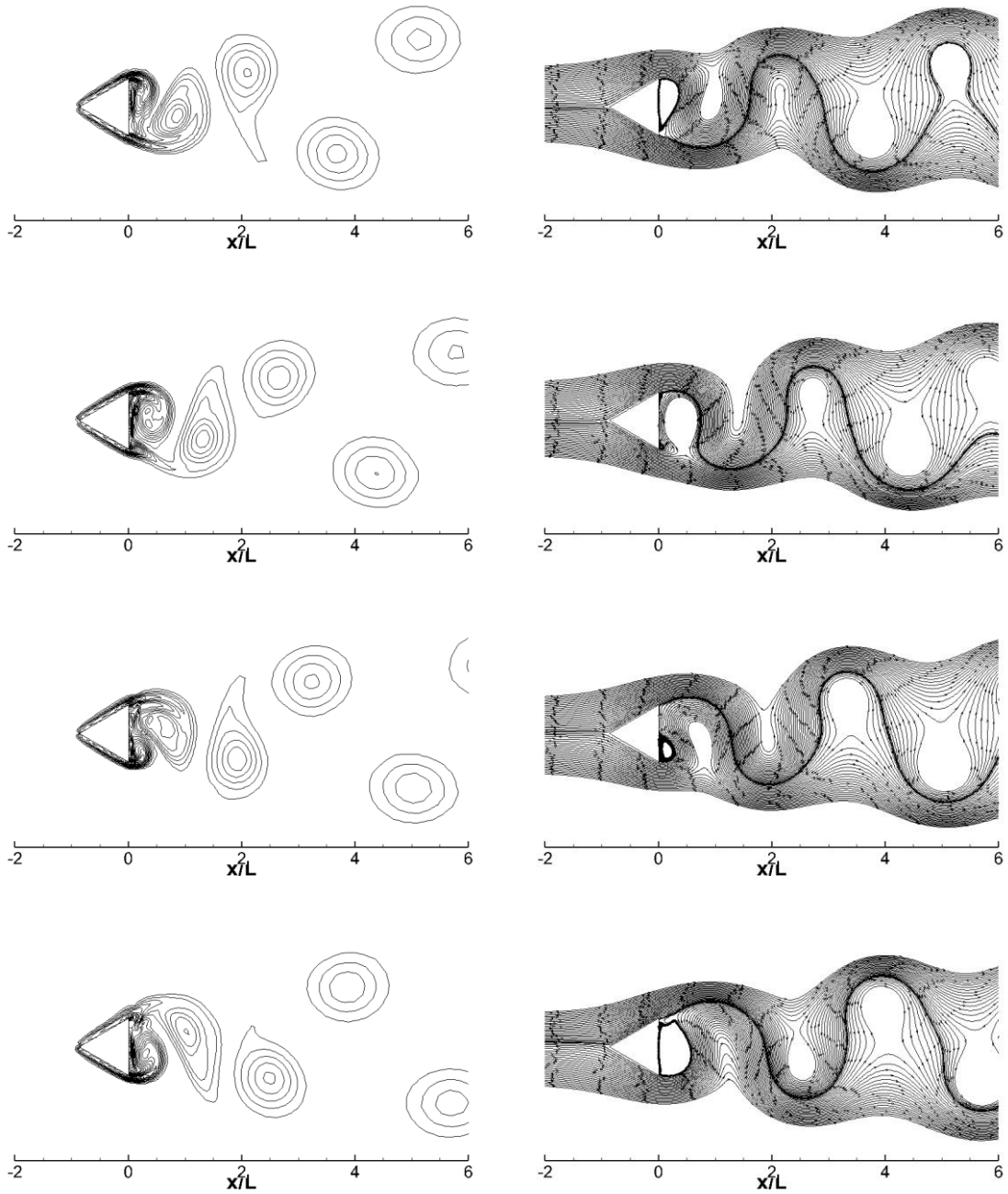


**Fig. 68** Snapshots of instantaneous vorticity (left) and streamlines (right) in different time steps within a shedding cycle,  $Re=250$ , and  $M=0.1$ ,  $\beta=0.1$ .

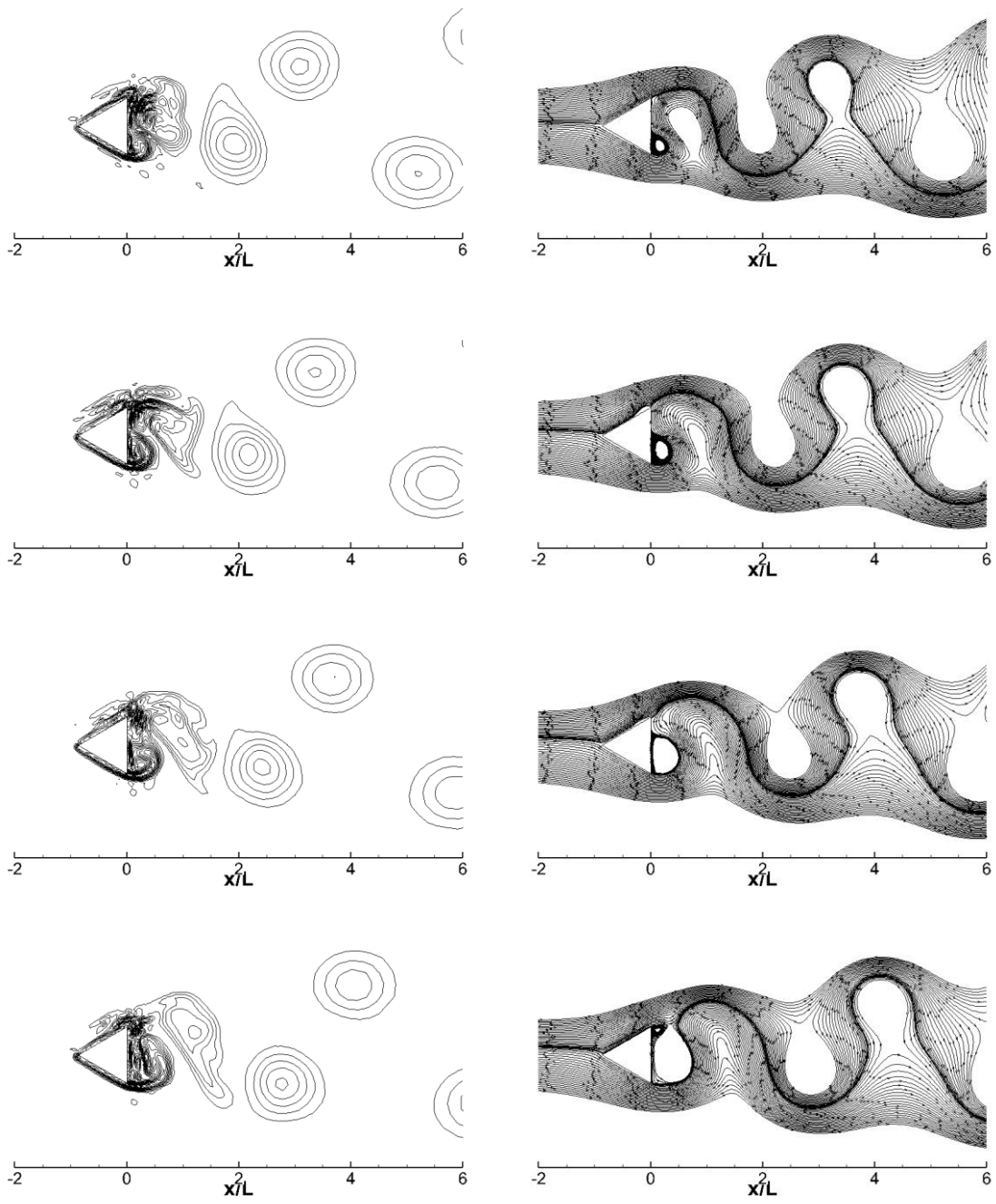


**Fig. 69** Snapshots of instantaneous vorticity (left) and streamlines (right) in different time steps within a shedding cycle,  $Re=250$ , and  $M=0.1$ ,  $\beta=0.5$ .

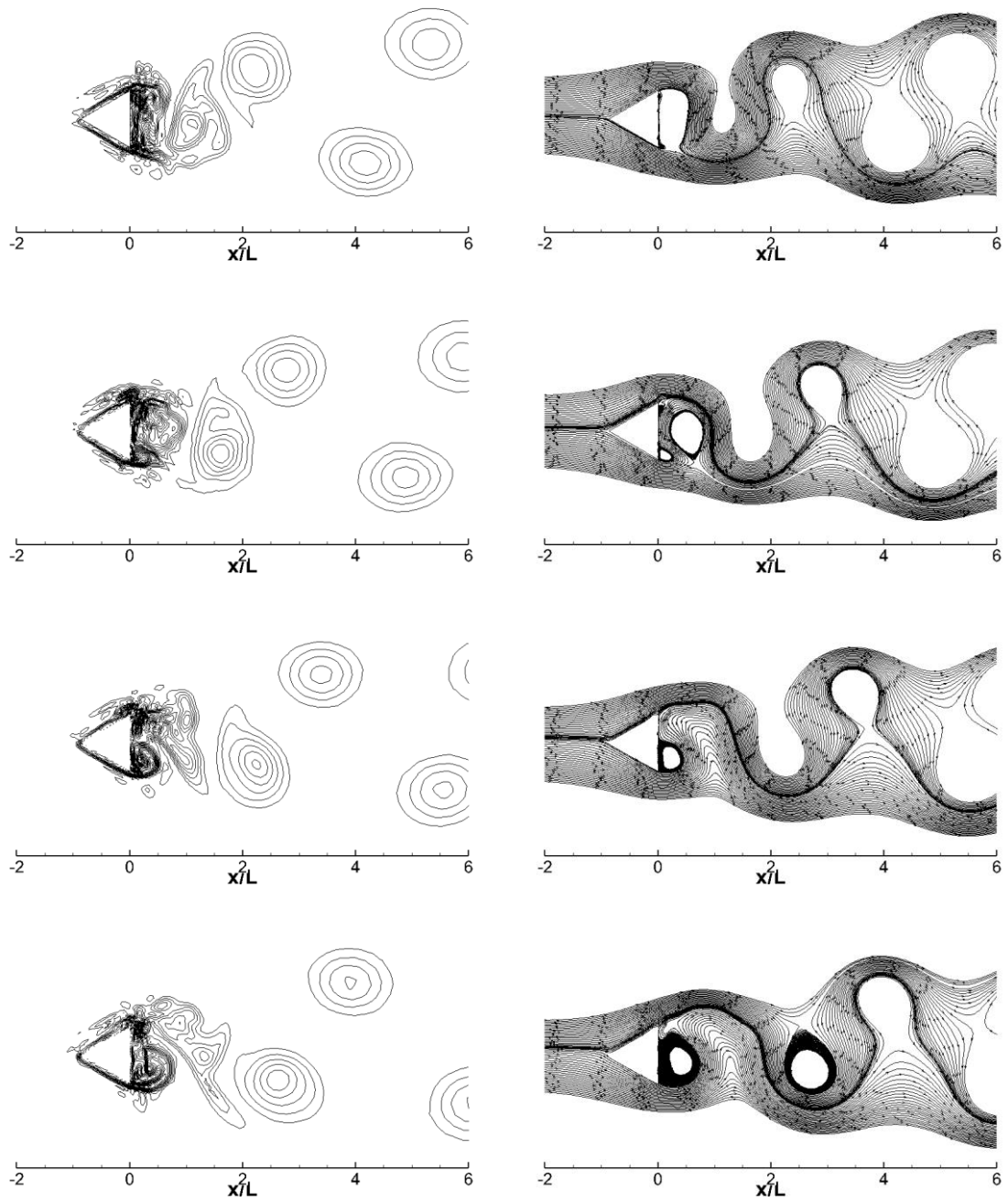


**Fig. 70** Snapshots of instantaneous vorticity (left) and streamlines (right) in different time steps within a shedding cycle,  $Re=250$ , and  $M=0.1$ ,  $\beta=1.0$ .

The effect of the addition of particles in  $Re=30$  and different Mach number flows is also investigated in Fig. 71 and Fig. 72 for  $M=0.1$  and  $M=1.2$ , respectively. In low Mach number flows, adding particles to the gas flow would lead to an increase in the size of the symmetrical vortices. In high Mach number flow, particles would produce an instability when the particulate loading is higher than a specific value.

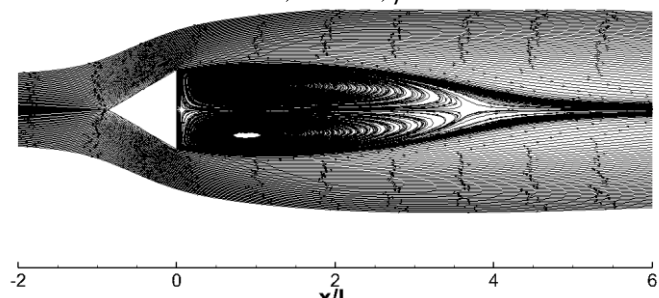
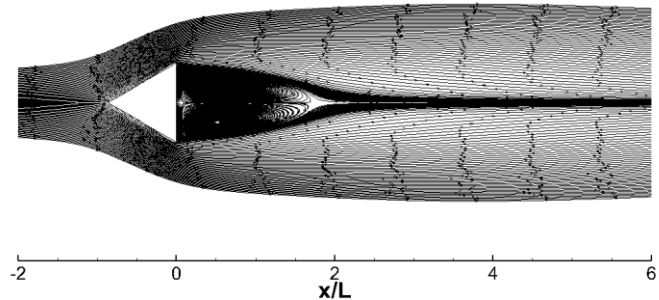
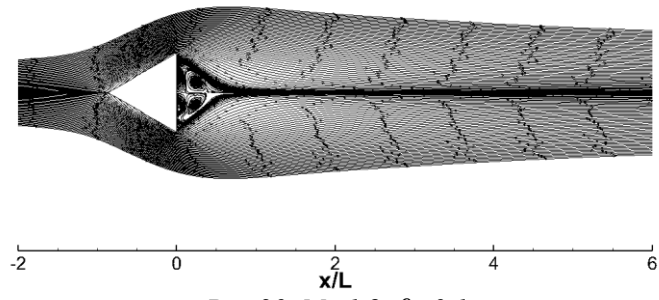
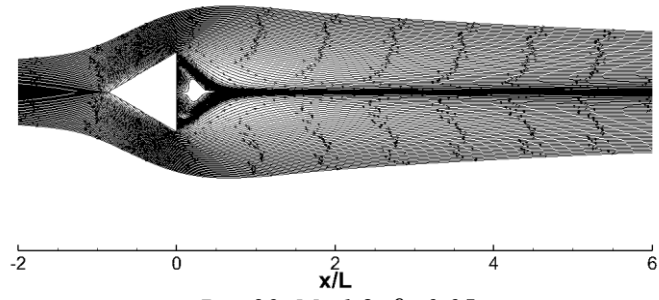
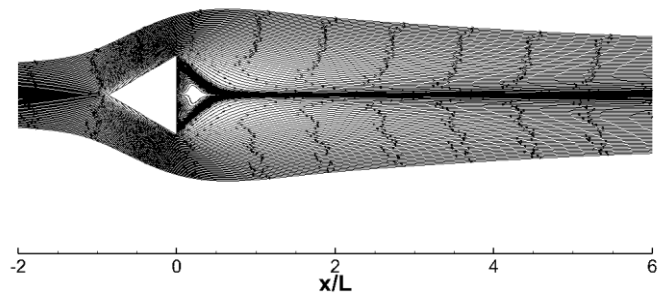
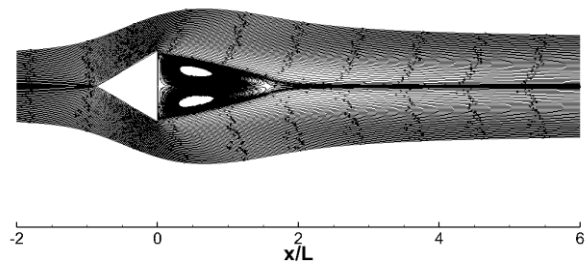
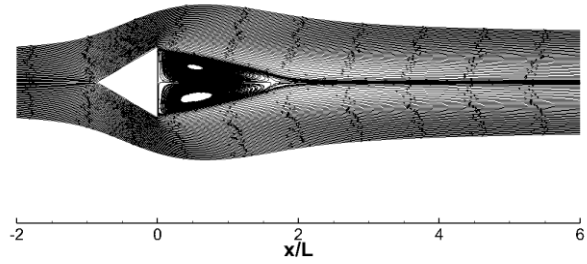


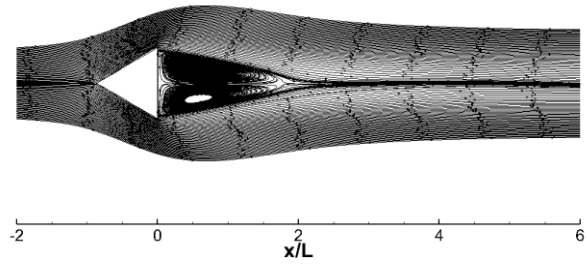
**Fig. 71** Effect of variation of particulate loading ( $\beta$ ) in low  $Re$  and high  $M$  number flow past the triangular prism



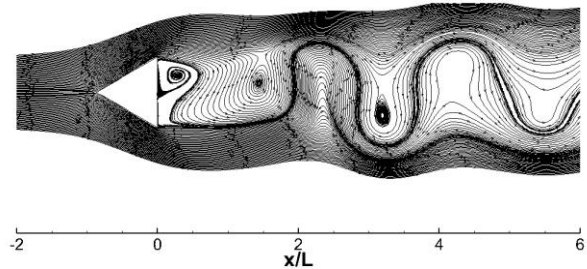
$Re=250, M=0.1, \beta=0.0$



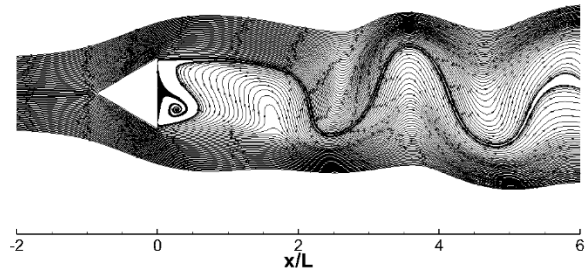
$Re=250, M=1.2, \beta=0.05$



$Re=250, M=1.2, \beta=0.1$



$Re=250, M=1.2, \beta=0.5$



$Re=250, M=1.2, \beta=1.0$

**Fig. 72** Effect of variation of particulate loading ( $\beta$ ) in low  $Re$  and high  $M$  number flow past the triangular prism

Regarding the dispersion of the particles by the vortices, as mentioned in [257] both the particle parameters and the carrier phase properties are in effect. The level of interaction of gas and particles depends on the Stokes number which depends on the relaxation time of the particles and the time scale of the fluid flow. As schematically shown in Fig. 73, for very small particles ( $St \ll 1$ ), the particulate phase will be in dynamic equilibrium with the carrier phase. Therefore particles would closely follow the streamlines of the vertical flow. On the other hand, large particles ( $St \gg 1$ ) will be unaffected by the vortices of the fluid flow due to large inertia. There may be an intermediate case where intermediate particle sizes ( $St \approx 1$ ) tend to be centrifuged from the vortex cores and accumulate at the edge of the vortices leading to inhomogeneous particle concentrations.

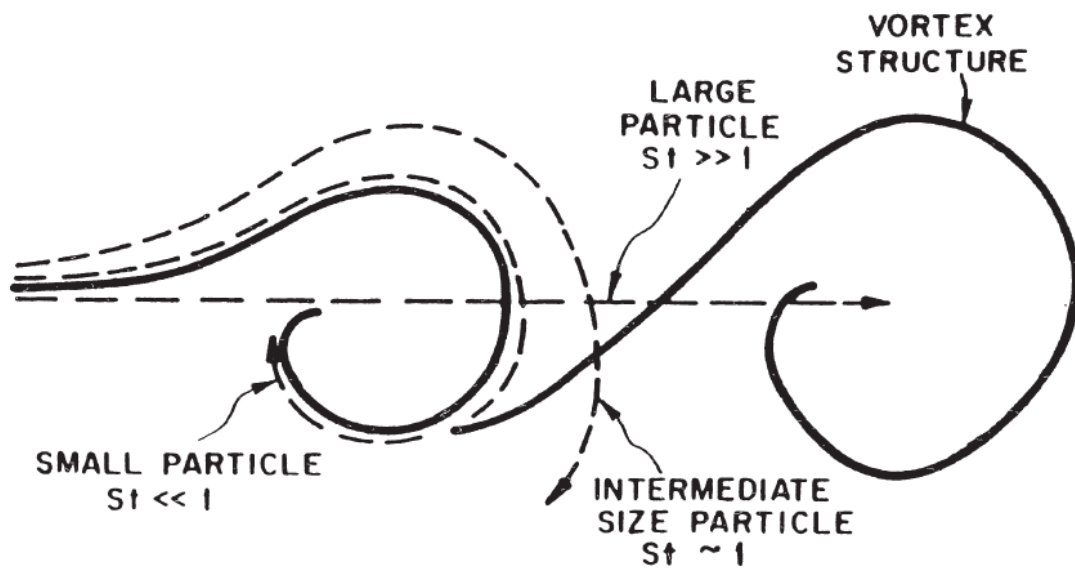
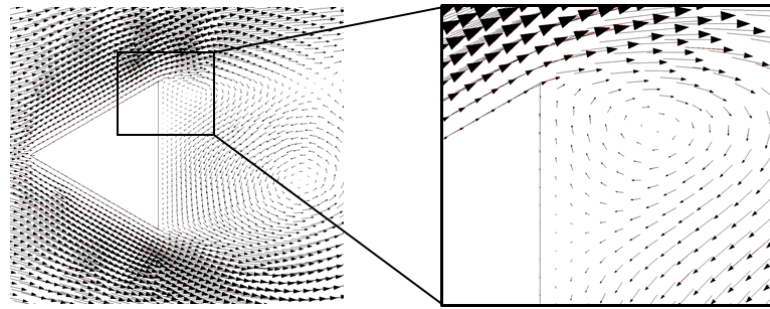


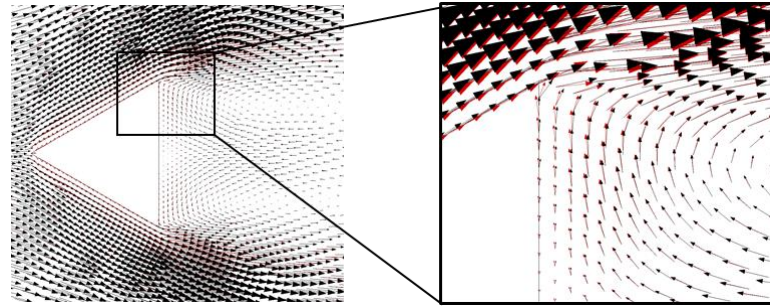
**Fig. 73** The schematic representation of the effect of Stokes number on particle dispersion in vortices. Reprinted from [257] with permission.

While the above discussions are on the particle parameters, similar interpretation can be inferred regarding the variation of Stokes number by fluid flow. In Fig. 74, the velocity vectors of the dust phase and gas phase are compared for two different Mach and Re numbers. In both cases, as the flow is decelerated behind the cylinder, particles cannot

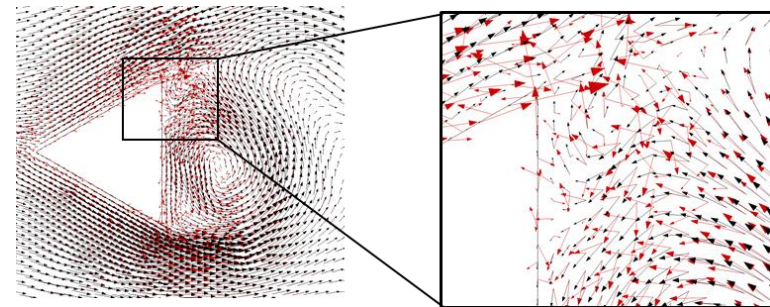
follow the gas phase trajectory. When the Reynolds number is low ( $Re=30$ ), particles can follow the gas streamlines. In this case, by an increase of the Mach number, the velocity vectors of particles show a slight deviation from that of the gas. However, when the Reynolds number of the flow is large ( $Re=250$ ), deviation of particles path from gas is more significant. Unlike the low Reynolds test case, this deviation is more critical for the case of low Mach number flow. This effect is probably due to the two-way coupling effects, by which the gas phase itself is affected by the particle phase.



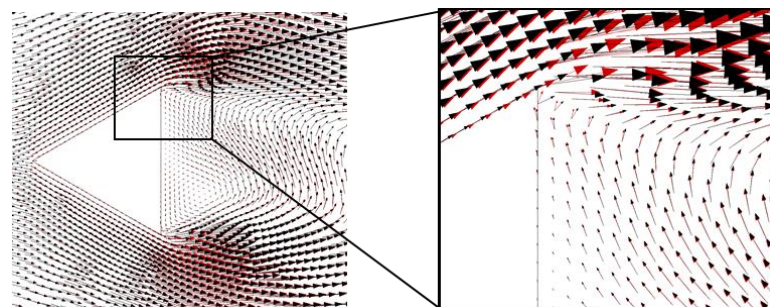
$Re=30, M=0.1, \beta=1.0$



$Re=30, M=1.2, \beta=1.0$



$Re=250, M=0.1, \beta=1.0$



$Re=250, M=1.2, \beta=1.0$

*Fig. 74 The effect of fluid properties on particle dispersion in vortices using velocity vectors of gas (black) and particle (red) phases.*

### 7.3 Axisymmetric particle-laden under-expanded jet

The under-expanded jet which was partly investigated in Chapter 6 for zeroth-order constitutive relations (Euler-type) is further investigated using first-order constitutive

relations (NSF-type) in this chapter. Here, in addition to providing the similar verification and comparison with experimental solutions (Fig. 75), the effect of particle phase on the flow is studied in terms of Stokes number. According to equations (5) and (8), the Stokes number can be assigned by variation of different parameters including particle diameter, the density of the particle phase, the viscosity of the carrier phase or characteristics time of the flow. Here Stokes number is artificially assigned by multiplying a constant coefficient in the source terms so that only coupling effects are investigated. It has been demonstrated through experiments of Sommerfeld [143] and simulations in Chapter 6 that the Mach disk location moves towards the jet exit plane by the increase of the particulate loadings. However, in Fig. 76 a counter-intuitive behavior is observed in case of high Stokes numbers. It can be seen that not only the Mach disk distance from jet exit plane do not decrease, but also it increases for Stokes number higher than 10. In high Stokes number flows dust particles can follow the gas streamlines closely as shown in Fig. 77.

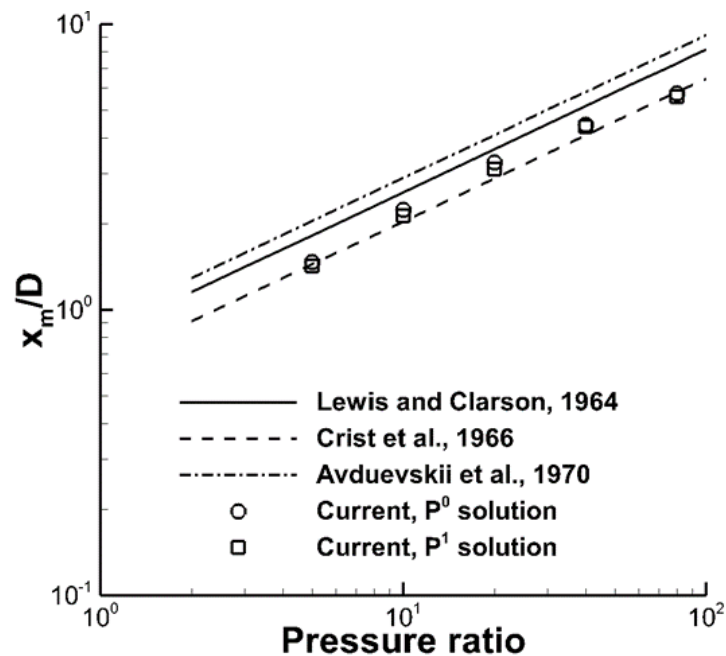


*Fig. 75 Prediction of Mach disk location in comparison with experimental results*

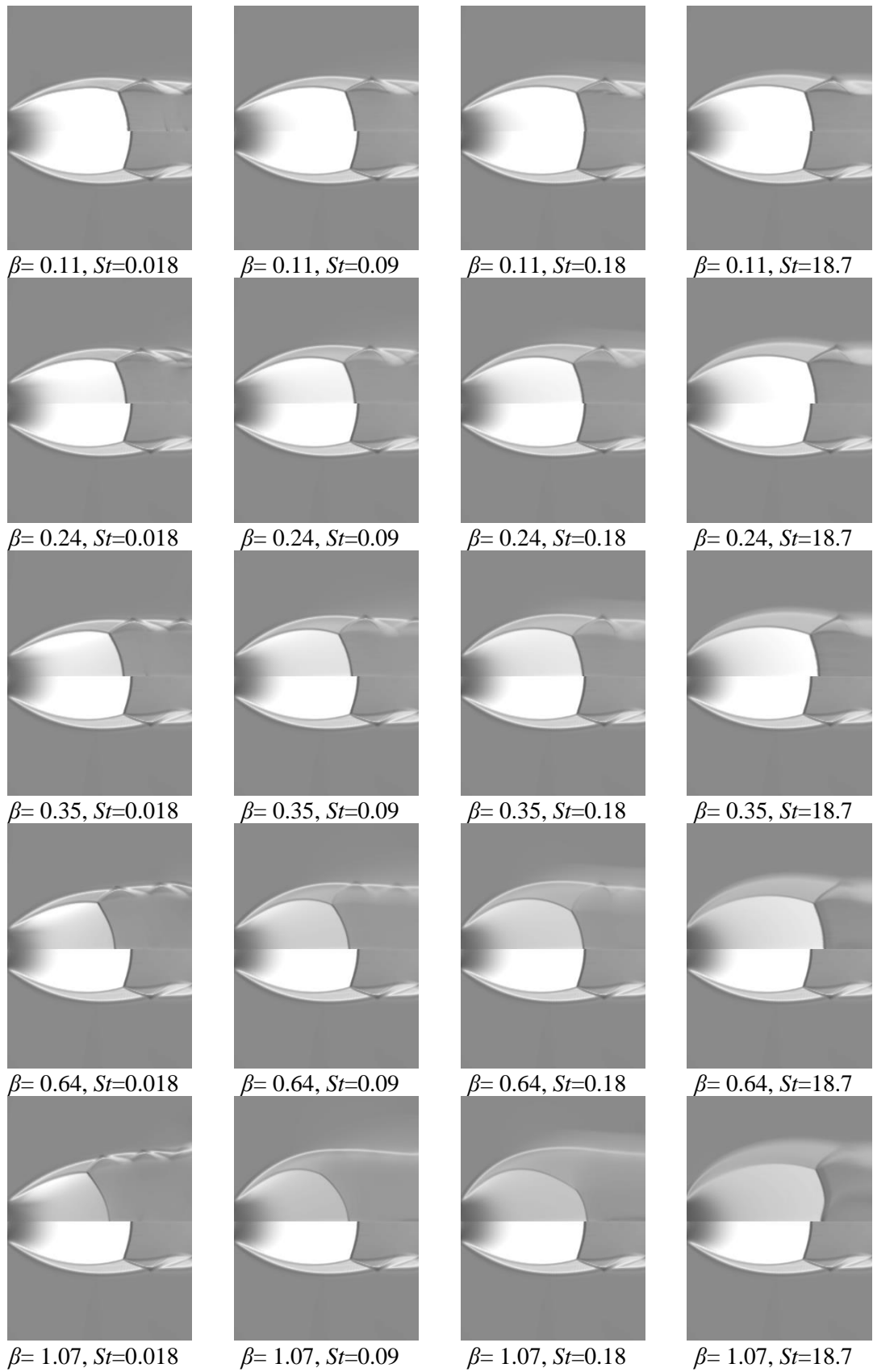


**Fig. 76** Effect of variation of particulate loading and Stokes number on Mach contours in the under-expanded jet problem

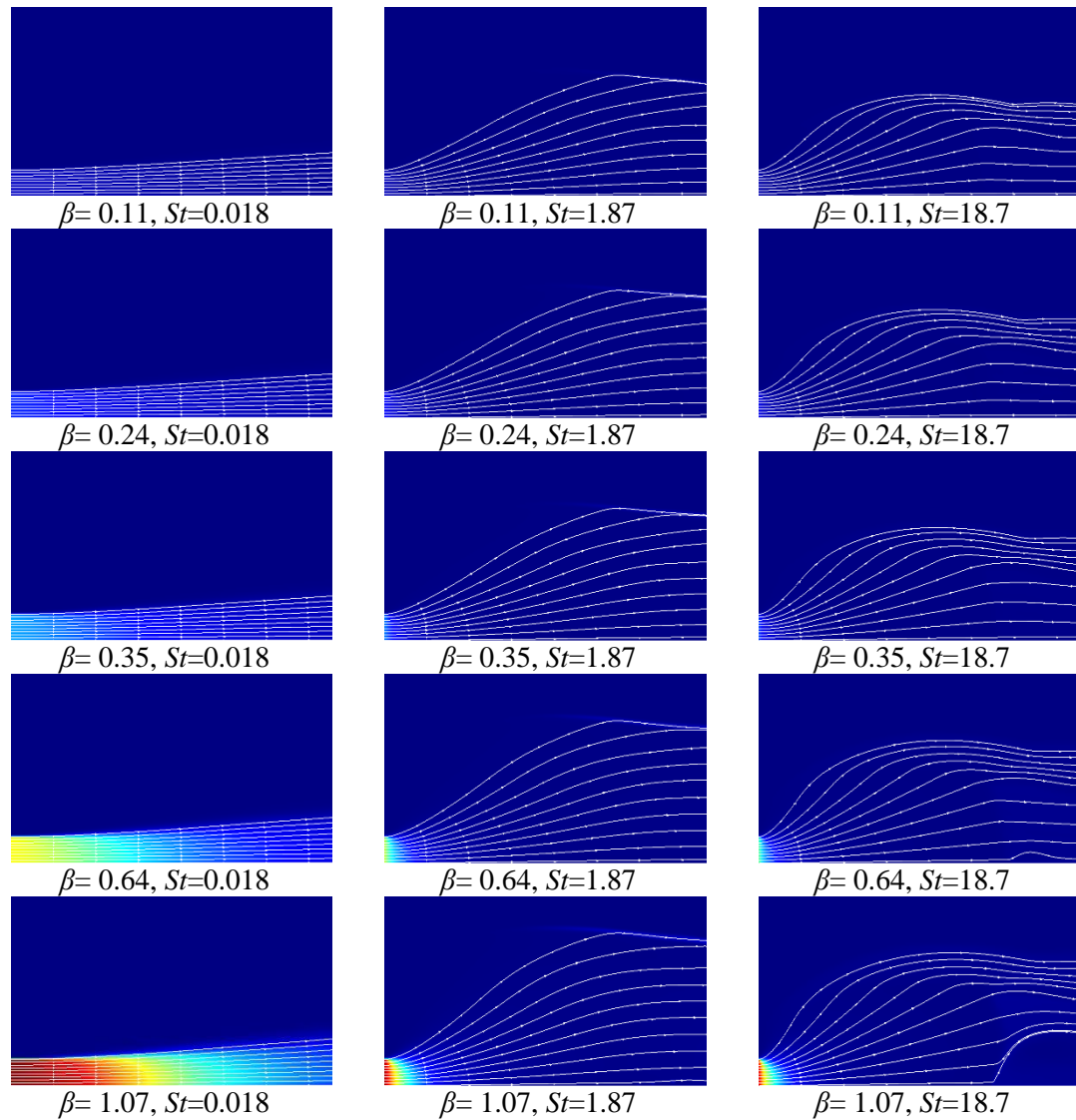


**Fig. 77** *Effect of variation of particulate loading and Stokes number on density contours and particles streamlines in the under-expanded jet problem*

## 7.4 Tone producing under-expanded impinging jets

When it comes to dynamics of compressible jets, a classical problem of interest is the impingement of a supersonic jet onto a perpendicular plate. A jet is called under-expanded when the pressure ratio exceeds a critical value (1.893 for air). During the interaction of an under-expanded jet with an impingement surface, the flow field is dominated by the complex shock structures. In atmospheric pressure condition or in case of high inflow Re numbers, this structure experiences an intense acoustic field with discrete-frequency sound (also known as a tone-producing jet). While the steady-state structure of the flow will be

characterized only by the nozzle pressure ratio and the impingement distance, the unsteady behavior of the acoustic waves depends on the exit jet Re number as well. An under-expanded jet itself (without considering wall impingement) can experience instabilities. These instabilities (demonstrated in ) are due to the reflection of expansion waves (produced at the nozzle lip) from the constant pressure jet boundary in the form of shock waves and generation of new expansion waves as the shock is reflected from the axis. The shearing process in the interaction of supersonic flow of the jet boundary and the atmospheric gas generate vortices. The shock cell structure and vortices interaction account for the noise radiated from the jet.

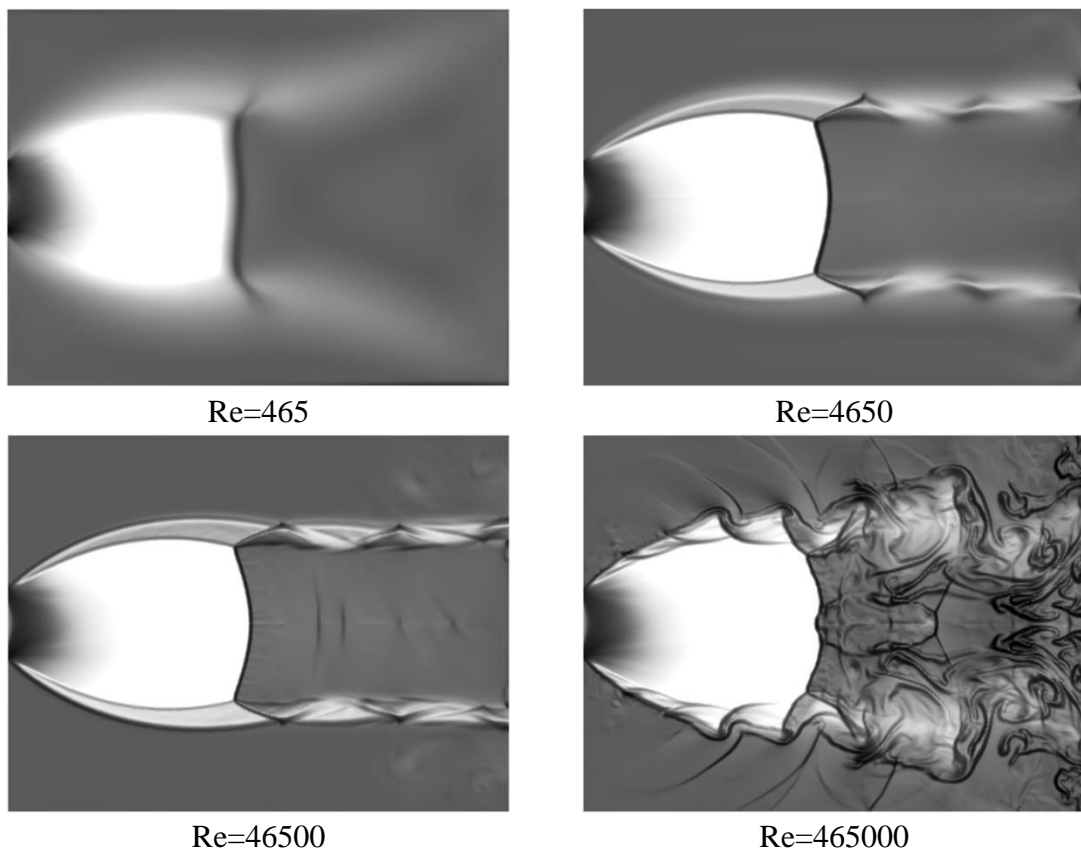
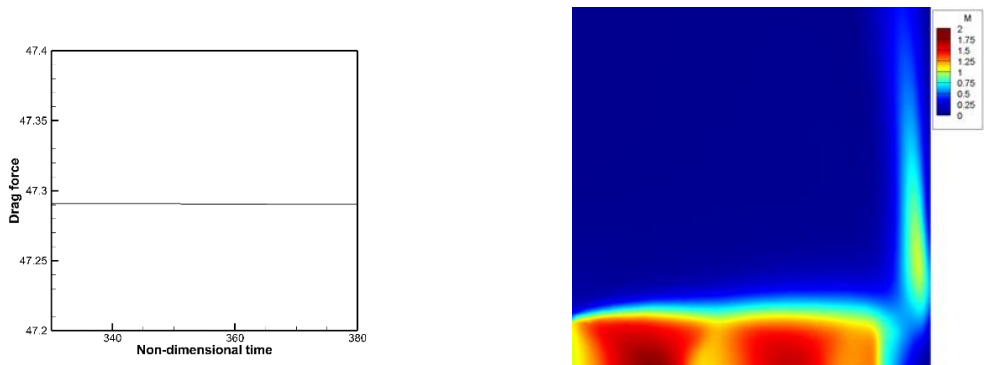


**Fig. 78 Instantaneous Mach contours of under-expanded jet depicting the flow instabilities for high Re flows**

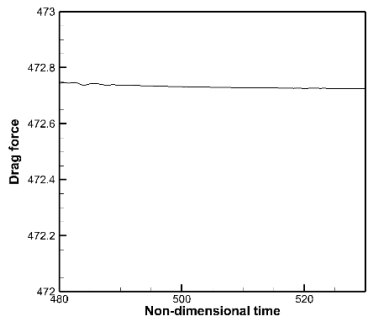
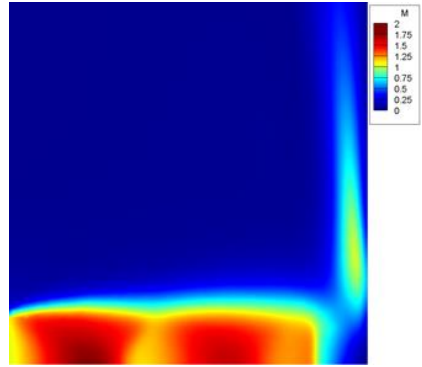
These oscillations are illustrated in Fig. 78. It should be noticed that for low Reynolds number test cases the viscosity damps these oscillations.

In case a surface is placed downstream of the jet a feedback model is formed. The waves at the impinging locations are reflected towards the nozzle perturbing the shear layer. Then a process known as collective interaction makes large-scale structures to form which impinge on the plate and the cyclical loop is repeated continuously.

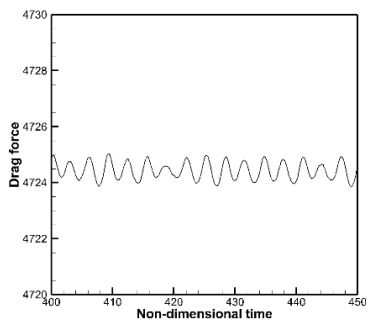
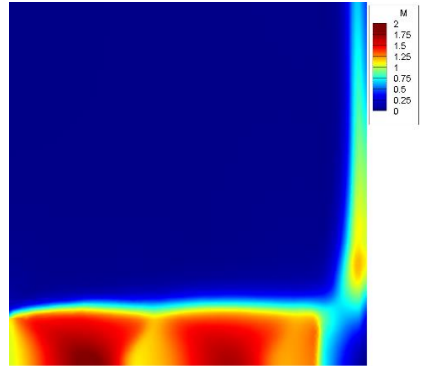
This oscillatory behavior is investigated via plotting the drag force on the impingement surface for different jet Re number. A transition from steady drag behavior to unsteady is observed which is due to the feedback loop discussed above. Therefore, for higher Re number flows a non-uniform jet with lateral or helical oscillations.



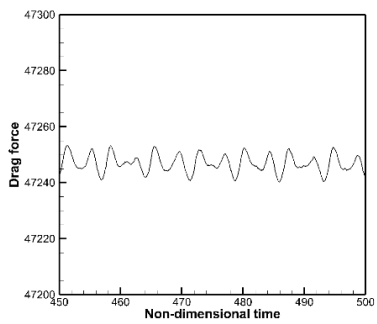
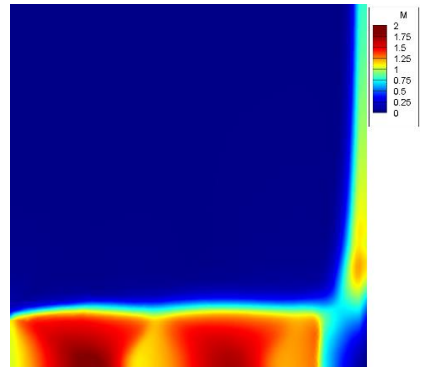
(a)  $Re=1000$



(b)  $Re=10000$



(c)  $Re=100000$



(a)  $Re=1000000$

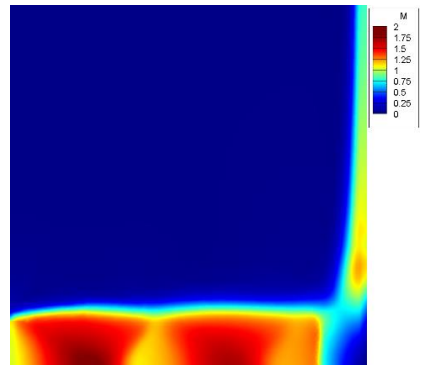


**Fig. 79 Effect of variation of jet Reynolds number on oscillatory behavior of the impinging jet**

To further validate the applied scheme for impinging jets in low pressure-ratios and in the atmospheric condition, the density solution in comparison with mean schlieren image is provided. A good qualitative agreement is demonstrated in Fig. 80.

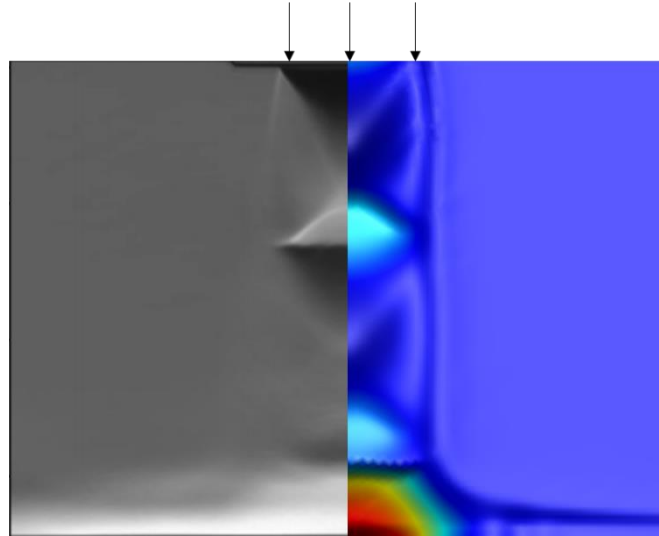


*Fig. 80 Comparison of mean schlieren image (left) and DG density solution (right)*

# Chapter 8. Numerical experiments on second-order NCCR-type systems of equation

## 8.1 The problem of Lunar landing

Moon has a tremendously different environment compared to that of the earth. The extremely weak gravity on the Moon cannot hold an atmosphere. Therefore, only the heavy gas particles that rarely collide with one another would form an exosphere (100 molecules per cubic centimeter compared to 100 billion billion molecules per cubic centimeter on Earth's atmosphere at sea level). In such a rarefied atmosphere where the Sunlight would not be blocked, and heat cannot be trapped, temperature variations are also significant (i.e., 123 Celsius in the daytime and -233 Celsius at night). As explained before, during the final stages of a *soft landing* on the Moon, when the Lunar lander approaches the dusty surface of the Moon, the interaction of engine plume and Lunar regolith cause a surface erosion and consequently dispersion of particles into the flow-field. This interaction would lead to some severe consequences, including the pilot's vision reduction, damage to the descent module or previously established sites on the Moon, false instrument readings, to name a few. Apart from the rarefied condition and presence of dust particles there exists a number of other complexities (e.g., mixed subsonic-supersonic regimes, shock-expansion interaction, shear layers) which make the simulation of descent phase an exciting subject from CFD point of view. In this section, we first introduce the prevailing physics observed in a Lunar landing problem, then our methodology for the simulation will be outlined, and finally, some simulation results will be presented.

## 8.2 Prevailing physics

In Fig. 81 the schematic of the problem (descent phase of Lunar lander) is illustrated. To explain the physical phenomena that govern the flow, some of the regions of the domain with essential features are marked by numbers on the figure. Region 1, shows the formation of the expansion fan at the lip of the nozzle. Region 2 marks the continuum flow exhausting from the descent engine characterized by high Mach and low Knudsen numbers. Number 3 defines the surface through which continuum assumption breaks down. Due to the presence of a surface opposing the exiting jet a strong stand-off bowl-shaped shock (number 4) forms and gradually weakens by deviation from the axis. The location of this shock wave will largely depend upon the external ambient pressure or exit to ambient pressure ratio. Right after the normal shock and exactly underneath the nozzle the flow recompresses to a near-continuum condition in the stagnation region marked by number 5. The virtual diverging channel formed by the stand-off shock and the Lunar surface expands the flow in the radial direction. The flow after reaching to sonic speed at the sonic line (number 6) gains supersonic speeds and expands further into the near vacuum condition. In a region in the proximity of the sonic line, a supersonic boundary layer forms causing dynamic pressure which is the source of viscous erosion to maximize. Hence peak of the mass flux of the eroded particles can be observed at somewhere near this point. The entrained particles then gain supersonic velocities and can travel significant distances away from the landing site as negligible drag force of rarefied atmosphere cannot impede the debris particles seriously.

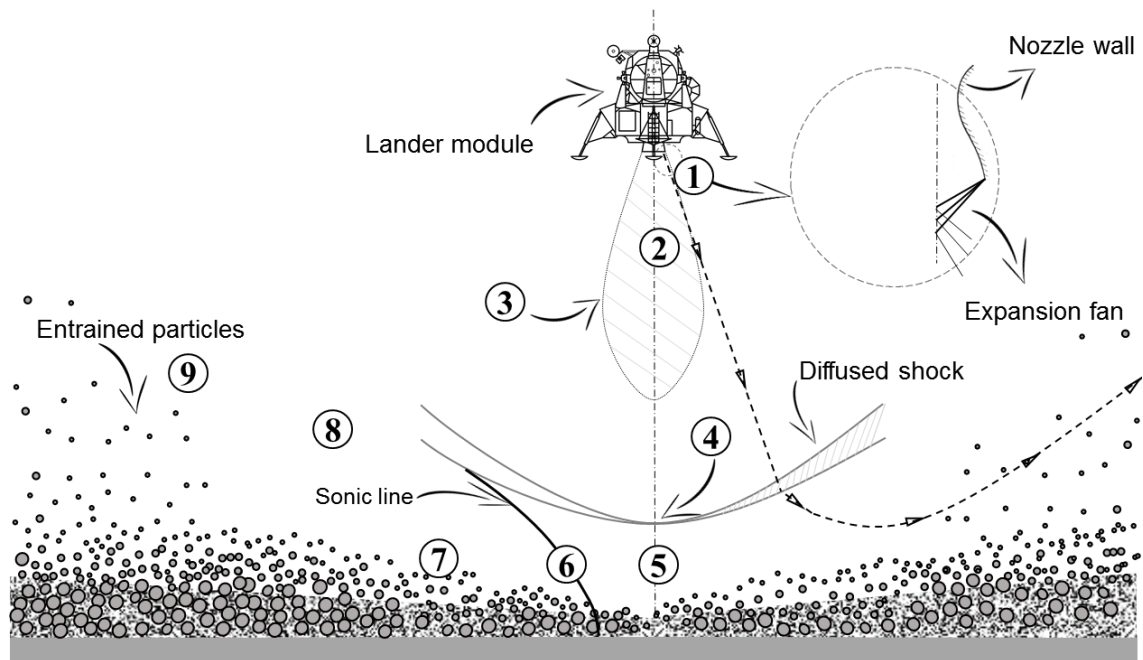


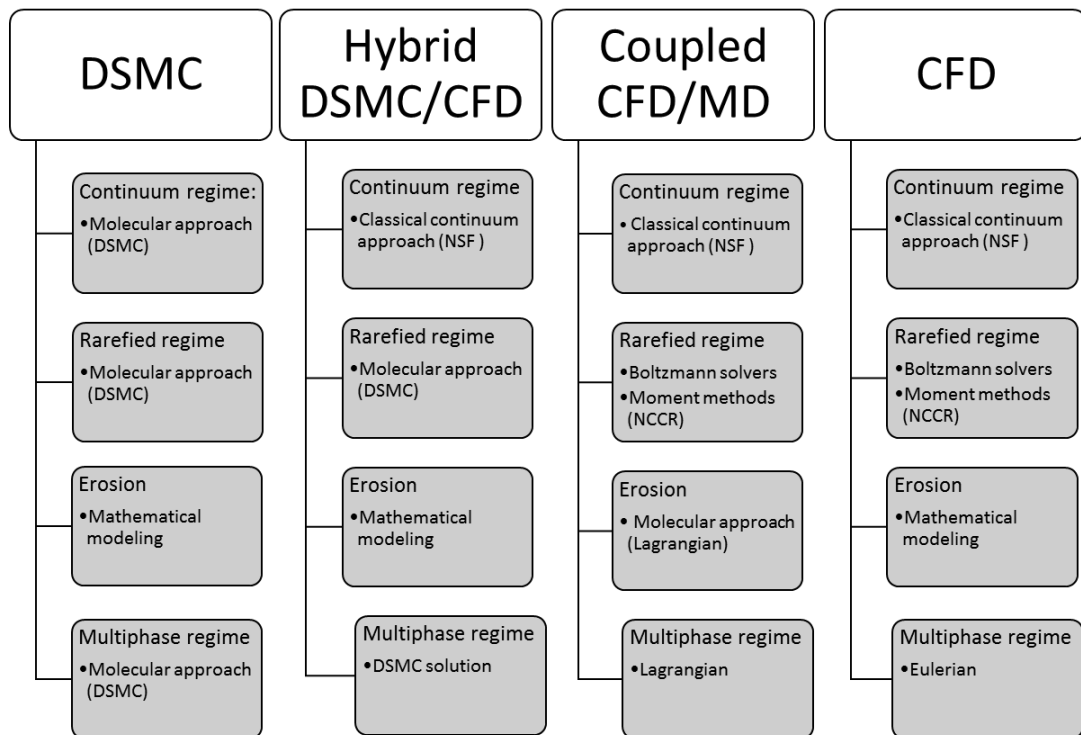
*Fig. 81 The prevailing physics in the descent phase of a Moon landing*

### **8.3 The approach for simulation of the Lunar landing problem**

Various strategies can be applied in order to simulate this problem numerically. Almost all of the works in which this problem was investigated were briefly reviewed in Chapter 1. A summary of the four possible strategies among many other strategies is provide in Table 19. Other approaches by combinations of other methods for handling the rarefied regime and the dust phase can be also achieved which may suggest positive and negative consequences. To the best knowledge of the author, this is the first fully continuum-based approach for solving this problem to date. A full continuum-based approach is beneficial in various aspects. First and foremost, this methodology is computationally efficient. With the various parameters which can influence the physics of non-equilibrium multiphase flow, availability of a tool which can provide the final solution in a matter of few computational hours with an acceptable level of accuracy is an asset. Moreover, the implementation of this strategy can be easily achieved. Almost all the well-developed schemes for the gas

phase can be applied to the dust phase directly (or with some modifications). The other advantage is that the applied strategy allows for a broader range of Mach-Knudsen regime for the gas phase as well as a more broad range of particulate loadings for the dust phase making it a general tool for investigation of various other problems with similar pre-requisites.

**Table 19 Four possible approaches for solving the Lunar landing problem**



The chart in Fig. 82 depicts how the desired algorithm is implemented in an in-house CFD code. The procedure is straightforward: the mesh produced by grid generation software will be fed into the computational code. The flow-field is initialized and solved with the assigned boundary conditions. The NCCR module which was discussed in detail in Chapters 3 and 4, can take into account the non-equilibrium effects. The erosion modeling is made possible by an extra boundary condition. This boundary condition applies the gas phase solution and estimates the local mass flow rate of the particles based on either the dynamic pressure or the shear stress on the erosive wall surface. The estimated

mass flux is then in-fluxed into the computational domain through surface cell faces. With the Eulerian-Eulerian algorithm, both loose and strong couplings can be achieved via source terms. As the applied Eulerian solver uses an explicit algorithm, the transient phase can also be captured. The calculation can be stopped as soon as the criteria for steady-state solution are met.

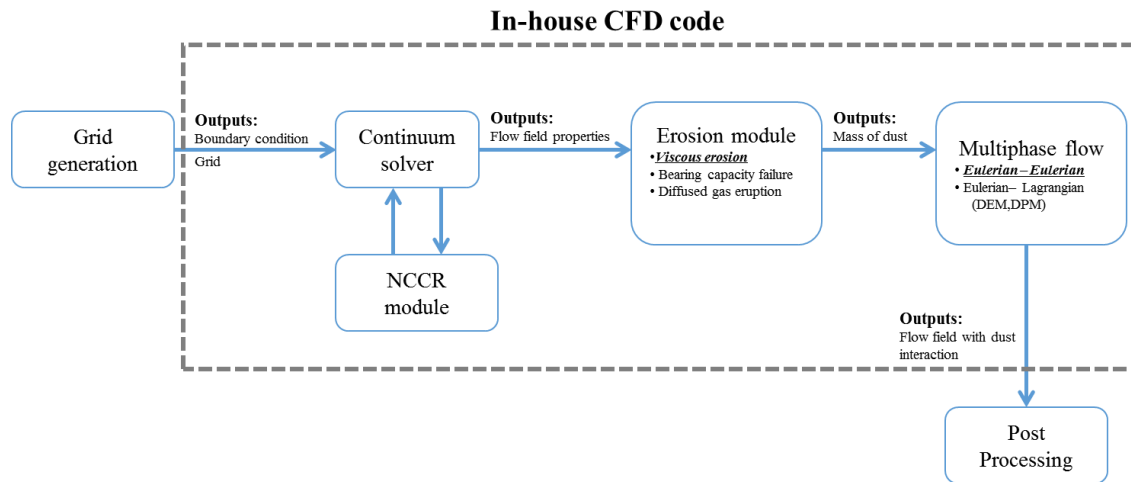


**Fig. 82 Schematic of the implemented algorithm depicting the input and output of each module.**

The computational domain and the type of boundary conditions that are applied are demonstrated in Fig. 83. Viscous wall boundary condition is applied on the nozzle and Lunar surface. Symmetry condition is assigned on the axis. The nozzle chamber condition can be assigned on the inlet of the converging-diverging nozzle. On the other boundaries of the domain, the ambient condition of the Lunar atmosphere can be assigned. The other alternative for these boundaries is the application of supersonic outflow condition.

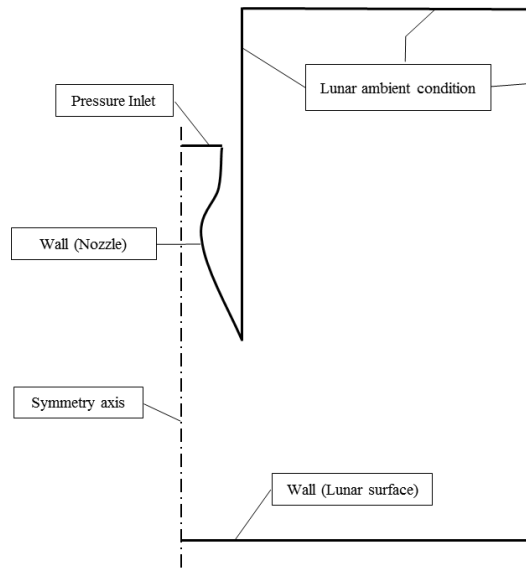


**Fig. 83 The schematic of the computational domain and type of applied boundary conditions**

In all the simulations of this chapter axisymmetric equations are applied. On the nozzle inlet, a pressure inlet boundary condition is assigned. The viscous wall boundary condition is applied to the nozzle wall and lunar surface. The symmetry condition is used on the symmetry axis. The rest of the boundaries are assigned as the Lunar ambient condition.

Before proceeding to the simulation of the plume and its interaction with the surface, the internal flow inside the nozzle is investigated. The contoured nozzle profile of Apollo descent module [258, 259] is selected to keep consistent with [48], and thus to make a comparison with Apollo observations possible. The details of the Lunar module descent engine (LMDE) is also provided in [48]. However, we briefly repeat some of the essential features that may find importance in our simulations. The LMDE (a throttleable hypergolic engine) had a maximum thrust of approximately 44.5 kN. Exit to throat area ratio, specific impulse and exit diameter for this engine is reported to be 47.5, 305 s, and 1.67m, respectively. Furthermore, the designed propellant is Aerozine-50 (hydrazine and unsymmetrical dimethylhydrazine). The primary exhaust products are  $H_2O$ ,  $NH_3$ ,  $CO$ ,  $NO$ ,  $O_2$ ,  $CO_2$ , and  $NO_2$  [260]. However, in our simulations, either water vapor ( $H_2O$ ) or ammonia ( $NH_3$ ) which constitute the highest mole fractions in the exhaust product are

applied. It should be noticed that inside the nozzle the flow is mostly inviscid and either Euler or NSF system of equations can provide satisfactory results. Also, the high temperature makes the gas chemically and vibrationally active. These effects are however neglected to simplify the problem.

In Fig. 84, the solution of internal nozzle flow is presented. As is evident from Fig. 84, the density, pressure, and temperature decrease as the gas expands through the nozzle contour and the velocity increases. An important feature is the presence of a weak internal shock characterized by the pressure ratio across the wave. The shock strength is variant in different cross-sections of the nozzle. Moreover, a thin boundary layer is formed which can be observed in Fig. 84 (e).

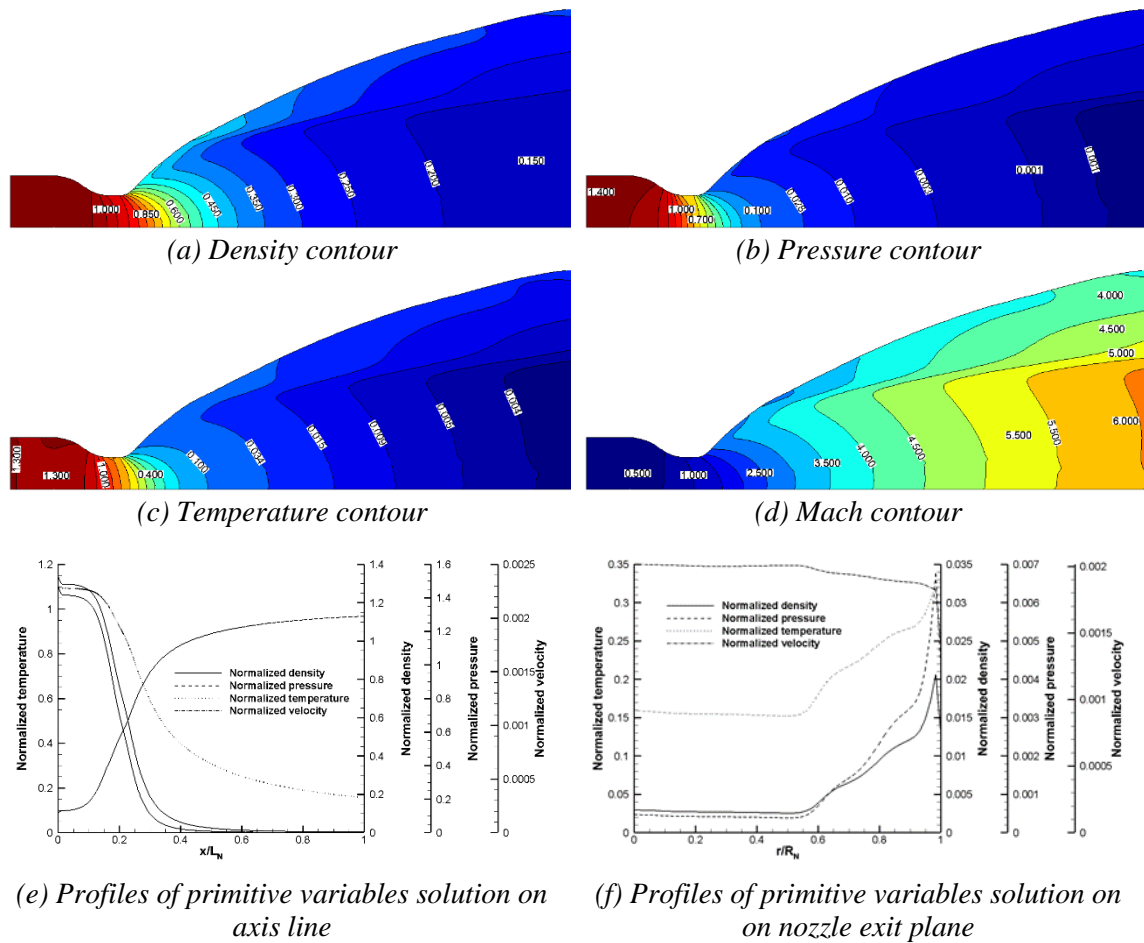


**Fig. 84** Solution of internal nozzle flow ( $P_{\text{ref}}= 141251.1542 \text{ Pa}$ ,  $T_{\text{ref}}= 2317.596567 \text{ K}$ ,  $u_{\text{ref}}= 1192.698279 \text{ m/s}$ ,  $L_{\text{ref}}=1 \text{ m}$ )

## 8.4 Pure gas simulations

In this section simulation results for verification and validation of the pure gas solver is provided. Fig. 85 presents a comparison of Mach solution with experimental mean schlieren image conducted by Land and Clark [44]. The applied gas here is the Nitrogen, and the exit Mach number is set equal to 5. The numerical results are in a good agreement with experiments.

Due to complexities that arise for setting up an experiment for this problem, very few experimental results are available. Even in these few experiments, the exact Moon conditions cannot be accurately simulated experimentally. Therefore, we continue our verification process by comparing our results with the previously done DSMC simulations, specifically the works of Morris [48].

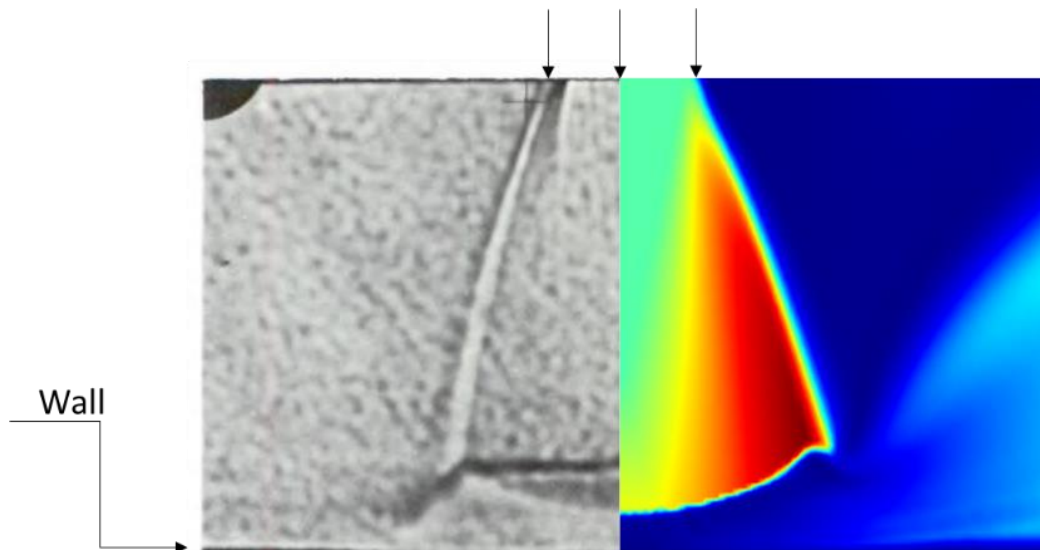


*Fig. 85 Validation of jet impingement on the surface with the experiment of [44] (Nitrogen gas,  $M=5.0$ ,  $Re=10000$ , Pressure ratio=3.79,  $h/D=6.7$ ) Comparison of mean schlieren image (left) and DG Mach solution (right)*

## 8.5 Verification of results with DSMC solutions for single-phase flow (pure gas)

In this section, the simulation results for Apollo LMDE are presented, and results are compared with solutions of [48]. A sample grid which is used in the simulation is shown in Fig. 86. It must be noted that the computational grid should be extended a reasonable distance from the exit jet in order to omit the boundary effects on the solution. Our numerical experiments show that when a finer grid is used the effect of boundary becomes smaller. In Fig. 87, the pressure solution of the second-order Boltzmann-based constitutive relationships (NCCR) with DSMC solutions are compared. It can be seen that the results are in a very good qualitative agreement. Slight deviations in height prediction of the normal shock and also the location of the reflection wave can be observed. These deviations may be due to the different nozzle profiles, differences in some of the setup parameters that are not explicitly mentioned in the [48] or the inherent different nature of the models in the DSMC and continuum theory.

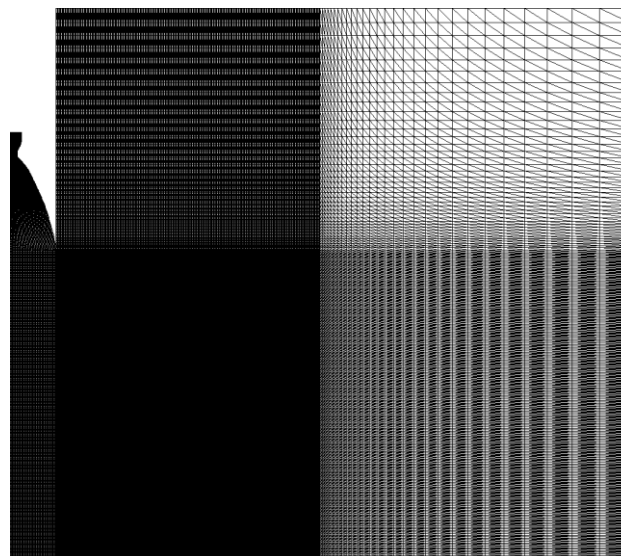


*Fig. 86 A sample computational grid for 5m of hover altitude.*

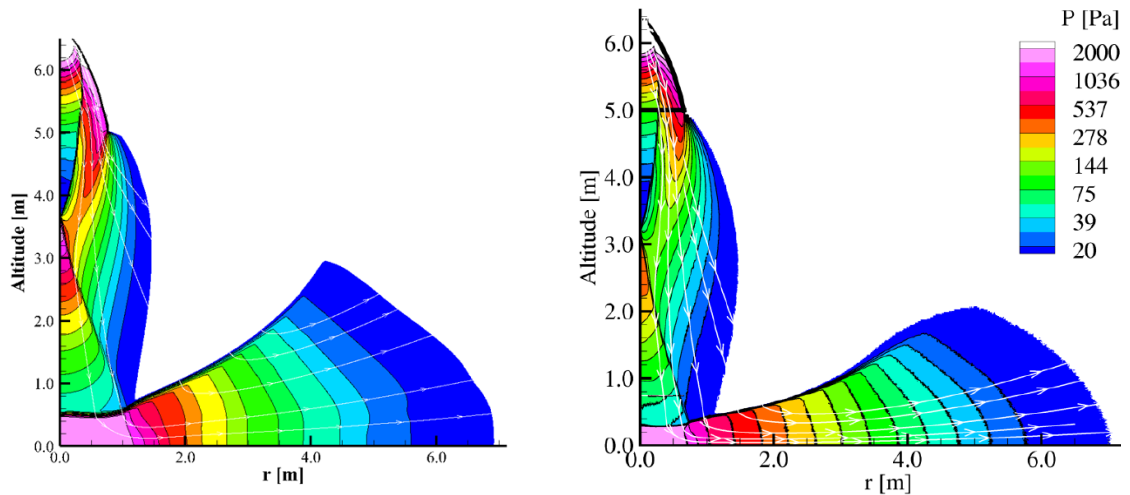
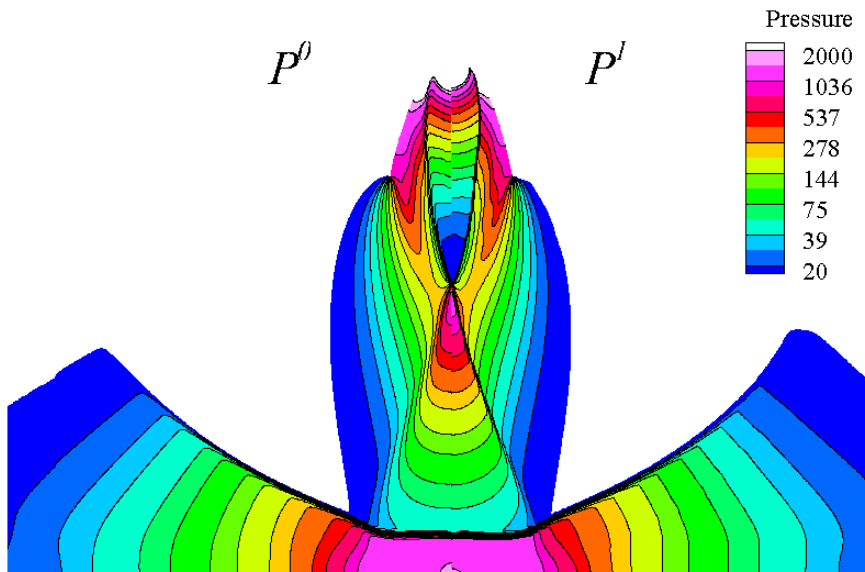


**Fig. 87 Comparison of pressure solution NCCR (left) and DSMC (right) solution of [48].  
Hover altitude: 5m**

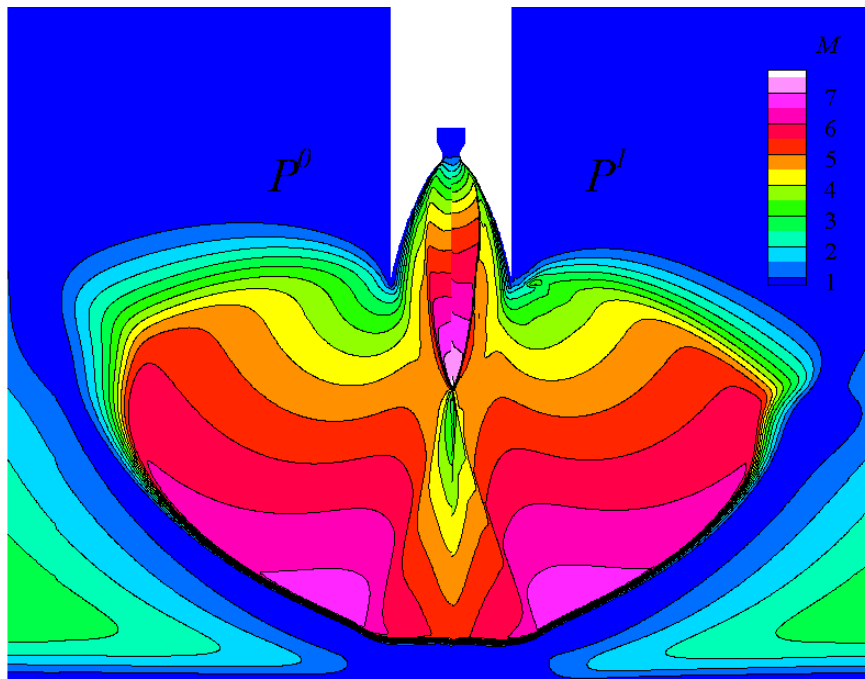
A comparison of first and second order solutions is provided in Fig. 88. Due to the application of a relatively fine grid resolutions, the second-order solution does not improve the quality of the solution significantly. However, it is expected to gain a better resolution (sharp discontinuities) when coarser grids are used.

Also shown are the comparison of NCCR and NSF solutions of pressure and Mach. Surprisingly the comparison shows that the application of first-order Boltzmann-based constitutive relationships in near-field flow can provide acceptable solutions. This is justified by the fact that the gas exiting the nozzle is in high density and most of the simulated region is in near-equilibrium condition.

To demonstrate the degree of non-equilibrium the Rayleigh-Onsager dissipation function is shown in Fig. 90. It is expected that for higher hover altitudes or when the far-field simulation is of interest the deviation from equilibrium gets more. The most important parameter which affects the structure of the under-expanded jet and impinging under-expanded jets is the exit to ambient pressure ration. The effect of variation of the jet structure in different ambient pressures is investigated in Fig. 91. In this figure, the left side contour shows the pressure distribution and the right one is the Mach contour.

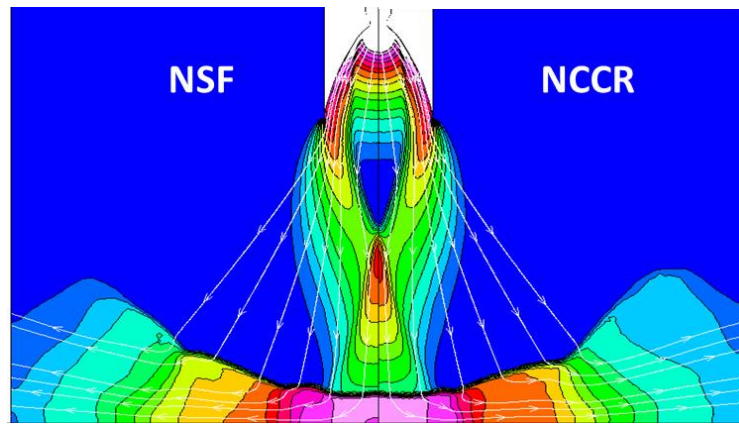


(a) Pressure solution

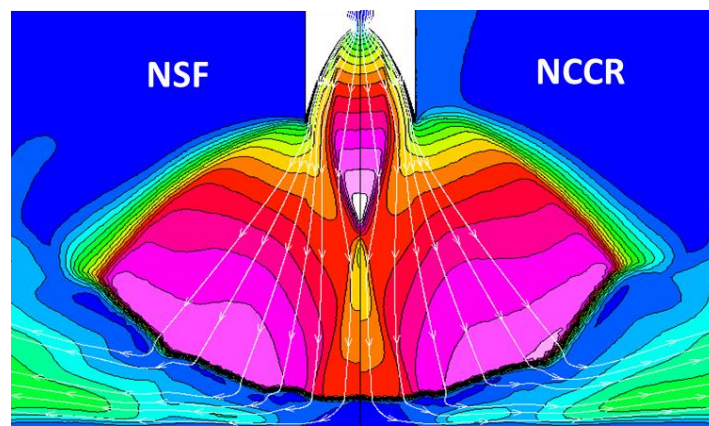


(b) Mach solution

**Fig. 88 Comparison of first-order (left) and second-order (right) solutions of pressure and Mach. Hover altitude: 5m.**



(a) Non-dimensional pressure contour



(b) Mach contour

**Fig. 89** Comparison of pressure (top) and Mach (bottom) solutions of first-order Boltzmann-based (NSF) with second-order Boltzmann-based (NCCR), Hover altitude: 5m.

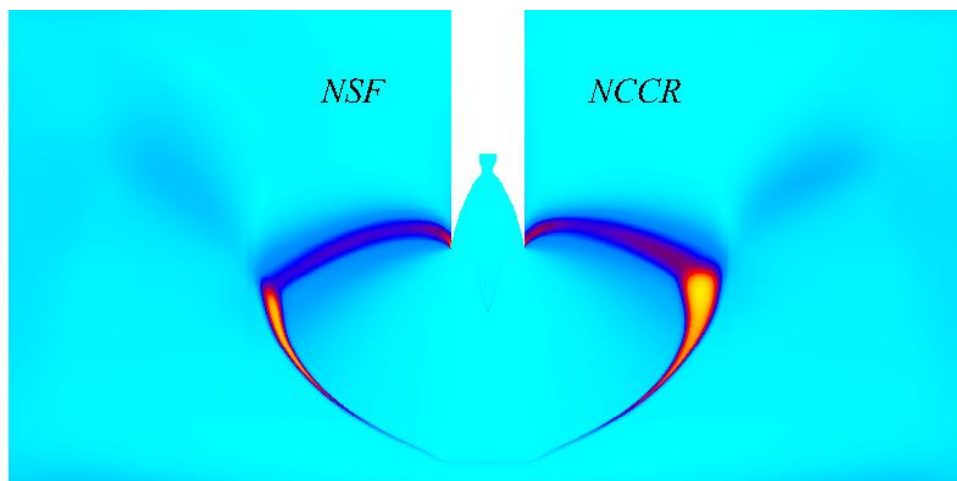
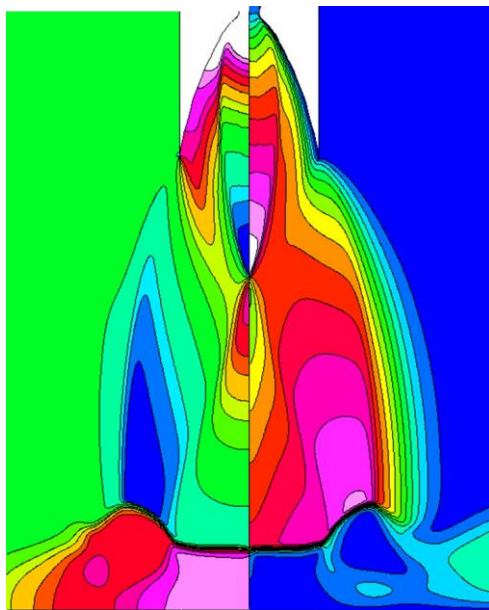
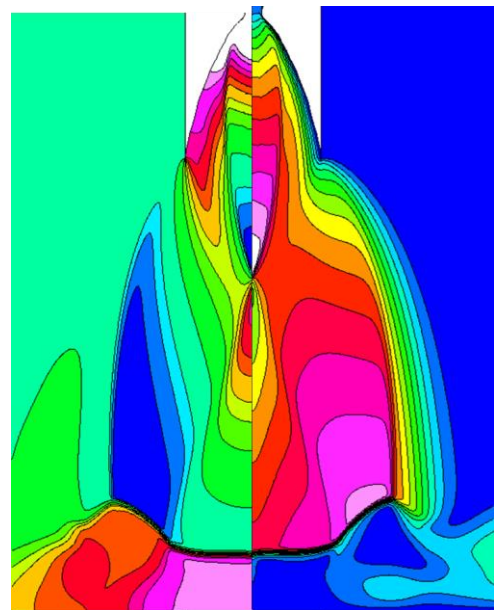


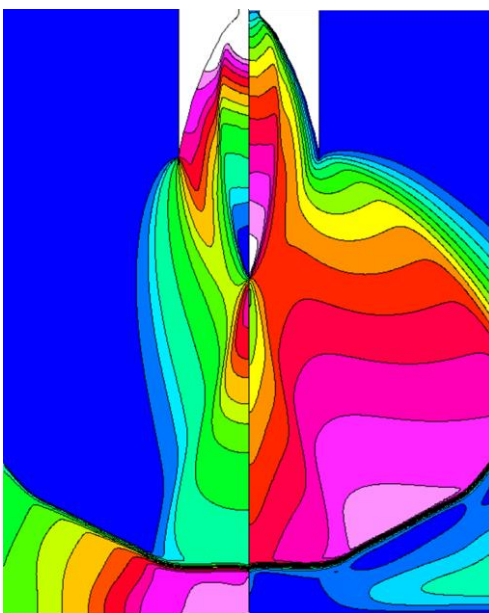
**Fig. 90** Comparison of Rayleigh-Onsager dissipation function for NSF (left) and NCCR (right)



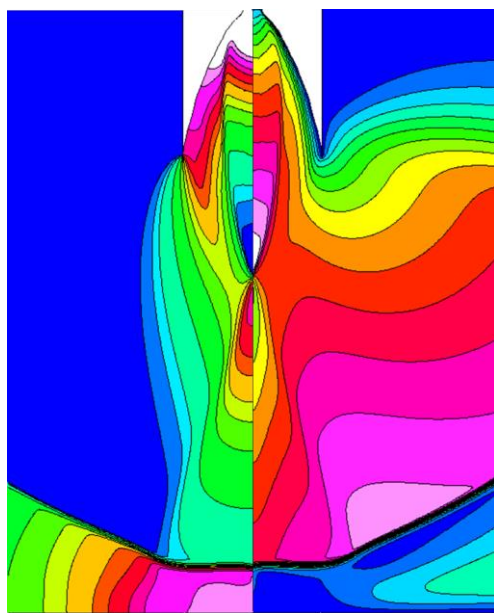
$P_{amb} = 50 \text{ Pa}$



$P_{amb} = 15 \text{ Pa}$



$P_{amb} = 5 \text{ Pa}$



$P_{amb} = 1 \text{ Pa}$

**Fig. 91** The effect of ambient pressure on pressure (right) and Mach (left) solution of the impinging jet.

As can be seen, the stand-off shock location gets closer to the surface as the ambient pressure decreases. Also, the radius of the normal shock wave changes substantially. The degree by which the jet is under-expanded is also strongly dependent on these parameters. As Mach contours reveal, the lower the ambient pressure, the more is the under-expansion.

## **8.6 Verification of results with DSMC solutions for multiphase flow (dusty gas)**

When the problem is simulated with the inclusion of nozzle the flow-field will be more complicated due to the presence of internal and reflected shocks. These complexities require higher grid resolutions to be captured properly. Moreover, as demonstrated in [48] the effect of the presence of the nozzle compared to the uniform flow on the erosion properties is negligible. Comparison of the number density solutions of NCCR with DPLR and hybrid DPLR-DSMC pressure solutions are provided in Fig. 92. It can be seen that the NCCR solutions are in a better agreement with DSMC solutions.

The shear stress on the surface is used in the erosion model in order to estimate the eroded mass flux. Morris [48] used the dynamic pressure in a distance (above the boundary layer) from the wall as the effective shear stress. The dynamic pressure at different distances from the wall is plotted in Fig. 93. It can be seen that the variation of this parameter can be large at different distances from the wall. Therefore, the application of dynamic pressure in Roberts' model might be improper. In order to omit the dependency of the model on such parameters it might be better to use a surface parameter such as wall shear stress.

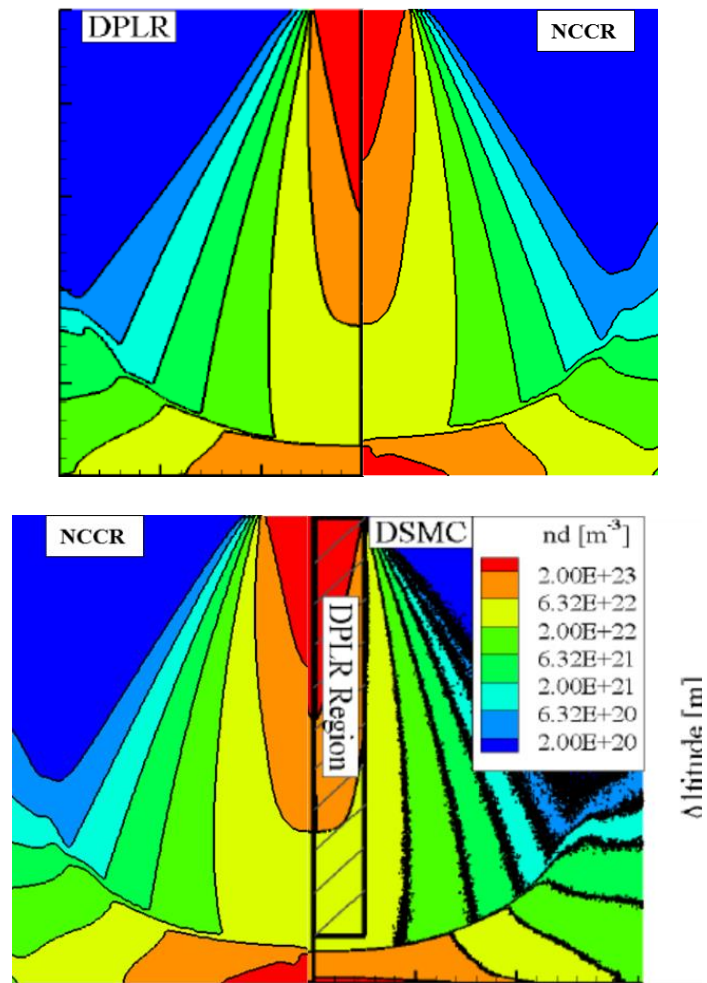


*Fig. 92 Comparison of NCCR solution with DPLR and Hybrid solution of [47]*

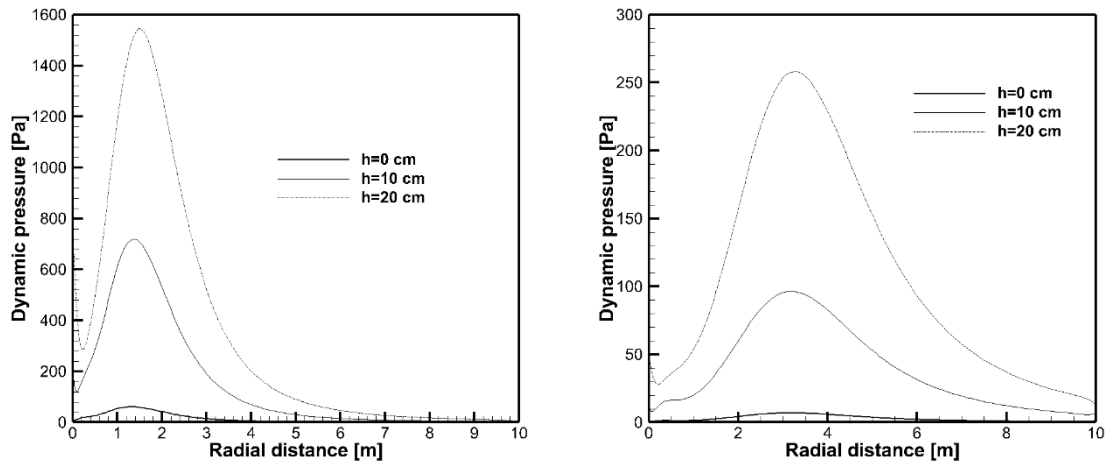


**Fig. 93** Distribution of the dynamic pressure on the different distances from the surface for two hover altitude

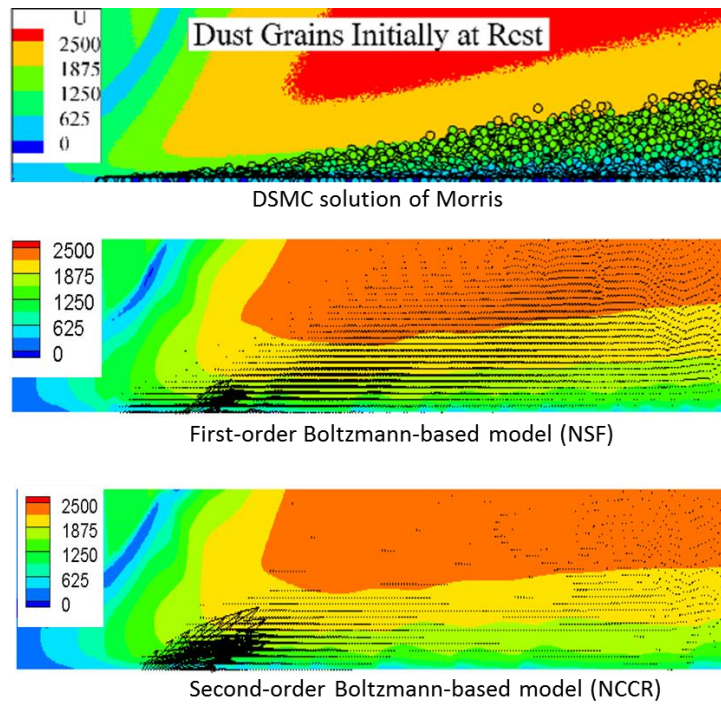


**Fig. 94** Vectors of eroded mass flux overlaid on radial velocity

The model of Roberts is shown to be capable of providing promising results for the erosion rate [9, 47, 48]. However, in the works of Morris [48], the dynamic pressure of the gas in a distance from the surface (slightly more than the height of boundary layer) is selected as the shear stress acting on the surface. This assumption would add to the complexity of the model implementation in an unstructured algorithm. In this work, we

applied a more straightforward strategy in which the excess shear stress is calculated based on the shear stress of the gas phase on the surface (rather than dynamic pressure) and the critical shear stress based on the available data in [261, 262]. In our used model a parameter known as the coefficient of soil erosion can be adjusted as a scaling factor which allows providing predictions in agreement with experiments or the observations gathered from previous Lunar missions through Aoppllo program for example. It should be noted that accurate erosion modeling has not been a prime interest in the current thesis. If the sophisticated erosion mechanism is necessary to be taken into account, conducting more extensive research using microscale modeling (e.g., using MD or DEM) in order to provide the adjustable parameters which will be used in the erosion model is necessary.

It is worth to note that when such an erosion model is used, the importance of second-order constitutive relations would be heightened. This significance is due to the fact that not only the gas phase is governed by non-equilibrium effects but also the mass flow rate of the eroded particles will be determined by a second-order non-conserved variable (shear stress).

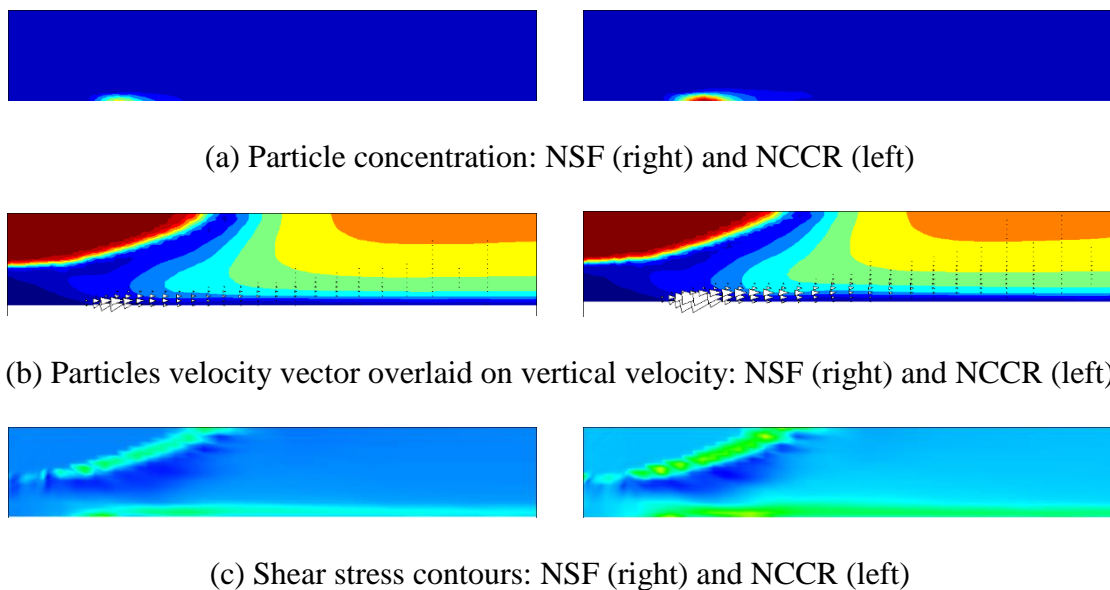
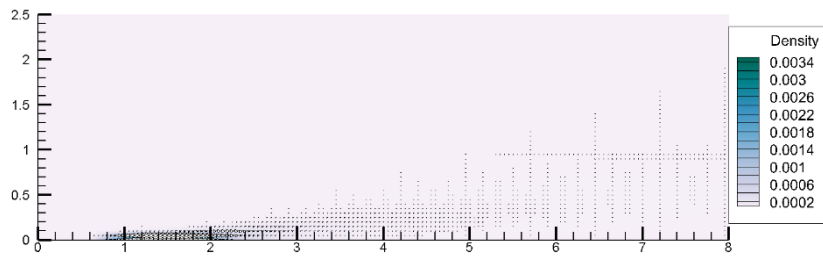


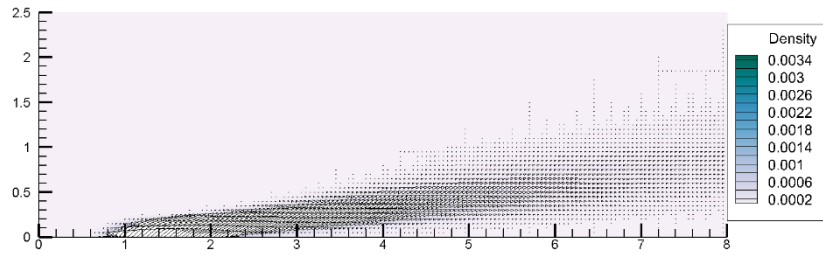
***Fig. 95 Comparison of first-order and second-order constitutive relationships in erosion modeling***

### **8.6.1 Effect of particle diameter**

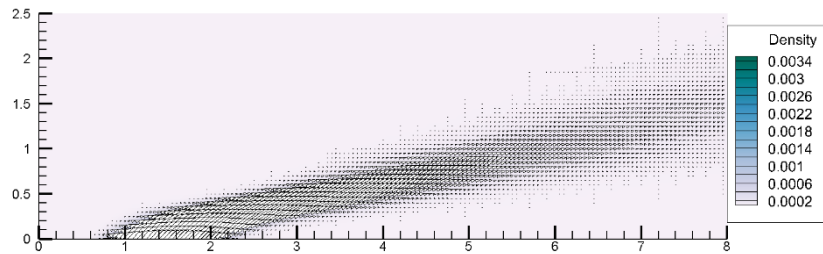
The effect of different particle diameters is briefly discussed in this section. Fig. 96 shows the simulation results for five different particle diameters in the vicinity of the erosive surface. It can be seen that when the particle diameter is large, the path that eroded particles go through is substantially affected. The main reason behind this behavior is the higher drag force on the solid particles exerted from the gas phase. It should be noted that the flow Stokes number which defines the dynamics of gas-dust interaction is greatly dependent on the molecular diameter.



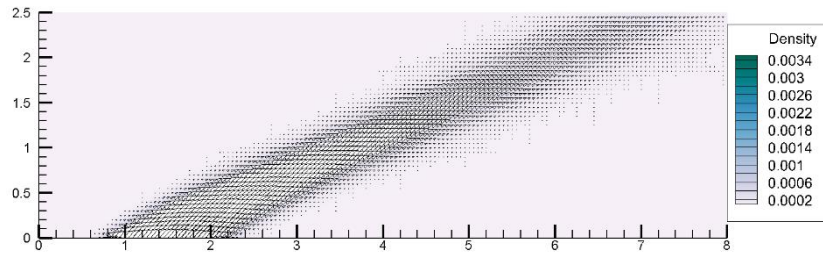
(a)  $1\mu\text{m}$  particles



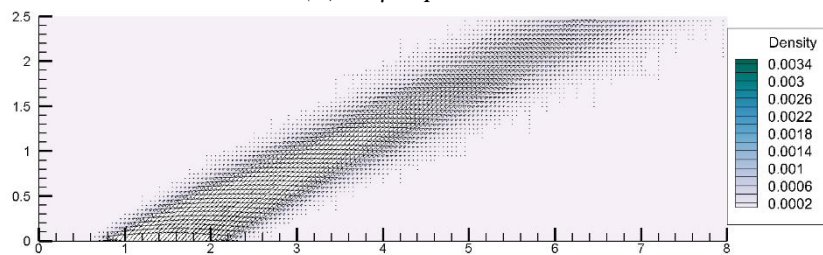
(b)  $5\mu\text{m}$  particles



(c)  $10\mu\text{m}$  particles



(d)  $30\mu\text{m}$  particles

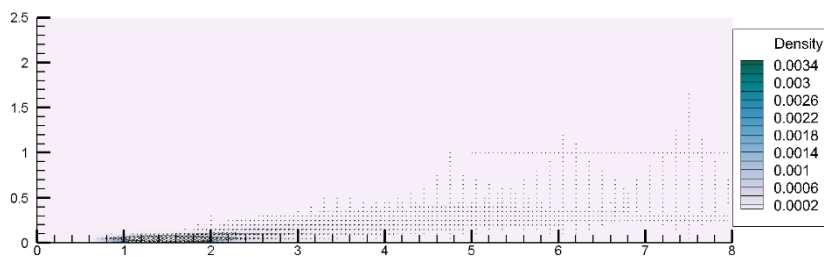


(e)  $45\mu\text{m}$  particles

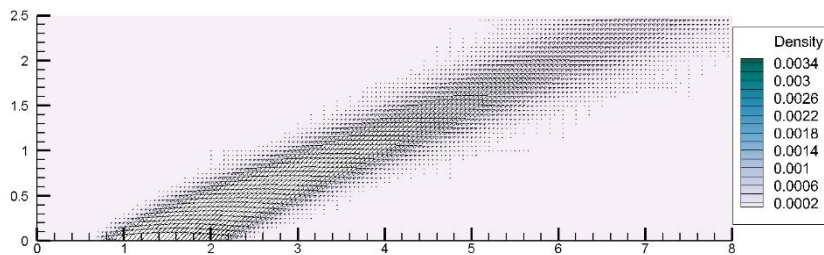
**Fig. 96** Effect of particle diameter on dust momentum vectors of the eroded particles in the vicinity of the surface overlaid on normalized density ( $P_{amb}=3\text{ Pa}$ )

## 8.6.2 Effect of pressure ratio

Another parameter which can affect the erosion characteristics is the pressure ratio of the exit jet to ambient condition. Simulation results to highlight this effect are presented in the Fig. 97. This parameter can change the structure of the gas phase flow field, and consequently, the shear stress exerted on the surface may vary significantly. As illustrated in Fig. 97, the higher the pressure ratios (lower ambient pressure for a constant exit pressure) the higher is the eroded mass flux.



(a)  $P_{amb}=10$  Pa



(b)  $P_{amb}=3$  Pa

**Fig. 97 Effect of ambient pressure on dust momentum vectors of the eroded particles in the vicinity of the surface overlaid on normalized density ( $P_{amb}=3$  Pa)**

## 8.6.3 Effect of cohesive strength

The characteristics of the regolith Moon surface in a different location is expected to be different. The surface cohesive stress which plays a vital role in the erosion prediction is one these variable parameters. In Fig. 106, the effect of variation of surface cohesive stress is investigated. As can be seen, this parameter affects the domain of eroded area as well as the magnitude of eroded mass flux. The larger the cohesive surface, the lower is the eroded

mass flux and the area in which erosion occurs. In the particular case investigated here, it can be seen that for surface cohesive stresses of larger than 40 Pa almost the eroded mass flux is negligible.

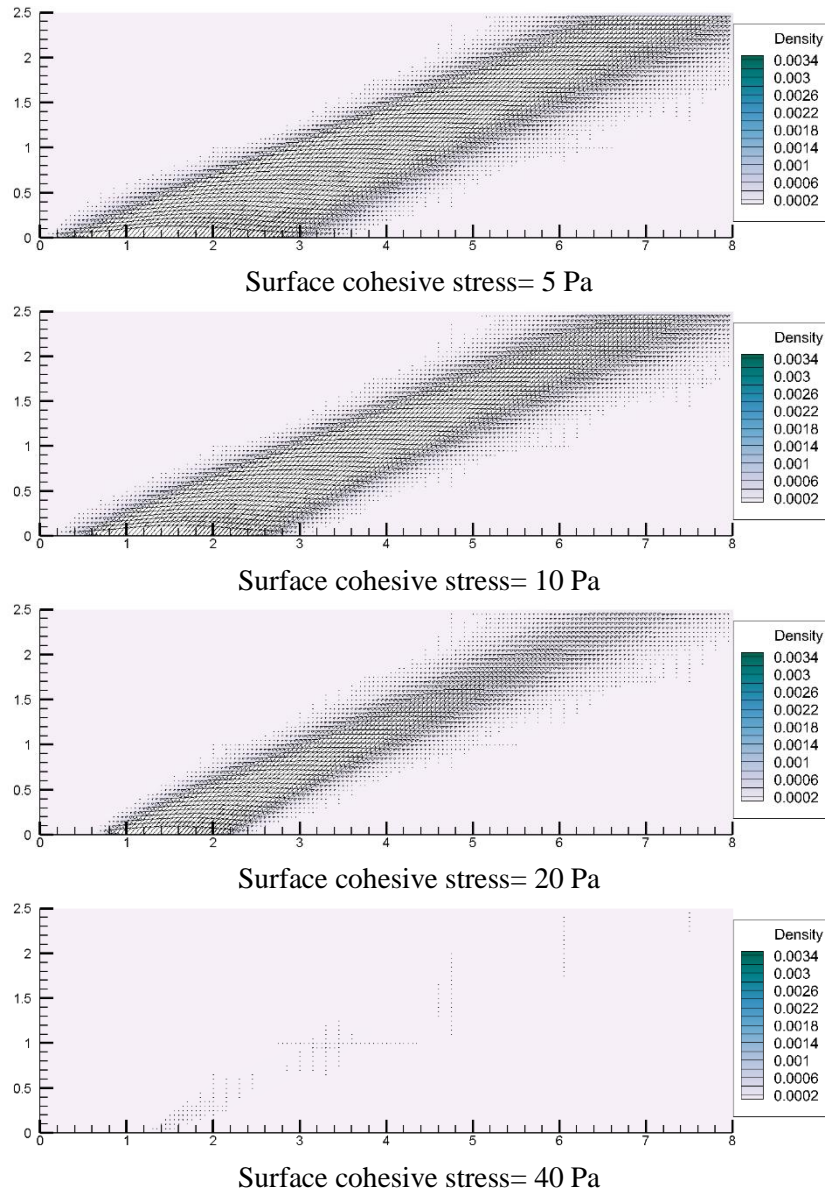


**Fig. 98** Effect of particle diameter on dust momentum vectors of the eroded particles in the vicinity of the surface overlaid on normalized density ( $P_{amb}=3$  Pa,  $d=30$   $\mu\text{m}$ )

### 8.6.4 Effect of erosion model parameters

One of the critical parameters in the Roberts erosion model is the parameter  $a$  defined in Equation (141). This parameter is a function of various conditions including the engine chamber viscosity and density, thrust, hover altitude, the ratio of the specific heats, Mach

number at the nozzle exit, gas constant, the ratio of specific heats and the drag coefficient. The values of coefficient  $a$  for the case of Apollo landing for two different altitudes and four different particle diameters is provided in Table 20.

**Table 20 Coefficient  $a$  values for different hover altitudes and particle diameters.**

Hover altitude (m)	Particle diameter ( $\mu\text{m}$ )	Coefficient $a$
5	1	0.998
	10	0.86
	30	0.54
	50	0.39
10	1	0.999
	10	0.92
	30	0.66
	50	0.51

A number of simulations have been conducted in order to independently investigate the effect of this parameter on erosion properties with keeping other variables constant. It should be noted that here the coefficient  $a$  is set artificially rather than changing the simulated problem parameters to check the sensitivity of the solutions only on this parameter. This parameter should be appropriately calculated and set in the model with the help of equations (143) and (144). As shown in Fig. 107, the larger the coefficient  $a$  is set, the less is the rate of erosion. However, this parameter does not affect the area in which the erosion occurs. This is obvious because the limits of the area in which erosion occurs are defined by the gas solution and the surface cohesive stress and the coefficient  $a$  is only a modeling parameter which its value is not critical on other physical properties of the flow. This analysis is only important for code verifications purposes.

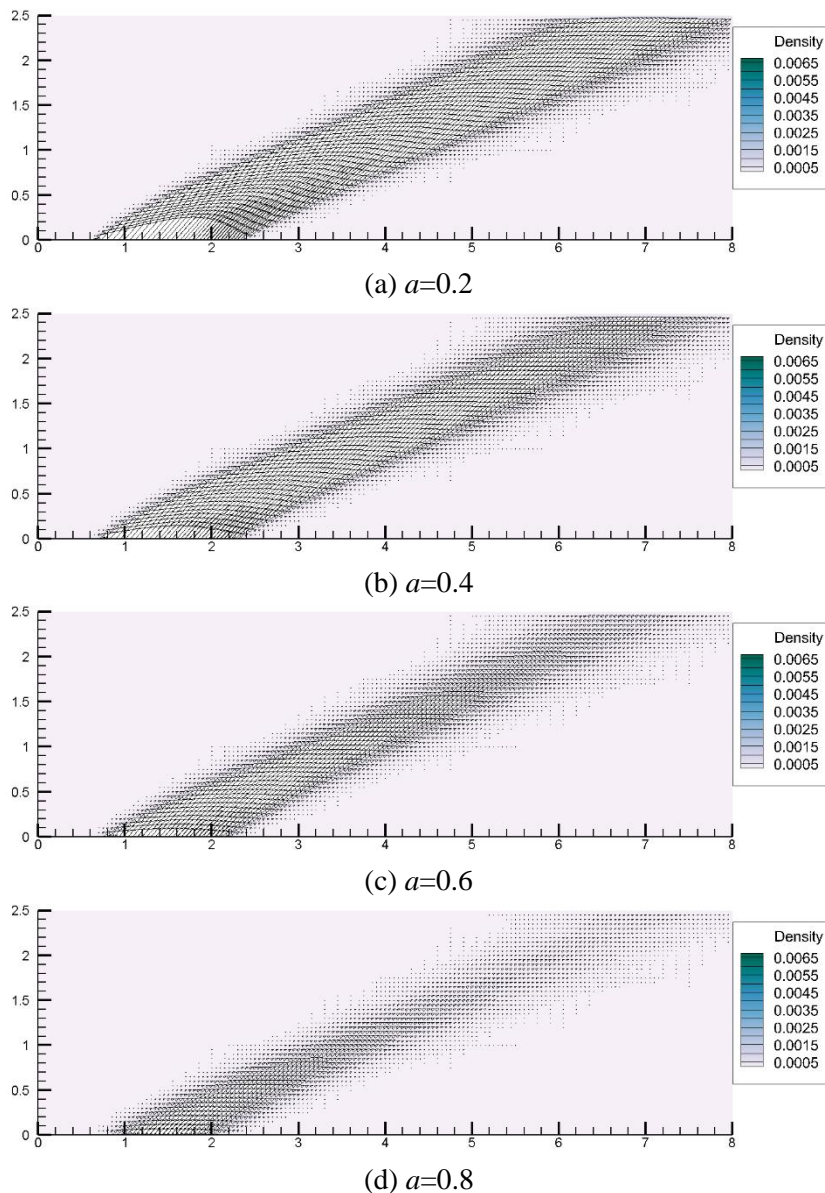


**Fig. 99** Effect of particle diameter on dust momentum vectors of the eroded particles in the vicinity of the surface overlaid on normalized density ( $P_{amb}=3$  Pa,  $d=30$   $\mu\text{m}$ )

## 8.7 Application of commercial CFD software package

### (FLUENT)

The comparison of solutions obtained by second-order Boltzmann-based constitutive relations with DSMC as well as first-order Boltzmann-based models shows that in low hover altitudes and in the vicinity of the surface due to high-density and pressure of exiting jet from the nozzle most of the simulated area is in continuum regime. This observation

has motivated applying the CFD software package FLUENT in which NSF equations are solved for solving the Lunar landing problem. Application of such system of equations for this problem, even though might look controversial at first glance, can provide an acceptable prediction of the flow quantities which can be used for an assisting engineering design tool. The strategy applied here is different from the one developed in in-house code in two essential aspects:

1. Only first-order constitute relationships (NSF equations) can be applied.
2. For simulation of the particulate phase, the Lagrangian formulation (discrete element method DEM module) is applied.

In order to represent the validity of the continuum assumption the test case simulated in section 8.5 is simulated and local  $M$ ,  $Kn$  and  $N_\delta$  numbers are plotted in Fig. 100. It can be seen that in this special case only a small portion of the domain (i.e., point 7) considerably deviates from equilibrium state. As evident in the figure, points 5 and 6 slightly deviate from equilibrium, and the rest of the numbered areas are in equilibrium or near-equilibrium condition. A similar comparison has been conducted for the under-design Korean Lunar lander. The preliminary design of this lander suggests clustering of five 200 N monopropellant thrusters for hover altitude control [263]. A schematic of Lunar lander demonstrator Descending Control Thruster (DCT) mounting location and direction is shown in Fig. 101. Due to the low thrust engine, it is expected that rarefaction is more dominant when a single nozzle approaches the surface. This presumption has been examined in Fig. 102 by plotting the local Mach, Knudsen, and  $N_\delta$  numbers. As the figure implies more points in the simulated domain are in non-equilibrium, compared to the case of Apollo. However, the interaction of the plumes in five-nozzle configuration would increase the number of points which fall into continuum or near-continuum limits. The simulation results of a three-dimensional analysis for a five-nozzle configuration are

summarized in Fig. 103. For this simulation also, the deviation from non-equilibrium similar to what has been presented in Fig. 100 and Fig. 102 is analyzed. This analysis, as summarized in Fig. 104, confirms the presumption of less non-equilibrium areas due to nozzles plumes interactions.

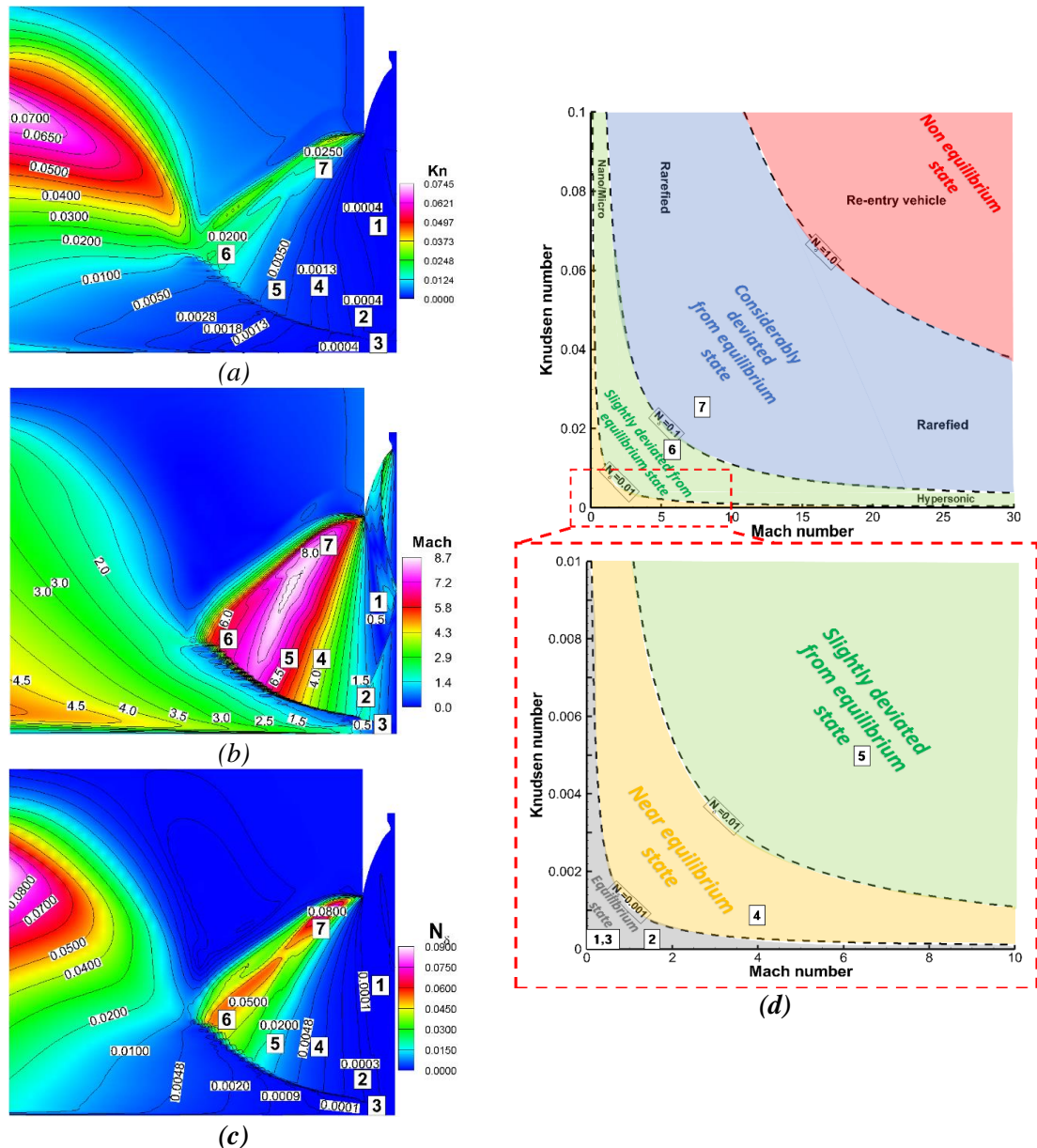


**Fig. 100** Contours of local a)  $Kn$ , b)  $M$ , c)  $N_\delta$  numbers and d) degree of deviation of different regions from equilibrium for Apollo descent engine at 5 m hover altitude.

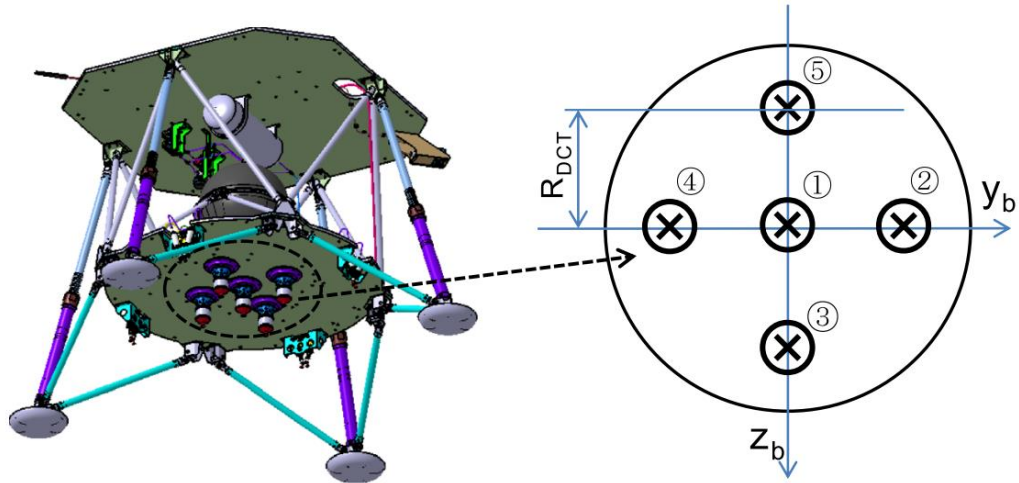


**Fig. 101 Schematic representation of Korean Lunar lander descent module with a five-nozzle configuration. Reprinted from [263] with permission.**

As mentioned earlier the strategy for prediction of particulate phase is based on the Lagrangian model. The UDF feature of the FLUENT package is applied to provide the non-uniform influx of particles into domain estimated by the erosion model. The solution of a sample test case and comparison with DSMC simulation is provided in Fig. 105. A good qualitative agreement between the radial velocity solution as well as the trajectory of the particles can be observed in this figure. As mentioned earlier, such simulations can be helpful for preliminary estimates for engineering design purposes and further analysis, especially when the behavior of the flow and particles in the far-field is of interest, is necessary.

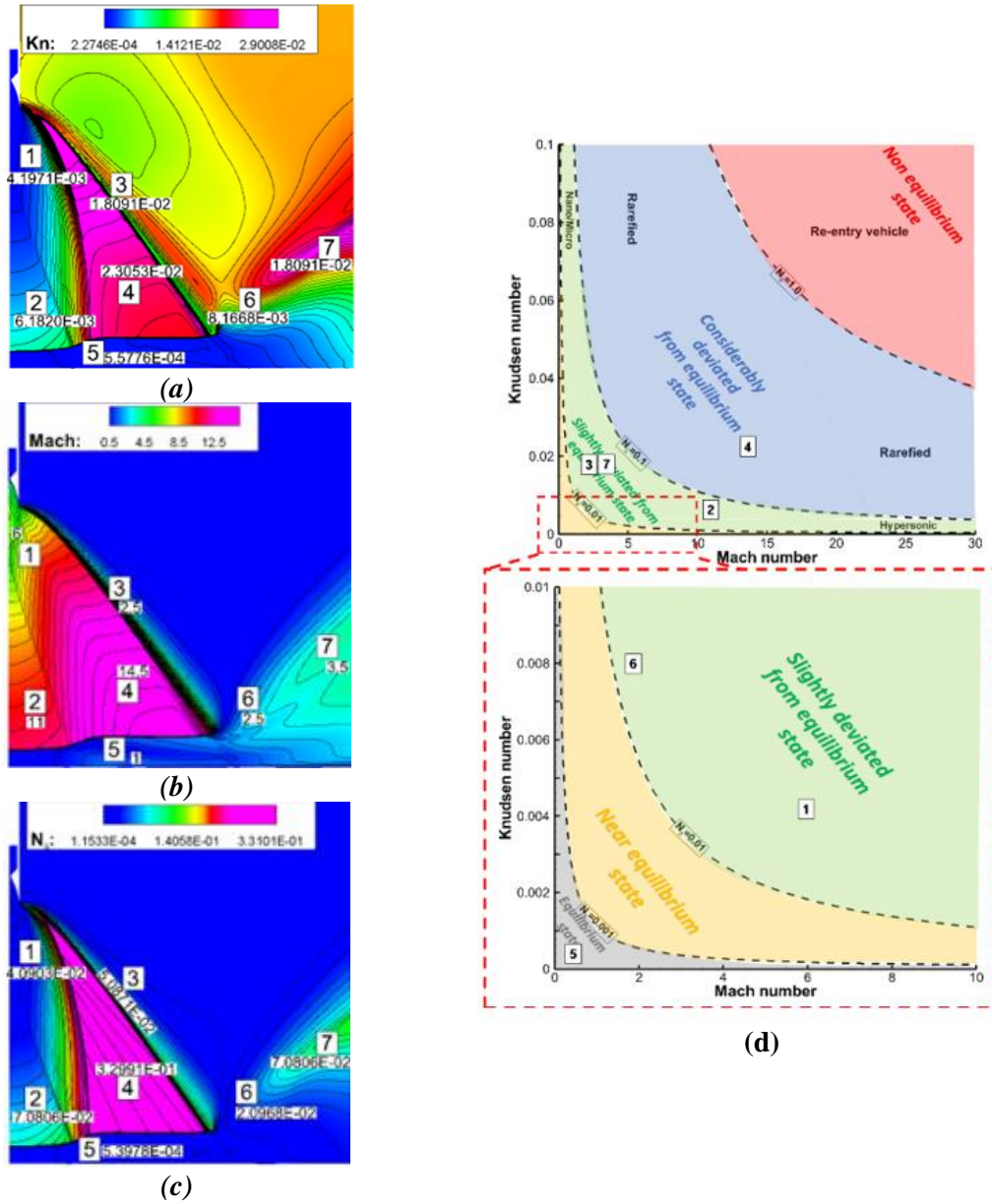
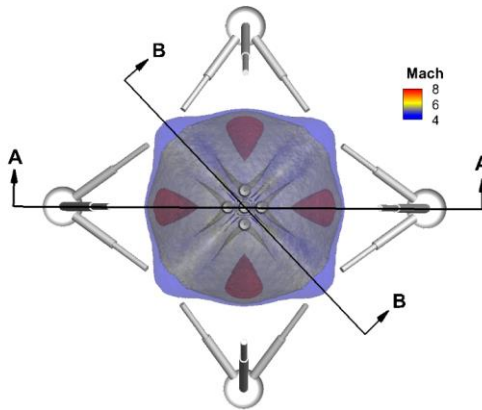
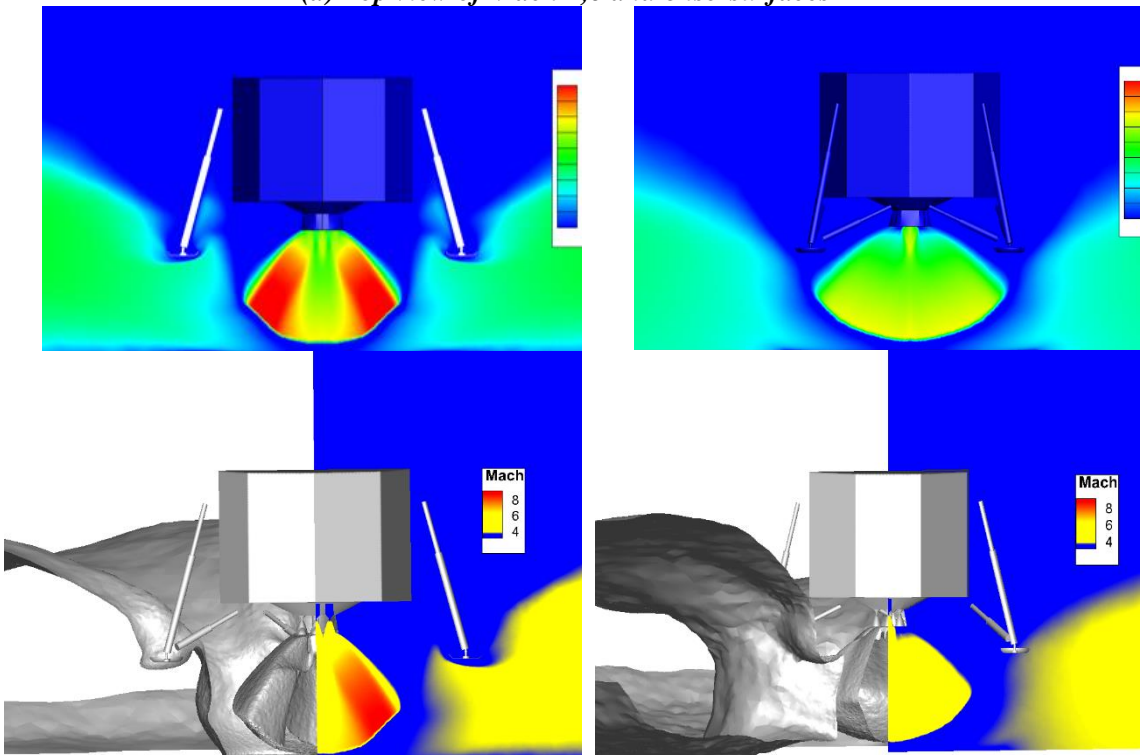


*Fig. 102 Contours of local a)  $Kn$ , b)  $M$ , c)  $N_\delta$  numbers and d) degree of deviation of different regions from equilibrium for the single nozzle operation of Korean lunar lander descent engine at 5 m hover altitude.*



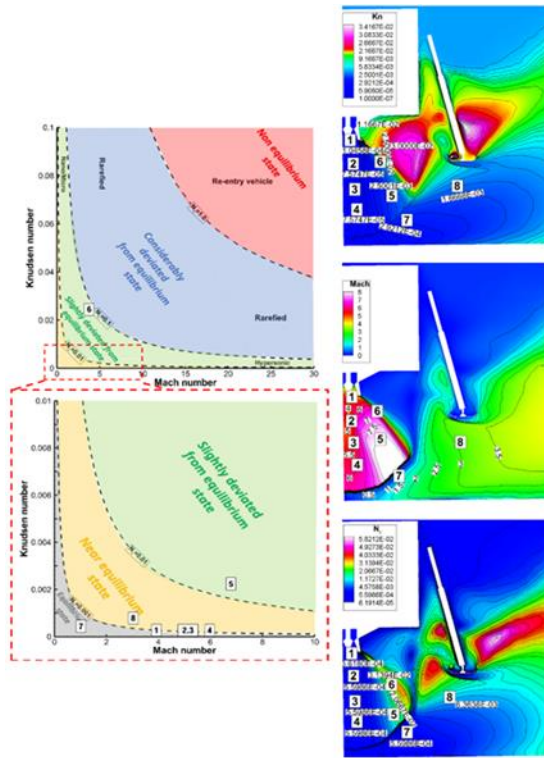
*(a) Top view of Mach 4,6 and 8 iso-surfaces*



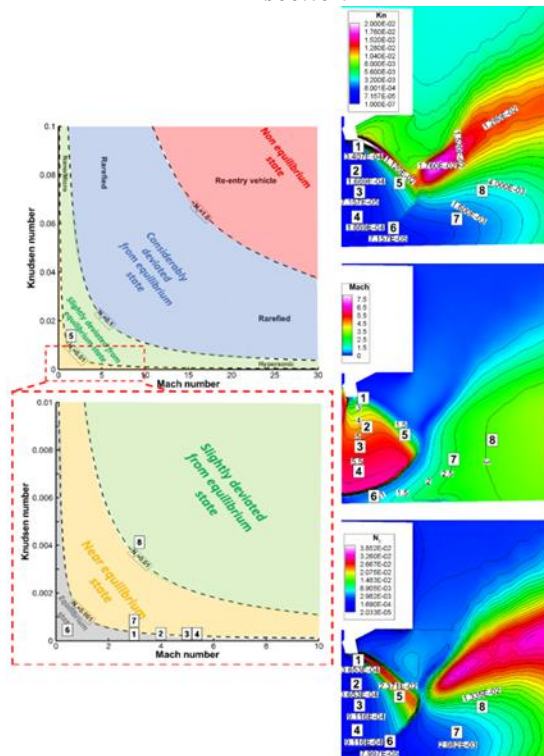
*(b) Mach contour at A-A slice*

*(c) Mach contour at B-B slice*

*Fig. 103 3D solution of local Mach number*

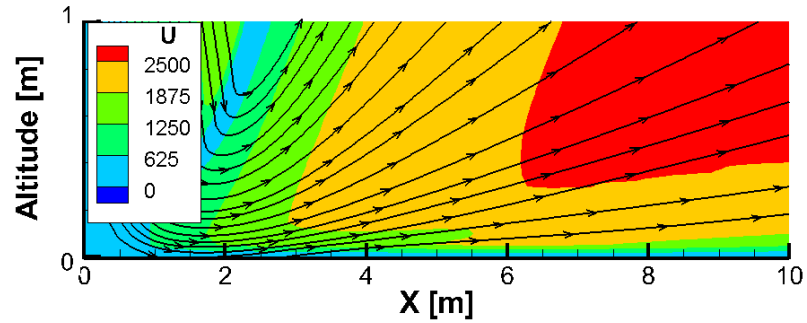


A-A section

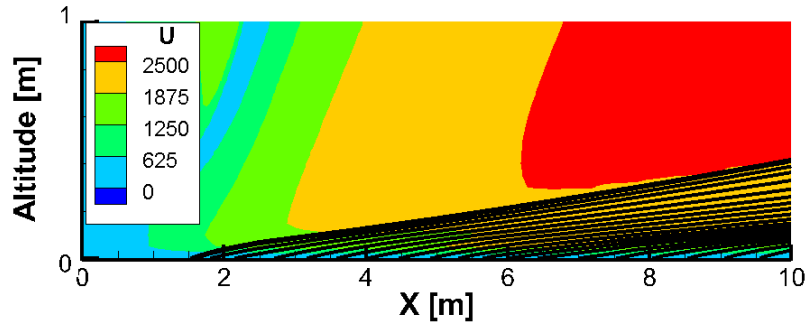


B-B section

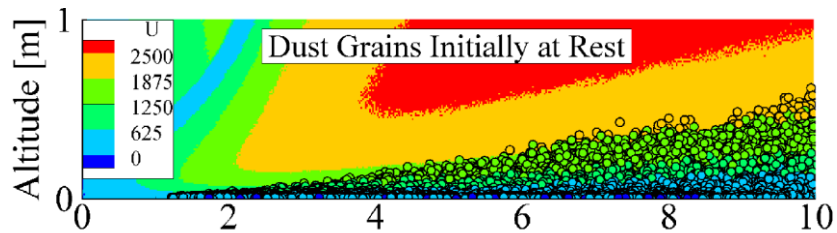
Fig. 104 Contours of local  $Kn$ ,  $M$ ,  $N_8$  numbers and degree of deviation of different regions from equilibrium for the single nozzle operation of Korean lunar lander descent engine at 5 m hover altitude.



(a) Streamline of exhausted gas from nozzle overlaid upon the gas radial velocity



(b) The trajectory of eroded particle overlaid upon the gas radial velocity



(c) Injected particles in DSMC solution [47]

Fig. 105 Dust grains overlaid upon radial velocity ( $d=30\mu\text{m}$ ,  $h=5\text{m}$ )

## 8.8 Applications of the model in pressure impactors

In the problem of jet impingement on a surface, the non-equilibrium can be due to either low ambient pressures (e.g., the Lunar landing problem) or because of the low exit pressures. In pressure impactors, a low-pressure sonic jet is expanded into a low(er)-pressure ambient forming a supersonic free jet. The high velocity and low-pressure avail to decrease the interphase drag force acting on particles (typically nanoparticles) that are contained in the jet. The particles bigger than a certain size cannot follow the sharp changes in career phase direction and will be deposited on the impact plate. This process is called

inertial impactation mechanism. This problem is very similar to the Lunar landing problem and can be studied by the developed model.

In this section, some preliminary results will be reported which can be helpful in the simulation of pressure impactors. We emphasize that comparison of solutions of different models (NSF and NCCR) when Re number is high, should be done in a way that the unsteady behavior of the jet does not mislead the conclusions. In such cases, a better analysis can be provided by comparison of time-averaged solutions. As depicted in Fig. 98, the frequency and domain of the oscillations which can be characterized by plotting the drag force on the impingement surface is different in each model. However, for low-Re (or high Knudsen) cases there is no oscillation, and therefore such type of analysis is not necessary.

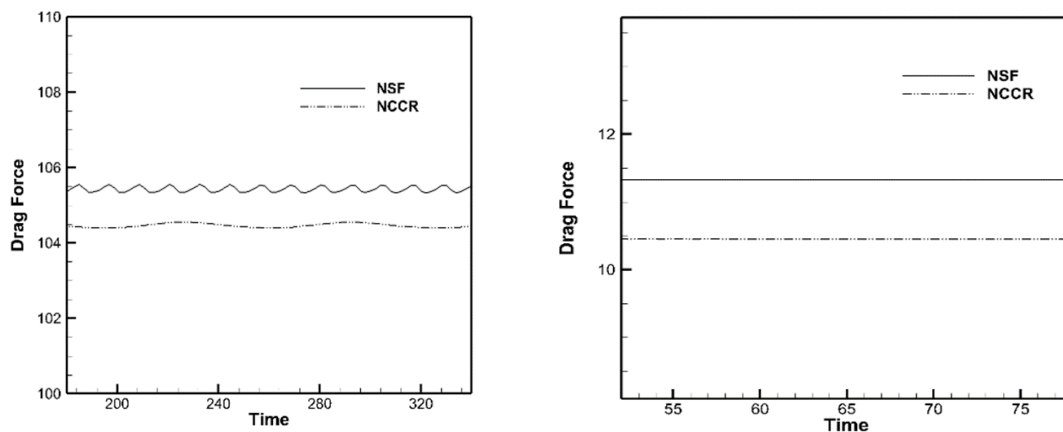
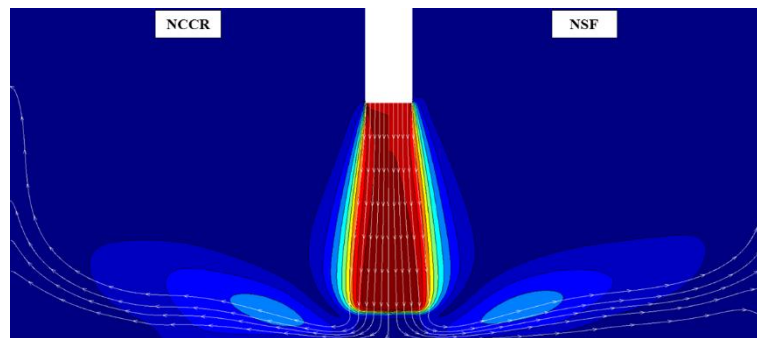


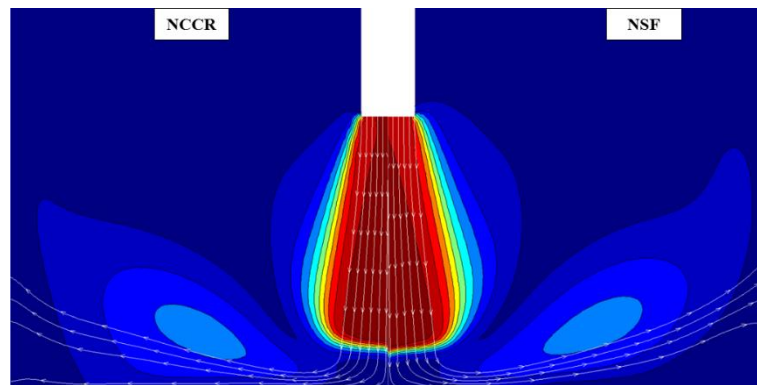
**Fig. 106 Comparison of drag force of high-Re (left) and low-Re (right) jet on the surface**

In Fig. 107, a comparison of Mach solutions for different exit pressures and pressure ratios is provided. For an exit pressure of 1 Pa and the pressure ratio of 2.5, both models provide almost identical Mach solutions. However, a slight deviation in the streamlines can be observed in Fig. 107 (a). When the pressure ratio increase by reducing the ambient pressure, the models deviation in prediction of the flow becomes more evident. Here, the location of the Mach disk, in this case, is under-predicted by the NSF model. For lower

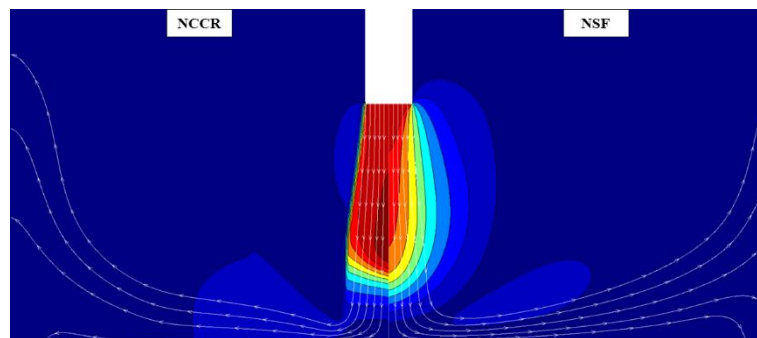
exit pressures, as shown in Fig. 107, the deviation of models in the Mach solutions is more evident.



$P_{exit}=1 Pa$ , Exit to ambient pressure ratio=2.5



$P_{exit}=1 Pa$ , Exit to ambient pressure ratio=5

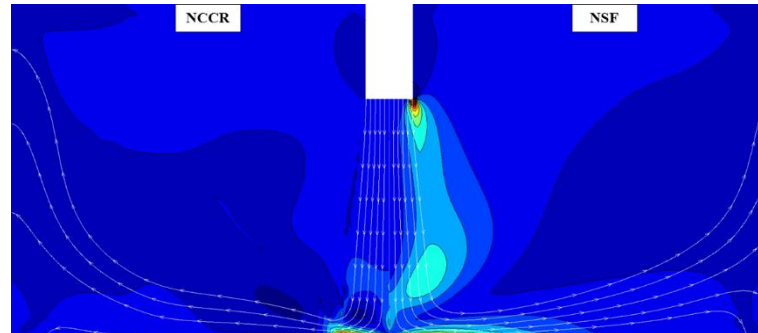


$P_{exit}=0.1 Pa$ , Exit to ambient pressure ratio=2

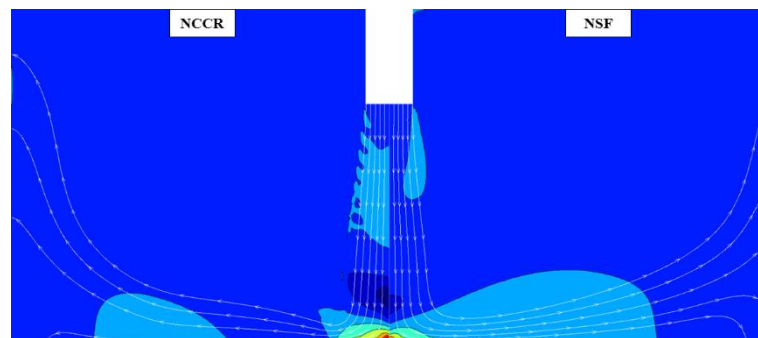
**Fig. 107 Comparison of Mach solution achieved by application of first-order and second-order Boltzmann-based constitutive relationships**

The comparison of non-conserved variables highlights the deviation of models. In Fig. 108,  $xy$  component of shear stress tensor in and heat flux in axial direction for  $P_{exit}=0.1 Pa$  and exit to ambient pressure ratio of 2 are plotted. The differences in prediction by first-

order and second-order models are quite obvious. This observation necessitates the application of higher-order constitutive relations when rarefaction effects are dominant (low exit pressure, high pressure-ratios).



Shear stress ( $\Pi_{xy}$ )



Heat flux in the axial direction ( $Q_y$ )

*Fig. 108 Comparison of non-conserved variables solution achieved by application of first-order and second-order Boltzmann-based constitutive relationships*

# Chapter 9. Conclusion and future works

## 9.1 Concluding remarks

In this thesis, the application of Boltzmann-based constitutive relations in order to investigate dusty gas flows in a non-equilibrium condition was investigated. The research was motivated by providing a solution to the problem of Lunar landing. For this purpose, discontinuous Galerkin method was applied to solve the conservation laws equipped with high order constitutive relations in the two-fluid model framework. Application of DG made a novel treatment of source terms in two-fluid model equation possible. Various bench mark problems for zeroth-order, first-order, and second-order Boltzmann-based models were put into numerical experiments and results were discussed.

### 9.1.1 Conclusions regarding the zeroth-order constitutive relationships

In case of zeroth-order constitutive equations (Euler equations), the complex wave patterns which are rarely investigated in the literature were extensively investigated and justifications to explain the physical phenomena such as are provided. In particular, it was shown that, when a dust contact discontinuity is present in the dusty gas flow, a pseudo-compound wave, as well as a composite wave, can form. Further, the new DG scheme not only meets the demand for high order accuracy (at least second-order) to accurately simulate dusty gas flows, but it can also handle the tricky source terms of coupling effects between the two phases, without resorting to the complicated operator splitting method commonly employed in the conventional method. In fact, in the study of multiphase flow, developing a robust DG solver for dusty gas flows has recently been considered a challenging topic deserving attention.

It turned out that the orthogonality of the basis functions, the backbone of the DG method, again played a critical role in the novel treatment of the high order moments of

the polynomial approximations to the source-term. Based on the new DG scheme, various benchmark problems with different physical features in one- and two-dimensional space were studied. In order to elaborate the complex wave patterns in gas-particle flows, the wave propagation mechanisms in the one-dimensional shock tube problem of the dusty gas were first investigated in detail. Several abnormal waves in dusty gas flows—most of them not previously identified—were highlighted and a physical explanation on the origin of such abnormal waves was given.

In addition, the new unstructured DG scheme was applied to two different types of problems with and without the presence of boundary effects. The results in both cases were shown to be in accordance with the previous data. The explosion case was first simulated in such a way that radial symmetry was preserved to confirm the one-dimensional behavior. Then, the multiphase explosion problem was considered to examine the ability of the numerical method to capture more complex flow patterns. The new scheme was then applied to investigate the compression corner problem for both the single and multi-phase applications. Both single and double Mach reflection problems were solved, and the higher order solutions (up to a polynomial order of two) were successfully obtained.

Furthermore, a detailed parametric study on particulate loading and particle diameter size was conducted. Isopycnic surfaces indicated that the particulate loading substantially affects the structure of the double Mach reflection, including the configuration of triple points. The main reason for this change is the amplification of the relaxation region, that is, the main element of the abnormal waves in dusty gas flows. In all cases, it was found that the secondary triple point was much more affected by the dust particles. Moreover, the convex Mach stem formed in the pure gas flow changed into a perpendicular Mach stem in the dusty gas flows. It was found that the particle diameter and mass loading affect the

slope and curvature of the reflected waves as well. While an increase in particle diameter causes the secondary reflected wave to align along the primary wave, the increase in mass loading leads to increase of the intersection angle of these two waves. It was also found that as the particle diameter and mass loading increase, the structure of the DMR becomes blurrier.

Lastly, based on axisymmetric formulation, the problem of the particle-laden free under-expanded jet was investigated for the purpose of validating the numerical simulation in capturing multiphase interactions. Even though a slight over-estimation of Mach disk location and jet boundary width was found in the numerical solutions, the important feature of upstream movement of the Mach disk was shown to be in good agreement with experimental results.

### **9.1.2 Conclusions regarding the first-order constitutive relationships**

Most of the numerical results regarding the first-order constitutive relationships were on flow past a triangular prism and under-expanded jet. Some attention-grabbing (in some cases, counter-intuitive) results were observed.

The results presented on the flow past the triangular prism in this thesis are the first comprehensive investigation of dusty gas flow past a bluff body which takes into account both viscous and compressibility effects. The viscous effects are investigated by variation of Re number up to the limit of laminar flow. The compressibility effects are taken into account by variation of Mach number. It was observed that compressibility effects could alter the critical Re number for which transition from steady flow to unsteady vortex shedding flow occurs. The critical Re number is higher as the flow becomes more and more compressible (or as the  $M$  number increases). It was also shown that the addition of particles could induce instabilities in the flow leading to lower critical Reynolds numbers.

In the problem of under-expanded jet also interesting results were observed. The counter-intuitive phenomenon of downstream movement of the Mach disk was demonstrated for high Stokes number flows, and physical justifications were provided based on the particles streamlines.

### **9.1.3 Conclusions regarding the second-order constitutive relationships**

Finally, a novel strategy for the solution of the Lunar landing problem (initial motivation of this thesis) was put forward by the help of second-order Boltzmann-based constitutive relationships. The challenging issues in this problem based upon the level of complexity in implementation in the suggested strategy can be summarized as in Fig. 109.

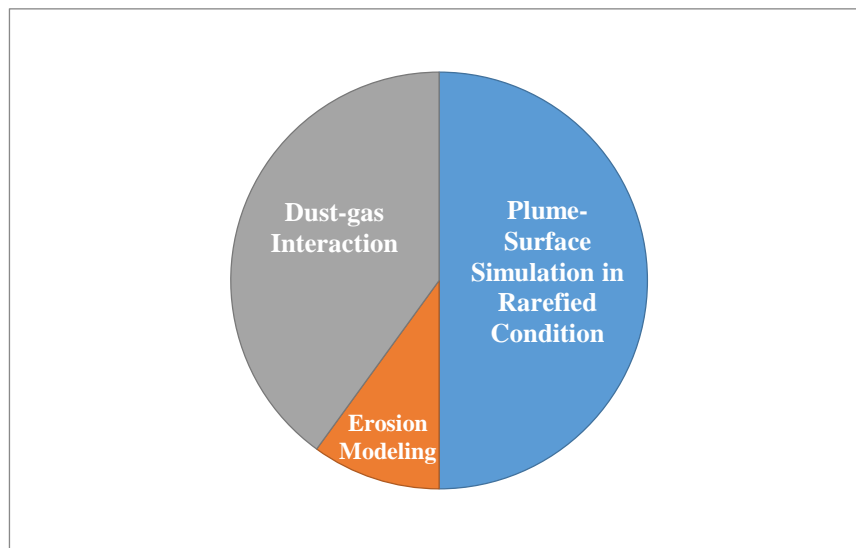


*Fig. 109 The relative level of complexity of the implementation of challenging issues in the proposed strategy of solving Lunar landing problem.*

The proposed strategy is achieved using fully continuum-based methods for handling both the rarefied and the dust phase flow. Therefore, it can suggest considerable computational time savings. It was shown that second-order Boltzmann-based constitutive equations could provide solutions almost identical to DSMC solutions. Moreover, a new boundary condition was developed through which the prediction of erosion rate was made

possible. It has also been demonstrated that the multiphase solver could qualitatively predict the dust dispersion in the domain. A number of parametric studies were also presented, and the physical features were discussed.

## 9.2 Future works

There are various directions through which this work can be extended. From a modeling point of view extension of the second-order Boltzmann-based constitutive equation for the dust phase is an attractive subject. Also a classification of dusty gas flow regimes based on solid phase Knudsen number or a similar parameter like  $N_\delta$  which shows the range of validity of the existing models is not available in the literature. The  $N_\delta$  parameter for the gas itself is not well-defined, and the existing ranges are based on insufficient numerical observations. The refining of the Knudsen regimes based on this parameter can be achieved by applying more comprehensive comparisons of classical models with DSMC or NCCR solutions.

From the numerical point of view, comparison of the previously developed methods for handling the source terms with the current approach or using the current idea in combination with other methods for example with splitting. In Euler-type problems, the non-strictly hyperbolic equations of dust can be converted to strictly hyperbolic by adding a pressure-like term to both sides of the equations. This simple idea has been applied to shallow water equations in the simulation of atmospheric aircraft icing problems and can be equivalently applied in two-fluid equations of dusty gas. In some of the test cases of this work, it was observed that the convergence of the method improves extensively when source terms are present. This feature combined with the idea explained before (adding a term in both sides of the equation) might be useful as a new acceleration method for a specific class of problems.

There are a variety of problems which were discussed very briefly in this thesis, and more extensive investigation of physical features in those problems can be followed in future. For example, it was observed that in the one-dimensional problem of dusty gas shock tube a wave is reflected into the high-pressure side. The type of reflected wave depends on the specific heats of the solid particle and gas as well as the particulate loading of the mixture. Reflection of shock wave was investigated in this work. However, the reflection of rarefaction wave was not investigated which can be a topic of future studies. There are various benchmark problems which can be used in the dusty gas framework to provide more fundamental knowledge on the complex behavior of the dusty gas flows.

Dusty gas flows past streamlined and also blunt bodies which were partly investigated for flow past NACA0012 aerofoil and a triangular prism in Chapter 6 can be further examined by considering a wider range of Mach numbers, Reynolds number, Knudsen number, Stokes number (with variation of particulate loadings, particle diameters, particle mass, gas viscosity). Providing the critical Re number which depicts the onset of separation and transition depending on these numbers is also lacking in the literature and can be achieved via the developed tool with a little extra effort.

A number of unsolved issues in the problem of under-expanded jets which has been extensively investigated either experimentally or numerically still exists. These can be poorly managed Mach disk diameter and curvature, the effect of viscous forces on the transition to turbulence as well as interactions with hydrodynamic instabilities [228]. With the efficient and high-order numerical tool developed in this work not only those issues can be investigated but also more areas where either rarefaction or presence of dust play a role can be further investigated. Effect of the addition of particles on under-expanded jets which has applications in volcanic eruptions is one of the other directions which can be followed. Asymmetric under-expanded jet can be investigated within the three-

dimensional formulation framework. The effect of rarefaction and dust has never been investigated on the structure of these 3D configuration types of flows.

Investigation of dusty gas micro-flows, pressure impactors are the other directions which can be followed.

More detailed investigations on the Lunar landing problem including parametric studies and inclusion of more accurate erosion models in another direction.

Comparison of the method with Lagrangian counterpart can also provide more details on the strength and weaknesses of the currently developed tool.

Moreover, multiphase turbulent flows can be called an almost new topic in fluids dynamics.

The current tool with the incorporation of turbulence models (or approaches) can be used in this area as well. In this case, one of the most interesting problems at hand is the aircraft atmospheric icing. Here, instead of solid particles, liquid droplets or bubbles should be modeled, and further necessary modifications to simulate the ice formation after collection of droplets on the surface should be taken into account.

There are other classes of two-fluid models with interphase tracking, and the developed code can be further extended to be applied to problems in which interphase shape and location is important.

## **Appendix A. List of Moon and Mars missions with a soft landing**

The most famous Lunar landings include unmanned Luna missions (Luna 13 1966, Luna 16 and 17 in 1970, Luna 20 in 1972, Luna 21 in 1973 and Luna 24 in 1976) operated by the Soviet Union as well as Surveyor 3, 5 and 6 operated by the United States in 1967 and recent Chang'E-3 mission operated by China in 2013. The only successful manned missions are the well-known Apollo missions (Apollo 11 in 1969, Apollo 12 in 1969, Apollo 14 and 15 in 1971, Apollo 16 and 17 in 1972). The future Moon landing missions are summarized in Table 21.

A series of Mars missions some of which included a landing has been carried out in the past. Successful missions which could land on the Mars include Viking 1 and 2 landers in 1975, Mars Pathfinder in 1996, Spirit (MER-A) in 2003 and Phoenix in 2007 all operated by NASA. The recent en route mission, InSight (also operated by NASA) is due to land on Mars by November 2018. The future Mars missions which include a soft landing is provided in Table 22.

*Table 21 List of future Lunar missions with a soft landing involved*

Country (Organization)	Launch	Mission	Status
China (CNSA)	2018	Chang'E-4 landing and roving	Funded/ In development
India (ISRO)	2018	Chandrayaan-2 (landing, roving, sample analyzing)	
China (CNSA)	2019	Chang'E-5 (Sample return)	
Private	2019	PTScientists (Landing and roving)	
Private	2020	Lander and 3+ rovers: Hakuto, AngelicvM	
Japan (JAXA)	2021	Pinpoint landing, roving	
China (CNSA)	2020s	Chang'E-6 (Sample return)	
Japan (JAXA)	2020s	SELENE-2 (orbiting, landing and roving)	
Private	2019	TeamIndus (Landing and roving)	
Korea (KARI)	2025*	Moon Lander	
Russia (Roscosmos)	2028	Luna-Glob (Manned lunar orbiter)	Proposal/ Unclear funding
Russia (Roscosmos)	2030	Luna-Glob (Manned lunar orbiter)	
Japan (JAXA)	2030	Manned moon landing	
China (CNSA)	2036	CLEP Manned moon landing	
Russia (Roscosmos)	2037	Lunnyj Poligon (Completion of robotic lunar base)	

*Table 22 List of future Mars missions with a soft landing involved*

Country (Organization)	Launch	Mission	Status
Japan (JAXA)	2020	Mars Terahertz Microsatellite	Funded / In development
EU (ESA/ASE)	2020	ExoMars 2020	
China (CNSA)	2020	2020 Chinese Mars Mission	
USA (SpaceX)	2022	Demo mission	Proposal/ Unclear funding
Netherlands (Mars One)	2022	Mars One, demo mission	
USA (SpaceX)	2024	Crewed mission	
Netherlands (Mars One)	2026	Mars One, rover & ComSat mission	
Netherlands (Mars One)	2029	Mars One, cargo missions	
China (CNSA)	2030	Sample return phase of the Chinese Mars exploration program	
Netherlands (Mars One)	2031	Orbiter, lander, cargo, crew of 4	
Netherlands (Mars One)	2033	Orbiter, lander, cargo, crew of 4	
China (CNSA)	2036	Crewed phase of the Chinese Mars exploration program	
Russia (Roscosmos)	2040-45	Crewed phase of the Russian Mars exploration program	

## Appendix B. Derivation of conservation laws from the Boltzmann transport equation

The Boltzmann transport equation (BTE) for monatomic, diatomic and linear polyatomic particles known as Boltzmann-Curtiss equation in the absence of external body forces can be written as [2, 117, 264],

$$\left( \frac{\partial}{\partial t} + \mathbf{v} \cdot \nabla + \frac{j}{I} \frac{\partial}{\partial \theta} \right) f(\mathbf{v}, \mathbf{r}, t) = C[f, f_1] \quad (209)$$

In the above equation  $j$ ,  $I$ , and  $\theta$  are the magnitude of the angular momentum, moment of inertia and azimuthal angle. We derive the conservation laws for the Boltzmann-Curtis which is an extended version of the Boltzmann equation. The third term in the above relation (and in the rest of the derivation process accordingly) will vanish for the case of monatomic gases.

Before deriving the conservation equations, statistical mechanics definitions of some macroscopic parameters which are necessary for the derivation process are provided in the table below.

*Table 23 Statistical definition of macroscopic parameters*

Macroscopic quantity	Statistical definition
Number density	$n = \langle f(t, \mathbf{r}, \mathbf{v}) \rangle$
Density	$\rho = \langle mf(t, \mathbf{r}, \mathbf{v}) \rangle$
Momentum	$\rho \mathbf{u} = \langle m\mathbf{v}f(t, \mathbf{r}, \mathbf{v}) \rangle$
Energy	$\rho E = \left\langle \left( \frac{1}{2} mc^2 + H_{rot} \right) f(t, \mathbf{r}, \mathbf{v}) \right\rangle$
Stress tensor	$\mathbf{P} = \langle m\mathbf{c}\mathbf{c}f(t, \mathbf{r}, \mathbf{v}) \rangle$

$$\begin{aligned}
\text{Shear stress tensor} \quad \mathbf{\Pi} &= \left\langle m[\mathbf{cc}]^2 f(t, \mathbf{r}, \mathbf{v}) \right\rangle \\
\text{Excess normal stress} \quad \Delta &= \left\langle \left( \frac{1}{3} \text{Tr}(m\mathbf{cc}) - \frac{p}{n} \right) f(t, \mathbf{r}, \mathbf{v}) \right\rangle \\
\text{Heat flux vector} \quad \mathbf{Q} &= \left\langle \left( \frac{1}{2} mc^2 + H_{rot} - m\hat{h} \right) \mathbf{c} f(t, \mathbf{r}, \mathbf{v}) \right\rangle
\end{aligned}$$

Differentiating the above statistical definitions introduced above with time and combining with BTE will give the conservation equations and constitutive relations. It should be noticed that the  $t$ ,  $\mathbf{r}$ , and  $\mathbf{v}$  are independent variables, whereas peculiar velocity is not independent of space and time. Moreover, molecular, average and peculiar (random) velocities are related by  $\mathbf{v} = \mathbf{u} + \mathbf{c}$ . By defining the material time derivative as  $\frac{D}{Dt} = \frac{\partial}{\partial t} + \mathbf{u} \cdot \nabla$ , equation (209) can be written as,

$$\frac{Df}{Dt} + \mathbf{c} \cdot \frac{\partial f}{\partial \mathbf{x}} + \frac{j}{I} \frac{\partial f}{\partial \theta} = C[f, f_1]. \quad (210)$$

For the derivation of the mass conservation, the Boltzmann-Curtiss equation is multiplied by  $m$  and integrated over velocity space to yield

$$\left\langle m \frac{\partial f}{\partial t} \right\rangle + \langle m \mathbf{v} \cdot \nabla f \rangle + \left\langle m \frac{j}{I} \frac{\partial f}{\partial \theta} \right\rangle = \langle m C[f, f_1] \rangle. \quad (211)$$

As mass is a collision invariant of BTE the right-hand-side term will be zero:

$$\left\langle m \frac{\partial f}{\partial t} \right\rangle + \langle m \mathbf{v} \cdot \nabla f \rangle + \left\langle m \frac{j}{I} \frac{\partial f}{\partial \theta} \right\rangle = 0. \quad (212)$$

The above relation can be further simplified as

$$\frac{\partial}{\partial t} \langle m f \rangle + \nabla \cdot \langle m \mathbf{v} f \rangle + \left\langle m \frac{j}{I} \frac{\partial f}{\partial \theta} \right\rangle = 0. \quad (213)$$

Curtiss stated that  $f$  does not depend on the azimuthal angle and it only depends weakly on the position of gas molecules. With the use of statistical definition of density and momentum in Table 23, we can get the mass conservation equation:

$$\frac{\partial \rho}{\partial t} + \nabla \cdot (\rho \mathbf{u}) = 0. \quad (214)$$

The above equation is the same as the mass conservation form in continuum theory. With a similar approach, it can be shown that the Boltzmann equation fulfills the requirement of the momentum conservation law. This is achieved by differentiation of statistical definition of momentum and use of Boltzmann-Curtiss equation as follows

$$\left\langle m \mathbf{v} \frac{\partial f}{\partial t} \right\rangle + \langle m \mathbf{v} \mathbf{v} \cdot \nabla f \rangle + \left\langle m \mathbf{v} \frac{j}{I} \frac{\partial f}{\partial \theta} \right\rangle = \langle m \mathbf{v} C[f, f_1] \rangle. \quad (215)$$

The other collision invariant of the BTE is the momentum. Therefore,

$$\left\langle m \mathbf{v} \frac{\partial f}{\partial t} \right\rangle + \langle m \mathbf{v} \mathbf{v} \cdot \nabla f \rangle + \left\langle m \mathbf{v} \frac{j}{I} \frac{\partial f}{\partial \theta} \right\rangle = 0. \quad (216)$$

The Curtiss's assumption implies that

$$\left\langle m \mathbf{v} \frac{\partial f}{\partial t} \right\rangle + \langle m \mathbf{v} \mathbf{v} \cdot \nabla f \rangle = 0. \quad (217)$$

By substituting the molecular velocity in terms of thermal and macroscopic velocities in the second term, and use of statistical definitions of viscous stress tensor and excess normal stress we get

$$\begin{aligned} \nabla \cdot \langle m \mathbf{v} \mathbf{v} f \rangle &= \nabla \cdot \langle m (\mathbf{c} + \mathbf{u})(\mathbf{c} + \mathbf{u}) f \rangle \\ &= \nabla \cdot \langle m \mathbf{c} \mathbf{c} f \rangle + \nabla \cdot \langle m \mathbf{c} \mathbf{u} f \rangle + \nabla \cdot \langle m \mathbf{u} \mathbf{c} f \rangle + \nabla \cdot \langle m \mathbf{u} \mathbf{u} f \rangle \\ &= \nabla \cdot \left\langle m \left( [\mathbf{c} \mathbf{c}]^2 - \frac{1}{3} \text{Tr}(\mathbf{c} \mathbf{c}) \mathbf{I} \right) f \right\rangle + \nabla \cdot \langle m f \rangle \mathbf{u} \mathbf{u} \\ &= \nabla \cdot \langle m [\mathbf{c} \mathbf{c}]^2 f \rangle - \nabla \cdot \left\langle \frac{1}{3} \text{Tr}(\mathbf{c} \mathbf{c}) f \right\rangle \mathbf{I} + \nabla \cdot (\rho \mathbf{u} \mathbf{u}) \\ &= \nabla \cdot \mathbf{\Pi} - \nabla \cdot \left\langle \frac{1}{3} \text{Tr}(\mathbf{c} \mathbf{c}) f \right\rangle \mathbf{I} + \nabla \cdot (\rho \mathbf{u} \mathbf{u}) \\ &= \nabla \cdot \mathbf{\Pi} - \nabla \cdot (\Delta + p) \mathbf{I} + \nabla \cdot (\rho \mathbf{u} \mathbf{u}) \\ &= \nabla \cdot (\rho \mathbf{u} \mathbf{u}) + \nabla \cdot ((\Delta + p) \mathbf{I} + \mathbf{\Pi}) \\ &= \nabla \cdot (\rho \mathbf{u} \mathbf{u}) + \nabla \cdot \mathbf{P}. \end{aligned} \quad (218)$$

In the above relation,  $\mathbf{P}$  is the stress tensor which is decomposable into hydrostatic pressure, excess trace part and traceless part. Finally, the momentum equation can be expressed as,

$$\frac{\partial}{\partial t} \rho \mathbf{u} + \nabla \cdot (\rho \mathbf{u} \mathbf{u} + p \mathbf{I}) + \nabla \cdot (\mathbf{\Pi} + \Delta \mathbf{I}) = 0. \quad (219)$$

Accordingly, with the help of the statistical definition of the internal energy density of the fluid and consequent substitution and differentiation as has been done for the derivation of mass and momentum conservation equations, we can derive the energy conservation law or the first law of thermodynamics.

$$\begin{aligned} & \left\langle \left( \frac{1}{2} mc^2 + H_{rot} \right) \frac{\partial f}{\partial t} \right\rangle + \left\langle \left( \frac{1}{2} mc^2 + H_{rot} \right) \mathbf{v} \cdot \nabla f \right\rangle + \left\langle \left( \frac{1}{2} mc^2 + H_{rot} \right) \frac{j}{I} \frac{\partial f}{\partial \theta} \right\rangle \\ & = \left\langle \left( \frac{1}{2} mc^2 + H_{rot} \right) C[f, f_1] \right\rangle. \end{aligned} \quad (220)$$

The third collisional invariant of the Boltzmann equation is the energy, therefore,

$$\left\langle \left( \frac{1}{2} mc^2 + H_{rot} \right) \frac{\partial f}{\partial t} \right\rangle + \left\langle \left( \frac{1}{2} mc^2 + H_{rot} \right) \mathbf{v} \cdot \nabla f \right\rangle + \left\langle \left( \frac{1}{2} mc^2 + H_{rot} \right) \frac{j}{I} \frac{\partial f}{\partial \theta} \right\rangle = 0 \quad (221)$$

The above equation can be further simplified as follows

$$\begin{aligned} & \frac{\partial}{\partial t} \left\langle \left( \frac{1}{2} mc^2 + H_{rot} \right) f \right\rangle + \left\langle \frac{1}{2} mc^2 \mathbf{v} \cdot \nabla f \right\rangle + \langle H_{rot} \mathbf{v} \cdot \nabla f \rangle = 0 \\ & \frac{\partial}{\partial t} \left\langle \left( \frac{1}{2} mc^2 + H_{rot} \right) f \right\rangle + \left\langle \frac{1}{2} m \mathbf{v} (c^2 \cdot \nabla f) \right\rangle + \langle \mathbf{v} (H_{rot} \cdot \nabla f) \rangle = 0 \\ & \frac{\partial}{\partial t} \left\langle \left( \frac{1}{2} mc^2 + H_{rot} \right) f \right\rangle + \left\langle \frac{1}{2} m \mathbf{v} \nabla \cdot (c^2 f) \right\rangle - \left\langle \frac{1}{2} m \mathbf{v} (f \cdot \nabla c^2) \right\rangle \\ & + \nabla \cdot \langle \mathbf{v} (H_{rot} f) \rangle - \langle \mathbf{v} f (\nabla \cdot H_{rot}) \rangle = 0 \\ & \frac{\partial}{\partial t} \left\langle \left( \frac{1}{2} mc^2 + H_{rot} \right) f \right\rangle + \left\langle \frac{1}{2} m \mathbf{v} \nabla \cdot (c^2 f) \right\rangle - \left\langle \frac{1}{2} m \mathbf{v} (f \cdot \nabla c^2) \right\rangle \\ & + \nabla \cdot \langle \mathbf{v} (H_{rot} f) \rangle = 0. \end{aligned} \quad (222)$$

By substituting the molecular velocity in terms of thermal and macroscopic velocities:

$$\begin{aligned}
& \frac{\partial}{\partial t} \left\langle \left( \frac{1}{2} mc^2 + H_{rot} \right) f \right\rangle + \nabla \cdot \left\langle \frac{1}{2} m(\mathbf{c} + \mathbf{u}) c^2 f \right\rangle \\
& + \langle m(\mathbf{c} + \mathbf{u}) \mathbf{c} f \rangle \cdot (\nabla \cdot \mathbf{u}) + \nabla \cdot \langle (\mathbf{c} + \mathbf{u})(H_{rot} f) \rangle = 0 \\
& \frac{\partial}{\partial t} \left\langle \left( \frac{1}{2} mc^2 + H_{rot} \right) f \right\rangle + \nabla \cdot \left\langle \frac{1}{2} m \mathbf{c} \mathbf{c}^2 f \right\rangle + \nabla \cdot \mathbf{u} \left\langle \frac{1}{2} mc^2 f \right\rangle \\
& + \langle m \mathbf{c} \mathbf{c} f \rangle \cdot (\nabla \cdot \mathbf{u}) + \mathbf{u} \langle m \mathbf{c} f \rangle \cdot \nabla \mathbf{u} + \nabla \cdot \langle \mathbf{c} H_{rot} f \rangle + \nabla \cdot \langle \mathbf{u} H_{rot} f \rangle = 0
\end{aligned} \tag{223}$$

$$\begin{aligned}
& \frac{\partial}{\partial t} \left\langle \left( \frac{1}{2} mc^2 + H_{rot} \right) f \right\rangle + \nabla \cdot \left\langle \left( \frac{1}{2} mc^2 + H_{rot} \right) \mathbf{c} f \right\rangle \\
& + \nabla \cdot \mathbf{u} \left\langle \left( \frac{1}{2} mc^2 + H_{rot} \right) f \right\rangle + \langle m \mathbf{c} \mathbf{c} f \rangle \cdot (\nabla \cdot \mathbf{u}) = 0
\end{aligned}$$

Finally, we can write the energy conservation as

$$\frac{\partial}{\partial t} \rho E + \nabla \cdot [(\rho E) \mathbf{u} + \mathbf{Q}] + \mathbf{P} : \nabla \mathbf{u} = 0 \tag{224}$$

Alternatively, the above equation can be written as

$$\frac{\partial}{\partial t} \rho E + \nabla \cdot [(\rho E + p) \mathbf{u}] + \nabla \cdot [(\mathbf{\Pi} + \Delta \mathbf{I}) \cdot \mathbf{u} + \mathbf{Q}] = 0 \tag{225}$$

## Appendix C. Derivation of constitutive relations from the Boltzmann transport equation

It was shown in Chapter 3 that the moment equations can be obtained by differentiating the statistical definition of the variable with respect to time and combining it with Boltzmann (Boltzmann-Curtiss for diatomic and linear polyatomic) transport equation which yields the general moment  $h^{(n)}$  as follows [2, 264, 265],

$$\begin{aligned} & \left( \frac{\partial}{\partial t} + \mathbf{u} \cdot \nabla \right) \langle h^{(n)} f \rangle + \langle h^{(n)} f \rangle \cdot \nabla \mathbf{u} + \nabla \cdot \langle \mathbf{c} h^{(n)} f \rangle \\ & - \left\langle f \left( \frac{\partial}{\partial t} + \mathbf{u} \cdot \nabla + \mathbf{c} \cdot \nabla + \frac{j}{I} \frac{\partial}{\partial \theta} \right) h^{(n)} \right\rangle = \Lambda^{(n)} \end{aligned} \quad (226)$$

By defining  $\Psi^{(n)}$  as the flux of  $\langle h^{(n)} f \rangle$  (high-order moments),  $\mathbf{Z}^{(n)}$  kinematic term due to hydrodynamic streaming effect and  $\Lambda^{(n)}$  the dissipation term to account for energy dissipation in the irreversible process as

$$\begin{aligned} \Psi^{(n)} &= \langle \mathbf{c} h^{(n)} f \rangle \\ \mathbf{Z}^{(n)} &= \left\langle f \left( \frac{D}{Dt} + \mathbf{c} \cdot \nabla + \frac{j}{I} \frac{\partial}{\partial \theta} \right) h^{(n)} \right\rangle \\ \Lambda^{(n)} &= \langle h^{(n)} C[f, f_1] \rangle \end{aligned} \quad (227)$$

Moreover, after denoting  $\langle h^{(n)} f \rangle / \rho$  as  $\hat{h}^{(n)}$  the general evolution can be written as

$$\rho \frac{D}{D} \hat{h}^{(n)} + \nabla \cdot \Psi^{(n)} - \mathbf{Z}^{(n)} = \Lambda^{(n)} \quad (228)$$

The constitutive equation for viscous stress tensor  $\mathbf{\Pi} = \langle m[\mathbf{c}\mathbf{c}]^{(2)} f \rangle$  can be derived by taking  $h^{(l)} = m[\mathbf{c}\mathbf{c}]^{(2)}$  as follows

$$\rho \frac{D}{D} \left( \frac{\mathbf{\Pi}}{\rho} \right) + \nabla \cdot \Psi^{(\Pi)} - \mathbf{Z}^{(\Pi)} = \Lambda^{(\Pi)} \quad (229)$$

The kinematic term can be expanded as follows

$$\begin{aligned}
\mathbf{Z}^{(\Pi)} &= \left\langle f \left( \frac{D}{Dt} + \mathbf{c} \cdot \nabla + \frac{j}{I} \frac{\partial}{\partial \theta} \right) h^{(1)} \right\rangle \\
&= \left\langle f \frac{D}{Dt} h^{(1)} \right\rangle + \left\langle f \mathbf{c} \cdot \nabla h^{(1)} \right\rangle + \left\langle f \frac{j}{I} \frac{\partial}{\partial \theta} h^{(1)} \right\rangle \\
&= \left\langle f \frac{D}{Dt} m[\mathbf{c}\mathbf{c}]^{(2)} \right\rangle + \left\langle f \mathbf{c} \cdot \nabla h^{(1)} \right\rangle + \left\langle f \frac{j}{I} \frac{\partial}{\partial \theta} h^{(1)} \right\rangle \\
&= \left\langle f \frac{D}{Dt} m[\mathbf{c}\mathbf{c}]^{(2)} \right\rangle + \left\langle f \frac{D}{Dt} m[\mathbf{c}\mathbf{c}]^{(2)} \right\rangle + \left\langle f \mathbf{c} \cdot \nabla h^{(1)} \right\rangle + \left\langle f \frac{j}{I} \frac{\partial}{\partial \theta} h^{(1)} \right\rangle \\
&= -2 \left[ \mathbf{J} \frac{D\mathbf{u}}{Dt} \right] - 2(p + \Delta) [\nabla \mathbf{u}]^{(2)} - 2[\Pi \cdot \nabla \mathbf{u}]^{(2)}
\end{aligned} \tag{230}$$

In the above equation  $\mathbf{J} = \langle m\mathbf{c}f \rangle$  is the diffusion flux which can be neglected for single species flows. The final equation of constitutive equation for shear stress then reduces to

$$\rho \frac{D}{D} \left( \frac{\Pi}{\rho} \right) + \nabla \cdot \Psi^{(\Pi)} + 2(p + \Delta) [\nabla \mathbf{u}]^{(2)} + 2[\Pi \cdot \nabla \mathbf{u}]^{(2)} = \Lambda^{(\Pi)} \tag{231}$$

The excess normal stress  $\Delta = \left\langle (mC^2/3 - p/n) f \right\rangle$  balance equation can be achieved by setting  $h^{(2)} = mc^2/3 - p/n$ , with  $n$  as number density in the general evolution equation,

$$\rho \frac{D}{D} \hat{h}^{(2)} + \nabla \cdot \Psi^{(2)} - \mathbf{Z}^{(2)} = \Lambda^{(2)} \tag{232}$$

Equivalently,

$$\rho \frac{D}{D} \left( \frac{\Delta}{\rho} \right) + \nabla \cdot \Psi^{(\Delta)} - \mathbf{Z}^{(\Delta)} = \Lambda^{(\Delta)} \tag{233}$$

Again the kinematic term can be expanded as

$$\begin{aligned}
\mathbf{Z}^{(\Delta)} &= \left\langle f \left( \frac{D}{Dt} + \mathbf{c} \cdot \nabla + \frac{j}{I} \frac{\partial}{\partial \theta} \right) h^{(2)} \right\rangle \\
&= \left\langle f \frac{D}{Dt} h^{(2)} \right\rangle + \left\langle f \mathbf{c} \cdot \nabla h^{(2)} \right\rangle + \left\langle f \frac{j}{I} \frac{\partial}{\partial \theta} h^{(2)} \right\rangle \\
&= \left\langle f \frac{D}{Dt} \left( \frac{1}{3} mC^2 - \frac{p}{n} \right) \right\rangle + \left\langle f \mathbf{c} \cdot \nabla \left( \frac{1}{3} mC^2 - \frac{p}{n} \right) \right\rangle + \left\langle f \frac{j}{I} \frac{\partial}{\partial \theta} \left( \frac{1}{3} mC^2 - \frac{p}{n} \right) \right\rangle \\
&= -2\gamma' (\Pi + \Delta \mathbf{I}) : \nabla \mathbf{u} - \frac{2}{3} \gamma' p \nabla \cdot \mathbf{u}
\end{aligned} \tag{234}$$

Therefore, the excess normal stress constitutive relation can be written as

$$\rho \frac{D}{D} \left( \frac{\Delta}{\rho} \right) + \nabla \cdot \Psi^{(\Delta)} + 2\gamma' (\mathbf{\Pi} + \Delta \mathbf{I}) : \nabla \mathbf{u} + \frac{2}{3} \gamma' p \nabla \cdot \mathbf{u} = \Lambda^{(\Delta)} \quad (235)$$

The heat flux  $\mathbf{Q} = \left\langle \left( mC^2 / 2 + H_{rot} - m\hat{h} \right) \mathbf{c} f \right\rangle$  balance equation can be achieved by setting  $h^{(3)} = \left( mC^2 / 2 + H_{rot} - m\hat{h} \right) \mathbf{c}$ , with  $H_{rot}$  and  $\hat{h}$  as rotational Hamiltonian of the molecule and the enthalpy density per unit mass, in the general evolution equation,

$$\rho \frac{D}{D} \hat{h}^{(3)} + \nabla \cdot \Psi^{(3)} - \mathbf{Z}^{(3)} = \Lambda^{(3)}. \quad (236)$$

Similar to derivation previous in previous parameters the kinematic term can be expanded as

$$\rho \frac{D}{D} \left( \frac{\mathbf{Q}}{\rho} \right) + \nabla \cdot \Psi^{(Q)} - \mathbf{Z}^{(Q)} = \Lambda^{(Q)}. \quad (237)$$

Expanding the kinematic term yields

$$\begin{aligned} \mathbf{Z}^{(Q)} &= \left\langle f \left( \frac{D}{Dt} + \mathbf{c} \cdot \nabla + \frac{j}{I} \frac{\partial}{\partial \theta} \right) h^{(3)} \right\rangle \\ &= \left\langle f \frac{D}{Dt} h^{(3)} \right\rangle + \left\langle f \mathbf{c} \cdot \nabla h^{(3)} \right\rangle + \left\langle f \frac{j}{I} \frac{\partial}{\partial \theta} h^{(3)} \right\rangle \\ &= \left\langle f \frac{D}{Dt} \left( \frac{1}{2} mC^2 + H_{rot} - m\hat{h} \right) \right\rangle + \left\langle f \mathbf{c} \cdot \nabla \left( \frac{1}{2} mC^2 + H_{rot} - m\hat{h} \right) \right\rangle \\ &\quad + \left\langle f \frac{j}{I} \frac{\partial}{\partial \theta} \left( \frac{1}{2} mC^2 + H_{rot} - m\hat{h} \right) \right\rangle \\ &= -\psi^{(P)} : \nabla \mathbf{u} - \frac{d\mathbf{u}}{dt} \cdot (\mathbf{\Pi} + \Delta \mathbf{I}) - (p + \Delta) C_p \nabla T - \mathbf{\Pi} \cdot C_p \nabla T - \mathbf{Q} \nabla \mathbf{u} \end{aligned} \quad (238)$$

Finally, the constitutive equation for heat flux can be written as

$$\begin{aligned} \rho \frac{D}{D} \left( \frac{\mathbf{Q}}{\rho} \right) + \nabla \cdot \Psi^{(Q)} + \psi^{(P)} : \nabla \mathbf{u} + \frac{d\mathbf{u}}{dt} \cdot (\mathbf{\Pi} + \Delta \mathbf{I}) + (p + \Delta) C_p \nabla T \\ + \mathbf{\Pi} \cdot C_p \nabla T + \mathbf{Q} \nabla \mathbf{u} = \Lambda^{(Q)} \end{aligned} \quad (239)$$

## Appendix D. Applied basis functions and integration process of the source term vector for triangular elements

In this appendix, the applied basis functions and the analytical integration, which shows that only the first term of  $\Theta'$  vector has non-zero value is provided.

$$\Theta' = \begin{bmatrix} \int_{\Omega_k} \varphi_1(\mathbf{x}) |J'| d\Omega_k \\ \int_{\Omega_k} \varphi_2(\mathbf{x}) |J'| d\Omega_k \\ \vdots \\ \int_{\Omega_k} \varphi_n(\mathbf{x}) |J'| d\Omega_k \end{bmatrix} = \begin{bmatrix} \text{Cell Area}/2 \\ 0 \\ \vdots \\ 0 \end{bmatrix} \quad (240)$$

The vector of basis functions, which is used in order to achieve a third order ( $P^2$ ) solution, is as follows:

$$\begin{bmatrix} \varphi_1(a,b) \\ \varphi_2(a,b) \\ \varphi_3(a,b) \\ \varphi_4(a,b) \\ \varphi_5(a,b) \\ \varphi_6(a,b) \end{bmatrix} = \begin{bmatrix} 1 \\ \frac{1}{2}(1+3b) \\ -\frac{1}{4}(-1+b)(3+5b)a \\ -\frac{1}{2}(-1+b)a \\ \left(\frac{-1}{2}+b+\frac{5b^2}{2}\right) \\ -\frac{1}{8}(-1+b)(1+3b(6+7b))a \end{bmatrix} \quad (241)$$

The transformation Jacobian is  $(1-b)/2$ ; therefore,

$$\begin{aligned} \int_{\Omega_k} \varphi_1(\mathbf{x}) |J'| d\Omega_k &= \int_{-1}^1 \int_{-1}^1 1 \cdot \frac{(1-b)}{2} dadb \\ &= \int_{-1}^1 \int_{-1}^1 1 \cdot \frac{(1-b)}{2} dbda = 1/2 \int_{-1}^1 \left( \left( b - \frac{b^2}{2} \right) \Big|_{-1}^1 \right) da = \frac{1}{2} \int_{-1}^1 \left( \left( 1 - \frac{1}{2} \right) - \left( -1 - \frac{1}{2} \right) \right) da \\ &= \frac{1}{2} \int_{-1}^1 (2) da = a \Big|_{-1}^1 = 1 - (-1) = 2 \end{aligned} \quad (242)$$

$$\begin{aligned}
\int_{\Omega_k} \varphi_2(\mathbf{x}) |J'| d\Omega_k &= \int_{-1}^1 \int_{-1}^1 \frac{1}{2} (1+3b) \frac{(1-b)}{2} dadb = \frac{1}{4} \int_{-1}^1 \int_{-1}^1 (1+2b-3b^2) dadb \\
&= \frac{1}{4} \int_{-1}^{-1} \int_{-1}^{-1} (b+b^2-b^3) dbda = \frac{1}{4} \int_{-1}^1 (b+b^2-b^3) \Big|_{-1}^1 da = \\
&\frac{1}{4} \int_{-1}^1 ((1+1-1) - (-1+1+1)) da = \frac{1}{4} \int_{-1}^1 (0) da = 0
\end{aligned} \tag{243}$$

$$\begin{aligned}
\int_{\Omega_k} \varphi_3(\mathbf{x}) |J'| d\Omega_k &= \int_{-1}^1 \int_{-1}^1 \frac{-1}{2} (-1+b)(3+5b)a \frac{(1-b)}{2} dadb \\
&= \frac{-1}{8} \int_{-1}^1 (-1+b)(3+5b)(1-b) \int_{-1}^1 adadb \\
&= \frac{-1}{16} \int_{-1}^1 (-1+b)(3+5b)(1-b)(a^2) \Big|_{-1}^1 db \\
&= \frac{-1}{16} \int_{-1}^1 (-1+b)(3+5b)(1-b)(1-1) db = 0
\end{aligned} \tag{244}$$

$$\begin{aligned}
\int_{\Omega_k} \varphi_4(\mathbf{x}) |J'| d\Omega_k &= \int_{-1}^1 \int_{-1}^1 \frac{-1}{2} (-1+b)a \frac{(1-b)}{2} dadb \\
&= \frac{-1}{4} \int_{-1}^1 (-1+b)(1-b) \int_{-1}^1 adadb = \frac{-1}{4} \int_{-1}^1 (-1+b)(1-b)(a^2) \Big|_{-1}^1 db \\
&= \frac{-1}{4} \int_{-1}^1 (-1+b)(1-b)(1-1) db = 0
\end{aligned} \tag{245}$$

$$\begin{aligned}
\int_{\Omega_k} \varphi_5(\mathbf{x}) |J'| d\Omega_k &= \int_{-1}^1 \int_{-1}^1 \left( \frac{-1}{2} + b + \frac{5b^2}{2} \right) \frac{(1-b)}{2} dadb \\
&= \int_{-1}^1 \int_{-1}^1 \left( -\frac{5b^3}{2} + \frac{3b^2}{2} + \frac{3b}{2} - \frac{1}{2} \right) dadb = \frac{1}{2} \int_{-1}^1 \left( \left( -\frac{5b^4}{8} + \frac{3b^3}{6} + \frac{3b^2}{4} - \frac{b}{2} \right) \Big|_{-1}^1 \right) da \\
&= \frac{-1}{4} \int_{-1}^1 (0) da = 0
\end{aligned} \tag{246}$$

$$\begin{aligned}
\int_{\Omega_k} \varphi_6(\mathbf{x}) |J'| d\Omega_k &= \int_{-1}^1 \int_{-1}^1 \left( -\frac{1}{8}(-1+b)(1+3b(6+7b))a \right) \frac{(1-b)}{2} dadb \\
&= \int_{-1}^1 \int_{-1}^1 \left( -\frac{1}{8}(-1+b)(1+3b(6+7b)) \frac{(1-b)}{2} \right) adadb \\
&= \int_{-1}^1 \int_{-1}^1 \left( -\frac{1}{8}(-1+b)(1+3b(6+7b)) \frac{(1-b)}{2} \right) \left( \frac{a^2}{2} \Big|_{-1}^1 \right) db \\
&= \int_{-1}^1 \int_{-1}^1 \left( -\frac{1}{8}(-1+b)(1+3b(6+7b)) \frac{(1-b)}{2} \right) \left( \frac{1}{2} - \frac{1}{2} \right) db = 0
\end{aligned} \tag{247}$$

# Bibliography

1. Balachandar, S. and J.K. Eaton, Turbulent dispersed multiphase flow. *Annual Review of Fluid Mechanics*, 2010. **42**: p. 111-133.
2. Myong, R.S., A generalized hydrodynamic computational model for rarefied and microscale diatomic gas flows. *Journal of Computational Physics*, 2004. **195**(2): p. 655-676.
3. Myong, R.S., A full analytical solution for the force-driven compressible Poiseuille gas flow based on a nonlinear coupled constitutive relation. *Physics of Fluids*, 2011. **23**(1): p. 012002.
4. Myong, R.S., On the high Mach number shock structure singularity caused by overreach of Maxwellian molecules. *Physics of Fluids*, 2014. **26**(5): p. 056102.
5. Immer, C., et al., Apollo video photogrammetry estimation of plume impingement effects. *Icarus*, 2011. **214**(1): p. 46-52.
6. Stubbs, T.J., R.R. Vondrak, and W.M. Farrell, Impact of dust on lunar exploration. URL: <http://hefd.jsc.nasa.gov/files/StubbsImpactOnExploration>, 2007. **4075**.
7. Gaier, J.R., *The effects of lunar dust on EVA systems during the Apollo missions*. 2007, NASA Glenn Research Center; Cleveland, OH, United States.
8. He, X., B. He, and G. Cai, Simulation of rocket plume and lunar dust using DSMC method. *Acta Astronautica*, 2012. **70**: p. 100-111.
9. Morris, A., et al., *Modeling the interaction between a rocket plume, scoured regolith, and a plume deflection fence*, in *Earth and Space 2012: Engineering, Science, Construction, and Operations in Challenging Environments*. 2012. p. 189-198.
10. Morris, A.B., et al., Approach for modeling rocket plume impingement and dust dispersal on the moon. *Journal of Spacecraft and Rockets*, 2015. **52**(2): p. 362-374.

11. Abouali, O. and G. Ahmadi, A model for supersonic and hypersonic impactors for nanoparticles. *Journal of Nanoparticle Research*, 2005. **7**(1): p. 75-88.
12. Zare, A., O. Abouali, and G. Ahmadi, Computational investigation of airflow, shock wave and nano-particle separation in supersonic and hypersonic impactors. *Journal of Aerosol Science*, 2007. **38**(10): p. 1015-1030.
13. Abouali, O., S. Saadabadi, and H. Emdad, Numerical investigation of the flow field and cut-off characteristics of supersonic/hypersonic impactors. *Journal of Aerosol Science*, 2011. **42**(2): p. 65-77.
14. Abarghouei, F.K., O. Abouali, and R. Kamali, Numerical investigation of impinging jets in rarefied condition using DSMC method. *Iranian Journal of Science and Technology. Transactions of Mechanical Engineering*, 2014. **38**(M1): p. 69.
15. Yoshihara, H., Rocket exhaust impingement on a ground surface. *Journal of Fluid Mechanics*, 1963. **15**(1): p. 65-73.
16. Carling, J. and B. Hunt, The near wall jet of a normally impinging, uniform, axisymmetric, supersonic jet. *Journal of Fluid Mechanics*, 1974. **66**(1): p. 159-176.
17. Kalghatgi, G. and B. Hunt, The occurrence of stagnation bubbles in supersonic jet impingement flows. *The Aeronautical Quarterly*, 1976. **27**(3): p. 169-185.
18. Lamont, P. and B. Hunt, The impingement of underexpanded, axisymmetric jets on perpendicular and inclined flat plates. *Journal of Fluid Mechanics*, 1980. **100**(3): p. 471-511.
19. Al-Qutub, A. and M. Budair. Experiments on the flow over a flat surface impinged by a supersonic jet, in *31st Joint Propulsion Conference and Exhibit*. 1995.

20. Nakai, Y., N. Fujimatsu, and K. Fujii, Experimental study of underexpanded supersonic jet impingement on an inclined flat plate. *AIAA journal*, 2006. **44**(11): p. 2691-2699.
21. Pamadi, B., On the impingement of supersonic jet on a normal flat surface. *The Aeronautical Quarterly*, 1982. **33**(3): p. 199-218.
22. Powell, A., The sound-producing oscillations of round underexpanded jets impinging on normal plates. *The Journal of the Acoustical Society of America*, 1988. **83**(2): p. 515-533.
23. Krothapalli, A., et al., Flow field and noise characteristics of a supersonic impinging jet. *Journal of Fluid Mechanics*, 1999. **392**: p. 155-181.
24. Henderson, B., The connection between sound production and jet structure of the supersonic impinging jet. *The Journal of the Acoustical Society of America*, 2002. **111**(2): p. 735-747.
25. Inman, J., et al. The effect of impingement on transitional behavior in underexpanded jets, in *47th AIAA Aerospace Sciences Meeting Including The New Horizons Forum and Aerospace Exposition*. 2009.
26. Buchmann, N., et al. High spatial resolution imaging of a supersonic underexpanded jet impinging on a flat plate, in *6th Australian Conference on Laser Diagnostics in Fluid Mechanics and Combustion*. 2011.
27. Mitchell, D.M., D.R. Honnery, and J. Soria, The visualization of the acoustic feedback loop in impinging underexpanded supersonic jet flows using ultra-high frame rate schlieren. *Journal of Visualization*, 2012. **15**(4): p. 333-341.
28. Mason-Smith, N., et al., Shock structures and instabilities formed in an underexpanded jet impinging on to cylindrical sections. *Shock Waves*, 2015. **25**(6): p. 611-622.

29. Khasawneh, K., H. Liu, and C. Cai, Highly rarefied two-dimensional jet impingement on a flat plate. *Physics of Fluids*, 2010. **22**(11): p. 117101.
30. Cai, C., Gaskinetic modeling on dilute gaseous plume impingement flows. *Aerospace*, 2016. **3**(4): p. 43.
31. Cai, S., et al., Rarefaction Effects on Jet Impingement Loads. *Aerospace*, 2017. **4**(3): p. 48.
32. Gimelshein, S., A. Ketsdever, and D. Wadsworth, *Particle Simulation of Plume-Plume and Plume-Surface Interactions*. 2004, California University Los Angeles Department of Mechanical and Aerospace Engineering.
33. Gimelshein, S., et al. The influence of particulates on thruster plume/shock layer interaction at high altitudes, in *43rd AIAA Aerospace Sciences Meeting and Exhibit*. 2004.
34. Lumpkin, F., J. Marichalar, and A. Piplica, *Plume Impingement to the Lunar Surface: A Challenging Problem for DSMC*. 2007, NASA Johnson Space Center; Houston, TX, United States.
35. Lumpkin III, F.E., J. Marichalar, and B.D. Stewart, High fidelity simulations of plume impingement to the international space station. 2012.
36. He, B., et al., Plume aerodynamic effects of cushion engine in lunar landing. *Chinese Journal of Aeronautics*, 2013. **26**(2): p. 269-278.
37. Grabe, M., et al. Numerical investigation of two interacting parallel thruster-plumes and comparison to experiment, in *AIP Conference Proceedings*. 2014. AIP.
38. Wu, J.S., et al., Parallel DSMC simulation of a single under-expanded free orifice jet from transition to near-continuum regime. *Journal of fluids engineering*, 2005. **127**(6): p. 1161-1170.

39. Marichalar, J., et al. Study of plume impingement effects in the lunar lander environment, in *AIP Conference Proceedings*. 2011. AIP.
40. Tosh, A., et al., Numerical analysis of spacecraft rocket plume impingement under lunar environment. *Journal of Spacecraft and Rockets*, 2011. **48**(1): p. 93-102.
41. Roberts, L., The action of a hypersonic jet on a dust layer. 1963.
42. Roberts, L., The interaction of a rocket exhaust with the lunar surface. 1966.
43. Hutton, R.E., Comparison of soil erosion theory with scaled LM jet erosion tests. 1968.
44. Land, N.S. and L.V. Clark, *Experimental investigation of jet impingement on surfaces of fine particles in a vacuum environment*. Vol. 2633. 1965: National Aeronautics and Space Administration.
45. Metzger, P.T., J.E. Lane, and C.D. Immer, *Modification of Roberts' Theory for Rocket Exhaust Plumes Eroding Lunar Soil*, in *Earth & Space 2008: Engineering, Science, Construction, and Operations in Challenging Environments*. 2008. p. 1-8.
46. Metzger, P.T., et al., Jet-induced cratering of a granular surface with application to lunar spaceports. *Journal of Aerospace Engineering*, 2009. **22**(1): p. 24-32.
47. Morris, A., et al. Plume impingement on a dusty lunar surface, in *AIP Conference Proceedings*. 2011. AIP.
48. Morris, A.B., *Simulation of rocket plume impingement and dust dispersal on the lunar surface*. 2012, The University of Texas at Austin.
49. Burt, J. and I. Boyd. Development of a two-way coupled model for two phase rarefied flows, in *42nd AIAA Aerospace Sciences Meeting and Exhibit*. 2004.
50. Gallis, M., J. Torczynski, and D. Rader, An approach for simulating the transport of spherical particles in a rarefied gas flow via the direct simulation Monte Carlo method. *Physics of Fluids*, 2001. **13**(11): p. 3482-3492.

51. Liu, D., et al. On rocket plume, lunar crater and lunar dust interactions, in *48th AIAA Aerospace Sciences Meeting Including the New Horizons Forum and Aerospace Exposition*. 2010.
52. Wright, M.J., G.V. Candler, and D. Bose, Data-parallel line relaxation method for the Navier-Stokes equations. *AIAA journal*, 1998. **36**(9): p. 1603-1609.
53. Roberts, L. and J. South, Comments on exhaust flow field and surface impingement. *AIAA Journal*, 1964. **2**(5): p. 971-973.
54. Roddy, D., J. Rittenhouse, and R.F. Scott, Dynamic penetration studies in crushed rock under atmospheric and vacuum conditions. *AIAA Journal*, 1963. **1**(4): p. 868-873.
55. Scott, R. and H.Y. Ko, Transient rocket-engine gas flow in soil. *AIAA Journal*, 1968. **6**(2): p. 258-264.
56. Lane, J.E., P.T. Metzger, and C.D. Immer, *Lagrangian trajectory modeling of lunar dust particles*, in *Earth & Space 2008: Engineering, Science, Construction, and Operations in Challenging Environments*. 2008.
57. Guet, S. and G. Ooms, Fluid mechanical aspects of the gas-lift technique. *Annual Review of Fluid Mechanics*, 2006. **38**(1): p. 225-249.
58. Sapko, M.J., et al., Experimental mine and laboratory dust explosion research at NIOSH. *Journal of Loss Prevention in the Process Industries*, 2000. **13**(3): p. 229-242.
59. Wan, G., et al., Solids concentration simulation of different size particles in a cyclone separator. *Powder Technology*, 2008. **183**(1): p. 94-104.
60. Metzger, P.T., J. Smith, and J.E. Lane, Phenomenology of soil erosion due to rocket exhaust on the Moon and the Mauna Kea lunar test site. *Journal of Geophysical Research: Planets*, 2011. **116**(E6).

61. Walker, G.P., Generation and dispersal of fine ash and dust by volcanic eruptions. *Journal of Volcanology and Geothermal Research*, 1981. **11**(1): p. 81-92.
62. Popel, S. and A. Gisko, Charged dust and shock phenomena in the solar system. *Nonlinear Processes in Geophysics*, 2006. **13**(2): p. 223-229.
63. Kührt, E. and H. Keller, On the importance of dust in cometary nuclei. *Earth, Moon, and Planets*, 1996. **72**(1): p. 79-89.
64. Marble, F.E., Dynamics of dusty gases. *Annual Review of Fluid Mechanics*, 1970. **2**(1): p. 397-446.
65. Rudinger, G., Some properties of shock relaxation in gas flows carrying small particles. *Physics of Fluids*, 1964. **7**(5): p. 658-663.
66. Satofuka, N. and K. Tokita, Finite difference calculation of gas-particle flows in shock tubes. *Mem. Fac. Ind. Arts, Kyoto Techn. Univ*, 1979. **28**: p. 28-39.
67. Sommerfeld, M., The unsteadiness of shock waves propagating through gas-particle mixtures. *Experiments in Fluids*, 1985. **3**(4): p. 197-206.
68. Lock, G., Experimental measurements in a dusty-gas shock tube. *International Journal of Multiphase Flow*, 1994. **20**(1): p. 81-98.
69. Brennen, C.E., *Fundamentals of Multiphase Flow*. 2005: Cambridge University Press.
70. Miura, H. and I.I. Glass. On a dusty-gas shock tube, in *Proceedings of the Royal Society of London A: Mathematical, Physical and Engineering Sciences*. 1982. The Royal Society.
71. Igra, O., G. Ben-Dor, and Z. Rakib, The effect of dust and water droplets on the relaxation zone developed behind strong normal shock waves. *International Journal of Multiphase Flow*, 1985. **11**(2): p. 121-132.

72. Toumi, I. and A. Kumbaro, An approximate linearized Riemann solver for a two-fluid model. *Journal of Computational Physics*, 1996. **124**(2): p. 286-300.
73. Tiselj, I. and S. Petelin, Modelling of two-phase flow with second-order accurate scheme. *Journal of Computational Physics*, 1997. **136**(2): p. 503-521.
74. Sainsaulieu, L., Finite volume approximation of two phase-fluid flows based on an approximate Roe-type Riemann solver. *Journal of Computational Physics*, 1995. **121**(1): p. 1-28.
75. Saito, T., Numerical analysis of dusty-gas flows. *Journal of Computational Physics*, 2002. **176**(1): p. 129-144.
76. Saito, T., M. Marumoto, and K. Takayama, Numerical investigations of shock waves in gas-particle mixtures. *Shock Waves*, 2003. **13**(4): p. 299-322.
77. Igra, O., I. Elperin, and G. Ben-Dor, Dusty gas flow in a converging-diverging nozzle. *Journal of Fluids Engineering*, 1999. **121**(4): p. 908-913.
78. Igra, O., et al., Shock wave reflection from a wedge in a dusty gas. *International Journal of Multiphase Flow*, 2004. **30**(9): p. 1139-1169.
79. Volkov, A., Y.M. Tsirkunov, and B. Oesterle, Numerical simulation of a supersonic gas–solid flow over a blunt body: The role of inter-particle collisions and two-way coupling effects. *International Journal of Multiphase Flow*, 2005. **31**(12): p. 1244-1275.
80. Pelanti, M. and R.J. LeVeque, High-resolution finite volume methods for dusty gas jets and plumes. *SIAM Journal on Scientific Computing*, 2006. **28**(4): p. 1335-1360.
81. Gurriss, M., D. Kuzmin, and S. Turek, Finite element simulation of compressible particle-laden gas flows. *Journal of Computational and Applied Mathematics*, 2010. **233**(12): p. 3121-3129.

82. Carcano, S., et al., A semi-implicit, second-order-accurate numerical model for multiphase underexpanded volcanic jets. *Geoscientific Model Development*, 2013. **6**(6): p. 1905-1924.
83. Carcano, S., et al., Influence of grain-size distribution on the dynamics of underexpanded volcanic jets. *Journal of Volcanology and Geothermal Research*, 2014. **285**: p. 60-80.
84. Vié, A., et al., Particle-laden flows forced by the disperse phase: Comparison between Lagrangian and Eulerian simulations. *International Journal of Multiphase Flow*, 2016. **79**: p. 144-158.
85. Maxwell, J.C., IV. On the dynamical theory of gases. *Philosophical transactions of the Royal Society of London*, 1867. **157**: p. 49-88.
86. Chapman, S. and T.G. Cowling, *The mathematical theory of non-uniform gases: an account of the kinetic theory of viscosity, thermal conduction and diffusion in gases*. 1970: Cambridge university press.
87. Leaf, B., Derivation of the Boltzmann equation from the Liouville equation. *Physica*, 1972. **59**(2): p. 206-227.
88. Cercignani, C., *Mathematical methods in kinetic theory*. 1969: Springer.
89. Sone, Y., *Kinetic theory and fluid dynamics*. 2012: Springer Science & Business Media.
90. Karniadakis, G., A. Beskok, and N. Aluru, *Micro Flows and Nano Flows: Fundamentals and Simulation*. 2005, New York: Springer-Verlag.
91. Myong, R.S., *Numerical Simulation of Hypersonic Rarefied Flows Using the Second-Order Constitutive Model of the Boltzmann Equation*, in *Advances in Some Hypersonic Vehicles Technologies*. 2018, InTech.

92. Tsien, H.S., Superaerodynamics, mechanics of rarefied gases. *Journal of the Aeronautical Sciences*, 1946. **13**(12): p. 653-664.
93. Macrossan, M.N., *Scaling parameters in rarefied Flow: breakdown of the Navier-Stokes equations*. 2006.
94. Arkilic, E.B., M.A. Schmidt, and K.S. Breuer, Gaseous slip flow in long microchannels. *Journal of Microelectromechanical systems*, 1997. **6**(2): p. 167-178.
95. Myong, R.S., Thermodynamically consistent hydrodynamic computational models for high-Knudsen-number gas flows. *Physics of Fluids*, 1999. **11**(9): p. 2788-2802.
96. Bird, G.A., Breakdown of translational and rotational equilibrium in gaseous expansions. *Aiaa Journal*, 1970. **8**(11): p. 1998-2003.
97. Cheng, H.K., *Hypersonic shock-layer theory of the stagnation region at low Reynolds number*. 1961: Cornell Aeronautical Laboratory.
98. Rapaport, D.C., *The Art of Molecular Dynamics Simulation*. 2 ed. 2004, Cambridge: Cambridge University Press.
99. Fermi, I., et al., *Studies of the nonlinear problems*. 1955, Los Alamos Scientific Lab., N. Mex.
100. Bird, G.A., *Molecular Gas Dynamics and the Direct Simulation of Gas Flows*. 1994: Clarendon Press, Oxford, United Kingdom. 458.
101. Cercignani, C., *Rarefied gas dynamics. From basic concepts to actual calculations*. 2000: Cambridge University Press
102. Xu, K. and J.-C. Huang, A unified gas-kinetic scheme for continuum and rarefied flows. *Journal of Computational Physics*, 2010. **229**(20): p. 7747-7764.
103. Higuera, F., S. Succi, and R. Benzi, Lattice gas dynamics with enhanced collisions. *EPL (Europhysics Letters)*, 1989. **9**(4): p. 345.

104. Benzi, R., S. Succi, and M. Vergassola, The lattice Boltzmann equation: theory and applications. *Physics Reports*, 1992. **222**(3): p. 145-197.
105. Chen, H., S. Chen, and W.H. Matthaeus, Recovery of the Navier-Stokes equations using a lattice-gas Boltzmann method. *Physical Review A*, 1992. **45**(8): p. R5339.
106. Chen, S. and G.D. Doolen, Lattice Boltzmann method for fluid flows. *Annual review of fluid mechanics*, 1998. **30**(1): p. 329-364.
107. Succi, S. and S. Succi, *The lattice Boltzmann equation: for fluid dynamics and beyond*. 2001: Oxford university press.
108. Lallemand, P., et al., Theory of the lattice Boltzmann method: three-dimensional model for linear viscoelastic fluids. *Physical Review E*, 2003. **67**(2): p. 021203.
109. Gressman, P. and R. Strain, Global classical solutions of the Boltzmann equation without angular cut-off. *Journal of the American Mathematical Society*, 2011. **24**(3): p. 771-847.
110. Aristov, V.V.e., *Direct methods for solving the Boltzmann equation and study of nonequilibrium flows*. Vol. 60. 2012: Springer Science & Business Media.
111. Nordsieck, A. and B.L. Hicks, *Monte Carlo evaluation of the Boltzmann collision integral*. 1966, Illinois University at Urbana Coordinated Science Laboratory
112. Yen, S. and H. Schmidt, Monte Carlo solutions of the Boltzmann equation for heat transfer problems. *Rarefied Gas Dynamics*, 1969. **1**: p. 205.
113. Aristov, V.V. and F. Cheremisin, Conservative splitting method for solving the Boltzmann equation. *Zhurnal Vychislitelnoi Matematiki i Matematicheskoi Fiziki*, 1980. **20**: p. 191-207.
114. Aristov, V. Solving the Boltzmann equation for discrete velocities, in *Akademiia Nauk SSSR Doklady*. 1985.

115. Aristov, V., Method of solving the Boltzmann equation by integration over collision parameters in piecewise-constant approximation. *Modern problems in computational aerodynamics*, 1991: p. 357-375.
116. Grad, H., On the kinetic theory of rarefied gases. *Communications on pure and applied mathematics*, 1949. **2**(4): p. 331-407.
117. Eu, B.C., *Kinetic theory and irreversible thermodynamics*. 1992: John Wiley and Sons, Inc.
118. Crowe, C.T., *Multiphase flow handbook*. Vol. 59. 2005: CRC press.
119. Dobran, F., A. Neri, and G. Macedonio, Numerical simulation of collapsing volcanic columns. *Journal of Geophysical Research: Solid Earth*, 1993. **98**(B3): p. 4231-4259.
120. Ongaro, T.E., et al., A parallel multiphase flow code for the 3D simulation of explosive volcanic eruptions. *Parallel Computing*, 2007. **33**(7): p. 541-560.
121. Zhang, Y. and J.M. Reese, Continuum Modelling of Granular Particle Flow with Inelastic Inter-Particle Collisions. *Chemical Engineering Research and Design*, 2003. **81**(4): p. 483-488.
122. Mitter, A., J. Malhotra, and H. Jadeja, The two-fluid modelling of gas-particle transport phenomenon in confined systems considering inter particle collision effects. *International Journal of Numerical Methods for Heat & Fluid Flow*, 2004. **14**(5): p. 579-605.
123. Zhang, Y. and J.M. Reese, Particle–gas turbulence interactions in a kinetic theory approach to granular flows. *International journal of multiphase flow*, 2001. **27**(11): p. 1945-1964.
124. Gidaspow, D., *Multiphase flow and fluidization: continuum and kinetic theory descriptions*. 1994: Academic press.

125. Morsi, S. and A. Alexander, An investigation of particle trajectories in two-phase flow systems. *Journal of Fluid mechanics*, 1972. **55**(2): p. 193-208.
126. Durst, F., D. Miloievic, and B. Schönung, Eulerian and Lagrangian predictions of particulate two-phase flows: a numerical study. *Applied Mathematical Modelling*, 1984. **8**(2): p. 101-115.
127. Soo, S.I., *Fluid dynamics of multiphase systems*. 1967: Waltham, Mass., Blaisdell Pub. Co.
128. Fuks, N.A., *The mechanics of aerosols*. 1989: Dover Publications.
129. Gilbert, M., Velocity lag of particles in linearly accelerated combustion gases. *Journal of Jet Propulsion*, 1955. **25**(1): p. 26-30.
130. Clift, R., J.R. Grace, and M.E. Weber, *Bubbles, drops, and particles*. 2005: Courier Corporation.
131. Henderson, C.B., Drag coefficients of spheres in continuum and rarefied flows. *AIAA journal*, 1976. **14**(6): p. 707-708.
132. White, F.M. and I. Corfield, *Viscous fluid flow*. Vol. 3. 2006: McGraw-Hill New York.
133. Ben-Dor, G., O. Igra, and L. Wang, Shock wave reflections in dust-gas suspensions. *Journal of fluids engineering*, 2001. **123**(1): p. 145-153.
134. Knudsen, J.G. and D.L. Katz, *Fluid dynamics and heat transfer*. 1958: New York, McGraw-Hill Book Company.
135. Ranz, W. and W.R. Marshall, Evaporation from drops. *Chem. Eng. Prog*, 1952. **48**(3): p. 141-146.
136. Gunn, D., Transfer of heat or mass to particles in fixed and fluidised beds. *International Journal of Heat and Mass Transfer*, 1978. **21**(4): p. 467-476.

137. Feng, Z.-G. and E.E. Michaelides, A numerical study on the transient heat transfer from a sphere at high Reynolds and Peclet numbers. *International Journal of Heat and Mass Transfer*, 2000. **43**(2): p. 219-229.
138. van der Hoef, M.A., et al., *Multiscale Modeling of Gas-Fluidized Beds*, in *Advances in Chemical Engineering*, G.B. Marin, Editor. 2006, Academic Press. p. 65-149.
139. Deschambault, R. and I. Glass, An update on non-stationary oblique shock-wave reflections: Actual isopycnics and numerical experiments. *Journal of Fluid Mechanics*, 1983. **131**: p. 27-57.
140. Saito, T. and I.I. Glass, Application of random-choice method to problems in gasdynamics. *Progress in Aerospace Sciences*, 1984. **21**(Supplement C): p. 201-247.
141. Ishii, R., Y. Umeda, and M. Yuhi, Numerical analysis of gas-particle two-phase flows. *Journal of fluid mechanics*, 1989. **203**: p. 475-515.
142. Kim, S.W. and K.S. Chang, Reflection of shock wave from a compression corner in a particle-laden gas region. *Shock Waves*, 1991. **1**(1): p. 65-73.
143. Sommerfeld, M., The structure of particle-laden, underexpanded free jets. *Shock waves*, 1994. **3**(4): p. 299-311.
144. Castellanos, A., et al., Flow regimes in fine cohesive powders. *Physical review letters*, 1999. **82**(6): p. 1156.
145. Anderson, T.B. and R. Jackson, Fluid mechanical description of fluidized beds. Equations of motion. *Industrial & Engineering Chemistry Fundamentals*, 1967. **6**(4): p. 527-539.
146. Tsuo, Y.P. and D. Gidaspow, Computation of flow patterns in circulating fluidized beds. *AIChE Journal*, 1990. **36**(6): p. 885-896.

147. Kuipers, J., et al., A numerical model of gas-fluidized beds. *Chemical Engineering Science*, 1992. **47**(8): p. 1913-1924.
148. Lun, C., et al., Kinetic theories for granular flow: inelastic particles in Couette flow and slightly inelastic particles in a general flowfield. *Journal of fluid mechanics*, 1984. **140**: p. 223-256.
149. Reeks, M., On the constitutive relations for dispersed particles in nonuniform flows. I: Dispersion in a simple shear flow. *Physics of Fluids A: Fluid Dynamics*, 1993. **5**(3): p. 750-761.
150. Gantt, J.A. and E.P. Gatzke, Kinetic theory of granular flow limitations for modeling high-shear mixing. *Industrial & engineering chemistry research*, 2006. **45**(20): p. 6721-6727.
151. Schneiderbauer, S., A. Aigner, and S. Pirker, A comprehensive frictional-kinetic model for gas-particle flows: Analysis of fluidized and moving bed regimes. *Chemical engineering science*, 2012. **80**: p. 279-292.
152. Hansen, J.P. and I.R. McDonald, *Theory of simple liquids*. 1990: Elsevier.
153. Carnahan, N.F. and K.E. Starling, Equation of state for nonattracting rigid spheres. *The Journal of Chemical Physics*, 1969. **51**(2): p. 635.
154. Ma, D. and G. Ahmadi, An equation of state for dense rigid sphere gases. *The Journal of chemical physics*, 1986. **84**(6): p. 3449-3450.
155. Song, Y., E. Mason, and R.M. Stratton, Why does the Carnahan-Starling equation work so well? *The Journal of Physical Chemistry*, 1989. **93**(19): p. 6916-6919.
156. Alder, B. and T. Wainwright, Phase transition in elastic disks. *Physical Review*, 1962. **127**(2): p. 359.
157. Woodcock, L., LV Woodcock, Ann. NY Acad. Sci. 371, 274 (1981). *Ann. NY Acad. Sci.*, 1981. **371**: p. 274.

158. Syal, M. and J.G. Leishman, Modeling of bombardment ejections in the rotorcraft brownout problem. *AIAA journal*, 2013. **51**(4): p. 849-866.
159. Shao, Y., *Physics and modelling of wind erosion*. Vol. 37. 2008: Springer Science & Business Media.
160. Kundu, P. and L. Cohen, Fluid mechanics, 638 pp. *Academic, Calif*, 1990.
161. Chepil, W., The use of evenly spaced hemispheres to evaluate aerodynamic forces on a soil surface. *Eos, Transactions American Geophysical Union*, 1958. **39**(3): p. 397-404.
162. Tritton, D., *Physical fluid dynamics*. Clarendon. 1988, Oxford.
163. White, B.R. and J.C. Schulz, Magnus effect in saltation. *Journal of Fluid Mechanics*, 1977. **81**(3): p. 497-512.
164. Anderson, R.S. and B. Hallet, Sediment transport by wind: toward a general model. *Geological Society of America Bulletin*, 1986. **97**(5): p. 523-535.
165. Zheng, X., L. He, and Y. Zhou, Theoretical model of the electric field produced by charged particles in windblown sand flux. *Journal of Geophysical Research: Atmospheres*, 2004. **109**(D15).
166. Bagnold, R.A., *The physics of blown sand and desert dunes*. 2012: Courier Corporation.
167. Metzger, P.T., et al. Craters formed in granular beds by impinging jets of gas, in *AIP Conference Proceedings*. 2009. AIP.
168. Metzger, P., et al., *Scaling of erosion rate in subsonic jet experiments and Apollo lunar module landings*, in *Earth and Space 2010: Engineering, Science, Construction, and Operations in Challenging Environments*. 2010. p. 191-207.
169. Hirsch, C., *Numerical computation of internal and external flows*. 1990, John Willy & Son.

170. Wang, Z.J., Spectral (finite) volume method for conservation laws on unstructured grids. Basic formulation: Basic formulation. *Journal of Computational Physics*, 2002. **178**(1): p. 210-251.
171. Liu, Y., M. Vinokur, and Z.J. Wang, Spectral difference method for unstructured grids I: Basic formulation. *Journal of Computational Physics*, 2006. **216**(2): p. 780-801.
172. Huynh, H.T. A reconstruction approach to high-order schemes including discontinuous galerkin for diffusion, in *47th AIAA Aerospace Sciences Meeting Including the New Horizons Forum and Aerospace Exposition*. 2009.
173. Wang, Z. and H. Gao. A unifying lifting collocation penalty formulation for the Euler equations on mixed grids, in *47th AIAA Aerospace Sciences Meeting including The New Horizons Forum and Aerospace Exposition*. 2009.
174. Ekaterinaris, J.A., High-order accurate, low numerical diffusion methods for aerodynamics. *Progress in Aerospace Sciences*, 2005. **41**(3-4): p. 192-300.
175. Wang, Z.J., High-order methods for the Euler and Navier–Stokes equations on unstructured grids. *Progress in Aerospace Sciences*, 2007. **43**(1): p. 1-41.
176. Shu, C.W., *Discontinuous Galerkin methods for time-dependent convection dominated problems: Basics, recent developments and comparison with other methods*, in *Building Bridges: Connections and Challenges in Modern Approaches to Numerical Partial Differential Equations*. 2016, Springer. p. 371-399.
177. Reed, W.H. and T.R. Hill, *Triangular mesh methods for the neutron transport equation*, in *Technical Report LA-UR-73-479*. 1973, Los Alamos Scientific Lab., N. Mex.(USA).

178. Cockburn, B. and C.W. Shu, The Runge-Kutta local projection  $P^1$ -discontinuous-Galerkin finite element method for scalar conservation laws. *Rairo-Modélisation Mathématique et Analyse Numérique*, 1988. **25**(3): p. 337-361.
179. Cockburn, B. and C.W. Shu, TVB Runge-Kutta local projection discontinuous Galerkin finite element method for conservation laws. II. General framework. *Mathematics of Computation*, 1989. **52**(186): p. 411-435.
180. Cockburn, B. and C.W. Shu, The Runge–Kutta discontinuous Galerkin method for conservation laws V: multidimensional systems. *Journal of Computational Physics*, 1998. **141**(2): p. 199-224.
181. Cockburn, B., G.E. Karniadakis, and C.W. Shu, *The development of discontinuous Galerkin methods*, in *Discontinuous Galerkin Methods*. 2000, Springer. p. 3-50.
182. Sun, S. and M.F. Wheeler, Discontinuous Galerkin methods for coupled flow and reactive transport problems. *Applied Numerical Mathematics*, 2005. **52**(2): p. 273-298.
183. Klieber, W. and B. Rivière, Adaptive simulations of two-phase flow by discontinuous Galerkin methods. *Computer Methods in Applied Mechanics and Engineering*, 2006. **196**(1–3): p. 404-419.
184. Franquet, E. and V. Perrier, Runge–Kutta discontinuous Galerkin method for the approximation of Baer and Nunziato type multiphase models. *Journal of Computational Physics*, 2012. **231**(11): p. 4096-4141.
185. Franquet, E. and V. Perrier, Runge–Kutta discontinuous Galerkin method for reactive multiphase flows. *Computers & Fluids*, 2013. **83**: p. 157-163.
186. Owkes, M. and O. Desjardins, A discontinuous Galerkin conservative level set scheme for interface capturing in multiphase flows. *Journal of Computational Physics*, 2013. **249**: p. 275-302.

187. Lu, H., et al., Runge–Kutta discontinuous Galerkin method with front tracking method for solving the compressible two-medium flow. *Computers & Fluids*, 2016. **126**: p. 1-11.
188. de Frahan, M.T.H., S. Varadan, and E. Johnsen, A new limiting procedure for discontinuous Galerkin methods applied to compressible multiphase flows with shocks and interfaces. *Journal of Computational Physics*, 2015. **280**: p. 489-509.
189. Dumbser, M. and R. Loubère, A simple robust and accurate a posteriori sub-cell finite volume limiter for the discontinuous Galerkin method on unstructured meshes. *Journal of Computational Physics*, 2016. **319**: p. 163-199.
190. Moortgat, J. and A. Firoozabadi, Mixed-hybrid and vertex-discontinuous-Galerkin finite element modeling of multiphase compositional flow on 3D unstructured grids. *Journal of Computational Physics*, 2016. **315**: p. 476-500.
191. Diehl, D., et al., Numerical solution of Navier–Stokes–Korteweg systems by Local Discontinuous Galerkin methods in multiple space dimensions. *Applied Mathematics and Computation*, 2016. **272**: p. 309-335.
192. Barth, T.J. and D.C. Jespersen, *The design and application of upwind schemes on unstructured meshes*, in *27th Aerospace Sciences Meeting*. 1989, American Institute of Aeronautics and Astronautics.
193. Zhang, X. and C.W. Shu, On positivity-preserving high order discontinuous Galerkin schemes for compressible Euler equations on rectangular meshes. *Journal of Computational Physics*, 2010. **229**(23): p. 8918-8934.
194. Wang, C., et al., Robust high order discontinuous Galerkin schemes for two-dimensional gaseous detonations. *Journal of Computational Physics*, 2012. **231**(2): p. 653-665.

195. Kontzialis, K. and J.A. Ekaterinaris, High order discontinuous Galerkin discretizations with a new limiting approach and positivity preservation for strong moving shocks. *Computers & Fluids*, 2013. **71**: p. 98-112.
196. Dubiner, M., Spectral methods on triangles and other domains. *Journal of Scientific Computing*, 1991. **6**(4): p. 345-390.
197. Karniadakis, G. and S. Sherwin, *Spectral/hp element methods for computational fluid dynamics*. 2013: Oxford University Press.
198. Bassi, F. and S. Rebay, A High-Order Accurate Discontinuous Finite Element Method for the Numerical Solution of the Compressible Navier–Stokes Equations. *Journal of Computational Physics*, 1997. **131**(2): p. 267-279.
199. Harten, A., P.D. Lax, and B.v. Leer, On upstream differencing and Godunov-type schemes for hyperbolic conservation laws. *SIAM review*, 1983. **25**(1): p. 35-61.
200. Toro, E.F., *Riemann Solvers and Numerical Methods for Fluid Dynamics: a Practical Introduction*. 2013: Springer Science & Business Media.
201. LeVeque, R.J., *Conservative Methods for Nonlinear Problems*, in *Numerical Methods for Conservation Laws*. 1990, Springer. p. 122-135.
202. Thomas, J.W., *Numerical partial differential equations: conservation laws and elliptic equations*. Vol. 33. 2013: Springer Science & Business Media.
203. Rusanov, V.V.e., *Calculation of interaction of non-steady shock waves with obstacles*. 1962: NRC, Division of Mechanical Engineering.
204. Nishikawa, H. and K. Kitamura, Very simple, carbuncle-free, boundary-layer-resolving, rotated-hybrid Riemann solvers. *Journal of Computational Physics*, 2008. **227**(4): p. 2560-2581.
205. Arnold, D.N., et al., *Discontinuous Galerkin methods for elliptic problems*, in *Discontinuous Galerkin Methods*. 2000, Springer. p. 89-101.

206. Arnold, D.N., et al., Unified analysis of discontinuous Galerkin methods for elliptic problems. *SIAM journal on numerical analysis*, 2002. **39**(5): p. 1749-1779.
207. Brezzi, F., et al., Discontinuous finite elements for diffusion problems. *Atti Convegno in onore di F. Brioschi (Milano 1997), Istituto Lombardo, Accademia di Scienze e Lettere*, 1999: p. 197-217.
208. Cockburn, B. and C.-W. Shu, The local discontinuous Galerkin method for time-dependent convection-diffusion systems. *SIAM Journal on Numerical Analysis*, 1998. **35**(6): p. 2440-2463.
209. Douglas, J. and T. Dupont, *Interior penalty procedures for elliptic and parabolic Galerkin methods*, in *Computing methods in applied sciences*. 1976, Springer. p. 207-216.
210. Bassi, F., et al. A high-order accurate discontinuous finite element method for inviscid and viscous turbomachinery flows, in *Proceedings of the 2nd European Conference on Turbomachinery Fluid Dynamics and Thermodynamics*. 1997. Antwerpen, Belgium.
211. Zhang, X. and C.W. Shu, Positivity-preserving high order discontinuous Galerkin schemes for compressible Euler equations with source terms. *Journal of Computational Physics*, 2011. **230**(4): p. 1238-1248.
212. Zhang, X. and C.W. Shu, On maximum-principle-satisfying high order schemes for scalar conservation laws. *Journal of Computational Physics*, 2010. **229**(9): p. 3091-3120.
213. Saurel, R., E. Daniel, and J.C. Loraud, Two-phase flows: Second-order schemes and boundary conditions. *AIAA Journal*, 1994. **32**(6): p. 1214-1221.

214. Béreux, F., Zero-relaxation limit versus operator splitting for two-phase fluid flow computations. *Computer Methods in Applied Mechanics and Engineering*, 1996. **133**(1): p. 93-124.
215. LeVeque, R.J. and H.C. Yee, A study of numerical methods for hyperbolic conservation laws with stiff source terms. *Journal of Computational Physics*, 1990. **86**(1): p. 187-210.
216. Lucier, B.J., Error bounds for the methods of Glimm, Godunov and LeVeque. *Siam Journal on Numerical Analysis*, 1985. **22**(6): p. 1074-1081.
217. Myong, R.S., A computational method for Eu's generalized hydrodynamic equations of rarefied and microscale gasdynamics. *Journal of Computational Physics*, 2001. **168**(1): p. 47-72.
218. Karchani, A., *Discontinuous Galerkin Methods for the Second-Order Boltzmann-Based Hydrodynamic Models*. 2017, Gyeongsang National University.
219. Singh, S., *Development of a 3D Discontinuous Galerkin Method for the Second-Order Boltzmann-Curtiss Based Hydrodynamic Models of Diatomic and Polyatomic Gases*. 2018, Gyeongsang National University.
220. Qiu, J., B.C. Khoo, and C.W. Shu, A numerical study for the performance of the Runge–Kutta discontinuous Galerkin method based on different numerical fluxes. *Journal of Computational Physics*, 2006. **212**(2): p. 540-565.
221. Perot, J.B., An analysis of the fractional step method. *Journal of Computational Physics*, 1993. **108**(1): p. 51-58.
222. Myong, R.S. and P.L. Roe, Shock waves and rarefaction waves in magnetohydrodynamics. Part 2. The MHD system. *Journal of Plasma Physics*, 1997. **58**(3): p. 521-552.

223. Woodward, P. and P. Colella, The numerical simulation of two-dimensional fluid flow with strong shocks. *Journal of Computational Physics*, 1984. **54**(1): p. 115-173.
224. Li, H. and G. Ben-Dor, Analysis of double-Mach-reflection wave configurations with convexly curved Mach stems. *Shock Waves*, 1999. **9**(5): p. 319-326.
225. Lewis, C. and D. Carlson, Normal shock location in underexpanded gas and gas-particle jets. *AIAA Journal*, 1964. **2**(4): p. 776-777.
226. Crist, S., D. Glass, and P. Sherman, Study of the highly underexpanded sonic jet. *AIAA journal*, 1966. **4**(1): p. 68-71.
227. Avduevskii, V.S., et al., Flow in supersonic viscous under expanded jet. *Fluid Dynamics*, 1970. **5**(3): p. 409-414.
228. Franquet, E., et al., Free underexpanded jets in a quiescent medium: a review. *Progress in Aerospace Sciences*, 2015. **77**: p. 25-53.
229. Carlson, D. and C. Lewis, Normal shock location in underexpanded gas and gas-particle jets. *AIAA Journal*, 1964. **2**(4): p. 776-777.
230. Draper, J. and P. Jarvinen, Underexpanded gas-particle jets. *AIAA Journal*, 1967. **5**(4): p. 824-825.
231. Bristeau, M.O., *Numerical simulation of compressible Navier-Stokes flows: a GAMM workshop*. Vol. 18. 2013: Springer Science & Business Media.
232. Williamson, C.H., Vortex dynamics in the cylinder wake. *Annual review of fluid mechanics*, 1996. **28**(1): p. 477-539.
233. Zdravkovich, M.M., *Flow around Circular Cylinders: Volume 2: Applications*. Vol. 2. 1997: Oxford university press.
234. Davis, R.W. and E. Moore, A numerical study of vortex shedding from rectangles. *Journal of Fluid Mechanics*, 1982. **116**: p. 475-506.

235. Okajima, A., Strouhal numbers of rectangular cylinders. *Journal of Fluid Mechanics*, 1982. **123**: p. 379-398.
236. Tamura, T. and K. Kuwahara, Numerical study of aerodynamic behavior of a square cylinder. *Journal of Wind Engineering and Industrial Aerodynamics*, 1990. **33**(1-2): p. 161-170.
237. Kelkar, K.M. and S.V. Patankar, Numerical prediction of vortex shedding behind a square cylinder. *International Journal for Numerical Methods in Fluids*, 1992. **14**(3): p. 327-341.
238. Norberg, C., A. Sohankar, and L. Davidson. Numerical simulation of unsteady flows around a square twodimensional cylinder, in *Twelfth Australian Fluid Mechanics Conference*. 1995.
239. Saha, A., G. Biswas, and K. Muralidhar, Three-dimensional study of flow past a square cylinder at low Reynolds numbers. *International Journal of Heat and Fluid Flow*, 2003. **24**(1): p. 54-66.
240. Sharma, A. and V. Eswaran, Heat and fluid flow across a square cylinder in the two-dimensional laminar flow regime. *Numerical Heat Transfer, Part A: Applications*, 2004. **45**(3): p. 247-269.
241. Jackson, C., A finite-element study of the onset of vortex shedding in flow past variously shaped bodies. *Journal of fluid Mechanics*, 1987. **182**: p. 23-45.
242. Zielinska, B. and J. Wesfreid, On the spatial structure of global modes in wake flow. *Physics of Fluids*, 1995. **7**(6): p. 1418-1424.
243. Goujon-Durand, S., P. Jenffer, and J. Wesfreid, Downstream evolution of the Bénard–von Kármán instability. *Physical Review E*, 1994. **50**(1): p. 308.
244. Wesfreid, J., S. Goujon-Durand, and B. Zielinska, Global mode behavior of the streamwise velocity in wakes. *Journal de Physique II*, 1996. **6**(10): p. 1343-1357.

245. Johansson, S.H., L. Davidson, and E. Olsson, Numerical simulation of vortex shedding past triangular cylinders at high Reynolds number using  $k-\epsilon$  turbulence model. *International Journal for Numerical Methods in Fluids*, 1993. **16**(10): p. 859-878.
246. De, A.K. and A. Dalal, Numerical simulation of unconfined flow past a triangular cylinder. *International journal for numerical methods in fluids*, 2006. **52**(7): p. 801-821.
247. Prhashanna, A., A.K. Sahu, and R. Chhabra, Flow of power-law fluids past an equilateral triangular cylinder: Momentum and heat transfer characteristics. *International Journal of Thermal Sciences*, 2011. **50**(10): p. 2027-2041.
248. Chatterjee, D. and B. Mondal, Forced convection heat transfer from an equilateral triangular cylinder at low Reynolds numbers. *Heat and Mass Transfer*, 2012. **48**(9): p. 1575-1587.
249. Crowe, C.T., T.R. Troutt, and J.N. Chung, *Particle Interactions with Vortices*, in *Fluid Vortices*, S.I. Green, Editor. 1995, Springer Netherlands: Dordrecht. p. 829-861.
250. Hunt, J., Industrial and environmental fluid mechanics. *Annual review of fluid mechanics*, 1991. **23**(1): p. 1-42.
251. Saffman, P., On the stability of laminar flow of a dusty gas. *Journal of fluid mechanics*, 1962. **13**(1): p. 120-128.
252. Damseh, R.A., On boundary layer flow of a dusty gas from a horizontal circular cylinder. *Brazilian Journal of Chemical Engineering*, 2010. **27**(4): p. 653-662.
253. Mehrizi, A.A., M. Farhadi, and S. Shayamehr, Natural convection flow of Cu–Water nanofluid in horizontal cylindrical annuli with inner triangular cylinder using

- lattice Boltzmann method. *International Communications in Heat and Mass Transfer*, 2013. **44**: p. 147-156.
254. Xu, J., et al., Fine particle behavior in the air flow past a triangular cylinder. *Aerosol Science and Technology*, 2013. **47**(8): p. 875-884.
255. Bai, B. and X. Li, Deposition of particles in the supersonic flow past a wedge. *Powder Technology*, 2016. **304**: p. 268-273.
256. Zeitoun, O., M. Ali, and A. Nuhait, Convective heat transfer around a triangular cylinder in an air cross flow. *International Journal of Thermal Sciences*, 2011. **50**(9): p. 1685-1697.
257. Green, S., *Fluid vortices*. Vol. 30. 2012: Springer Science & Business Media.
258. Cherne, J.M., *Mechanical Design of the Lunar Module Descent Engine*. 1967: TRW Systems.
259. Hammock Jr, W.R., E.C. Currie, and A.E. Fisher, Apollo experience report: Descent propulsion system. 1973.
260. Simoneit, B., et al., Apollo lunar module engine exhaust products. *Science*, 1969. **166**(3906): p. 733-738.
261. Mitchell, J., et al. Mechanical properties of lunar soil: Density, porosity, cohesion and angle of internal friction, in *Lunar and Planetary Science Conference Proceedings*. 1972.
262. Colwell, J., et al., Lunar surface: Dust dynamics and regolith mechanics. *Reviews of Geophysics*, 2007. **45**(2).
263. Rew, D.Y., et al., Control system design of the Korean lunar lander demonstrator. *Acta Astronautica*, 2014. **94**(1): p. 328-337.

264. Eu, B.C. and Y.G. Ohr, Generalized hydrodynamics, bulk viscosity, and sound wave absorption and dispersion in dilute rigid molecular gases. *Physics of Fluids*, 2001. **13**(3): p. 744-753.
265. Al-Ghoul, M. and B.C. Eu, Generalized hydrodynamic theory of shock waves in rigid diatomic gases. *Physical Review E*, 2001. **64**(4): p. 046303.